



HAL
open science

Coloration-bleaching mechanisms in nickel-tungsten mixed oxides

Simon Redor

► **To cite this version:**

Simon Redor. Coloration-bleaching mechanisms in nickel-tungsten mixed oxides. Material chemistry. Sorbonne Université, 2024. English. NNT : 2024SORUS272 . tel-04833448

HAL Id: tel-04833448

<https://theses.hal.science/tel-04833448v1>

Submitted on 12 Dec 2024

HAL is a multi-disciplinary open access archive for the deposit and dissemination of scientific research documents, whether they are published or not. The documents may come from teaching and research institutions in France or abroad, or from public or private research centers.

L'archive ouverte pluridisciplinaire **HAL**, est destinée au dépôt et à la diffusion de documents scientifiques de niveau recherche, publiés ou non, émanant des établissements d'enseignement et de recherche français ou étrangers, des laboratoires publics ou privés.



Distributed under a Creative Commons Attribution - NonCommercial - NoDerivatives 4.0 International License



COLLÈGE
DE FRANCE
— 1530 —



Sorbonne Université
École doctorale 397 – Physique et Chimie des Matériaux

Collège de France
Chaire Chimie du Solide et de l'Énergie – UMR 8260

Saint-Gobain Recherche Paris
Contrat CIFRE

Coloration-bleaching mechanisms in nickel-tungsten mixed oxides

Simon Redor

Doctoral thesis in Materials Science and Chemistry

Supervised by **Jean-Marie Tarascon** and **Amaury Patissier**

Presented and defended in public on November 4 2024 in front of the jury:

Dr Aline Rougier	Research director, ICMCB	Referee
Prof. Thierry Gacoin	Professor, Département de Physique et de Chimie, École Polytechnique	Referee
Dr Montserrat Casas Cabanas	Group leader, CICenergiGUNE	Examiner
Prof. Martin Bazant	Professor, Departments of Chemical Engineering and Mathematics, MIT	Examiner
Dr Jean-François Guillemoles	Research director, IPVF, ENSCP and École Polytechnique	Examiner & President
Prof. Jean-Marie Tarascon	Professor, CSE, Collège de France	Director
Dr Amaury Patissier	R&D project leader, Saint-Gobain Recherche Paris	Supervisor

This work is licensed under CC BY-NC-ND 4.0. To view a copy of this license, visit <https://creativecommons.org/licenses/by-nc-nd/4.0/>.



Acknowledgements

Acknowledgements

Doing a PhD is kind of an emotional rollercoaster. Throughout the past three years, I have experienced many challenges, but also many joyful moments. I have felt pride, frustration, curiosity, utter despair, and unreasonable hope. Now, I mostly feel grateful for all the people that helped me during this weird and tiresome journey.

I obviously have to thank Jean-Marie for giving me the opportunity to work in his lab and under his supervision. He managed to build an environment that reflects his passion for science and deeply inspired me. He left me a great deal of freedom to explore my subject, but was always available to deliver useful insights when needed. I hope that working in his lab has made me a good scientist.

Next, I have to thank Amaury for letting me discover the wonderful (and very complicated) world of electrochromism. I do not think I could have ever found a PhD subject with as many possibilities to follow. He always showed great interest in the experiments I was undertaking, and was always happy to offer me his help, either with science or with the administrative procedures at Saint-Gobain.

Speaking of which, I also have to thank everyone on the BEYONCE team at Saint-Gobain Research Paris. First of all, for having what is possibly the best project name anyone could ever come up with. Then, for helping me out here and there with my experiments, and sharing what they were working on with me. They are highly skilled, highly knowledgeable people, and it has been a pleasure to work with them, and discover just a little bit of Saint-Gobain through them. So yeah: thanks to Axel, Cynthia, Iryna, Samuel, and Pascal.

Regarding the PhD itself, a lot of the results showed in this manuscript could not have been obtained without the help of a small army of dedicated and wonderful scientists. Thanks to Prof. Artem Abakumov for the TEM imaging; to Frédéric Kanoufi and Louis Godeffroy for the *operando* optical microscopy experiments, and all the data treatment that went with it; to Biao, for being a great supervisor during my internship and in the early months of my PhD, and for teaching me the basics of synthesis and electrochemistry. Thanks as well to David Hrabovsky for the SQUID measurements, Prof. Maxim Avdeev for neutron powder diffraction, Antonella Iadecola for the XAS, and Juan, Ronan, Tatjana and Horyung for the SEM. Thanks a lot to Dominique Foix for welcoming me at IPREM and helping me with XPS experiments. Thanks to Elisa G. for the TGA. And thanks to all the technicians and engineers at Saint-Gobain Research Paris who taught me how to use various machines and equipment; I am especially grateful for the help of Elise Medina on the spin coating process.

Acknowledgements

I also have to give my deepest thanks to Gwenaëlle Rouse, for working with me on $\text{Li}_2\text{Ni}_2\text{W}_2\text{O}_9$. Solving with her the mysteries of $\text{Li}_2\text{Ni}_2\text{W}_2\text{O}_9$ was a very refreshing and a very exciting experience. Her passion for crystallography and solid-state chemistry is awe-inspiring, and it is always a pleasure to have a light-hearted chat with her, be it on science or any other subject. I am truly proud and grateful that I got the opportunity to do science with her.

And how would I have been able to finish my PhD without all the amazing people from the CSE lab? Doctoral students, post-docs, interns, engineers, and permanent researchers: the CSE lab's got them all, and all of them are great people! Whether you want to talk about science, or just have a little bit of chit-chat about life, in the kitchen at 4 PM or around a beer at 6:30, the people from the lab are there for you, and I could not have dreamt of a better crowd to live my day-to-day PhD life with. I have to give a huge shout out to the Synthesis Team (objectively the best team in the lab, sorry for the others): Jacques, Anshuman, Elisa G., Xu, and Biao. And I also have to deliver a special mention to Conrad and Clément M., whom I have taken with me down a rabbit hole of weird and infuriating materials (so sorry about that, guys). Thanks to my office mates: Florian, Mariia, Ezzoubair, Nour, Charlotte, and Maimunah. Thanks to Romain, Jacques, and Damien for Magic the Gathering. And for all the good times, thanks to Ivette, Elisabeth, Clémence, Benjamin, Elisa Q., Elisa G., Cédric, Ronan, Juan, Tatjana, Marina, Wei, and the other members of the lab, past and present.

I am also deeply grateful for the help of Jessica Duvoisin with all administrative endeavors in the lab.

I would also like to thank Dr Aline Rougier and Prof. Thierry Gacoin for agreeing to review this manuscript, as well as Dr Montserrat Casas Cabanas, Prof. Martin Bazant, and Dr Jean-François Guillemoles for accepting to be part of the jury.

I gratefully acknowledge the financial support of the Association Nationale de la Recherche et la Technologie through the CIFRE program. I also thank Clément Guibert and Frédéric Kanoufi for being part of my Comité de Suivi de Thèse.

Finally, I consider myself very lucky to be surrounded by loving friends and family, who supported me throughout the past three years. Thanks to the CPC people, Guilhem, Gina, Niki, Sarah, Alex, Alexis, Alexandre, Lucille, Marine, Valérian, Maxime, Camille, and Pierre, for the hangouts, the laughs, the love. Thanks to the Dream Team, Clémence, Anaïs, and Jérémy; it is always a pleasure to escape from a room with you three. Thanks to Pablo, Julien, and Thibault, for being the best DnD players I could have hoped for. Thanks to my best friend

Acknowledgements

Romane, who always got my back. Thanks to Lucas for being by my side this past year, and for being you. And thanks to my parents, my sisters, and my brother, who have always been there for me and have often listened to me talk about the silly little pieces of colorful glass I have been working on.

Table of Contents

Acknowledgements.....	I
Table of Contents	V
General introduction and thesis outline.....	1
General introduction	2
Thesis outline	4
Chapter 1 – Electrochromism: devices, materials, and challenges.....	7
1.A. The history of electrochromism, from its discovery to modern applications	8
Definition and early studies	8
The architecture of modern ECDs	12
Synthesis process for modern ECDs.....	14
Applications: the case of smart windows.....	16
1.B. Electrochromic materials.....	21
Different types of electrochromic materials	21
Organic electrochromic materials	22
Inorganic electrochromic materials: Prussian blue	24
Inorganic electrochromic materials: transition metal oxides	26
Selecting an electrochromic material for a smart window.....	28
1.C. Nickel oxide thin films: mechanisms and improvements	29
An elusive electrochemical mechanism.....	29
Coloration/bleaching mechanism of NiO in aqueous electrolytes.....	31
Coloration/bleaching mechanism of NiO in non-aqueous electrolytes	33
Improving the performances of NiO thin films: nanostructures and mixed oxides.....	36
Saint-Gobain’s standard magnetron sputtered Li-Ni-W-O thin film.....	43
1.D. Conclusion of the chapter	45
Chapter 2 – Solid-state synthesis, crystal structure, and properties of Li₂Ni₂W₂O₉.....	49
2.A. Motivations	50
2.B. Solid-state synthesis and structural characterization of Li ₂ Ni ₂ W ₂ O ₉	51

Table of contents

Solid-state synthesis.....	51
Crystal structure.....	52
2.C. Electrochemical properties and electrochromism of $\text{Li}_2\text{Ni}_2\text{W}_2\text{O}_9$	58
Electrochemical behavior in half-cells.....	58
Crystal structure changes during cycling.....	62
Electrochemical behavior at lower current densities and lower potentials.....	64
Electrochromism in $\text{Li}_2\text{Ni}_2\text{W}_2\text{O}_9$: insights from <i>operando</i> optical reflection microscopy.....	66
Quantification of the electrochromic properties: statistical and single particle approaches.....	68
2.D. Magnetic properties and magnetic structure of $\text{Li}_2\text{Ni}_2\text{W}_2\text{O}_9$	73
A quick reminder on magnetic properties.....	73
The “429” compounds.....	76
Antiferromagnetism in $\text{Li}_2\text{Ni}_2\text{W}_2\text{O}_9$	77
Magnetic structure of $\text{Li}_2\text{Ni}_2\text{W}_2\text{O}_9$	80
Relationships between magnetic structure and magnetic properties in $\text{Li}_2\text{Ni}_2\text{W}_2\text{O}_9$	85
2.E. Conclusion of the chapter.....	90
Chapter 3 – Understanding Li-Ni-W-O nanocomposite thin films.....	93
3.A. Motivations.....	94
3.B. Electrochemical behaviors of the $\text{Li}_x\text{Ni}_y\text{W}_z\text{O}_n$ powders in Li^+ -conducting electrolyte.....	96
The behavior of the $\text{Li}_x\text{Ni}_y\text{W}_z\text{O}_n$ at high and low potentials.....	96
Comparison with the electrochemical behavior of the nanocomposite Li-Ni-W-O thin films.....	98
3.C. XPS study of Li-Ni-W-O thin films.....	100
Comparison between $\text{Li}_x\text{Ni}_y\text{W}_z\text{O}_n$ powders and a pristine Li-Ni-W-O thin film.....	100
<i>Post-mortem</i> XPS on Li-Ni-W-O thin films at various states of charge.....	103
3.D. Preparation of spin-coated $\text{Li}_x\text{Ni}_y\text{W}_z\text{O}_n$ thin films.....	106
Why study thin films and why use spin coating?.....	106
General description of the spin coating process.....	107
Choice of the reactants.....	109
Citric acid to metallic cation ratio.....	111

Table of contents

Nature of the substrate	111
Other parameters to consider and final description of the spin-coating process	113
3.E. Compositions of the $\text{Li}_x\text{Ni}_y\text{W}_z\text{O}_n$ thin films studied	115
3.F. Microstructural characterization of the $\text{Li}_x\text{Ni}_y\text{W}_z\text{O}_n$ thin films.....	116
Film surface	116
Profilometry	118
3.G. Electrochemical and optical properties of the $\text{Li}_x\text{Ni}_y\text{W}_z\text{O}_n$ thin films.....	119
<i>Operando</i> UV-Visible electrochemistry setup.....	119
Electrochemical responses of $\text{Li}_x\text{Ni}_y\text{W}_z\text{O}_n$ thin films.....	120
XRD on $\text{Li}_x\text{Ni}_y\text{W}_z\text{O}_n$ powders synthesized from spin coating solutions	123
Electrochromic performances of the MS-LNWO and LNWOX thin films.....	125
Electrochemical mechanism in Li-Ni-W mixed oxide thin films.....	128
3.H. Perspectives on spin-coated $\text{Li}_x\text{Ni}_y\text{W}_z\text{O}_n$ thin films	130
The challenges of spin coating.....	130
High-crystallinity $\text{Li}_2\text{Ni}_2\text{W}_2\text{O}_9$ thin films	131
Absorbance spectra of $\text{Li}_x\text{Ni}_y\text{W}_z\text{O}_n$ systems.....	133
3.I. Conclusions of the chapter	134
Conclusions and perspectives.....	139
Abbreviations and symbols	145
Experimental methods.....	149
Experimental methods in Chapter 2.....	150
Experimental methods in Chapter 3.....	154
Appendix	161
A2. Appendix to Chapter 2	162
A3. Appendix to Chapter 3	170
Résumé en français de la thèse	175
References	185

General introduction and thesis outline

General introduction

Climate change represents one of the great environmental and social challenges of the 21st century. The International Panel on Climate Change (IPCC) notes in its Sixth Assessment Report that anthropogenic greenhouse gas (GHG) emissions have increased globally from about 5 GtCO₂-eq/year in 1850 to 59 GtCO₂-eq/year in 2019. This has led to an average increase in the surface temperature of the Earth of 1.1°C (Figure 1). Further global warming could cause an increase in the occurrence of extreme weather events (heatwaves, heavy precipitations, etc.), and have disastrous consequences on human health, food security, human infrastructures, and biodiversity; all of these effects would be observed globally, and especially in developing countries, which are likely to be the most vulnerable to the consequences of climate change. In order to avoid the worst-case scenario, it is necessary to limit the average increase in global warming to 2°C, or even 1.5°C by 2100 (compared to the 1850-1900 time range). Such a feat requires a worldwide effort to decrease GHG emissions, and thus the implementation of new environmental policies in the immediate future¹.

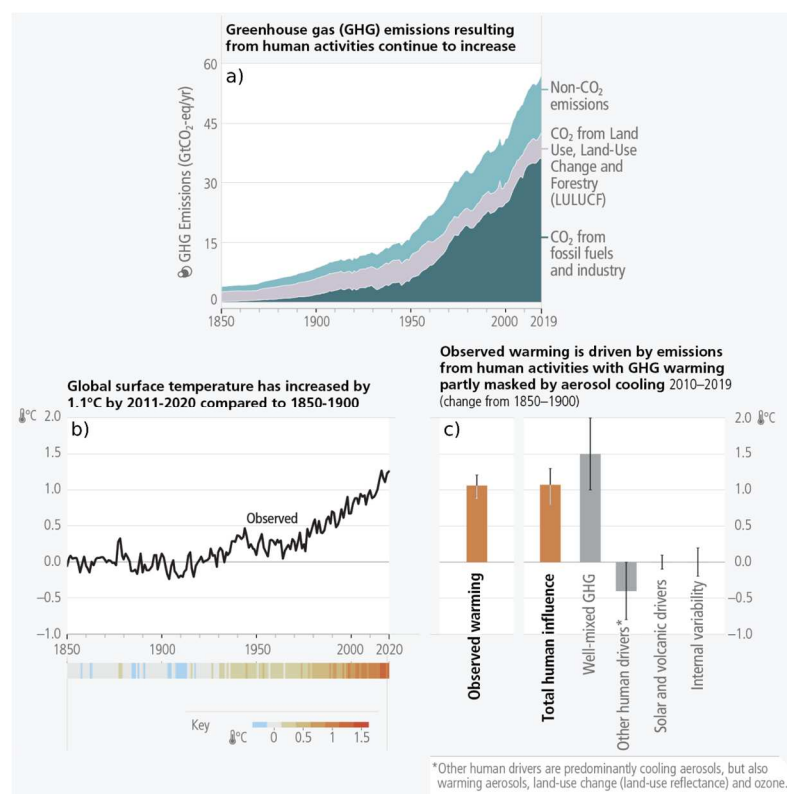


Figure 1 – (a) Global net GHG emissions from 1850 to 2019, in GtCO₂-eq/yr. CO₂ emissions from fossil fuels and the industry sector are in dark blue, those from land use, land-use change, and forestry are in grey, and non-CO₂ emissions are in light blue. (b) Variation in global surface temperature between 1850 and 2019. (c) Estimated contributions of different drivers to the observed global warming between 1850 and 2019. Adapted from IPCC’s AR6 Synthesis report¹.

In 2019, the buildings sector was responsible for 21 % of GHG emissions globally (12 GtCO₂-eq), and more than half of these emissions (57 %) were caused by the generation of heat and electricity (6.9 GtCO₂-eq). Moreover, CO₂ emissions related to the buildings sector increased by 50 % between 1990 and 2019. This increase can be explained by several factors:

- a global population growth, especially in developing countries,
- an increase in the floor area per capita,
- the inefficiency of newly constructed buildings in developing countries and the lack of renovation in developed countries,
- an increase in the number of appliances found in a given household (especially for cooling, and information and communication technologies),
- and the use of fossil fuels for the offsite production of heat and electricity.

From these observations, several pathways emerge to decrease the amount of emissions due to the buildings sector. One of these pathways is the design of buildings using efficient technologies, and thus, efficient materials; such buildings would consume less energy for thermal regulation, and therefore GHG emissions due to offsite heat generation would decrease. On top of that, it is essential to use technologies and materials that are adapted for future climates, which will be characterized by increased temperatures: the need for indoor cooling will become more significant as heatwaves become more common in the years to come².

One of many technologies that could be used for the design of energy efficient buildings is the electrochromic window. By application of a voltage bias, an electrochromic window can switch reversibly between two extreme optical states: a “bleached” state in which the transmittance of the window to visible and near-infrared radiations is at its highest, and a “colored” state, in which the same transmittance is at its lowest^{3,4}. If used correctly, electrochromic windows enable a better indoor temperature control all year long, while maintaining good visual comfort for the building’s occupants⁵.

The architecture of such electrochromic devices is quite similar to that of a battery: two electrodes are separated by an electrolyte; at least one of the electrode is an electrochromic material. When applying a voltage bias, the exchange of small, monovalent cations from one electrode to the other is done through the electrolyte, while the exchange of electrons is ensured by an external circuit and by transparent current collectors at the back of the electrodes. As

their oxidation state change, one or both electrodes change color: this change of optical properties is going to define the efficiency of the final electrochromic device³⁻⁵.

For this reason, it is essential to look into electrochromic materials and their properties. SAGE Electrochromics, Inc., a subsidiary of Saint-Gobain, produces SageGlass electrochromic windows, based on the reversible exchange of Li^+ ions between the device's electrodes⁶. In these devices, the negative electrode (often referred to as the "counter-electrode" or "CE") is a lithium-nickel-tungsten mixed oxide^{7,8}. Although, SageGlass products are very efficient electrochromic devices, there is a lack of understanding when it comes to the relationships between the composition, the structure, and the electrochemical and optical properties of the counter-electrode. Improved knowledge on these aspects could open new paths for the development of electrochromic materials.

The goal of this thesis is to look at several compositions in the $\text{Li}_2\text{O} - \text{NiO} - \text{WO}_3$ ternary phase diagram, in order to study their structural, electrochemical, and optical properties, and to use these results to shine a new light on the electrochromic behavior of the counter-electrode found in SageGlass products.

Thesis outline

This manuscript is divided into four chapters.

Chapter I is dedicated to an in-depth description of the working principles behind electrochromic devices, especially those applied to smart windows. It also provides a short description of the different types of electrochromic materials that can be found in electrochromic devices, with a special focus on inorganic oxides. Finally, it presents what is currently known about the $\text{Li}_x\text{Ni}_{1-y}\text{W}_y\text{O}_n$ counter-electrode used in SageGlass products, in order to identify what questions need to be answered regarding this specific material.

Chapter II deals with $\text{Li}_2\text{Ni}_2\text{W}_2\text{O}_9$, a new material found when exploring the $\text{Li}_2\text{O}-\text{NiO}-\text{WO}_3$ ternary phase diagram. This chapter details the synthesis process of $\text{Li}_2\text{Ni}_2\text{W}_2\text{O}_9$ powder, and the resolution of its crystal structure. It also describes the electrochemical, electrochromic and magnetic properties of this layered material.

Finally, Chapter 3 delves into the electrochemical reactions occurring in $\text{Li}_x\text{Ni}_{1-y}\text{W}_y\text{O}_n$ counter-electrodes when cycled against lithium metal in a liquid cell. In order to gain further insight into the origin of these reactions, a *post-mortem* X-ray photoelectron spectroscopy (XPS) study is conducted, and the electrochemical behavior of different powders in the

$\text{Li}_2\text{O-NiO-WO}_3$ ternary phase diagram (Li_2WO_4 , NiWO_4 , $\text{Li}_2\text{Ni}(\text{WO}_4)_2$, $\text{Li}_2\text{Ni}_2\text{W}_2\text{O}_9$) are used for comparison. Moreover, this chapter describes the optimization of a spin coating process, used to prepare $\text{Li}_x\text{Ni}_y\text{W}_z\text{O}_n$ thin films with different compositions, which can more rigorously be compared with SageGlass counter-electrodes. *Operando* UV-Visible experiments are conducted, in order to confront the optical and electrochemical properties of the spin coated films against those of the counter-electrode.

In the end, this manuscript offers a fresh understanding of the Li-Ni-W mixed oxides: it unveils the properties of a new phase, and offers new leads to comprehend the electrochromism of nanocomposite Li-Ni-W-O thin films.

Chapter 1 – Electrochromism: devices, materials, and challenges

1.A. The history of electrochromism, from its discovery to modern applications

Definition and early studies

The term “electrochromism” was coined by Platt in 1961⁹. It was initially used to describe how the absorption and emission spectra (thus, the color) of certain dyes could be shifted by application of a strong electric field. An updated definition, better fitted to the current state of this field of research, might be written as follow: electrochromism is a property of condensed matter, in which the application of an electrical current or an electric field induces changes in the optical properties of the material studied.

Here, “changes in optical properties” may be understood as changes in the absorption, scattering, and polarization of incident light by the electrochromic material^{10,11}. Although it is often added that these changes should be reversible and persistent³, these aspects are mostly required for modern commercial applications.

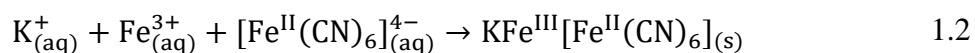


Figure 1.1 - (a) Prussian blue LUX pigment from Kremer Pigmente. Adapted from reference¹². (b) Colors of various tungsten oxides and tungsten metal. Adapted from reference¹³.

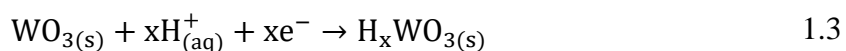
Historically, the discovery of electrochromism can be traced back to two distinct events. In 1706, Dippel and Diesbach perfected the synthesis of iron(III) hexacyanoferrate(II), $Fe_4^{III}[Fe^{II}(CN)_6]_3$, also known as Prussian blue (Figure 1.1a), which was then sold as a pigment. Part of its synthesis process was the oxidation of colorless iron(II) hexacyanoferrate(II) by ambient oxygen¹². A century later, in 1815, Berzelius observed that when heated in a flow of dry hydrogen, WO_3 , a pale yellow powder, was reduced and changed color (Figure 1.1b)^{13–15}. A similar effect was reported by Wöhler in 1824, this time induced by the reduction of WO_3 by sodium metal^{15,16}. The cases of Prussian blue and tungsten(VI) oxide are significant, because these are the first examples of materials changing optical properties due to an oxidation or

reduction reaction, i.e. due to a gain or loss of electrons. These two compounds paved the way for the conception of many devices relying on an electrical current to induce changes in colors.

One of the earliest example of such a device was an early prototype of the fax machine, based on the use of electrochromic reactions and patented by Bain in 1843^{15,17}. It relied on the formation of a Prussian blue compound, using an iron stylus and paper damped with a solution of potassium ferrocyanide, $K_4[Fe^{II}(CN)_6] \cdot 3H_2O$. An electrical current was applied through the tip of the iron stylus; when run across the paper, the metallic iron was oxidized to form ferric ions (Equation 1.1), which reportedly reacted with the potassium ferrocyanide to form the dark Prussian blue compound (Equation 1.2):



Hutchison used a similar approach in 1913, when he conceived an electrochromic display based on the electro-oxidation of phenolphthaleine^{10,18}. Then, in 1930, Kobosew and Nekrassow reported for the first time a coloration change in WO_3 following electrochemical reduction^{15,19}. Reportedly, they coated WO_3 on an unknown, inert electrode substrate, immersed it in an aqueous acid, and upon electrochemical reduction (Equation 1.3), the material went from transparent to dark blue.



This discovery led to the creation of an electrochromic printer, patented by Talmey in 1943^{15,20,21}. Talmey's printing device worked very similarly to those of Bain and Hutchison: a paper was damped with an electrolytic solution, and a stylus served as an electrode. When an electrical current was run through the stylus and it was put in contact with the paper, it would leave a dark blue or black mark. However, compared to Bain's fax machine, Talmey's "electrolytic recording device" used MoO_3 or WO_3 particles present in the paper paste to induce

a color change and make markings on the paper. The electrochemical reaction followed Equation 1.3, with protons coming from the ionization of the electrolytic water. This electrochemical printing method was meant to be faster and more precise than the thermal method also developed at the time; and the use of MoO_3 or WO_3 instead of Prussian blue meant that the stylus did not degrade upon using the printer, as the reaction did not require iron. Moreover, the markings made on the paper were more time-resistant than when other optically active compounds were used, and the paper did not require further treatment after the printing process.

A common point between Bain, Hutchison, and Talmey's inventions was that none of them required a *reversible* electrochromic process. For each device, once the markings were made on the paper, they were not meant to be removed, or at least not electrochemically. Reversibility in electrochromic processes was introduced by Brimm et al. in 1951^{15,22}: they completed the work of Kobosew and Nekrassow, by showing that some sodium tungsten bronze (Na_xWO_3) electrodes could electrochemically and reversibly switch between yellow and dark blue colorations when used as cathodes in dilute H_2SO_4 or NaCl aqueous electrolytes. The Na_xWO_3 material could go from one color to the other by switching the polarity between the cathode and the platinum counter-electrode; thus, the color of the sodium tungsten bronze could be selected by reducing or oxidizing it. Another result of note is that the Na_xWO_3 electrode would maintain an intermediate color if the current applied to the cell was interrupted before the complete transition from one extreme optical state to the other. With this, the Na_xWO_3 showed both *reversible* and *persistent* electrochromism, two characteristics that are very useful to modern ECDs.

It is widely considered that what truly kickstarted the research into electrochromism and ECDs was the work of Deb, first published in 1969^{23,24}. In this seminal paper, Deb presented an “electrophotographic system”, which allowed the user to record an image in an electrochromic WO_3 thin film (500 nm), coated on a photoconductive film of cadmium sulfide (CdS). The electrochromic effect was allowed by the ionization of water adsorbed/inserted in the tungsten oxide film (Equation 1.3)^{24,25}. However, what really stood out in that article was the preliminary work on the electrochromic WO_3 films, more so than the electrophotographic system itself. First, because it was one of the first examples of reversible electrochromism in a *thin film*. But more importantly, the paper presents two different architectures to study the properties of the tungsten oxide thin film. For the first architecture, two gold electrodes are evaporated on the surface of a WO_3 film, coated on a quartz substrate (Figure 1.2b); thus, the

coloration of the film occurs along its surface, between the two gold electrodes, and requires the application of a significant DC electric field ($\sim 10^4 \text{ V.cm}^{-1}$). The second architecture is described by Deb as a “sandwich structure” (Figure 1.2b), and was designed to decrease the voltage bias required to induce the coloration change. In this sandwich structure, the gold electrode is coated on the entire surface of a $\text{WO}_3/\text{SnO}_2/\text{Glass}$ stack. Thus, when the gold is used as a cathode and a 2 V voltage bias is applied through the device, a coloration occurs through the entire bulk of the film. Although, this coloration process is not reversible in this case, this set a precedent for the use of a *stack of thin films* as an ECD. A year later, in 1970, a patent by Deb and Shaw was published, describing a stack structure in which reversible electrochromism could be observed, thanks to the addition of an electron-insulating layer (SiO_2 , CaF_2 or MgF_2) between the electrochromic metal oxide and the counter-electrode (Figure 1.2c). This was what many would call the first ECD^{24,26}.

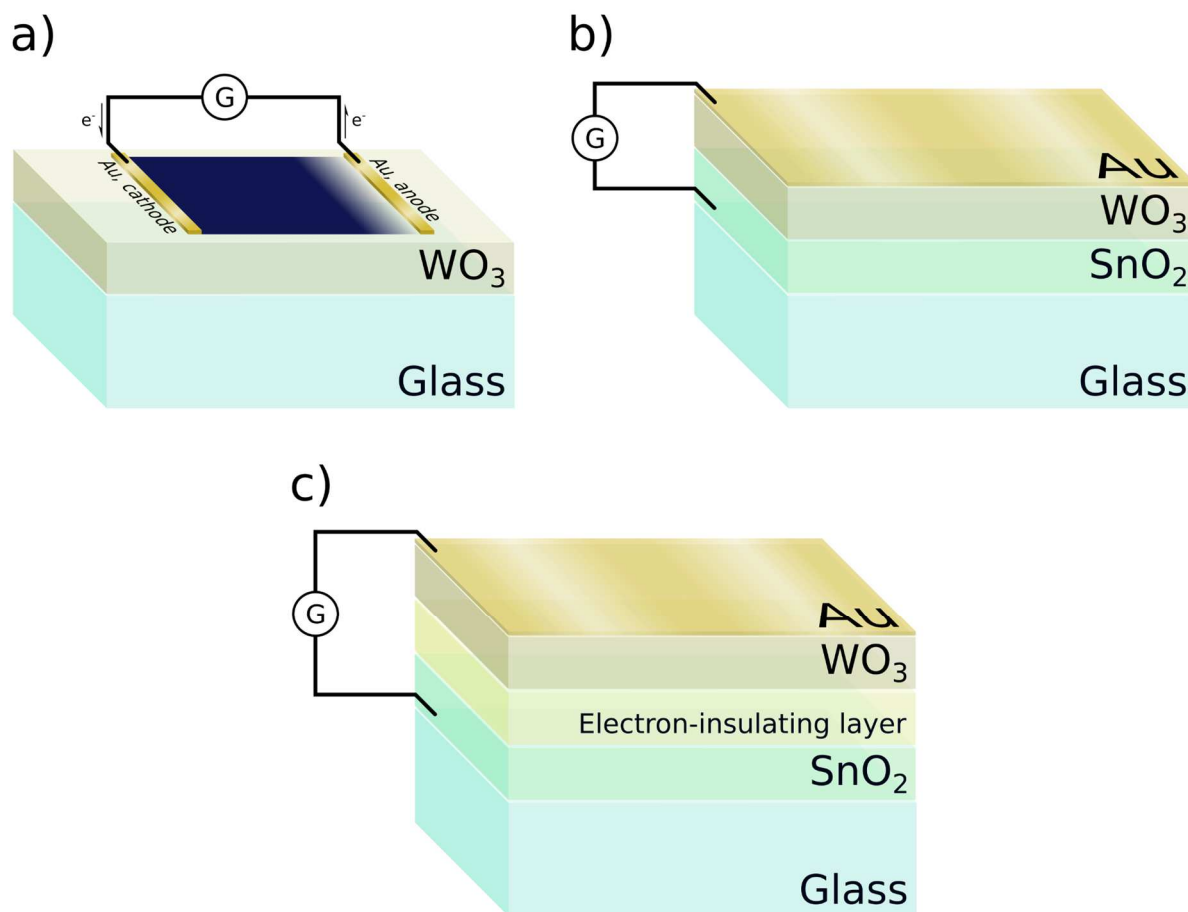


Figure 1.2 – (a) Reversible electrochromic system with a surface electrodes structure described in reference²³.
(b) Irreversible electrochromic system with a “sandwich” electrodes structure described in reference²³.
(c) Reversible electrochromic system with a “sandwich” electrode structure described in reference²⁶.

The architecture of modern ECDs

Following Deb's publications, a lot of work was poured into the development of ECDs, by researchers and companies worldwide. Based on the “sandwich” or “stack” architectures, several designs have been tested through the years, before the scientific community settled for one design in particular.

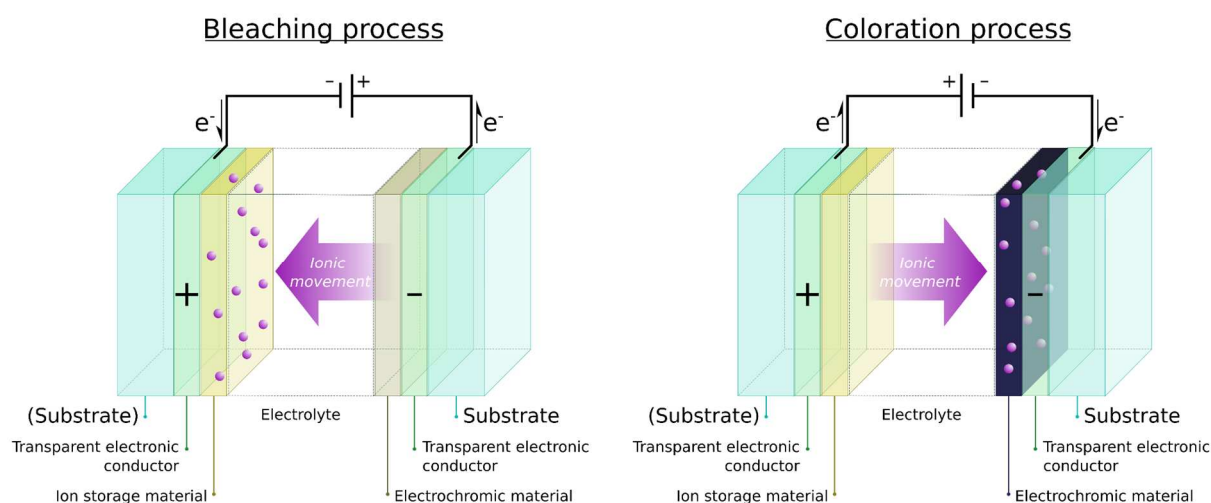


Figure 1.3 – Architecture and basic principles of a 5-layer ECD, during the bleaching process (left) and the coloration process (right).

Figure 1.3 shows the architecture of a typical 5-layer ECD, for which the coloration/bleaching process is based on electrochemical reactions at two electrodes, and the rocking of small cations between these electrodes^{27,28}. Although other electrochromic stack layouts exist^{29–32}, this is one of the most common configurations, that is used for smart windows and many other applications.

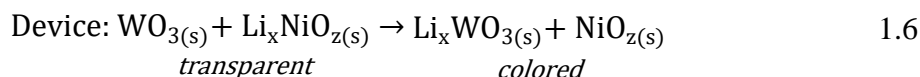
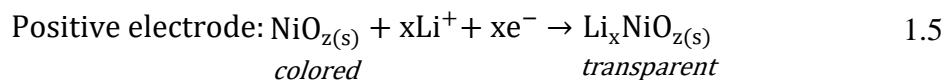
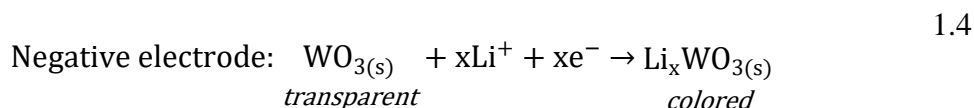
The actual ECD is coated on a substrate, which can be transparent to visible light or reflective, depending on the need the device has to fulfill. In the case of smart windows, the substrate is often transparent: glass can be used for flat windows commonly found in the building sector^{33,34}, while polymer substrates (polypropylene carbonate, polyethylene terephthalate, acrylic, etc.) are more suitable to design flexible windows found in vehicular application^{35–37}. On the other side of the ECD, another “substrate” layer may be in direct contact with the device to encapsulate it³⁵, although this is not always the case³⁸.

The device itself can be divided in three distinct parts: a positive electrode, a negative electrode, and an electrolyte layer. For each electrode, the electrochemically active material is coated on a transparent electronic conductor. These transparent conductors are essential to

efficiently and homogeneously deliver electrons from one electrode to the other during the electrochemical reactions. In the case of smart windows, they also need to be optically neutral in order to avoid disturbing the colorimetry of the window. Indium-doped tin oxide (ITO) is a very common choice for this role because of its relatively high conductivity and high transparency in the visible range^{33,35}, although the price and scarcity of indium have become driving forces behind the research into ITO-free ECDs³⁹. Meanwhile, the electrolyte layer serves as an ionic conductor and an electronic insulator, to protect the device from short-circuits while allowing the transport of the cations necessary for the electrochemical reactions to occur at the electrodes. It also needs to be transparent for the device to work properly. The electrolyte in ECDs can either be a solid inorganic film (lithiated tantalum oxide is a well-known example^{33,40}) or a polymer²⁸. Overall, the electrode/electrolyte/electrode structure of the ECD shown in Figure 1.3, and the reversible electrochemical processes behind its operation make it very similar to secondary batteries⁴¹.

As stated above, the coloration/bleaching process in 5-layer ECDs is based on the rocking of small cations, usually monovalent (H^+ or Li^+), from one electrode to the other. At the negative electrode, an electrochromic thin film is coated on top of the electronic conductor; it usually is a cathodic electrochromic material, which means that its optical transmittance decreases upon reduction. One of the most common material to be found in that position is WO_3 ^{3,27–29,42}. Meanwhile, at the positive electrode, the active material is an ion storage layer: as its name suggests, its main purpose is to store cations while the device is in its bleached state. Some optically passive ion storage materials have been looked into^{42–44}, to avoid disturbing the optical impact of the electrochromic layer at the negative electrode. However, several studies have shown that using another electrochromic material as the ion storage layer could improve the performances of the entire ECD. In particular, anodic electrochromic materials, which see their transmittance decrease upon oxidation, are a particularly good fit for the positive electrode of 5-layer ECD^{45,46}.

This observation is quite intuitive: using two complementary electrochromic materials in the same device, one can increase or decrease the optical density of the two materials at once. Thus, compared with an ECD that uses an optically passive ion storage layer, a device built with an electrochromic ion storage layer will yield a stronger optical response for the same amount of charges exchanged between the two electrodes. Equations 1.4, 1.5 and 1.6 illustrate this by using WO_3 as the cathodic electrochromic material, NiO as the anodic electrochromic ion storage material, and Li^+ as the exchanged cation:



As for the cation exchanged in ECDs, it usually is H^{+33} or $\text{Li}^{+34,47,48}$, since bigger cations are more difficult to insert in the electrochromic materials that constitute the electrodes^{49–53}.

Synthesis process for modern ECDs

Several methods exist to prepare the thin films required for an ECD, and to assemble them together: sol-gel coating^{54–56}, chemical vapor deposition (CVD)^{57,58}, spray pyrolysis^{59,60}, magnetron sputtering^{47,48,61,62}, thermal evaporation^{63,64}, pulsed laser deposition^{65,66}, electrodeposition^{67,68} etc. Of those, magnetron sputtering is probably the most widely used technique (Figure 1.4).

Sputtering is a physical phenomenon in which microscopic particles are ejected from the surface of a material after it has been bombarded by high-energy particles from a plasma or a gas. Sputtering *deposition* uses the sputtering phenomenon to produce a film, by collecting the particles ejected from a target material on a substrate.

In a sealed chamber, the target (cathode) and the substrate (anode) are connected to the same power supply; a vacuum pump and a gas inlet control the composition of the atmosphere in the sputtering chamber. An inert gas (most often a noble gas such as argon) is entered in the chamber through the gas inlet. The electric field between the cathode and the anode ionizes the argon gas and creates a plasma, while magnets behind the target creates a trap that confines the electrons and Ar^+ ions close to the target's surface. The electric field accelerates Ar^+ ions toward the target, and the impact of the ionized particles sputter-ejects superficial target particles. Since these particles are neutrally charged, they are not stopped by the plasma trap, and can travel through the chamber to be deposited on the substrate^{69,70}. *Magnetron* sputtering improves on the standard sputtering method, by designing the target as a magnetron. Electrons

follow an helical motion along the magnetic field lines created by magnets behind the target. Because of this helical motion, the number of collisions with neutral gas particles is more significant, the number of charged particles increases, and the deposition speed is faster. The nature of the power supply will depend, among other things, on the material constituting the target: for conductive targets, such as metals, a simple direct current (DC) voltage generator is enough. For insulating target materials, a radiofrequency (rf) generator coupled with a capacitor are used as the power supply in order to allow the sputtering to occur; rf magnetron sputtering also prevents the accumulation of charges at the cathode surface, and can be performed at lower gas pressure inside the chamber⁷¹.

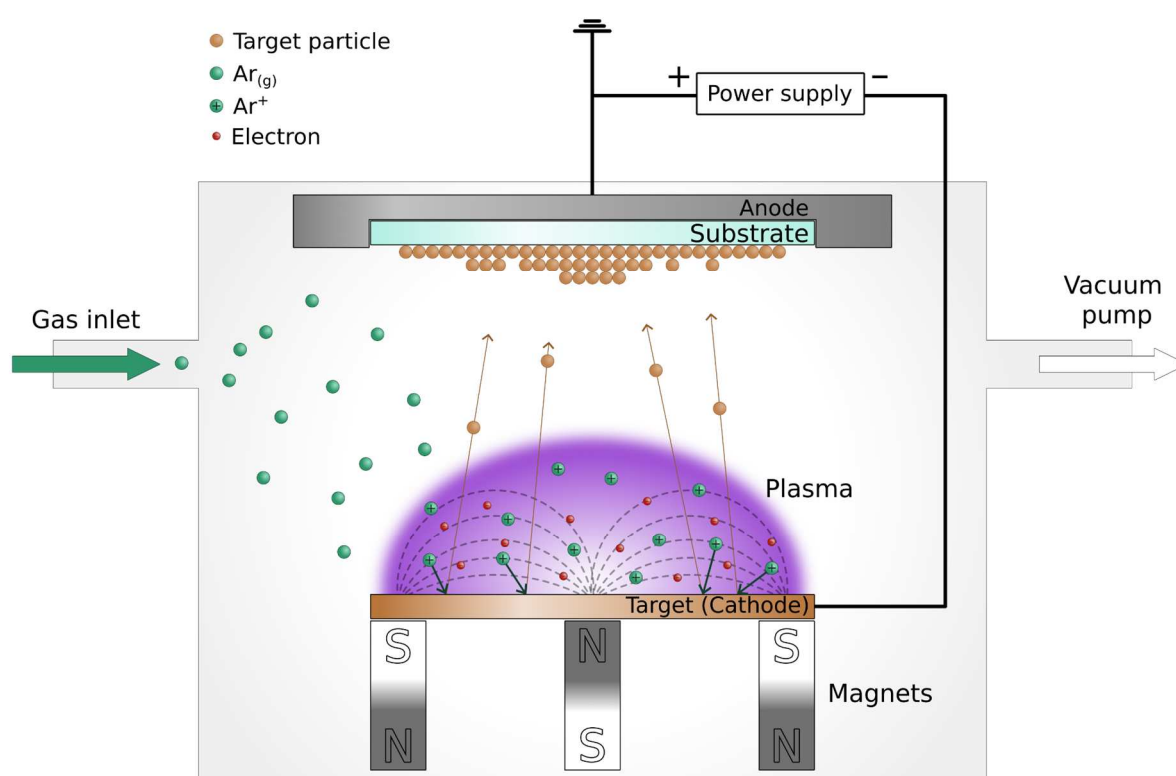


Figure 1.4 – Simplified representation of the magnetron sputtering process.

Magnetron sputtering is a very powerful technique, producing thin films with homogeneous thicknesses (as long as the substrate is smaller than the target). Although it is a complex deposition method, this complexity also means that it can be finely tuned in order to obtain films with a wide array of compositions, microstructures, and properties. For example, reactive sputtering, in which a reactive gas (such as O₂) is introduced at the same time as the inert gas, is very useful to synthesize oxide thin films from metallic targets^{62,72}. Another example is how the pressure and substrate temperature used during the deposition can affect the crystallinity and the morphology of the film^{73,74}. Co-sputtering, in which two or more

distinct targets are sputtered at the same time, can also allow the preparation of systems with a cation mix, such as mixed oxides^{72,75}. And finally, because many compositions can be magnetron sputtered, it is possible to prepare an entire inorganic ECD using this single technique, which is very practical for industrial applications^{34,47,62,76,77}.

Applications: the case of smart windows

The electrochromic effects has been the source of many innovations, with varying degrees of success. ECDs have been studied for applications to dynamic displays^{78–83}, car rearview mirrors⁸⁴, eyewear^{85–88}, thermal control for spacecrafts^{89–91}, and smart windows^{3,33–35}, to name the most important fields of work (Figure 1.5). From this point onward, this manuscript will mainly focus on ECDs used for smart windows, in particular those used in the buildings sector. This will leave room for an efficient discussion on the properties expected for electrochromic materials used for this specific application.

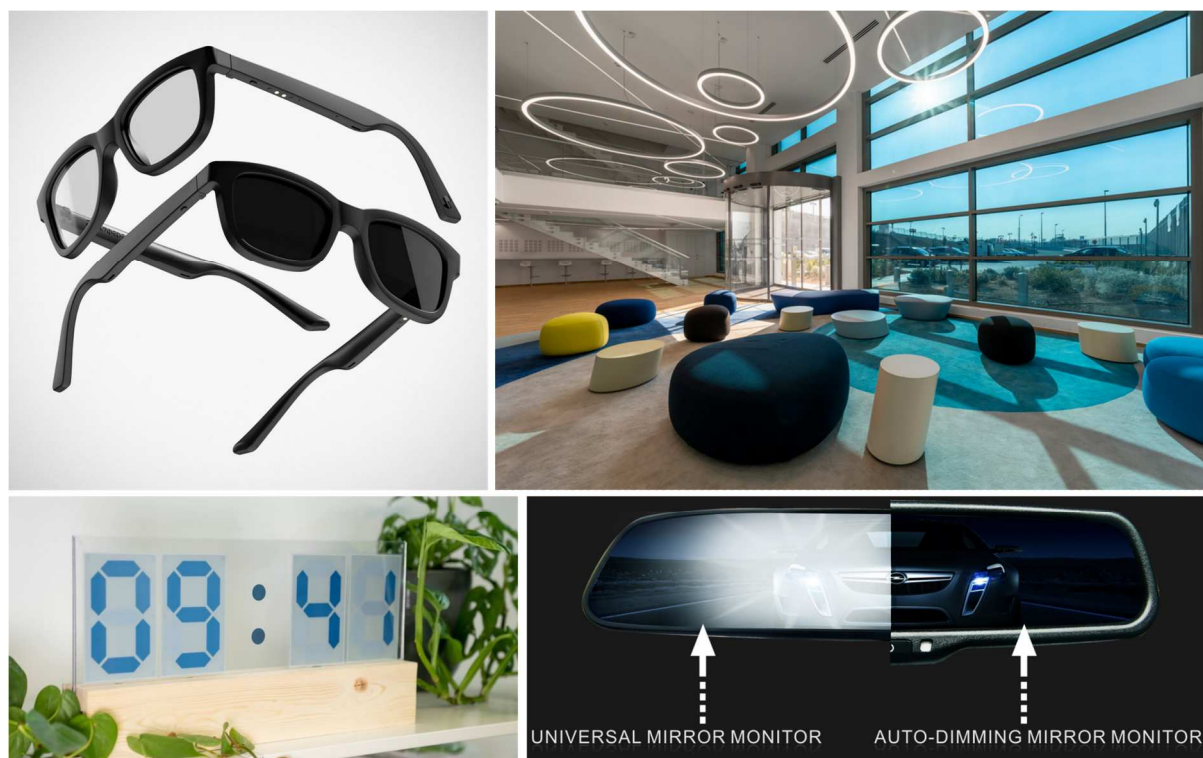


Figure 1.5 – A few examples of commercialized electrochromic devices. Top left: Dusk electrochromic sunglasses by Ampere LLC⁹². Top right: SageGlass Classic electrochromic smart windows by Sage Electrochromics Inc, at the MRS2 data center in Marseille, France⁹³. Bottom left: Electrochromic display by Ynvisible Interactive Inc⁹⁴. Bottom right: Electrochromic rearview mirror by Germid⁹⁵.

The appeal of smart windows in general is to control the amount of solar emissions (visible light and infrared emissions) entering a building, while keeping a constant visual contact with the outside. The latter aspect is one of the main selling point of smart windows,

as regular shading systems (i.e. blinds, shutters, or curtains) will usually completely block the field of view while in use.

The other main selling point of smart windows is the possibility to decrease the energy consumption of a building. Indeed, several studies have reported that buildings equipped with smart windows could consume less energy than with optically passive glazing, especially for indoor cooling⁹⁶⁻⁹⁹. This is because, in their darker/opaque state, smart windows are able to reflect and/or absorb a significant part of infrared emissions that would otherwise heat the equipped building and increase the indoor temperature (Figure 1.6).

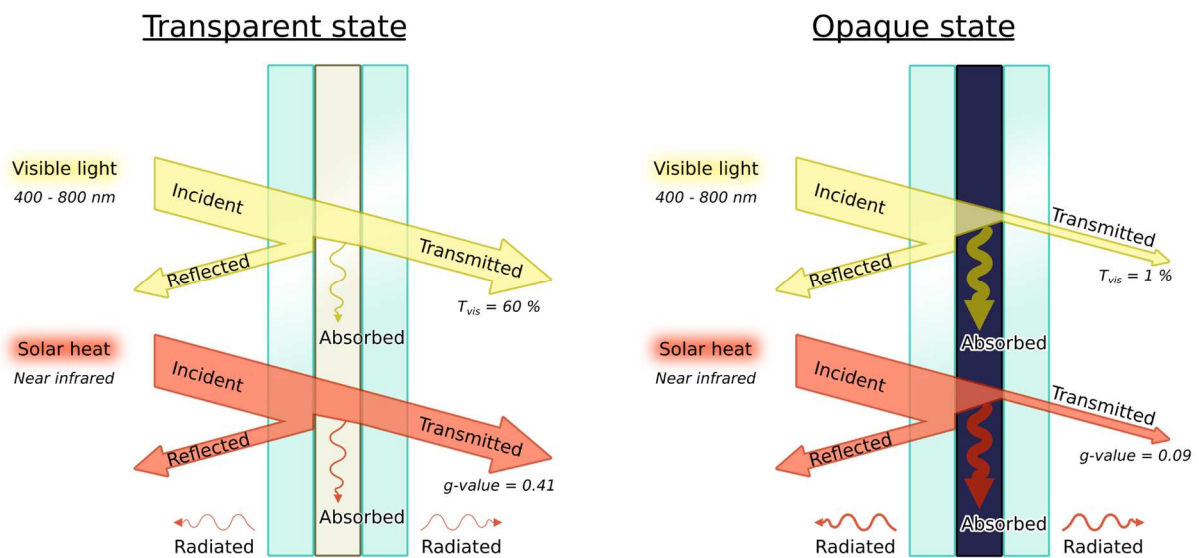


Figure 1.6 – Simplified representations of the main processes involved in the transmission of visible light and solar heat through a smart window, in its transparent state (left) and opaque state (right). The values of the visible light transmission (T_{vis}) and the g-value are those of a SageGlass Clear electrochromic window, as reported in reference⁹⁶.

Several technologies are grouped under the term “smart window”. Direct competitors to ECDs are thermochromic¹⁰⁰ and photochromic¹⁰¹ devices (TCDs and PCDs), which can modulate their optical state thanks to thermal- and photon-based stimuli, respectively. ECDs have a significant advantage over these other two technologies: because the optical state of an ECD is changed by the application of an electric field, it can easily be controlled by an algorithm. Therefore, using different environmental sensors, the optical modulation of an ECD-based smart window can be automated and adapted based on various parameters such as the temperature of the window, the amount of solar radiation entering the building, or the amount of daylight (i.e. illuminance) in a workspace area, to give a few examples^{96,102}. By contrast, the optical state of TCDs and PCDs depends on environmental parameters which cannot be controlled. Simulations show that this difference between “active” and “passive” optical

modulations leads to higher energy savings in buildings equipped with ECD-based windows compared to those equipped with TCD- or PCD-based windows^{96,99}. Other technologies are being researched for an application to external smart windows, such as gasochromic devices¹⁰³, nanocrystals-in-glass materials¹⁰⁴, electrokinetic devices¹⁰⁵, or mechanochromic materials¹⁰⁶. However, none of these technologies seems mature enough to be competitive with ECD smart windows yet.

On top of other dynamic technologies for smart glazing, ECD windows have to compete against static glazings (i.e. that do not go through variations of optical states). Simulation studies usually show that ECD-based windows can provide lower energy consumption in buildings compared to static double glazing units⁹⁶⁻⁹⁹. However, this decrease in energy consumption depends on a significant number of parameters. Firstly, electrochromic windows are not adapted for all locations: they are more energy efficient in regions with warm or hot climates, that is to say regions close to the equator. This can be easily explained by the fact that, since electrochromic windows are mostly reducing energy consumption related to indoor cooling, they are more energy-efficient in regions in which there is a lot of demand for cooling systems, i.e. regions with warm or hot climates. This also means that electrochromic windows are most efficient during the summer. At a local scale, the efficiency of an ECD-based smart window will also depend on the orientation of the façade on which it is placed: electrochromic windows are much more inefficient when they are facing north than when they are facing west, south, or east^{98,107}. Architectural considerations must also be taken into account in the efficiency of electrochromic smart windows: they will usually save more energy in buildings with a high window-to-wall ratio (the ratio of the total surface of external windows to the total surface of external walls)^{97,98}. This means that smart windows may not always be adapted for all types of buildings: office spaces and commercial areas may benefit more from ECDs than residential buildings, for example¹⁰⁸. Finally, the algorithm controlling the coloration of the ECD smart window can also have some impact on the total energy savings^{96,98,109}. Overall, these numerous factors tend to show that the implementation of smart windows has to be carefully thought through, on a case-by-case basis.

Having stated the importance of extrinsic conditions, it is also necessary to highlight that the intrinsic properties of the ECD will play a major role in the energy efficiency of an electrochromic window. Several figures of merits are considered to assess the performances of an ECD:

- **The transmittance modulation, $\Delta T(\lambda)$** , corresponds to the variation in transmittance of the ECD between its bleached state and its colored state. The higher ΔT is on the Visible/Near infrared (NIR) range, the easier it is to control the amount of daylight and solar heat going through the window. This notion is often used in the literature, even though the **optical contrast**, which corresponds to the ratio of the transmittances in the bleached and colored states, is more useful to quantify colorimetric and energetic variations.
- **The luminous transmittance (T_L)** is often expressed as a percentage, and is described by Equation 1.7:

$$T_L = \frac{\int I(\lambda)T(\lambda)V(\lambda)d\lambda}{\int I(\lambda)V(\lambda)d\lambda} \quad 1.7$$

where $I(\lambda)$ is the spectral intensity of a standard illuminant (i.e. a source of light)^{110,111}, $T(\lambda)$ is the spectral transmittance of the ECD, and $V(\lambda)$ is the luminous efficiency function^{112,113}, which corresponds to the average spectral sensitivity of the human eye (Figure 1.7). The T_L is a measure of the amount of optical intensity detectable by the human eye transmitted through the ECD and is independent from the wavelength of the optical signal.

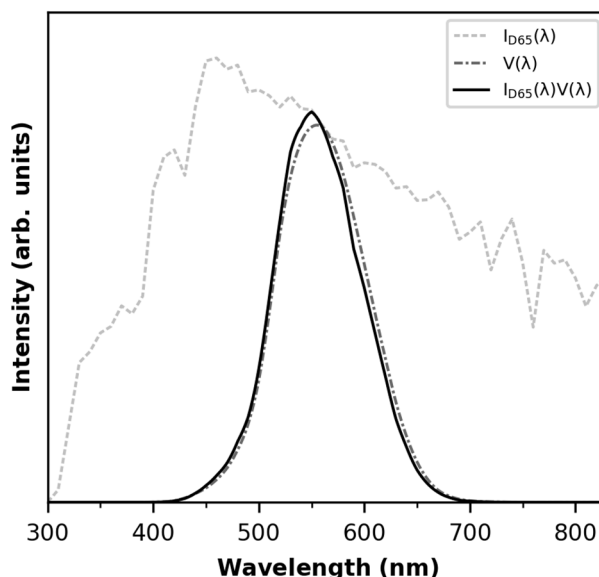


Figure 1.7 – Spectral intensity of the CIE D65 standard illuminant¹¹¹ ($I_{D65}(\lambda)$, dashed line, light gray), luminous efficiency function¹¹³ ($V(\lambda)$, dashdotted line, dark gray), and product of I_{D65} and V (solid line, black).

- **The coloration efficiency ($\eta(\lambda)$)** is expressed in $\text{cm}^2.\text{C}^{-1}$ and can be calculated using Equation 1.8:

$$\eta(\lambda) = \frac{\Delta\text{OD}(\lambda)}{Q} \approx \frac{\log\left(\frac{T_b(\lambda)}{T_c(\lambda)}\right)}{Q} \quad 1.8$$

where ΔOD is the variation in optical density (also called absorbance) of the ECD, T_b and T_c are the transmittance of the device in its bleached and colored states, respectively, and Q (in C.cm^{-2}) is the charge required to go from the bleached state to the colored state. The second half of the equation is acceptable for systems which display small changes in reflectance. The coloration efficiency is a measure of the amount of charges required to make the ECD switch between its bleached and colored state; by extension, it is a measure of how intrinsically energy efficient the bleaching/coloration process is. The higher the coloration efficiency is, the more efficient the ECD is.

- **The coloration and bleaching times (τ_c and τ_b)** are the amounts of time required for the material to go from its bleached state to its colored state (τ_c) and vice versa (τ_b). For a smart window, coloration and bleaching times of a few minutes are acceptable, considering the size of the devices and the fact that the change of optical state is not usually urgent.
- The color of the device can be expressed in **CIELAB coordinates (L^* , a^* , b^*)**¹¹⁴. The a^* and b^* coordinates characterize the saturation (“chroma”) and the hue of the device, and range from negative values (green for a^* ; blue for b^*) to positive values (red for a^* ; yellow for b^*). The exact range depends on the standard illuminant used for calculating the coordinates (for example, the D65 illuminant¹¹¹). L^* ranges from 0 (black) to 100 (white) and represents the optical lightness of the device. Compared to other color spaces, the CIELAB coordinate system offers an almost uniform spatial representation of the colors visible by the human eye (Figure 1.8). What this means in practice is that, for a human observer, a relative variation in coordinates will lead to the same color variation, no matter which part of the CIELAB color space is considered. For example, the color variation from $b^* = 10$ to $b^* = 20$ will be the same as the color variation from $b^* = 80$ to $b^* = 90$.

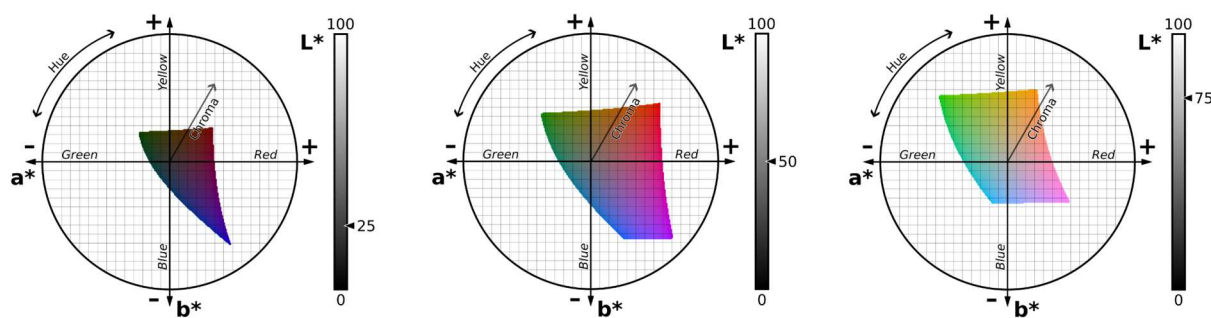


Figure 1.8 – CIELAB color space for $L^* = 25$ (left), 50 (center), and 75 (right), calculated using a D65 standard illuminant. The only colors shown are those that can be represented by the sRGB gamut (i.e. that can be displayed on a computer screen). Each square of the grid is 10 by 10 on the (a^* , b^*) scale.

It is worth pointing out that these figures of merits are not specific to smart windows, and can be applied to other electrochromic devices; the optimal values for each of the properties listed above can vary depending on the application (for example, faster coloration/bleaching times are desirable for electrochromic displays and eyewear). Moreover, these figures of merits are commonly used to study the performances of electrochromic *materials*, independently of any device. Indeed, the best way to improve the intrinsic properties of an ECD is to work on the materials that constitute it.

1.B. Electrochromic materials

Different types of electrochromic materials

Since the discovery of electrochromic properties in WO_3 and Prussian blue, many other electrochromic compounds have been found and studied. Electrochromism can be observed in materials that are very different in nature, from organic to inorganic, from polymers to molecular species. Because all these materials are very different, they display a wide variety of optical properties. This opens many possibilities to play with for the development of ECDs, so much so that one can easily find the right material for the type of device they are trying to make. Moreover, the electrochromism in these different materials can stem from very different electrochemical mechanisms; understanding the origin of the electrochromic properties in one material may not give you the insight you need to fully grasp the electrochromic properties of another material. This is true even for materials of similar nature; for example, the electrochromic mechanism of WO_3 is well reported, while the mechanism underlying the electrochromic properties of nickel oxide (NiO) remains a subject of debate, even though both materials are inorganic oxides. A final consequence of the diversity in electrochromic materials is the emergence of different types of electrochromism. These types were established by

Mortimer¹¹, and are based on the solubility of the electrochromic species. Type-I species are soluble in both oxidized and reduced states. Type-II species are soluble in one redox state, but forms a film on the working electrode when in the other redox state. Meanwhile, type-III species remain as films no matter the redox state. All of these aspects are to take into considerations when conceiving an ECD: because the electrochemical mechanism behind the electrochromic properties can be completely different from one material to another, the architecture of an ECD can vary greatly depending on the optically active material it is based on. Hence why the ECD architecture shown in Figure 1.3 is not universal.

Organic electrochromic materials

Organic electrochromic materials can be divided in smaller categories: molecular compounds, polymeric compounds, and complexes.

Viologens are parts of a family of organic compounds, based on the disubstitution of 4,4'-bipyridine to form 1,1'-disubstituted-4,4'-bipyridinium cations¹¹⁵. After synthesis, they are usually obtained as salts, and exist in three different oxidation states: the initial dicationic state (V^{2+}), a cationic radical state ($V^{\bullet+}$), and a neutral state (V^0) (Figure 1.9). The electrochromic effect in viologens is obtained by switching, through redox reactions, between the colorless/pale yellow dication and the intensely colored cation radical. This color can be controlled by the substituent(s) bonded to the nitrogen atoms, the counter-anion, and the liquid electrolyte used for the electrochemical reaction¹¹⁶; the color ranges from crimson to green¹¹⁷.

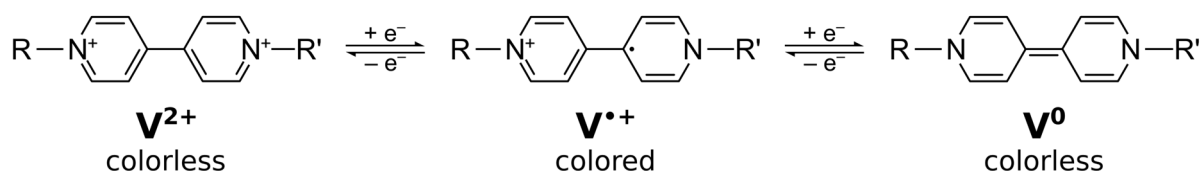


Figure 1.9 – The three main redox states of a standard viologen. R and R' represent any substituent, and can be identical.

Viologens are type-I or type-II electrochromic materials, depending again on the substituent(s); long alkyl chains and aryl substituents make the radical cation insoluble. For example, the original viologen, 1,1'-dimethyl-4,4'-bipyridine, also known as methyl viologen (MV) or paraquat¹¹⁵, is a type-I electrochromic material; this can lead to problems when using the material in an ECD, because the colored state is not persistent. As soon as the reduction current is removed, the colored species diffuses away from the electrode and the device loses its coloration. On the other hand, devices based on type-II viologens, such as heptyl viologen

(HV) display persistent electrochromism, as a stable, colored film is formed on the electrode upon the reduction of the dication to the cation radical¹¹⁸. Viologens can also be used to conceive type-III electrochromic materials, namely organic or inorganic composites. In these cases, the bipyridinium dications are immobilized in (or on) an (in)organic matrix^{119,120}. With this approach, electrochromic films based on viologen species can be elaborated and coated on transparent electrodes. All of these characteristics make viologens quite versatile, although they are not adapted for all commercial applications. They are mostly studied for products that require fast coloration/bleaching times, such as displays¹²¹ and rearview mirrors¹²².

Research about electrochromic polymers is mostly focused on conducting polymers; this rather broad term regroups several families of polymers, such as polythiophenes, polypyrroles, and polyanilines (Figure 1.10), which are heavily studied in the field of electrochromism. Similarly to viologens, the intrinsic optical properties of conducting polymers stems from their characteristic conjugated structure¹²³. Conducting polymers are insulating in their neutral state, but display remarkable electrical conductivities (hence their name) when they are doped, i.e. when they are positively or negatively charged by electrochemical or chemical redox reactions. In fact, they display conductivity values and behaviors that are comparable to those of a metallic material¹²⁴. In general, this high conductivity can be explained both by the delocalization of the electrons by the polymers' π -bonds, and the relatively small gap of the materials in their doped state, which let the electrons move freely along the conjugated polymer chain. But in a broader sense, this increase in conductivity can be explained by a change in the band structure of the polymer; this band structure change is also the source of changes in the optical properties of the conducting polymers.

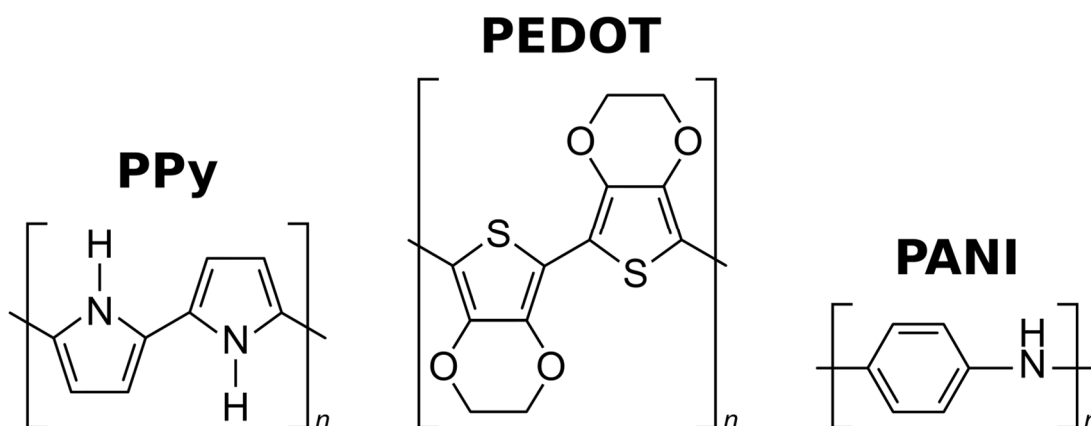


Figure 1.10 – Chemical structures of polypyrrole or PPy (left), poly(3,4-ethylenedioxythiophene) or PEDOT (middle), and polyaniline or PANI (right).

The interest in conducting polymers is due to their good performances as electrochromic materials (fast coloration/bleaching times, high CE, etc.)^{125–128}, but also to the fact that their optical properties can be finely tuned by slight modifications in the monomers used to synthesize them^{129,130}. In particular, in terms of color, those polymers can be blue, green, yellow, orange, red, pink, etc. depending on the monomer used¹³¹. Moreover, because of their mechanical properties, they are well adapted to the conception of flexible, type-III ECDs, especially smart displays^{125,130,132}.

It is also worth mentioning that there are numerous reports on transition metal complexes with organic ligands¹³³, or even polymeric complexes of transition metals¹³⁴. They also display a wide array of colors based on the choice of the transition metal and the ligands. Some MOFs^{135,136} have also been reported to show electrochromic properties.

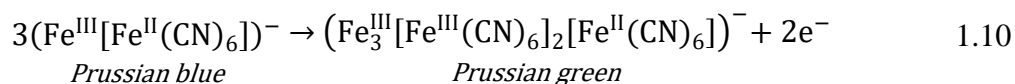
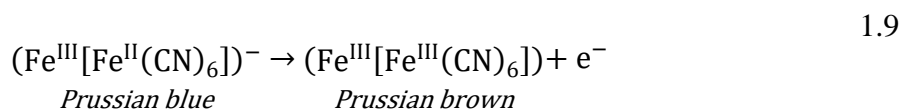
Despite the extensive research available on organic electrochromic materials, it seems that they have not often been considered for a commercial application to smart windows. This may be due to the fact that organic thin films are not always thermally stable, and can be difficult to process at the industrial scale. Liquid-based deposition methods are the only available options, and although they work well in a lab, they are not always adapted for the industrial scale, as it can be difficult to control the morphology of the films produced with these techniques. Moreover, in the case of smart windows for buildings, the surfaces over which the materials must be coated are quite large, making it even more difficult to ensure films of good quality by wet coating methods.

Inorganic electrochromic materials: Prussian blue

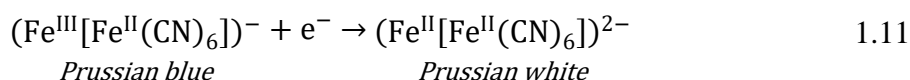
As stated before, Prussian blue played a crucial role in the initial research on electrochromism. Ever since the first report on its electrochemical (de)coloration as a thin film¹³⁷, numerous studies have been produced on the electrochromic properties and performances of Prussian blue, and on those of materials similar to it. Prussian blue and Prussian blue analogues (PBA) share the general formula $M'_j[M''(\text{CN})_6]_k \cdot n\text{H}_2\text{O}$, where M' and M'' are transition metals, and j , k are integers.

Prussian blue is characterized by various redox states, associated to different colors^{138–140}. Full oxidation of the ferrous cation in Prussian blue will lead to the formation of Prussian brown, a golden yellow compound (Equation 1.9); meanwhile, as a bulk material, partial

oxidation of the ferrous cation in Prussian blue yields Prussian green, also known as Berlin's green (Equation 1.10).



Although these two reactions can be associated to electrochromism, the redox process that is more interesting for an application to smart windows is the reduction of Prussian blue to Prussian white, also known as Everitt's salt. This reduction occurs by giving one electron to the ferric cation in Prussian blue (Equation 1.11).



As a thin film, Prussian white is transparent, and is well suited for the bleached state of electrochromic smart windows. Meanwhile, the intense blue coloration of Prussian blue is perfect to absorb incoming light. The reduction of Prussian blue to Prussian white is reversible, and Prussian blue thin films are type-III electrochromic materials, which means that coloration changes are also persistent once the electrical circuit is open¹⁴¹.

The redox processes in Prussian blue is often associated to the (de)insertion of cations in the material^{142–145}. This is due to its crystal structure: in its ideal state, Prussian blue displays a face-centered cubic, double perovskite structure, with wide interstitial sites that accommodates the insertion of small cations (Figure 1.11)¹⁴⁶.

In practice, the presence of defects (namely vacancies, coordinated and interstitial water, and inserted small cations) will often lead to a decrease in the symmetry of the structure, from cubic to rhombohedral, tetragonal or monoclinic^{147,148}. In any case, this redox (de)insertion process makes Prussian blue especially well suited for the five-layer ECD architecture described in Figure 1.3. Most devices based on this material found in the literature use that five-layer architecture, with a monovalent cation (Li^+ , Na^+ , K^+) as the insertion species^{149–152}. In fact, Gesimat has already commercialized such a device, with WO_3 and Prussian blue as the cathodic and anodic electrochromic materials, respectively¹⁵³. Some

studies are also looking into the electrochromic performances of PBAs^{154,155}, but so far it seems that the original $\text{Fe}_4[\text{Fe}(\text{CN})_6]_3$ compound remains the best electrochromic material in this family.

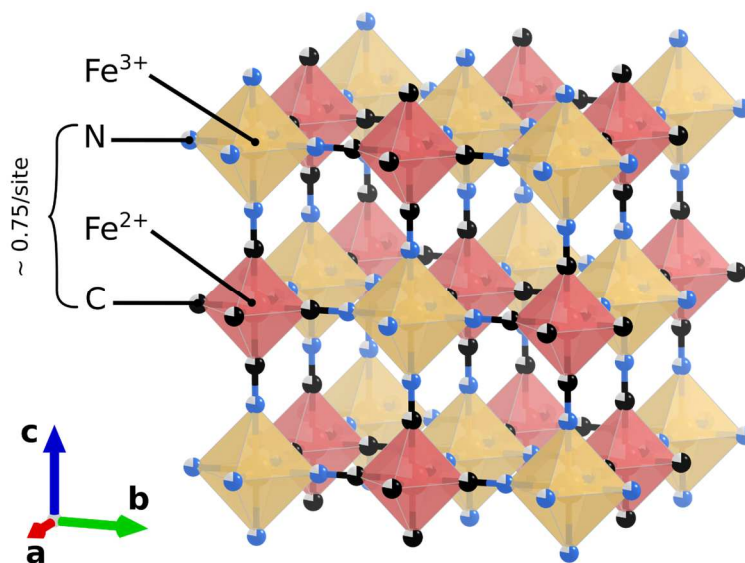


Figure 1.11 – Ideal cubic $Fm\bar{3}m$ crystal structure of Prussian blue $\text{Fe}_4[\text{Fe}(\text{CN})_6]_3$. Fe^{III} is in yellow, Fe^{II} is in red, N is in blue, C is in black.

Inorganic electrochromic materials: transition metal oxides

Following the discovery of electrochromic properties in WO_3 , the electro-optical properties of many other transition metal oxides were characterized in order to find other materials with similar behaviors. Electrochromic transition metal oxides have for general formula M_xO_y , with M the transition metal, and x and y integers dependent on the valence state of M.

Various transition metal oxides have been shown to display electrochromism (Figure 1.12). In addition to WO_3 , cathodic electrochromism has been observed in TiO_2 ¹⁵⁶, Nb_2O_5 ^{157,158}, Ta_2O_5 ¹⁵⁹, and MoO_3 ¹⁶⁰. As for anodic electrochromism, it has been reported in Cr_xO_y ¹⁶¹, Mn_xO_y ^{162,163}, Fe_2O_3 ^{164,165}, RuO_2 ¹⁶⁶, CoO ^{167,168}, Rh_2O_3 ¹⁶⁹, Ir_xO_y ^{170,171}, NiO ^{163,172}, and CuO ¹⁷³. V_2O_5 can display both cathodic and anodic electrochromism, depending on the amount of charges inserted into the material¹⁷⁴. Of all these compounds, WO_3 , MoO_3 , V_2O_5 , Ir_xO_y , and NiO encountered the most success, and are the most studied in the literature, most likely because of their superior properties as electrochromic materials¹⁷⁵.

It is difficult to establish a general mechanism for the electrochromic phenomenon in transition metal oxides, as the exact electrochemical process can vary from one oxide to the

next. Overall, the redox process in these compounds is based on reactions with small cations (H^+ , Li^+ , Na^+ ...) or anions (OH^-) to compensate the loss or the gain of electrons, which is associated to the oxidation/reduction of the transition metal^{3,28}. In that regard, transition metal oxides are similar to Prussian blue, and thus are well suited for five-layer ECDs (Figure 1.3).

Period	Group 1	2	3	4	5	6	7	8	9	10	11	12	13	14	15	16	17	18
1	H																	He
2	Li	Be											B	C	N	O	F	Ne
3	Na	Mg											Al	Si	P	S	Cl	Ar
4	K	Ca	Sc	Ti	V	Cr	Mn	Fe	Co	Ni	Cu	Zn	Ga	Ge	As	Se	Br	Kr
5	Rb	Sr	Y	Zr	Nb	Mo	Tc	Ru	Rh	Pd	Ag	Cd	In	Sn	Sb	Te	I	Xe
6	Cs	Ba	*	Hf	Ta	W	Re	Os	Ir	Pt	Au	Hg	Tl	Pb	Bi	Po	At	Rn
7	Fr	Ra	**	Rf	Db	Sg	Bh	Hs	Mt	Ds	Rg	Cn	Nh	Fl	Mc	Lv	Ts	Og

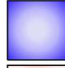

Legend:
 Anodic electrochromism
 Cathodic electrochromism

Figure 1.12 – Periodic table showing transition metals that can yield electrochromic oxides. Elements associated to anodic electrochromism have a blue background, while those associated to cathodic electrochromism have a red background. Lanthanides (*) and actinides (***) are not shown for the sake of simplicity.

The electrochemical behavior of any of these oxides is also dependent on the type of electrolyte used to charge/discharge it. The distinction is especially important between aqueous electrolytes, for which the inserted ions will often be H^+ or OH^- ^{176–180}, and polymer, inorganic liquid, or solid electrolytes^{77,171,181}, for which the redox process often relies on the insertion of an alkali cation like Li^+ .

One of the main strengths of transition metal oxides is the wide array of synthesis processes through which they can be produced. M_xO_y thin films can be obtained through liquid-based techniques^{182–184} and electrodeposition¹⁸⁵, but also through vacuum deposition techniques^{186,187}, such as the magnetron sputtering method described earlier in this chapter. This is especially useful to obtain uniform films on substrate with large surface area, and as a consequence, transition metal oxides are used in most ECDs for commercialized smart windows⁹⁶.

In particular, WO_3 is almost always the cathodic electrochromic material in these ECDs^{33–35,48,96,153}, owing to its great performances, the good understanding of its electrochemical mechanism, and its color range (from transparent to dark blue), which is pleasant for a building's inhabitants. As for the anodic electrochromic material, it can vary from one brand of smart window to the next. If it is also a transition metal oxide, it can either

be NiO or Ir_xO_y, as they display better performances than other anodic electrochromic oxides¹⁷⁵. However, the high cost of iridium seems to push both researchers and industrials toward the use of NiO thin films as the counter-electrode in ECDs¹⁸⁸. What is appealing about having both WO₃ and NiO as the electrode materials in a five-layer ECD is the opportunity of assembling the entire device using only one method. Indeed, if the electrolyte is an oxide (such as Ta₂O₅ or SiO_x) and a transparent conductive oxide (e.g. ITO) is used as the current collector for both electrodes, then the entire device can be prepared using a vacuum deposition technique. Each layer of the device simply needs to be coated successively, on the same substrate, by changing the target material^{47,48}.

Selecting an electrochromic material for a smart window

Table 1.1 – Performances of a few electrochromic materials found in the literature.

Material	Anodic/Cathodic	Type	Coloration range	$\eta(\lambda)$ (cm ² .C ⁻¹)	$\Delta T(\lambda)$ (%)	Cycling stability	Ref.
Methyl viologen	Cathodic	Type-I	Colorless ↔ Purple	/	/	/	189
Heptyl viologen	Cathodic	Type-II	Colorless ↔ Purple	/	/	/	177
PEDOT on halloysite nanotube	Cathodic	Type-III	Sky blue ↔ Dark blue	174.3 (600 nm)	59.3 (600 nm)	> 500 cycles	190
PANI/MXene composite	Anodic	Type-III	Gray ↔ Dark green	210.48 (1079 nm)	93 (1079 nm)	1000 cycles	191
Prussian blue	Anodic	Type-III	Colorless ↔ Dark blue	87.4 (680 nm)	44.9 (680 nm)	> 150 cycles	143
WO ₃	Cathodic	Type-III	Colorless ↔ Dark blue	~64 to 87 (528 nm)	~65 (528 nm)	> 500 cycles	192
MoO ₃	Cathodic	Type-III	Colorless ↔ Dark blue	13 (633 nm)	43 (633 nm)	/	193
NiO _x H _y	Anodic	Type-III	Colorless ↔ Dark brown	57 (550 nm)	21 (550 nm)	1000 cycles	194
Ir _x O _y	Anodic	Type-III	Colorless ↔ Blue-gray	26.6 (550 nm)	35 (550 nm)	> 2000 cycles	171

In the end, the choice of an electrochromic material for smart windows will depend on numerous parameters: its electrochromic performances, its long-term stability, its coloration range, how easy it is to process, its cost, etc. Table 1.1 summarizes some of the performances for a few electrochromic materials.

When comparing the electrochromic performances of different types of materials, it appears that if WO_3 and NiO are better than other transition metal oxides, they are not particularly superior to materials of different natures, such as conducting polymers and Prussian blue. In fact, they usually display lower coloration efficiency. However, WO_3 and NiO are transparent in their bleached state, a characteristic that sets them apart from conducting polymers. Thus, the choice of transition metal oxides for an application to smart windows probably stems from a compromise between sufficient electrochromic performances, an optimal coloration range, and an easy processing by magnetron sputtering.

1.C. Nickel oxide thin films: mechanisms and improvements

Using an electrochromic material for the counter electrode in an ECD-based smart window, on top of the electrochromic working electrode, can greatly improve the performances of the entire device, especially in terms of coloration efficiency and transmittance modulation. For this reason, there has been extensive research into understanding and improving electrochromic NiO thin films, to use them at the positive electrode of ECDs.

An elusive electrochemical mechanism

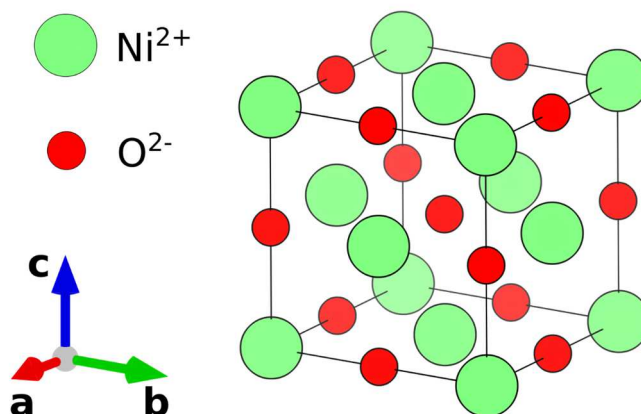


Figure 1.13 – Ideal crystal structure of cubic rocksalt NiO . Nickel centers are in green, oxygen centers are in red.

NiO thin films have been the source of many disagreements in the field of electrochromism, and there is a lack of consensus on their electrochemical behavior, both in aqueous electrolytes and in non-aqueous Li^+ -conducting electrolytes.

Theoretically, NiO has an ideal rocksalt-like cubic structure, crystallizing in the $Fm\bar{3}m$ space group with a lattice parameter of 4.178 \AA (Figure 1.13)¹⁹⁵. In practice, there is always a

slight deficit of nickel in the material; hence, the general formula NiO_z , with $z > 1$, is more accurate to describe nickel oxide. This nickel deficit manifests itself by the formation of nickel vacancies in the lattice structure of the compound¹⁹⁶, granting it a p-type conductivity¹⁹⁷.

In its initial Ni^{2+} state, NiO is mostly transparent to visible light. This can be explained by its band structure (Figure 1.14): NiO's bandgap, E_g , is roughly equal to 3.81 eV¹⁹⁸, and is characterized by a charge-transfer excitation process, due to a strong hybridization of the nickel's 3d orbitals and the oxygen's 2p orbitals^{199,200}. The maximum wavelength absorbed by NiO due to its bandgap transition, λ_g , can be estimated using Equation 1.12:

$$eE_g = h \frac{c}{\lambda_g} \quad 1.12$$

where e is the elementary charge of an electron (1.6×10^{-19} C), h is Planck's constant (6.63×10^{-34} J.s) and c is the speed of light (3×10^8 m.s⁻¹). For $E_g = 3.81$ eV, λ_g is equal to 382 nm, which is below the range of visible light (400 nm to 800 nm): NiO's bandgap is too high to efficiently absorb visible light.

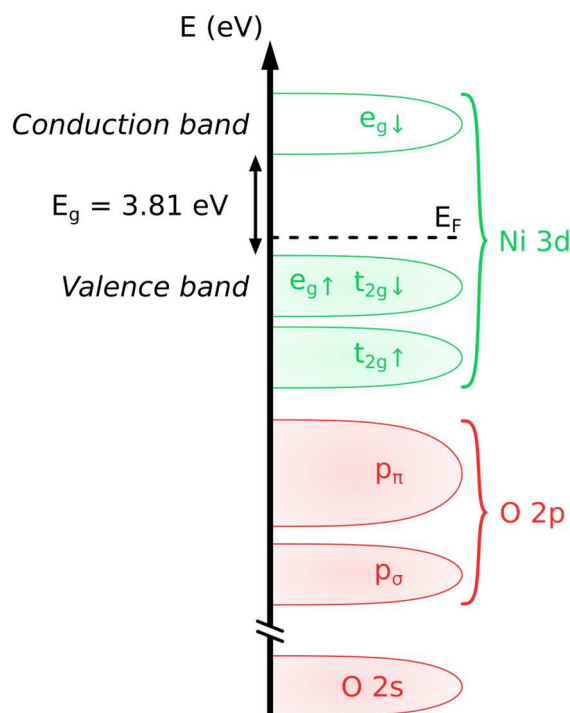


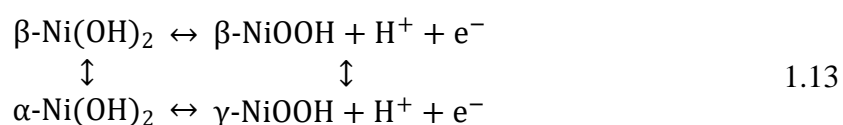
Figure 1.14 – Simplified representation of the band structure of NiO. E_F designates the Fermi level and E_g the bandgap. Majority spin states and minority spin states are represented by \uparrow and \downarrow , respectively. Filled states are shaded.

Things become more complicated when considering nickel oxide thin films in their oxidized state. Upon oxidation, NiO becomes dark brown and its transmittance across the

visible range decreases¹⁷⁵. However, the exact mechanism behind this redox reaction is uncertain.

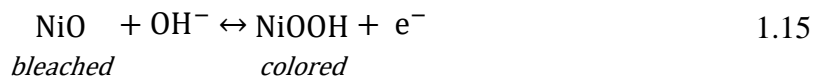
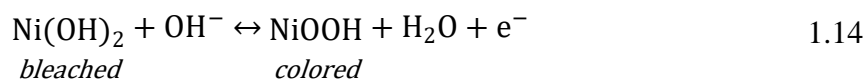
Coloration/bleaching mechanism of NiO in aqueous electrolytes

In the case of aqueous electrolytes, it has been suggested that NiO thin films, in their bleached state, are actually a mixture of oxide and hydroxide species, the latter being formed due to direct contact with the electrolyte or atmospheric water^{200,201}. The Bode reaction scheme^{202,203} offers a simplified explanation of how the oxidation of the hydroxide species occurs to form oxohydroxide NiOOH species (Equations 1.13):



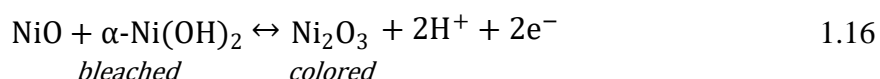
$\beta\text{-Ni(OH)}_2$ and $\alpha\text{-Ni(OH)}_2$ display similar crystal structures: a layered stacking with an hexagonal packing of hydroxyl ions, each layer being made of alternating rows of edge-sharing NiO₆ octahedra. However, $\alpha\text{-Ni(OH)}_2$ has a higher water content than $\beta\text{-Ni(OH)}_2$ (its actual formula is $\alpha\text{-Ni(OH)}_2 \cdot n\text{H}_2\text{O}$, with n between 0.41 and 0.7). The water molecules intercalates themselves between the Ni(OH)₂ layers; as a consequence, the interlayer distance in the α -phase is higher than in the β -phase, and adjacent layers have little to no tendency to orient relative to one another²⁰⁴. Those two distinct Ni(OH)₂ structures lead to two different NiOOH phases upon oxidation, $\beta\text{-NiOOH}$ for $\beta\text{-Ni(OH)}_2$, and $\gamma\text{-NiOOH}$ for $\alpha\text{-Ni(OH)}_2$. Nickel oxohydroxides species are much more absorbent in the visible light range than their hydroxide counterparts; indeed, NiOOH species have a lower bandgap (1.5-1.8 eV) than Ni(OH)₂ species (3.6-3.9 eV, similar to NiO). They can absorb electromagnetic radiation thanks to a band-to-band transition, allowed by a charge transfer process between oxygen anions and high valency nickel cations²⁰⁵.

Equation 1.13 supposes that the electrochemical mechanism in aqueous electrolytes is based upon the exchange of protons. However, another mechanism, based instead on the exchange of hydroxyl anions, has also been suggested by Carpenter et al.²⁰⁶ (Equation 1.14) and Delichère et al.²⁰⁷ (Equation 1.15):



Interestingly, Delichère et al. proposed the mechanism shown in Equation 1.15 because they believed their film, in its reduced state, did not contain any trace of nickel hydroxide. Raman spectroscopy of their pristine “NiO” film, left in an aqueous electrolyte (1 M NaOH), did show the features of NiO, but not those of Ni(OH)₂. Meanwhile, the Raman spectra of the same film after electrochemical oxidation clearly showed peaks matching with NiOOH²⁰⁷.

Another mechanism, reported by Avendaño and Granqvist^{200,208}, extends the Bode scheme described in Equation 1.13. Their idea, supported by X-ray Photoelectron Spectroscopy (XPS) experiments, was that for hydrated NiO films, only the surface of the material is transformed into nickel hydroxide, whereas the bulk remains nickel oxide. However, they also observed that, upon application of an anodic current, Ni²⁺ from the bulk oxide phase was oxidized to Ni³⁺, on top of the Ni²⁺ from the surface hydroxide phases. Thus, they extended the Bode scheme, to add a reaction between bulk NiO and surface Ni(OH)₂ upon the removal of two protons, leading to the formation of absorbing nickel superoxide Ni₂O₃ (Equation 1.16):



Yet, in a later study by Ren et al., the idea of nickel superoxide (or the mixed valency Ni₃O₄) forming during the redox process was dismissed, as it did not explain the electro-optical behavior of NiO thin films²⁰⁹. They observed that when cycled in aqueous electrolytes, NiO thin films showed improvements in both current density and transmittance modulation during the initial cycles, which then slowly degraded upon further cycling (Figure 1.15a,b).

Instead of stating that either protons or hydroxyl ions were (de)inserted into the thin film, Ren et al. stated that both ionic species were involved in the redox process. They proposed a mechanism in three steps. First, the “evolution” of NiO into NiOOH according to Equation 1.15; then, the reversible (de)insertion of H⁺ based on the reactions described in Bode’s scheme (Equation 1.13); finally, the isolation/degradation of several parts of the active

material, due to intercalated water being trapped as a result of the reaction described by Equation 1.14. This three-step process is summarized in Figure 1.15c,d.

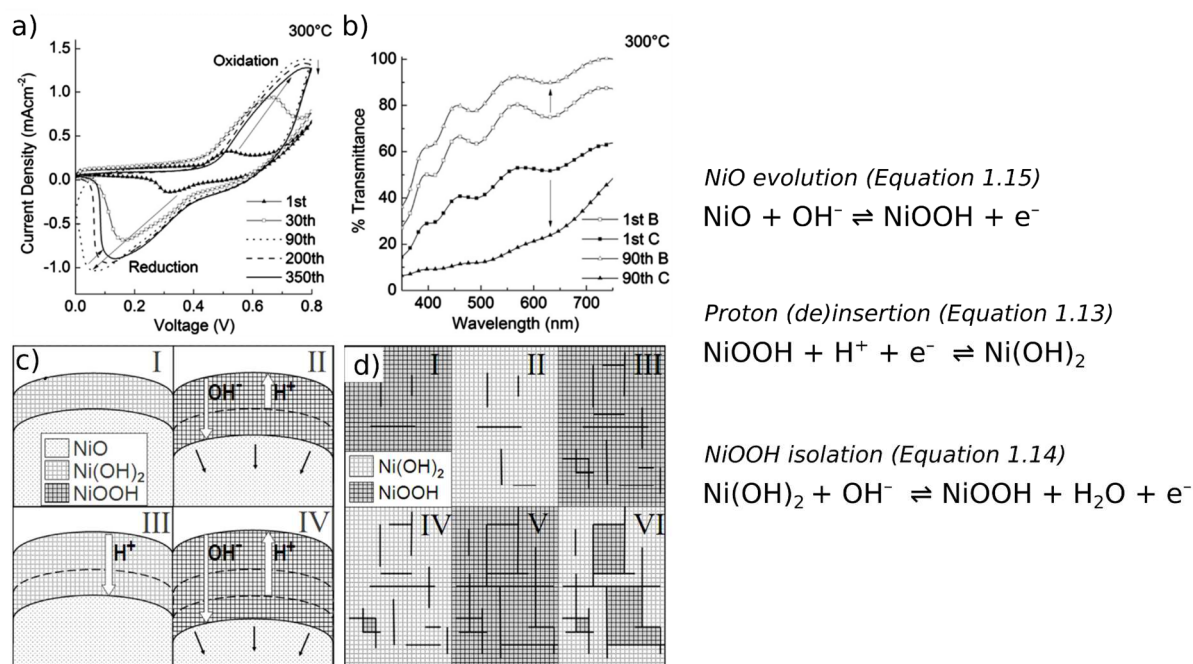
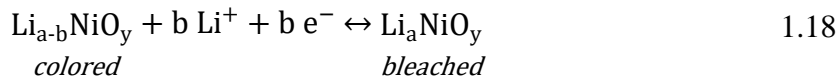
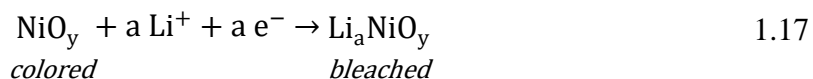


Figure 1.15 – (a) Cyclic voltammetry (CV) curves for a NiO thin film deposited by chemical bath deposition and annealed at 300 °C; the electrolyte was a 0.1 M KOH solution. (b) Transmittance curves for the NiO thin film in its bleached and colored state, during the first and the 90th cycle. (c) Schematic representation of the NiO evolution and the proton (de)insertion process. (d) Schematic representation of the NiOOH isolation process. Black lines represent intercalated water. Figures taken from reference²⁰⁹.

In the case of aqueous electrolytes, the mechanisms described through the years seem to agree on three aspects: the coloration/bleaching process is due to the Ni³⁺/Ni²⁺ redox couple, NiOOH is involved in the coloration of the films, and the redox reactions occur at the surface of the NiO particles. Besides these three constants, the nature of the inserted ion, whether the active material is NiO or Ni(OH)₂, and whether Ni₂O₃ (or even Ni₃O₄) is formed during the coloration process are still subjects which are up for debate.

Coloration/bleaching mechanism of NiO in non-aqueous electrolytes

Meanwhile, for non-aqueous electrolytes, numerous articles dealing with the electrochemical mechanism of nickel oxide thin films have been published. Like in aqueous electrolytes, NiO goes from dark brown in its oxidized state to transparent in its bleached state. Working with a non-stoichiometric NiO_z (1 < z < 1.66) thin film and a 1 M LiClO₄ in PC liquid electrolyte, Passerini et al²¹⁰ proposed a mechanism in two steps, an activation reaction and a reversible Li⁺ insertion reaction (Equations 1.17 and 1.18):



It seems that there are little reports in the literature on the specifics of the “activation reaction” (Equation 1.17); in fact, it is likely that the current density associated to this “activation” was solely due to an imbalance between the amount of charges inserted and extracted during the initial discharge/charge cycle¹⁸¹. Indeed, Passerini et al. worked with a relatively low potential window (1.0 to 3.5 V vs Li⁺/Li). Working at potentials below 2.0 V vs Li⁺/Li is likely to introduce irreversible parasitic reactions between lithium, oxides, and the electrolyte^{211–213}; Passerini et al. might have simply interpreted one of these parasitic reactions as an “activation reaction”.

As for the reversible “lithium insertion” reaction (Equation 1.18), it has also been a contentious subject. It is obvious, when looking at the crystal structure of cubic NiO (Figure 1.13), that it does not accommodate for the insertion of ions: it lacks efficient diffusion pathways. Campet et al. believed that lithium (de)insertion could occur nonetheless: they argued that, if the grain size of the material was small enough, Li⁺ cations could diffuse along grain boundaries, rather than in the bulk of the grains²¹⁴.

However, following Passerini’s and Campet’s works, several studies have highlighted the importance of surface reactivity in the electrochromic properties of nickel oxide thin films cycled in non-aqueous electrolytes. Adsorption of protons on oxygen sites and OH[−] anions on nickel sites can readily occur at the surface of NiO thin films in the presence of atmospheric water²¹⁵. Boschloo and Hagfeldt suggested that, in a similar way, cations from the electrolyte could replace protons at the surface of the films. They observed that the position of redox peaks for NiO thin films cycled in non-aqueous electrolyte depends on the cation present in said electrolyte, and suggested a mechanism in which the oxidation/reduction of nickel cations is coupled to the desorption/adsorption of electrolyte cations, following a pseudocapacitive behavior. As a consequence, the redox potentials of the Ni³⁺/Ni²⁺ couple should directly depends on the energy required to desorb/adsorb electrolyte cations, thus explaining the differences in redox behavior between Li⁺-conducting and tetrabutylammonium-conducting electrolytes in their study (Figure 1.16)²¹⁶.

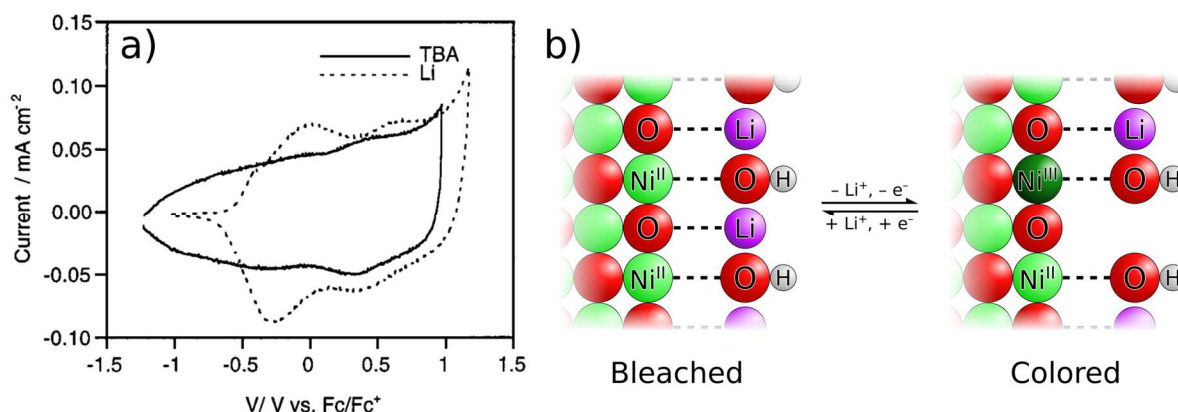


Figure 1.16 – (a) CV curves for a nanostructured NiO thin film working electrode cycled in 3-methoxypropionitrile with 0.2 M Li-triflate (dashed curve) or 0.2 M tetrabutylammonium-triflate (solid curve). The counter electrode was a Pt wire, the scan rate was $10 \text{ mV}\cdot\text{s}^{-1}$. Taken from reference²¹⁶. (b) Schematic representation of the adsorption/desorption mechanism described by Boschloo and Hagfeldt.

Boschloo and Hagfeldt stated that anion adsorption/desorption was not significant in the electrochemistry of NiO thin films, as they did not notice any difference between CV experiments performed in lithium triflate and lithium perchlorate electrolytes. However, several papers suggest to the contrary, showing proof that electrolyte anions may also participate in the electrochromic effect in NiO thin films^{46,217,218}. In particular, Da Rocha et al. demonstrated that a significant electrochromic effect could be observed in NiO thin films, even with a salt-free electrolyte (1-ethyl-3-methylimidazolium bis(tri-fluoromethanesulfonyl)imide or EMITFSI). Moreover, this specific study further confirms that the electrochromic behavior of NiO thin films does not have to be tied to the bulk (de)insertion of small monovalent cations, such as Li^+ or Na^+ ⁴⁶.

The fact that surface reactions are an essential part of the electrochemistry of NiO, and that cations and anions do not adsorb to the same sites, suggest that preferred orientation has a strong impact on the performances of NiO thin films. This was demonstrated by Wen et al., who worked on non-stoichiometric NiO_{1+z} thin films ($z = 0.16, 0.25, 0.32$) cycled in a LiClO_4 -PC electrolyte¹⁸¹. They noted that higher current densities and transmittance modulations were obtained in CV experiments for NiO_{1+z} films with $z = 0.32$. They also observed that for films with a higher oxygen content, there was a preferred orientation for the (111) plane of nickel oxide's cubic face-centered structure, which has a higher density of atomic sites than the (100) plane prominent for less oxidized films. Therefore, they concluded that the improved performances of $\text{NiO}_{1.32}$ compared to $\text{NiO}_{1.16}$ and $\text{NiO}_{1.25}$ was due to its preferred orientation, which offered more adsorption sites for cations (H^+ , Li^+) and anions (OH^- , ClO_4^-). Wen et al.¹⁸¹ also noted that, starting from the open-circuit voltage (OCV), a NiO_{1+z} thin film could be either

fully colored by the application of an anodic scan or fully bleached by a cathodic scan. They explained this ambivalence in the first half-cycle by suggesting that OH^- anions desorbed from the film's surface if the CV began with a cathodic scan; meanwhile, if the CV began with an anodic scan, the current density would instead come from the desorption of H^+ (Figure 1.17).

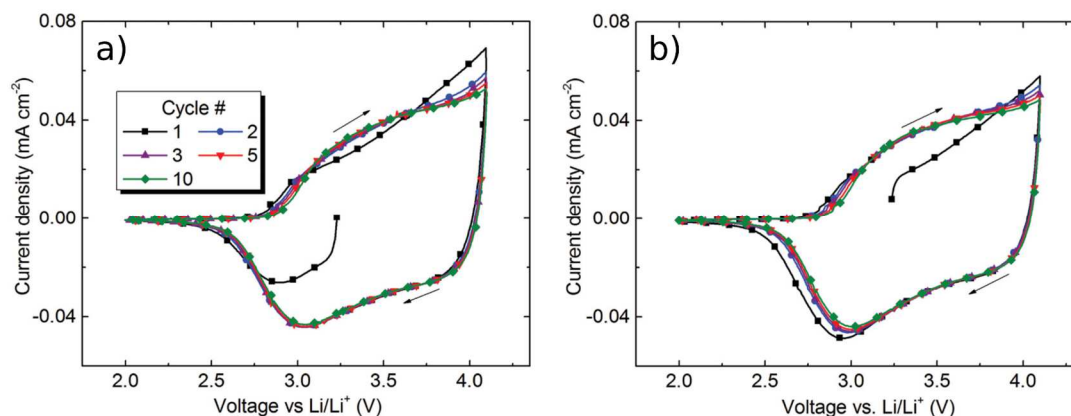


Figure 1.17 – CV curves for $\text{NiO}_{1.16}$ thin films immersed in a 1 M LiClO_4 in PC electrolyte. Reference electrode and counter electrodes where Li foils. (a) Cathodic scan and (b) anodic scan for the first half-cycle. Adapted from reference¹⁸¹.

It must be pointed out that most of the mechanisms proposed for NiO thin films in Li^+ -conducting electrolytes deal with aprotic liquid electrolytes. Less information is available for these thin films in inorganic solid electrolytes. Nonetheless, it can at least be ascertained that, if the electrochemistry of NiO thin films is due to an ion adsorption/desorption process, no anions would be available to participate in an all-solid-state electrochromic device.

Improving the performances of NiO thin films: nanostructures and mixed oxides

The exact mechanisms behind the electrochromic properties of NiO, whether in aqueous or non-aqueous electrolytes, remain the subject of numerous debates, although significant progress has been made since researchers started studying this material for its optical properties. Despite the lack of a complete mechanistic picture, there have been significant efforts to improve the electrochromic performances of NiO thin films.

Indeed, in order to prepare efficient ECDs with two electrochromic electrodes, both electrode materials need to have matching capacities. All the charges extracted from one electrode during the coloration/bleaching process must fit in the opposite electrode material. On top of that, if both electrode materials display good optical properties (i.e. transmission modulation and coloration/bleaching times), the overall ECD is also going to be more efficient.

Thus, if one wants to make an ECD using WO_3 and NiO as electrode materials, NiO needs to be as good as WO_3 , from both electrochemical and optical viewpoints.

A first approach to improve the performances of NiO thin films is to increase the surface area of the electrode through micro-/nanostructuration. This approach is in line with the general observation that the electrochemistry of NiO relies on surface reactions. On top of increasing the active surface area of the material, the microporosity of some nanostructured electrodes is supposed to facilitate the diffusion of electrolyte ions to active sites.

There are many examples of nanostructured NiO thin films to be found in the literature. Cao et al. were able to obtain nanowall arrays of NiO, using hydrothermal synthesis, and reported an increase in the current density, the transmission modulation, and the coloration efficiency compared to a dense NiO electrode²¹⁹ (Figure 1.18a). Scherer and Steiner used a polymeric template to perform the electrodeposition of a 3D gyroidal NiO thin film; its high surface area led again to increased optical modulation, and to fast switching times compared to other reports ($\tau_b = 0.053$ s, $\tau_c = 0.063$ s)²²⁰ (Figure 1.18b). Xie et al. performed a one-pot synthesis of NiO nanocrystals, which were then spin-coated on ITO in a pyridine solution in order to prepare an electrochromic thin film with an impressive coloration efficiency when cycled in a $\text{LiClO}_4\text{-PC}$ electrolyte ($114 \text{ cm}^2\cdot\text{C}^{-1}$ at 550 nm)²²¹ (Figure 1.18c). The detailed performances for these three examples and several others are listed in Table 1.2.

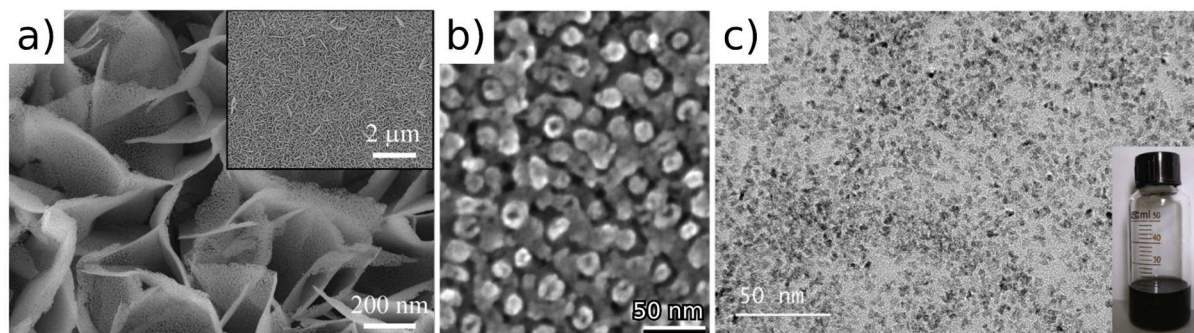


Figure 1.18 – (a) Scanning electron microscopy (SEM) images of nanowall arrays of NiO. Taken from reference²¹⁹. (b) SEM image of interconnected gyroid NiO thin film. Taken from reference²²⁰. (c) Low magnification transmission electron microscopy (TEM) images of NiO nanocrystals; inset is a pyridine solution containing the nanocrystals. Taken from reference²²¹

In general, these nanostructured films show good optical and electrochemical performances, which makes them very attractive for an application in ECDs. However, most of the methods used to prepare them would be difficult to apply to the preparation of electrochromic windows. Chemical precipitation²²², hydrothermal synthesis^{219,223,224}, spin-coating²²¹, solvothermal synthesis²²⁵ and other solvent-based method are not always adapted

to the deposition of uniform coatings over substrates with large dimensions (i.e. $> 1 \text{ m}^2$)²²⁶. Moreover, the use of templates to create precisely tailored nanostructures introduces a few more steps in the synthesis process of the thin films, making the process overall more complex^{220,227,228}. The issue is that these unique nanostructures often rely on these liquid-based techniques to be made.

Table 1.2 – Electrochromic performances of a small selection of nanostructured NiO thin films. A * symbol near a reference number indicates that the system was studied in a Li⁺-conducting aprotic electrolyte; otherwise, the system was studied in an aqueous electrolyte.

Structure	Synthesis method	ΔT (%)	τ_b/τ_c (s)	$\eta(\lambda)$ (cm ² .C ⁻¹)	Cycling stability	Ref
Nanowalls	Hydrothermal	77 (550 nm)	2.5/2	49 (550 nm)	3000	219
Gyroid	Electrodeposition	79.6 (630 nm)	0.053/0.063	40 (630 nm)	1000	220
Nanocrystals	One-pot + spin coating	41.5 (550 nm)	2.91/1.7	114.7 (550 nm)	~ 2000	221*
Nanotubes	Hydrolysis	78.5 (550 nm)	3.43/3.92	51.8 (550 nm)	1000	223
“Dandelions”	Chem. precipitation	68.1 (555 nm)	4.43/5.84	88 (555 nm)	/	222
Nanostacks	Hydrothermal	~42 (550 nm)	0.65/2.50	~120 (550 nm)	25000	229
Nanoflakes	Hydrothermal	68 (650 nm)	5/7	57.2 (650 nm)	14000	224
Nanoparticles	Solvothermal	63.6 (550 nm)	9.5/11.5	42.8 (550 nm)	1000	225
Porous nanopattern	Sol-gel	51 (550 nm)	5/7	40 (550 nm)	3000	227
Nanosheets	Template synthesis	40.1 (550 nm)	3.6/5.4	43.5 (550 nm)	/	228

Another approach to improve the performances of NiO is to incorporate other cations to prepare mixed oxide thin films. As the electrochromic properties of NiO heavily depends on its band structure, the introduction of “foreign” elements can disturb its crystal structure and thus greatly affect its electrochromic properties. A seminal paper on the matter, written by Avendaño et al., shows for example that magnetron-sputtered Ni-*M*-O (*M* = Mg, Al, Si, Zr, Nb, Ta) have a higher luminous transmittance than pure NiO thin films. On the other hand, Ni-V-O and Ni-Ag-O thin films have a lower luminous transmittance than pure NiO thin films¹⁷².

Several studies looked into the effect of heavy metal cations (namely Ta and W) on the structural and electrochromic properties of NiO. In terms of structure, the incorporation of these heavy elements disturbs the long-range order in crystalline NiO; Ni_{1-x}W_x oxide films with $x > 0.1$ are usually amorphous^{230–233}, and a similar observation can be made for Ni-Ta-O thin films^{234,235}. As for the electrochromic performances of these Ni-W and Ni-Ta mixed oxides,

the results can vary depending on the type of system studied (i.e. the type of electrolyte). Although some studies report improvements in the current density and optical modulation of these heavy metal systems compared to pure NiO thin films^{231,232}, their most striking feature is a stark increase in cycling stability^{231,233,234} (Figure 1.19). However, the cationic fraction of W (or Ta) in the film has to be finely tuned to obtain this increased durability: incorporating too much of a heavy element in the NiO thin film essentially suppresses its electrochromic properties.

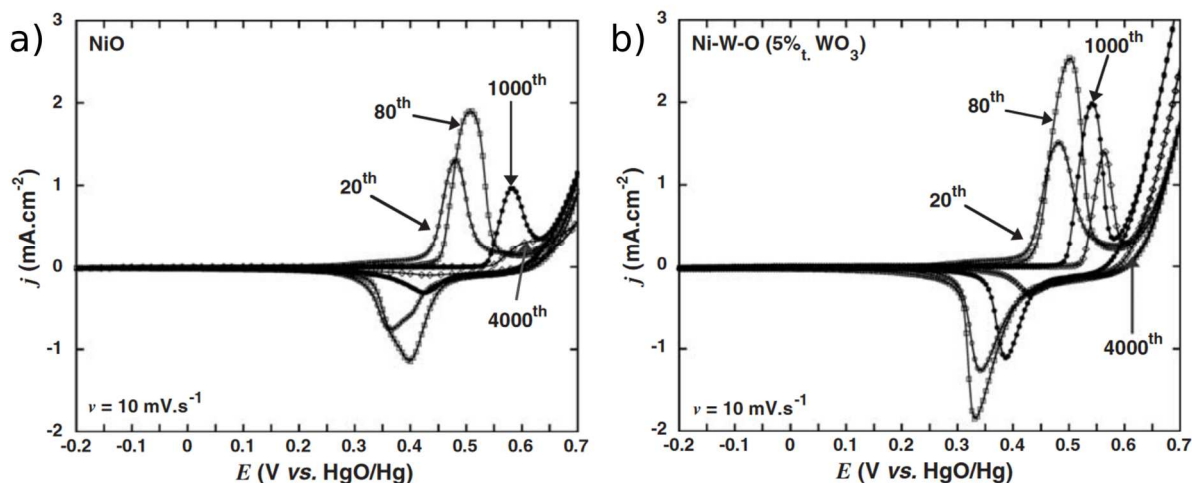


Figure 1.19 – CV curves for (a) NiO and (b) Ni-W-O (atomic fraction of W: 10 at%) thin films prepared by pulsed laser deposition technique. The films were cycled in a 1 M KOH aqueous electrolyte, with a platinum foil as the counter-electrode. Taken from reference²³¹.

Lithium is another element that has often been investigated for the preparation of nickel mixed oxide thin films. In Li-Ni-O thin films, the Li^+ cations occupy substitution sites and replace Ni^{2+} . In order to maintain charge neutrality, some of the remaining Ni^{2+} cations have to be oxidized to Ni^{3+} . Hence, the general formula of a Li-Ni-O thin film can be written as $\text{Li}_x\text{Ni}_{1-2x}^{2+}\text{Ni}_x^{3+}\text{O}$. For $x < 0.3$, the material retains the cubic rocksalt structure of pure NiO; its lattice parameter decreases as the amount of Li increases^{236–238}. Because the addition of lithium to the material increases the amount of Ni^{3+} in its pristine structure, its transmittance in both bleached and colored states will usually be lower than for pure NiO thin films^{239–241}. Aside from this characteristic, the improvements brought by Li-Ni mixing are not always obvious. Some studies describe clear increases in the transmittance modulation of Li-Ni-O thin films compared to pure NiO^{238,240,242} (Figure 1.20a), whereas others present less impressive performances^{239,241} (Figure 1.20b). These variations from one study to the other may very well stem from differences in synthesis methods and cycling conditions. As for *why* the

incorporation of Li^+ improves the performances of NiO thin films in some cases, it is there again quite a mystery.

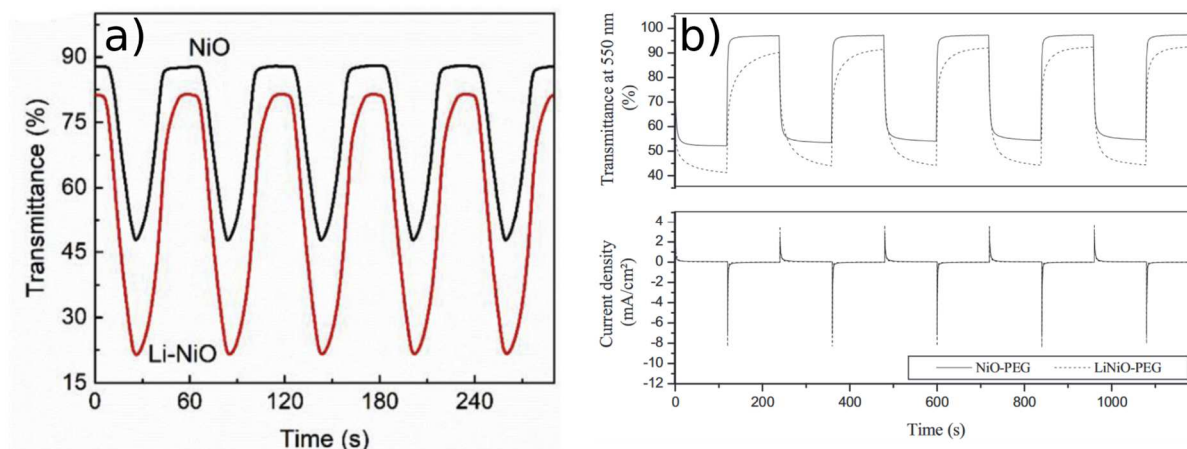


Figure 1.20 – (a) Evolution of the transmittance at 550 nm during a CV experiment for NiO and Li-Ni-O thin films prepared by reactive magnetron sputtering. The films were cycled in a 1 M LiClO_4 -PC electrolyte at a scan rate of $100 \text{ mV}\cdot\text{s}^{-1}$, between -1.5 V and 1.5 V vs AgCl/Ag ; the counter-electrode was a platinum foil. Taken from reference²⁴⁰. (b) Evolution of the transmittance at 550 nm (top) and of the current density (bottom) during a chronoamperometry experiment for NiO and Li-Ni-O thin films prepared by surfactant-assisted ultrasonic spray pyrolysis. The films were cycled in a 0.5 M LiClO_4 in PC electrolyte, between -1.4 V and 1.4 V vs AgCl/Ag ; the counter-electrode was a platinum foil. Taken from reference²⁴¹.

Other elements have been used to try to improve the electrochromic performances of NiO thin films. A couple of examples are given in Table 1.3, with other works mentioned previously.

In general, the electrochromic performances obtained for doped/mixed oxide NiO are not as good as those observed in nanostructured thin films (Table 1.2), possibly because the former lack the porosity and the high surface area of the latter. However, doped/mixed oxide thin films have the significant advantage of being compatible with vacuum deposition techniques such as magnetron sputtering. Thus, they can easily be deposited on large substrates for commercial applications to smart windows.

Thus, an ideal electrochromic system based on nickel oxide would present both the high optical performances of nanostructured thin films, and the large-scale deposition methods available for mixed oxide thin films. These two aspects are reunited in a few co-doped magnetron sputtered systems described in the literature^{243–245}. Gillaspie et al. prepared a Li/W co-doped NiO thin film by RF magnetron sputtering, with general formula $\text{Li}_{1.2}\text{NiW}_{0.1}\text{O}_x$, which displayed a unique nanocomposite structure²⁴³ (Figure 1.21a). The nanocrystallites, roughly 5-10 nm in size, are caught in an amorphous matrix, and their crystal structure matches with the cubic rocksalt structure of NiO. In terms of electrochromic performances, when cycled

in a 1 M LiClO₄-PC electrolyte with a lithium metal counter-electrode, the film displays a coloration efficiency at 670 nm of 28 cm².C⁻¹ after 180 cycles. Moreover, its transmittance modulation over the entire visible range is quite high ($\Delta T(550 \text{ nm}) \approx 60 \%$; $\Delta T(670 \text{ nm}) \approx 45 \%$), and it possesses a high transparency in its bleached state (Figure 1.21b).

Table 1.3 – Electrochromic performances for a small selection of doped/mixed nickel oxide thin films.

Element added	Synthesis method	ΔT (%)	$\eta(\lambda)$ (cm ² .C ⁻¹)	Cycling stability (% initial ΔT)	Electrolyte	Ref
W (10 at%)	Pulsed laser deposition	/	/	~ 4000	1 M KOH	231
W (~ 1 at%)	DC magnetron sputtering	~ 25 (633 nm)	~ 30 (633 nm)	1000 (~ 88 %)	1 M LiClO ₄ in PC	233
Ta (~ 3 at%)	DC magnetron sputtering	~ 60 (532 nm)	~ 30 (532 nm)	1000 (~ 100 %)	0.1 M NaOH	234
Li (~ 19 at%)	Sol-gel spin-coating	~ 20 (500 nm)	34.2 (500 nm)	~ 50 (~ 50 %)	0.1 M LiClO ₄ in PC	239
Ti (~ 11 at%)	Sol-gel spin-coating	~ 25 (500 nm)	15.5 (500 nm)	~ 100 (~ 40 %)	0.1 M LiClO ₄ in PC	239
Li	Ultrasonic spray deposition	50 (670 nm)	33 (670 nm)	/	1 M LiClO ₄ in PC	242
Li	DC magnetron sputtering	66.5 (550 nm)	36.3 (550 nm)	/	1 M LiClO ₄ in PC	240
Li (~ 6 at%)	Ultrasonic spray pyrolysis	43.5 (550 nm)	41.2 (550 nm)	100	0.5 M LiClO ₄ in PC	241
Li (~ 11 at%)	Pulsed laser deposition	36 (550 nm)	15 (550 nm)	1000 (~ 92 %)	1 M KOH	238
Sn (~ 4 at%)	RF magnetron sputtering	65.1 (550 nm)	39.1 (550 nm)	500 (~ 72 %)	1 M LiClO ₄ in PC	72

Although this nanocomposite material did not completely outperform other single-doped nickel oxide thin films (Table 1.3), a following work by Lin et al. presented the performances of another co-doped nickel oxide material, with higher transmittance modulation^{244,245}. Testing different compositions of Li/Zr co-doped NiO prepared by magnetron co-sputtering (Li₂O and Ni-Zr targets), they obtained a thin film with general formula Li_{1.966}NiZr_{0.231}O_x. Similarly to the Li-Ni-W-O thin film prepared by Gillaspie et al., this Li-Ni-Zr-O thin film is characterized by a nanocomposite structure, with nickel oxide-like nanocrystallites trapped in an amorphous matrix (Figure 1.22a). When used as the working electrode in a CV experiment with a standard 1 M LiClO₄-PC electrolyte, the film displayed a very high transmittance modulation after an activation period of 50 cycles. From cycle 50 to cycle 200, the transmittance modulation at 670 nm was of roughly 70 %, and the material was

highly transparent in its bleached state ($T_b > 90\%$) (Figure 1.22b). However, the coloration and bleaching times ($\tau_c = 56.4$ s and $\tau_b = 13.6$ s after 100 cycles) for the material were quite slow compared to other electrochromic thin films based on NiO; but this drawback is acceptable in the context of an application for smart windows.

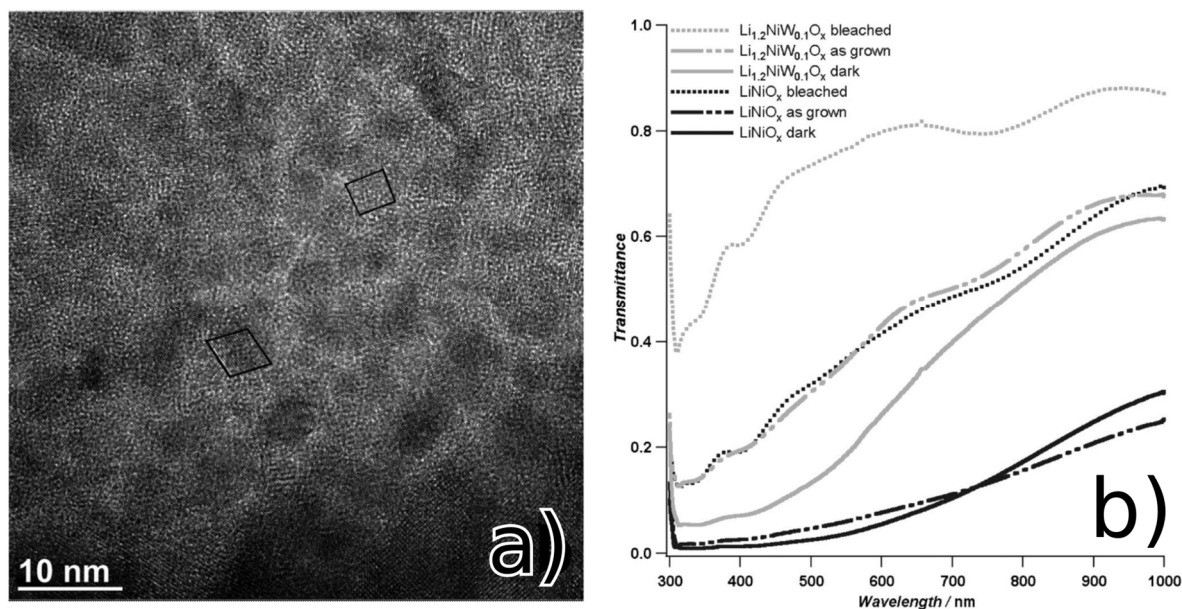


Figure 1.21 – (a) High resolution TEM image of a magnetron sputtered nanocomposite $\text{Li}_{1.2}\text{NiW}_{0.1}\text{O}_x$ thin film. Two nanocrystallites are highlighted by black diamonds. (b) *Ex situ* transmittance measurements for magnetron sputtered $\text{Li}_{1.2}\text{NiW}_{0.1}\text{O}_x$ (grey) and LiNiO_x (black) in various optical states: as-grown (dash-dotted lines), bleached (dotted lines), and colored (solid line). Taken from reference²⁴³.

The works of Gillaspie and Lin brings to light several crucial notions. First, it is possible to use magnetron sputtering to create nanostructured NiO thin films, by mixing nickel with lithium and another cation. Second, the electrochromic performances of these nanostructured films depend heavily on their composition, and especially on the lithium content (Figure 1.22b). Third, Lin et al. demonstrated through X-ray absorption spectroscopy (XAS) measurements that doping NiO with Li and Zr (or W) increased the number of oxidized Ni sites compared to pure NiO_y thin films, and suggested that the improved electrochromic effect in the co-doped films was related to this phenomenon²⁴⁴. They proposed that the amorphous matrix serves as an efficient diffusion pathway for Li^+ cations to the electrochemically active NiO nanocrystallites.

In short, the nanocomposite co-doped NiO thin films presented in these studies are interesting hybrids of the nanostructured materials prepared by solvent-based syntheses, and the dense thin films usually obtained by magnetron sputtering. With their high electrochromic performances and their simple synthesis process, adapted to large substrates, these

nanocomposites are great candidates for the positive electrode of ECDs in smart windows. Even so, there seems to be almost no reports on these types of co-doped nanocomposites applied to electrochromics in the literature.

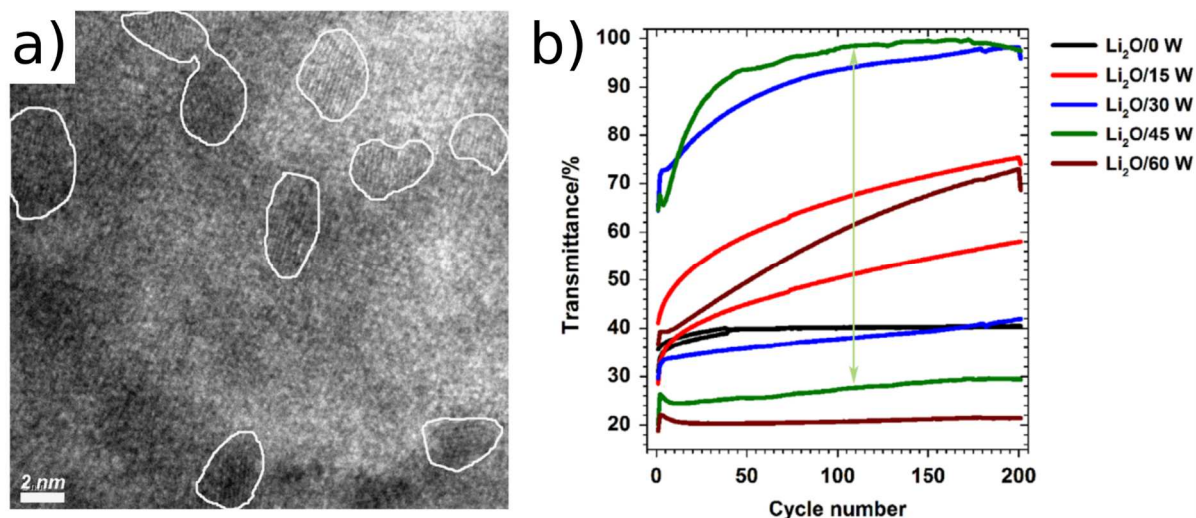


Figure 1.22 – (a) High resolution TEM image of the $\text{Li}_{1.966}\text{NiZr}_{0.231}\text{O}_x$ magnetron sputtered thin film. Cubic rocksalt nickel oxide-like nanocrystallites are circled in white. (b) Evolution of the transmittance at 670 nm during a CV experiment for different magnetron co-sputtered Li-Ni-Zr-O thin films. For each film, the power of the Ni-Zr alloy target used to prepare it was set to 60 W; only the power of the Li_2O target was modified to change the composition. The green curves correspond to the $\text{Li}_{1.966}\text{NiZr}_{0.231}\text{O}_x$ composition. The CV experiment was performed in 1 M $\text{LiClO}_4\text{-PC}$, with a lithium metal counter electrode and a scan rate of $20 \text{ mV}\cdot\text{s}^{-1}$. Taken from reference²⁴⁵.

Saint-Gobain's standard magnetron sputtered Li-Ni-W-O thin film

This thesis revolves around such nanocomposite systems, prepared by Saint-Gobain. They are NiO thin films, mixed with lithium and tungsten. Those films are prepared on ITO/Glass substrates, following a three-step process. During the first step, a Ni-W alloy target is used in an Ar/O_2 reactive atmosphere to sputter the transition metals on the substrate. Then, the second step is the sputtering of lithium on top of the Ni-W-O layer in an inert argon atmosphere. Finally, the sample is taken out of vacuum and heated between 300 and 500 °C, for several minutes, under an airflow. The entire process is summarized in Figure 1.23.

Inductively coupled plasma mass spectrometry (ICP-MS) measurements show that the Li/Ni ratio in the final film is roughly equal to 0.7, while the Ni/W ratio is roughly equal to 2. As for the nanostructure of the film, it was assessed by differentiated differential phase contrast scanning transmission electron microscopy (dDPC-STEM): a nanocomposite structure is clearly visible, similar to those reported by Gillaspie et al. and Lin et al.^{243–245} (Figure 1.24).

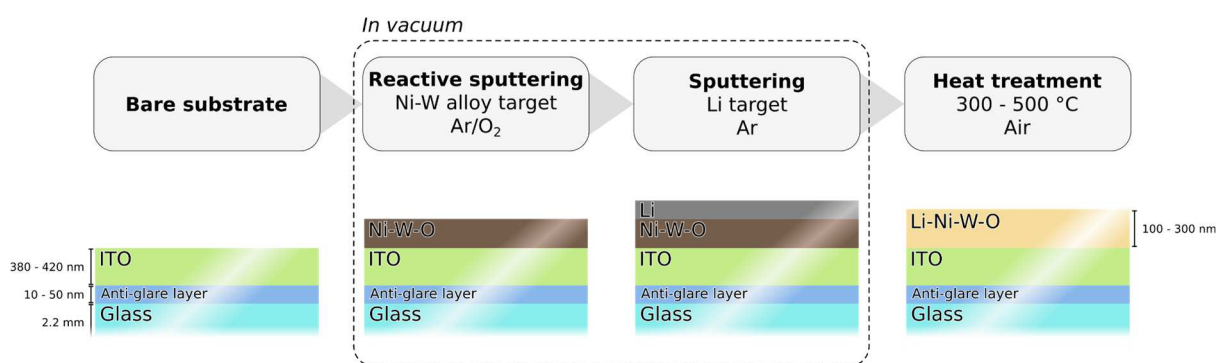


Figure 1.23 – Schematic representation of the synthesis process of Saint-Gobain’s magnetron sputtered Li-Ni-W-O thin films.

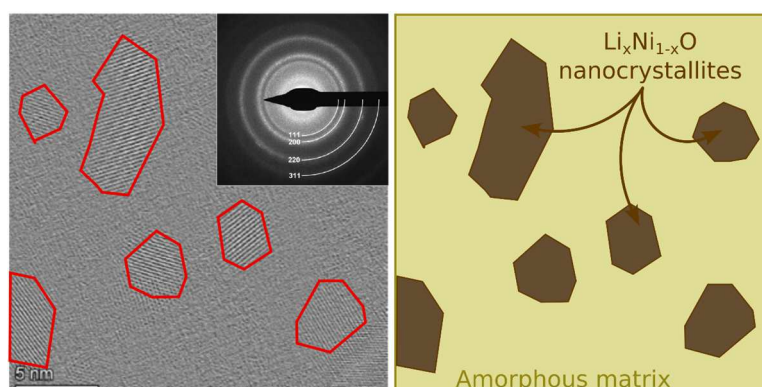


Figure 1.24 - dDPC-STEM image (left) and schematic representation of the nanostructure of a pristine magnetron sputtered Li-Ni-W-O thin film (right). Inlet is the electron diffraction pattern of the thin film.

Nanocrystallites of cubic rocksalt nickel oxide are caught in an amorphous matrix; they are possibly lithiated and about 2 to 5 nm in diameter. Electron diffraction measurements confirm that the crystallites have a face-centered cubic lattice, with lattice parameter $a \approx 4.2 \text{ \AA}$; the rings of the electron diffraction pattern are quite diffuse, in accordance with the nanometric size of the crystallites.

As for the electrochromic behavior of this Li-Ni-W-O thin film, it was qualitatively assessed by galvanostatic charge-discharge experiments, with a lithium metal counter-electrode and a 1 M lithium hexafluorophosphate (LiPF_6) in EC/DMC 1:1 (vol) electrolyte (Figure 1.25). The film is pale yellow in its pristine state, and becomes dark brown upon oxidation. This process is quite reversible, in terms both of optics and electrochemistry; it is referred to as the “main reaction”, and occurs when cycling the film between 2.0 and 4.5 V vs Li^+/Li . If the film is reduced from its pristine state, it will also become dark brown; but this overlithiation process is far less reversible. The film usually remains dark brown, even if it is oxidized back to its initial OCV. These irreversible reactions, occurring at low potentials (1.0 to 3.2 V vs Li^+/Li) are simply called secondary reactions.

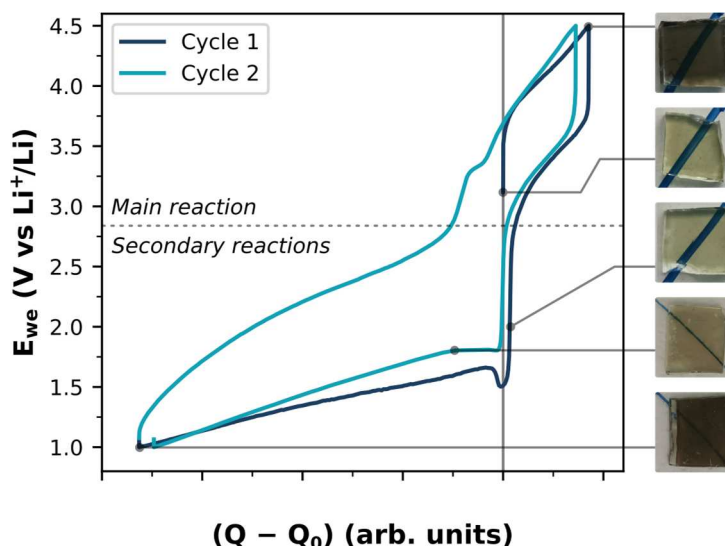


Figure 1.25 – Galvanostatic charge-discharge curves for a magnetron sputtered Li-Ni-W-O thin film cycled in 1 M LiPF₆ EC:DMC 1:1 (vol) electrolyte against a Li metal counter-electrode. The typical colorations of the film at different states of charge are shown on the right of the graph.

The goal of this doctoral project is to obtain a better fundamental understanding of the relationships between the composition, the (nano)structure and the electrochromic properties of Saint-Gobain’s magnetron sputtered Li-Ni-W-O nanocomposite thin films.

1.D. Conclusion of the chapter

Electrochromism is a centuries-old phenomenon, but it truly started attracting the attention of materials scientists in the middle of the 20th century. Its application to dynamic optics, and in particular to smart windows, is of great interest for solar control in the buildings sector. If used correctly, electrochromic smart windows could allow significant energy savings, specifically when it comes to cooling loads in summer and in environments with warm weather.

These energy savings depend on numerous factors. Among them, the intrinsic performances of the two electrode materials used in the window’s ECD are key aspects to tackle. Numerous electrochromic materials have been developed through the years: organic molecules, conducting polymers, Prussian blue and its analogues... In the case of smart windows, electrochromic oxides thin films are the go-to choice: they are transparent in the bleached state, display good transmittance modulation, and can easily be processed through vacuum deposition techniques. For the negative electrode of the ECD, cathodic electrochromic WO₃ is the usual pick; but it can prove more difficult to select its counterpart on the positive side.

Anodic electrochromic NiO is a good candidate to fill that role. However, the mechanisms behind its electrochemical and optical properties are still uncertain, whether in aqueous systems or aprotic Li⁺-conducting electrolytes. It seems that the coloration/bleaching process is associated to the Ni³⁺/Ni²⁺ redox couple, and that surface reactions play a significant role as well. Thus, a direct path to improve the performances of electrochromic NiO is to develop nanostructured thin films. An interesting and efficient approach, compatible with a magnetron sputtering process, is to prepare nanocomposite thin films by mixing NiO with lithium and another metal cation.

The rest of this manuscript focuses on such a nanocomposite material, a magnetron sputtered Li-Ni-W mixed oxide, meant to be used in Li⁺-based ECDs. The synthesis and the properties of Li₂Ni₂W₂O₉, a phase related to the Li-Ni-W-O thin film by their proximity in the Li₂O-NiO-WO₃ ternary phase diagram, are presented in Chapter 2.

Chapter 2 – Solid-state synthesis, crystal structure, and properties of $\text{Li}_2\text{Ni}_2\text{W}_2\text{O}_9$

Part of the results presented in this chapter were published in the following articles: Redor et al. *J. Am. Chem. Soc.* **2023**, *145* (23), 12823–12836²⁴⁶ and Redor et al. *Phys. Rev. B* **2024**, *109* (5), 054105²⁴⁷.

2.A. Motivations

In order to gain more insights into the relationships between the composition, the nanostructure, and the electrochromic properties of the standard nanocomposite Li-Ni-W-O thin films described in Chapter 1, a first approach was to synthesize crystallized powders in the $\text{Li}_2\text{O-NiO-WO}_3$ ternary phase diagram. The goal was then to compare the properties of these powders with those of the thin films.

Figure 2.1 shows the X-ray diffraction (XRD) pattern for a powder prepared by solid-state synthesis from Li_2CO_3 , NiO , and WO_3 . The chemical composition of the powder is meant to be identical to that of the Li-Ni-W-O thin film.

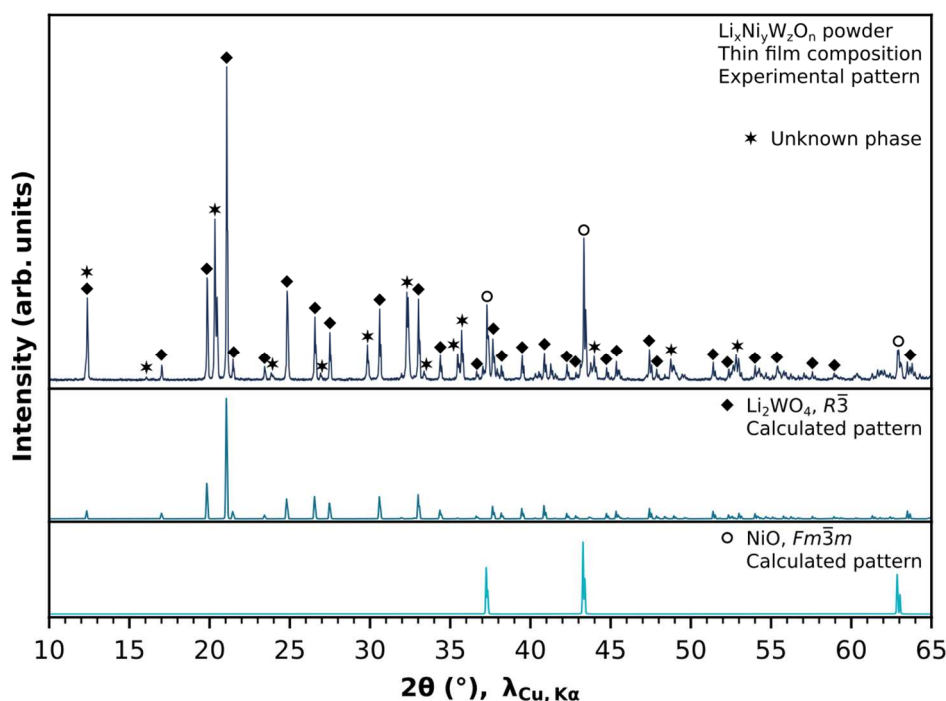


Figure 2.1 – Experimental XRD pattern for a powder produced by solid-state synthesis (600 °C, 12 h, +5 °C/min), with a similar chemical composition to the Li-Ni-W-O thin film (top). Below are the calculated patterns for trigonal Li_2WO_4 and cubic NiO .

The powder's XRD pattern features peaks that are indicative of a mix of three phases: trigonal lithium tungstate (Li_2WO_4 , $R\bar{3}$)^{248,249}, cubic rocksalt nickel oxide (NiO , $Fm\bar{3}m$)²⁵⁰, and a third phase, unidentified at the time. Understanding the nature of this unknown phase and its properties was critical to the comprehension of the Li-Ni-W-O thin films; a strategy based on the exploration of the $\text{Li}_2\text{O-NiO-WO}_3$ ternary phase diagram is only valid if all the phases of interest are uncovered.

This chapter deals with the synthesis of this new phase, $\text{Li}_2\text{Ni}_2\text{W}_2\text{O}_9$, and with the modeling of its crystal structure using diffraction techniques. Then, various properties of the material are discussed. Its electrochemical properties in Li^+ -conducting electrolytes is studied by galvanostatic charge-discharge experiments in coin cells, and *operando* XRD grants insights on the variation of structure of the material upon (de)lithiation. The electrochromism of $\text{Li}_2\text{Ni}_2\text{W}_2\text{O}_9$ is also established, using *operando* optical reflection microscopy. Finally, the magnetic properties of $\text{Li}_2\text{Ni}_2\text{W}_2\text{O}_9$ are assessed, through bulk magnetic measurements and neutron diffraction, and are compared with the properties of materials with a similar crystal structure, the “429” compounds ($M_4A_2O_9$, $M = \text{Co}, \text{Ni}, \text{Fe}, \text{Mn}, \text{etc.}$, $A = \text{Nb}, \text{Ta}$).

2.B. Solid-state synthesis and structural characterization of $\text{Li}_2\text{Ni}_2\text{W}_2\text{O}_9$

Solid-state synthesis

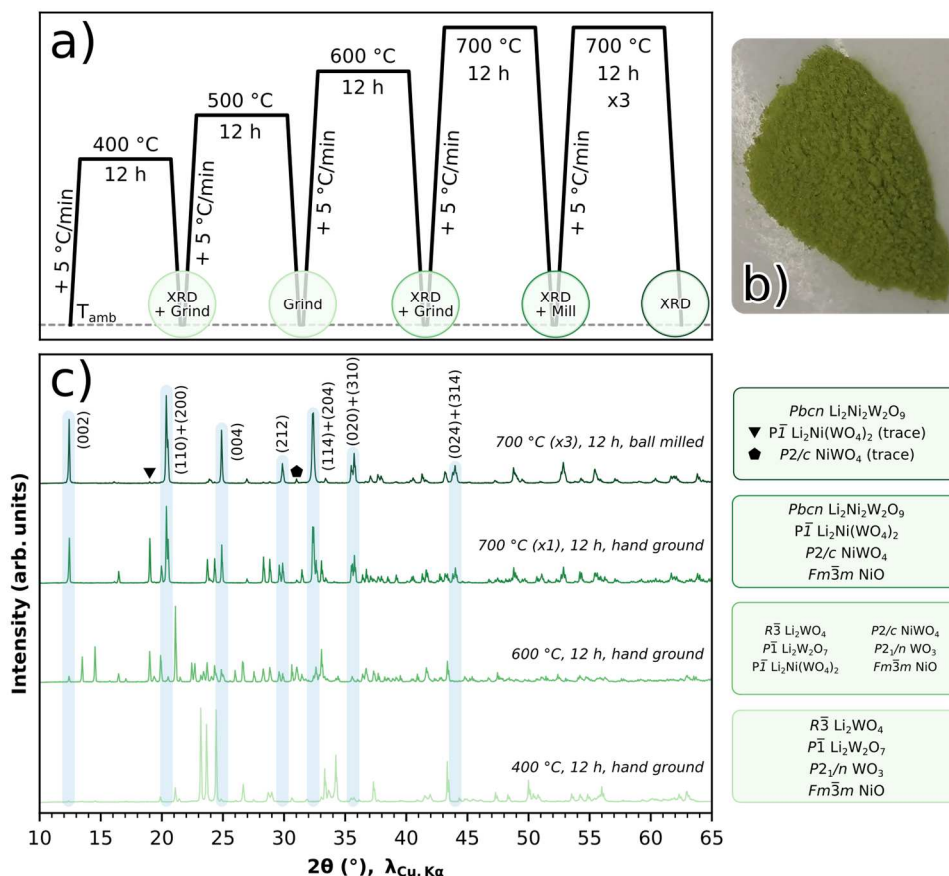
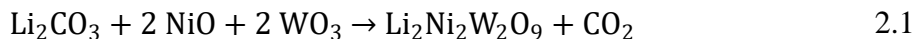


Figure 2.2 – (a) Heating process used in an experiment to determine the temperature required to form $\text{Li}_2\text{Ni}_2\text{W}_2\text{O}_9$ by solid-state synthesis in air. (b) Picture of pure $\text{Li}_2\text{Ni}_2\text{W}_2\text{O}_9$. (c) XRD patterns for the powder obtained at the end of different steps of the heating process shown in (a). The phases detected in each pattern are listed on the right. The major peaks of $Pbcn\ \text{Li}_2\text{Ni}_2\text{W}_2\text{O}_9$ are highlighted in blue, along with their Miller indices.

The solid-state synthesis of $\text{Li}_2\text{Ni}_2\text{W}_2\text{O}_9$ can be performed in air, by mixing together Li_2CO_3 , NiO , and WO_3 precursors and heating them at $700\text{ }^\circ\text{C}$ for several hours. Equation 2.1 represents the synthesis reaction:



The resulting powder may need to be ground and annealed a few more times to obtain high-purity $\text{Li}_2\text{Ni}_2\text{W}_2\text{O}_9$. High intensity ball milling is required to ensure a homogeneous mix and small particles, with a high reactivity.

The final pure powder is light green (Figure 2.2b). The heating temperature is important, as $\text{Li}_2\text{Ni}_2\text{W}_2\text{O}_9$ cannot be fully formed below $700\text{ }^\circ\text{C}$; even with the right stoichiometry, high amounts of impurities will remain if the sample is heated at lower temperatures; in fact, the phase may not form at all (Figure 2.2a, c).

Crystal structure

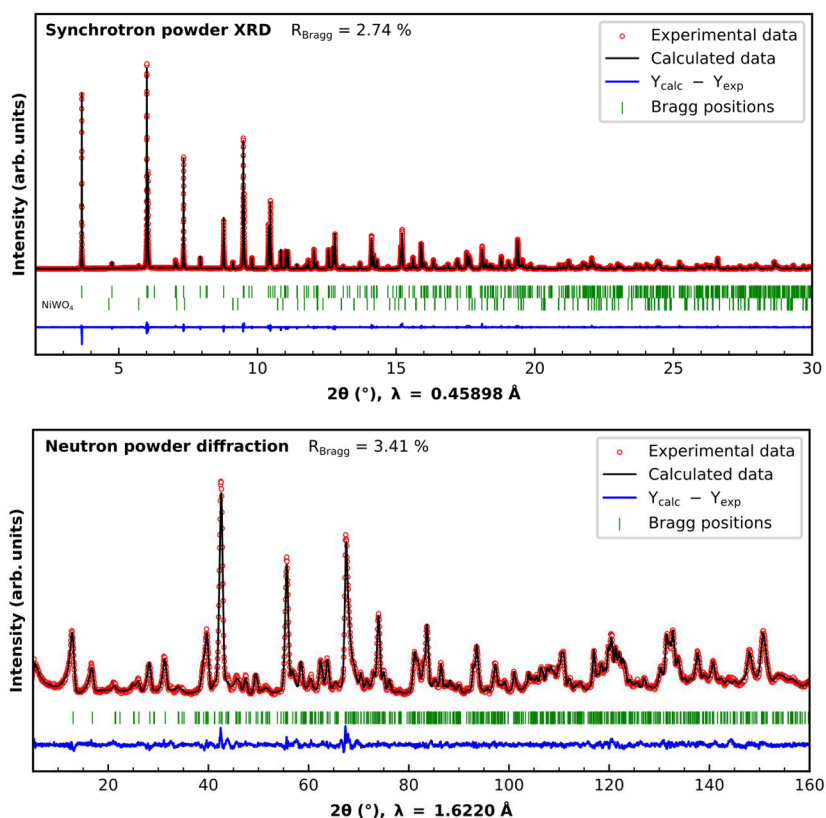


Figure 2.3 – Rietveld refinements of $\text{Li}_2\text{Ni}_2\text{W}_2\text{O}_9$ from the synchrotron XRD pattern (top) and neutron diffraction pattern (bottom) at room temperature (300 K). The red circles, black continuous line and bottom blue line represent the observed, calculated, and difference patterns respectively. Vertical green tick bars are the Bragg positions.

The crystal structure of $\text{Li}_2\text{Ni}_2\text{W}_2\text{O}_9$ was studied through X-ray and neutron powder diffraction. As little information was known about this new phase, the structure had to be solved *ab initio*. First, the X-ray diffraction peaks were indexed in an orthorhombic unit cell using the DICVOL program²⁵¹, with a volume of $632.29(2) \text{ \AA}^3$ and lattice parameters $a = 8.69523(8) \text{ \AA}$, $b = 5.06407(5) \text{ \AA}$, and $c = 14.34517(2) \text{ \AA}$. The observed reflection conditions are consistent with the $Pbcn$ space group. Thus, this space group was used to solve the structure of $\text{Li}_2\text{Ni}_2\text{W}_2\text{O}_9$ with the FOX software²⁵². The calculations were initialized assuming a structure built on NiO_6 octahedra. This led to an initial structural agreement with the X-ray powder diffraction pattern. Li atoms were placed in the structure using bond valence maps, which were calculated using the GFourier program from the FullProf Suite²⁵³. Their positions were confirmed through neutron powder diffraction. The final structural model was obtained through Rietveld refinements²⁵⁴ simultaneously from the neutron and synchrotron X-ray powder diffraction patterns (Figure 2.3). Electron diffraction patterns (Figure 2.4) are in good agreement with the $Pbcn$ space group and the lattice parameters determined from synchrotron powder XRD data.

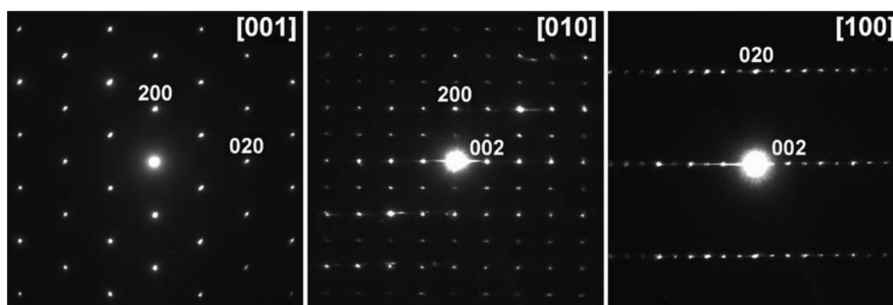


Figure 2.4 – Electron diffraction patterns for $\text{Li}_2\text{Ni}_2\text{W}_2\text{O}_9$, indexed in the $Pbcn$ space group. They reveal a pseudo-hexagonal structure based on an ABAB oxygen close-packing, reminiscent of a corundum-like structure. Cation ordering introduces the orthorhombic superstructure.

The crystal structure of the $\text{Li}_2\text{Ni}_2\text{W}_2\text{O}_9$ phase is shown in Figure 2.5, and the main crystallographic parameters can be found in Table 2.1. The $\text{Li}_2\text{Ni}_2\text{W}_2\text{O}_9$ phase is nearly pure: two low-intensity peaks, at $2\theta = 5.72^\circ$ and $2\theta = 9.11^\circ$ on the synchrotron XRD pattern (Figure 2.3) indicate the existence of a small amount of $P2/c$ nickel tungstate (NiWO_4 , ICSD n° 15852)²⁵⁵ as an impurity (less than 2 wt%). The relative purity of the synthesized material and the homogeneous distribution of Ni and W were also confirmed through STEM-EDX compositional maps (Figure 2.6).

$\text{Li}_2\text{Ni}_2\text{W}_2\text{O}_9$ displays a layered structure (Figure 2.5a). The layers are composed of chains of edge-sharing NiO_6 octahedra; in a given layer, these chains alternate between a lower and an upper z -coordinate along the c -axis (Figure 2.5a,c). The chains are linked to each other

by O1 oxygen atoms, and by face-sharing WO_6 dimers located between each chain as well. Each WO_6 octahedron shares three edges with a NiO_6 chain (O1-O4, O4-O3, O3-O2), a corner with another chain (O3) and a face with another WO_6 octahedron (O3-O3-O1) (Figure 2.5c).

Table 2.1 – Results of the Rietveld refinements (synchrotron powder XRD and neutron powder diffraction) for $Pbcn$ $\text{Li}_2\text{Ni}_2\text{W}_2\text{O}_9$. For oxygen atoms, B_{iso} values were all set equal. BVS: Bond valence sum.

Element	Wyckoff site	x/a	y/b	z/c	B_{iso} (\AA^2)	Occupancy	BVS ²⁵⁶
Li	8d	0.340(2)	0.522(4)	0.4947(6)	1.8(19)	1	0.944(2)
Ni	8d	0.6633(2)	0.5005(6)	0.81315(9)	0.364(17)	1	1.982(1)
W	8d	0.5242(4)	0.000(13)	0.6441(16)	0.022(4)	1	5.891(5)
O1	4c	1/2	0.281(11)	3/4	0.207(14)	1	1.989(2)
O2	8d	0.5083(4)	0.6791(7)	0.9091(2)	0.207(14)	1	1.933(3)
O3	8d	0.6494(4)	0.8518(7)	0.7469(2)	0.207(14)	1	1.945(2)
O4	8d	0.8426(5)	0.6635(6)	0.8952(19)	0.207(14)	1	1.831(2)
O5	8d	0.3386(5)	0.1539(6)	0.9257(19)	0.207(14)	1	2.114(3)

Space group: $Pbcn$. **Lattice parameters:** $a = 8.69523(8)$ \AA / $b = 5.06407(5)$ \AA / $c = 14.34517(2)$ \AA
 $V = 631.928(1)$ \AA^3 . $Z = 4$. **Reliability parameters:** $\chi^2 = 1.95$, $R_{\text{Bragg}} = 2.74$ % (Synchrotron X-Ray) /
 $\chi^2 = 2.70$, $R_{\text{Bragg}} = 3.41$ % (Neutron).

Interestingly, the WO_6 octahedra are heavily distorted: the W-O bonds pointing toward the interlayer (W-O2, W-O4, W-O5) are much shorter than those pointing toward the Ni-W-O layer (W-O1, W-O3, W-O3) (Figure 2.5a). The opposite trend is observed when looking at the Ni-O bond lengths for the NiO_6 octahedra: the Ni-O bonds pointing toward the interlayer (Ni-O2, Ni-O4, Ni-O4) are longer than those pointing in the opposite direction (Ni-O1, Ni-O3, Ni-O3). However, the distortion is less significant for the NiO_6 octahedra than for the WO_6 octahedra.

The distortion for an octahedron can be quantified by looking at its quadratic elongation²⁵⁷, given by Equation 2.2:

$$\langle \lambda \rangle = \frac{1}{6} \sum_{i=1}^6 \left(\frac{l_i}{l_0} \right)^2 \quad 2.2$$

where l_0 is the vertex-to-center distance for a regular octahedron of equal volume to the distorted polyhedron, with bond lengths l_i . For $\langle \lambda \rangle = 1$, the studied octahedron displays no

distortion. The quadratic elongation for a WO_6 octahedron in the $\text{Li}_2\text{Ni}_2\text{W}_2\text{O}_9$ phase is 1.06, whereas it is merely equal to 1.02 for a NiO_6 octahedron. These values highlight the severity of both the bond angles and bond lengths distortions in the WO_6 octahedra compared to the NiO_6 octahedra. Such distortions may arise from a second order Jahn-Teller effect, which is rather common for high-valence d^0 cations^{258,259}.

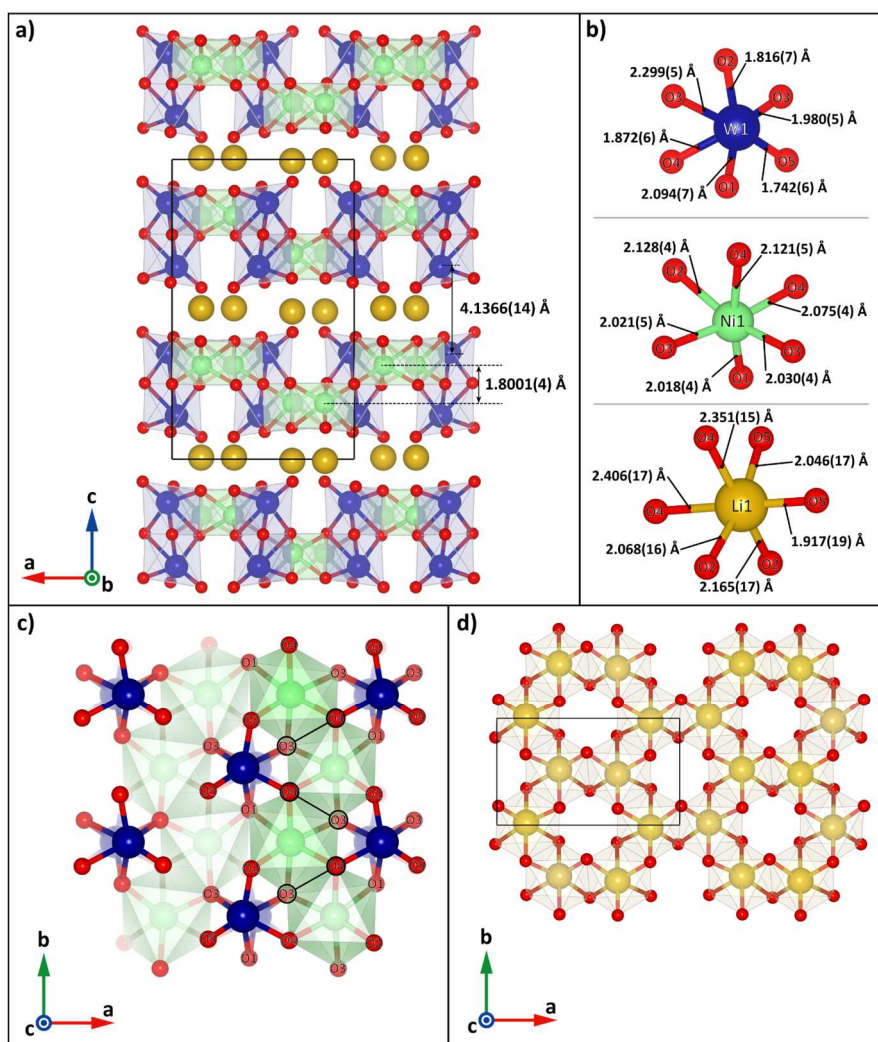


Figure 2.5 – Crystal structure of $\text{Li}_2\text{Ni}_2\text{W}_2\text{O}_9$. Lithium atoms are represented in yellow, nickel atoms in green, tungsten atoms in blue, and oxygen atoms in red. (a) Projection along $[010]$ of the layered structure. (b) Bond lengths for the WO_6 , NiO_6 , and LiO_6 octahedra. (c) Projection along $[001]$ highlighting the NiO_6 chains in the Ni-W-O layers. Atoms in a paler color have lower z -coordinates. (d) Projection along $[001]$ highlighting the lithium honeycomb configuration in the interlayer.

One of the most interesting features of $\text{Li}_2\text{Ni}_2\text{W}_2\text{O}_9$'s crystal structure comes from the lithium ions, which occupy the interlayer space, forming a “honeycomb” pattern (Figure 2.5d). Each lithium ion is located directly above or below a nickel ion, with a distorted octahedral coordination. Here, the longest Li-O bonds, Li-O4, point toward the neighboring NiO_6 octahedron, in such a way that the Li^+ cations are always closer to one Ni-W-O layer than the

other. In particular, the Li^+ ions are always closer to the W^{6+} ions than the Ni^{2+} ions (Figure 2.5a,b,d). This could be explained by the high valency of the W^{6+} ions, which have to get closer to low-valence cations (Li^+) to maintain local charge neutrality; this would also justify why the W^{6+} cations seem to deviate from the Ni^{2+} cations (Figure 2.5c)^{258,259}.

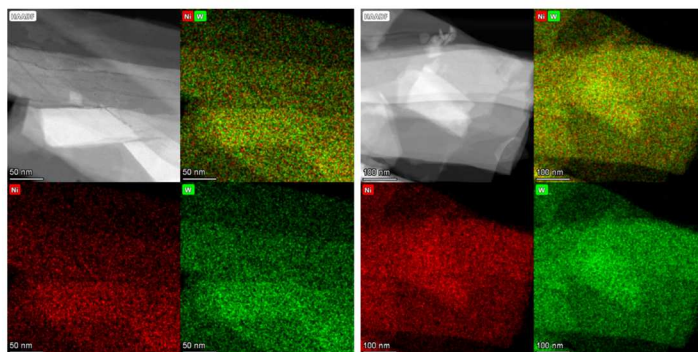


Figure 2.6 – HAADF-STEM images and EDX mappings for two different areas of a $\text{Li}_2\text{Ni}_2\text{W}_2\text{O}_9$ powder sample. Tungsten atoms are in red and nickel atoms are in green in the EDX mappings.

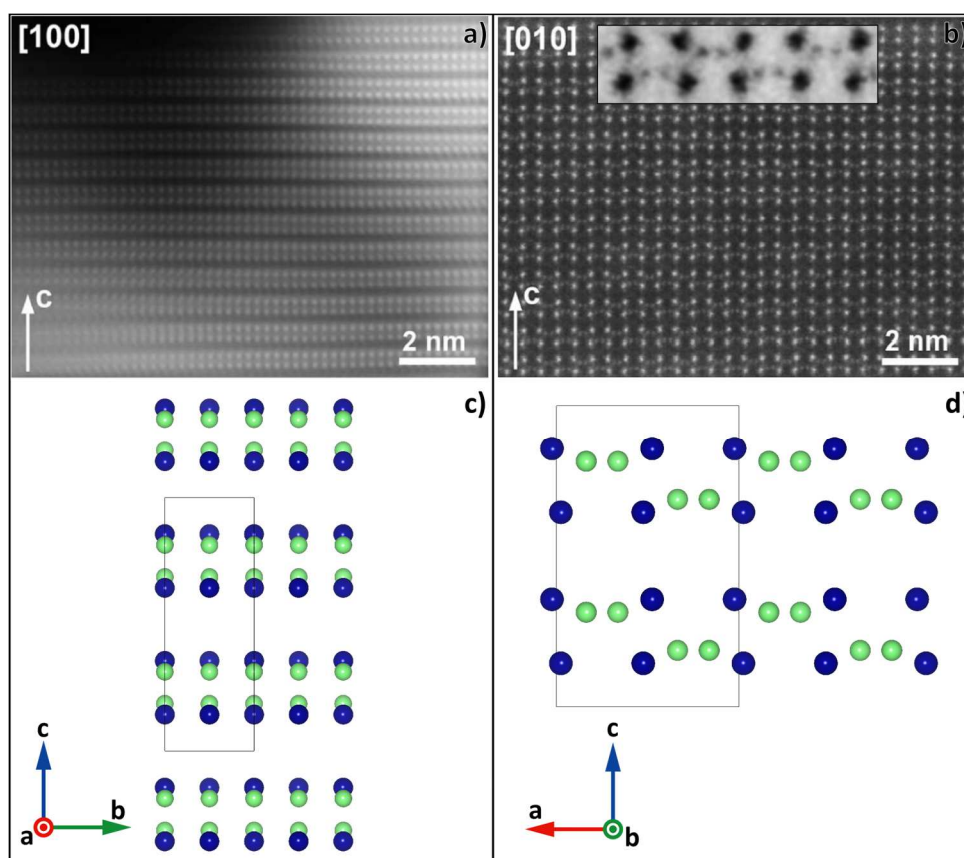


Figure 2.7 - HAADF-STEM images along (a) the [100] direction and (b) the [010] direction for a $\text{Li}_2\text{Ni}_2\text{W}_2\text{O}_9$ crystallite. The inset in (b) comes from the same HAADF-STEM image, in inverted contrast and zoomed in to highlight the positions of the Ni cations. (c, d): Projections of the nickel and tungsten atoms positions for the refined *Pbcn* $\text{Li}_2\text{Ni}_2\text{W}_2\text{O}_9$ structural model, along the (c) [100] direction and (d) [010] direction.

In order to validate the solved structure, $\text{Li}_2\text{Ni}_2\text{W}_2\text{O}_9$ was further analyzed by atomic resolution HAADF-STEM imaging (Figure 2.7a,b). On these images, the brightest dots

correspond to the tungsten atoms, which possess the highest atomic number; nickel atoms can be seen as slightly dimmer dots in Figure 2.7b. Lithium cannot be detected due to its very small atomic number. In Figure 2.7a, we can observe rows of bright dots which are two-dot wide, and correspond to atomic columns consisting of both nickel and tungsten atoms. These rows of dots are separated by a dark space corresponding to the interlayer gap described before. This placement of the tungsten and nickel atoms fully matches with the structure obtained through Rietveld refinement (Figure 2.7c). In Figure 2.7b, two-atom wide rows of bright dots (W) are observed when the structure is viewed along the [010] direction. A pair of dim dots (Ni) can be seen between the bright dots of each row; the position of each of these “dim pairs” alternates between the top and the bottom of the row. This configuration for the Ni and W atoms also matches quite well with the configuration found in the refined crystal structure (Figure 2.7d). Moreover, the W-W distance along the c -axis can be estimated to roughly 4 Å from the HAADF-STEM images, in agreement with the distance calculated from the structural model.

The crystal structure of $\text{Li}_2\text{Ni}_2\text{W}_2\text{O}_9$ derives from the corundum structure, with a pseudo-hexagonal lattice. Materials with similar lattice structures can frequently be found in the literature, the most prominent being the aforementioned corundum, also known as $\alpha\text{-Al}_2\text{O}_3$ ²⁶⁰. In fact, it is very easy to transform the lattice of $\alpha\text{-Al}_2\text{O}_3$ ($R\bar{3}c$) into the orthorhombic, $Pbcn$ lattice ($\text{Li}_2\text{Ni}_2\text{W}_2\text{O}_9$) through the following set of equations:

$$\begin{cases} a_{Pbcn} = a_{R\bar{3}c} - b_{R\bar{3}c} & 2.3 \\ b_{Pbcn} = a_{R\bar{3}c} + b_{R\bar{3}c} & 2.4 \\ c_{Pbcn} = c_{R\bar{3}c} & 2.5 \end{cases}$$

However, the positions of the atoms in the orthorhombic lattice of $\text{Li}_2\text{Ni}_2\text{W}_2\text{O}_9$ do not completely match with those of the atoms in $\alpha\text{-Al}_2\text{O}_3$. Hence, $\text{Li}_2\text{Ni}_2\text{W}_2\text{O}_9$ can only be qualified of “pseudocorundum” or “corundum-like”. Besides, $\text{Li}_2\text{Ni}_2\text{W}_2\text{O}_9$ is a compositionally mixed oxide.

There are many examples of binary or ternary oxides displaying a corundum or corundum-like structure ($\text{Co}_4\text{Nb}_2\text{O}_9$ ²⁶¹, Ni_3TeO_6 ²⁶², $\text{Mn}_2\text{ScTaO}_6$ ²⁶³, $\text{Li}_2\text{Mg}_2\text{W}_2\text{O}_9$ ²⁶⁴, $\text{Li}_2\text{GeTeO}_6$ ²⁶⁵, etc.). In fact, the crystal structure of $\text{Li}_2\text{Ni}_2\text{W}_2\text{O}_9$ matches with that of another compound, $\text{MgNi}_3\text{Nb}_2\text{O}_9$ ²⁶⁶, which displays (Mg,Ni)-honeycomb layers caught between Mg-Ni-Nb-O layers made of octahedra chains, in a pattern similar to what can be seen in $\text{Li}_2\text{Ni}_2\text{W}_2\text{O}_9$ (Figure 2.5). A few reports have been made on materials with a $\text{MgNi}_3\text{Nb}_2\text{O}_9$ -type

structure^{267,268} (also known as a “ramsayite” structure); however, as far as we know, none of them display “pure” lithium layers (without any cationic mixing).

Thus, what truly sets $\text{Li}_2\text{Ni}_2\text{W}_2\text{O}_9$ apart from other corundum or corundum-like materials is a combination of characteristics: an ordered structure, an interlayer suitable for lithium diffusion and an electrochemically active 3d transition metal.

Many insertion materials studied for an application as cathode in lithium-ion batteries display a layered structure: LiCoO_2 ^{269,270}, NMC materials ($\text{Li}[\text{Ni}_x\text{Co}_{1-2x}\text{Mn}_x]\text{O}_2$)^{271,272}, LiFeSO_4OH ²⁷³, and $\text{Li}_4\text{VO}(\text{PO}_4)_2$ ²⁷⁴, to name a few. However, although it is also a layered compound, its corundum-like structure make $\text{Li}_2\text{Ni}_2\text{W}_2\text{O}_9$ quite unique compared to what can be found among other cathode materials. As such, its electrochemical properties as a potential electrode material for Li-ion batteries were studied.

2.C. Electrochemical properties and electrochromism of $\text{Li}_2\text{Ni}_2\text{W}_2\text{O}_9$

Electrochemical behavior in half-cells

The electrochemical performances of $\text{Li}_2\text{Ni}_2\text{W}_2\text{O}_9$ were studied in coin cells. $\text{Li}_2\text{Ni}_2\text{W}_2\text{O}_9$ powder was mixed with carbon black (80:20 wt%) to prepare the cathode electrode, which was then cycled at $10 \text{ mA}\cdot\text{g}^{-1}$ against lithium metal through a galvanostatic charge-discharge process. The resulting curves, characteristic of a faradaic behavior, are shown in Figure 2.8.

When cycled between 2.5 and 5.0 V vs Li^+/Li at a current density of $10 \text{ mA}\cdot\text{g}^{-1}$, LNWO displays two distinct plateaus in its first charge: one appears at around 4.55 V vs Li^+/Li with a capacity of $23 \text{ mA}\cdot\text{h}\cdot\text{g}^{-1}$, while the other one appears above 4.8 V vs Li^+/Li , contributing a capacity of $18 \text{ mA}\cdot\text{h}\cdot\text{g}^{-1}$ (Figure 2.8a). In the following discharge, two slopes can be observed, but in a much narrower potential region: the first slope appears between 4.6 and 4.5 V vs Li^+/Li , and the other between 4.5 and 4.4 V vs Li^+/Li . This behavior indicates that we have two distinct redox couples.

The electrochemical activity is certainly due to the nickel cations: Ni^{2+} is the only cation that can be oxidized in the pristine compound. This was confirmed by *ex situ* and *post-mortem* XAS measurements, during which four samples were compared: pristine $\text{Li}_2\text{Ni}_2\text{W}_2\text{O}_9$, charged $\text{Li}_2\text{Ni}_2\text{W}_2\text{O}_9$ (1st cycle and 50th cycle), and discharged $\text{Li}_2\text{Ni}_2\text{W}_2\text{O}_9$ (1st cycle). (Figure 2.9).

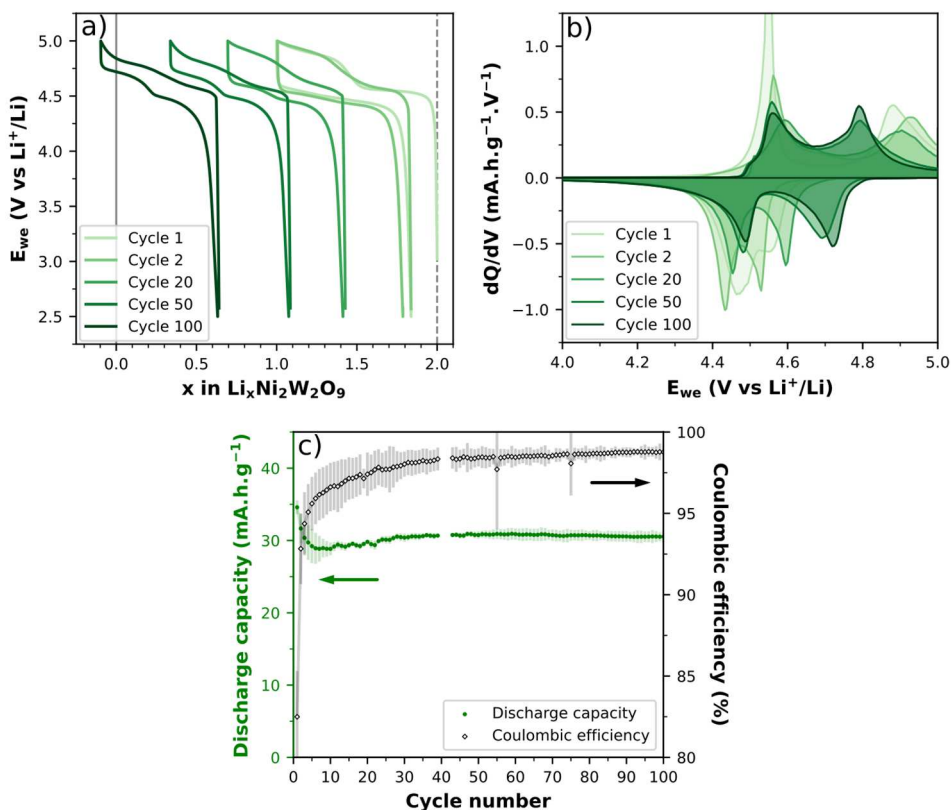


Figure 2.8 – (a) Galvanostatic charge-discharge curves and (b) dQ/dV curves for $\text{Li}_2\text{Ni}_2\text{W}_2\text{O}_9$ + 20 wt% carbon black, cycled at 10 mA.g^{-1} against Li metal at room temperature; the electrolyte was a solution containing 1 M LiPF_6 in a 1:1:4 (vol) EC:PC:DMC mix. (c) Average discharge capacity (green dots) and average coulombic efficiency (black diamonds) for three coin cells cycled according to the conditions set in (a).

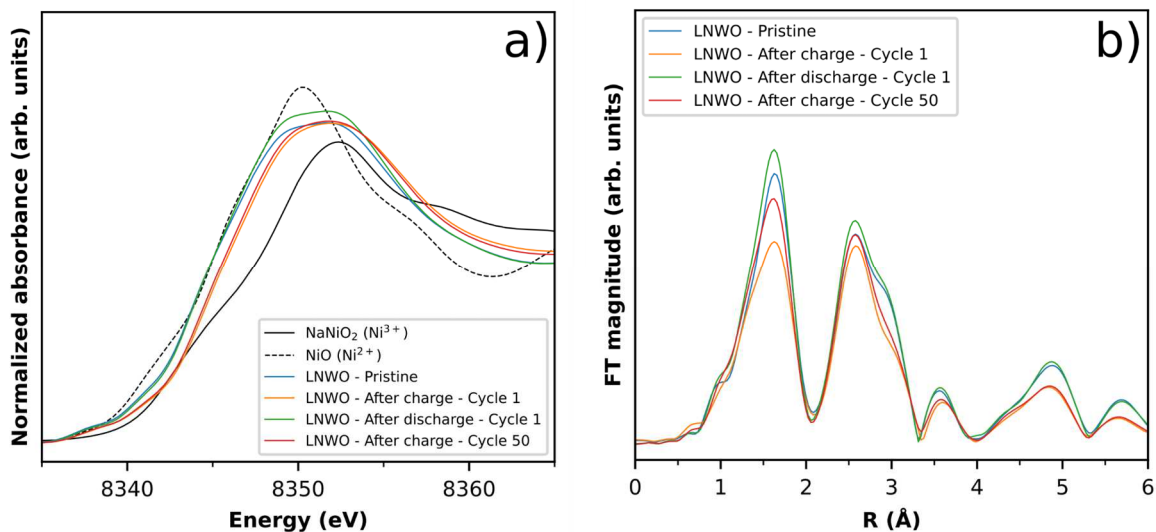


Figure 2.9 – Ni K-edge XAS. (a) XANES spectra and (b) magnitude of the FTs of the EXAFS oscillation for pristine $\text{Li}_2\text{Ni}_2\text{W}_2\text{O}_9$ (blue), $\text{Li}_2\text{Ni}_2\text{W}_2\text{O}_9$ cycled against lithium after one charge (orange), after one charge and one discharge (green) and after the 50th charge (red). The spectra for NiO (black, dashed) and NaNiO_2 (black, full) are shown as references in (a). $\text{Li}_2\text{Ni}_2\text{W}_2\text{O}_9$ was cycled against lithium metal, at 10 mA.g^{-1} , between 2.5 and 5.0 V vs Li^+/Li , in a Swagelok cell.

The energy shift of the X-ray absorption near-edge structure (XANES) spectra between pristine $\text{Li}_2\text{Ni}_2\text{W}_2\text{O}_9$ and charged $\text{Li}_2\text{Ni}_2\text{W}_2\text{O}_9$ in Figure 2.9a proves that Ni^{2+} is oxidized during galvanostatic charge; however, this shift accounts only for a 2.3+ oxidation state, whereas a 2.5+ oxidation state would be expected for the removal of 1 Li^+ equivalent during the first charge. This discrepancy between the expected and observed valence state of nickel after one galvanostatic charge to 5.0 V vs Li^+/Li could be explained by a self-discharge phenomenon²⁷⁵ or a partial reduction of nickel during the preparation of the *ex situ* samples for XAS measurements. A small difference in the edge position is observed when comparing a sample charged once and a sample charged after 50 cycles, corresponding to a slightly reduced Ni oxidation state after 50 charges. This matches with the extended X-ray absorption fine structure (EXAFS) results (Figure 2.9b); however, the origin of this difference remains unclear.

Moreover, the Ni oxidation state shifts back to its initial 2+ state, as confirmed by the XANES and EXAFS analysis after one full charge-discharge cycle, despite the electrochemical irreversibility observed in the first cycle on the cycling curves (Figure 2.8a). The local structure around the Ni cations is very similar for all four $\text{Li}_2\text{Ni}_2\text{W}_2\text{O}_9$ samples, as we can observe by a direct comparison of the magnitude of the Fourier transforms (FTs) of the EXAFS oscillations (Figure 2.9b), meaning that the local environment around Ni remains mostly unchanged throughout the charge-discharge process, even after 50 cycles.

Thus, it is clear that the $\text{Ni}^{3+}/\text{Ni}^{2+}$ couple is involved in the redox processes of $\text{Li}_2\text{Ni}_2\text{W}_2\text{O}_9$. However, the potentials at which the reactions occur are significantly higher than for other layered, nickel-active battery materials: an oxidation potential ranging from 3.8 to 4.3 V vs Li^+/Li is usually expected for the $\text{Ni}^{3+}/\text{Ni}^{2+}$ redox couple^{271,272,276,277}. The increase in the active potential range of $\text{Li}_2\text{Ni}_2\text{W}_2\text{O}_9$ may be explained by an inductive effect between the Ni^{2+} cations and the WO_6 octahedra, similarly to what can be found in LiNiPO_4 ^{278–280}.

Looking at the dQ/dV curves (Figure 2.8b), the first redox couple is initially characterized by a 100-mV polarization; this value increases slightly in the early cycles due to a shift of the reduction peak to lower potentials. However, this peak goes back to its initial position after cycle 50, and a 100-mV polarization is observed again. For the second, high-potential redox couple, the polarization decrease is much more significant: between cycle 2 and cycle 50, the polarization goes from more than 400 mV to around 80 mV. This indicates that there is a kinetic limitation to the second redox couple, which decreases through an activation process after several cycles. Because the oxidation potential diminishes steadily, the charge associated with the second oxidation plateau increases: at cycle 50, the plateau fully

appears in the charge profile. Overall, the activation process of $\text{Li}_2\text{Ni}_2\text{W}_2\text{O}_9$ leads to variations in discharge capacity: it decreases from 34 to 29 $\text{mA}\cdot\text{h}\cdot\text{g}^{-1}$ between cycles 1 and 7 before steadily increasing back to 31 $\text{mA}\cdot\text{h}\cdot\text{g}^{-1}$ in the subsequent cycles (Figure 2.8c). After 100 cycles, the material displays a capacity retention of 84 % when compared to the 1st cycle; this value increases to 98 % if cycle 50 is taken as the reference point. Although this activation process is reminiscent of what has been reported on electrochemical grinding in other materials²⁸¹, the capacity increase is actually quite small, and SEM pictures taken before and after cycling (Figure 2.10) show no clear evolution of the material's morphology correlated to the polarization decrease.

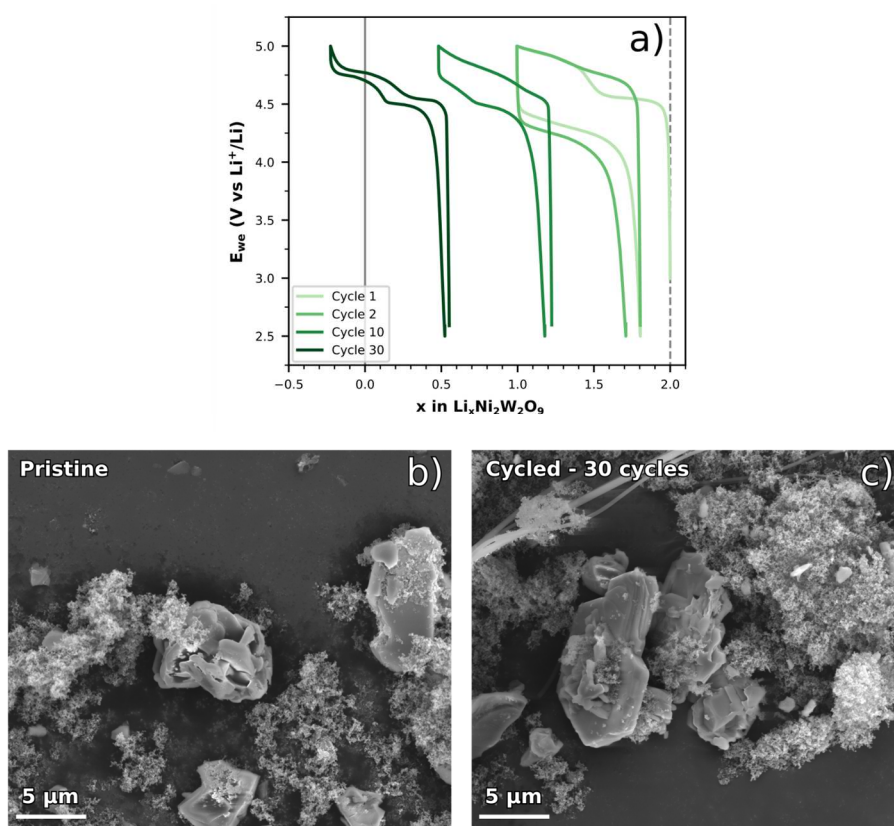


Figure 2.10 – (a) E_{we} vs x curves for a galvanostatic charge-discharge experiment at $10 \text{ mA}\cdot\text{g}^{-1}$ using $\text{Li}_2\text{Ni}_2\text{W}_2\text{O}_9\text{:C}$ (80:20 wt%) as a working electrode and 1 M LiPF_6 in EC:PC:DMC (1:1:4 vol.), in a Swagelok cell. (b) SEM picture of a pristine $\text{Li}_2\text{Ni}_2\text{W}_2\text{O}_9\text{:C}$ (80:20 wt%) powder sample. (c) *Post-mortem* SEM picture of a cycled (30 cycles) $\text{Li}_2\text{Ni}_2\text{W}_2\text{O}_9\text{:C}$ (80:20 wt%) powder sample, taken from the Swagelok cycled in (a).

Finally, an irreversible capacity of $\sim 7 \text{ mA}\cdot\text{h}\cdot\text{g}^{-1}$ is observed in the first cycle. The irreversibility decreases through the cycles, as indicated by a decrease in the slippage of the cycling curves (Figure 2.8a), and by a steady increase in coulombic efficiency (Figure 2.8c). However, this efficiency remains below 99 %, indicating that some irreversible processes are still occurring during charges, even after 100 cycles. Such residual irreversibility could be

associated with electrolyte decomposition, which would not be surprising considering how carbonate-based electrolytes suffer from high-potential cycling²⁸².

Crystal structure changes during cycling

In order to get a better picture of the electrochemical mechanism involved in the (de)lithiation of $\text{Li}_2\text{Ni}_2\text{W}_2\text{O}_9$, an *operando* XRD experiment was performed, using the same cycling conditions as before, in a cycling cell equipped with a Be window. The results of this experiment are shown in Figure 2.11.

Upon removing lithium from $\text{Li}_2\text{Ni}_2\text{W}_2\text{O}_9$, we observe that the (00 l) peaks shift toward lower Bragg angles (Figure 2.11b), while ($hk0$) peaks shift toward higher Bragg angles (Figure 2.11a), which matches with an increase in the c -lattice parameter, and a decrease in the a - and b -lattice parameters, respectively. The lattice expansion along the c -axis is easily explained by an increase of the coulombic repulsion between Ni-W-O layers upon Li^+ removal. Meanwhile, the oxidation of Ni^{2+} leads to a shortening of the Ni-O bond lengths, responsible for the lattice contraction along the a - and b -axis.

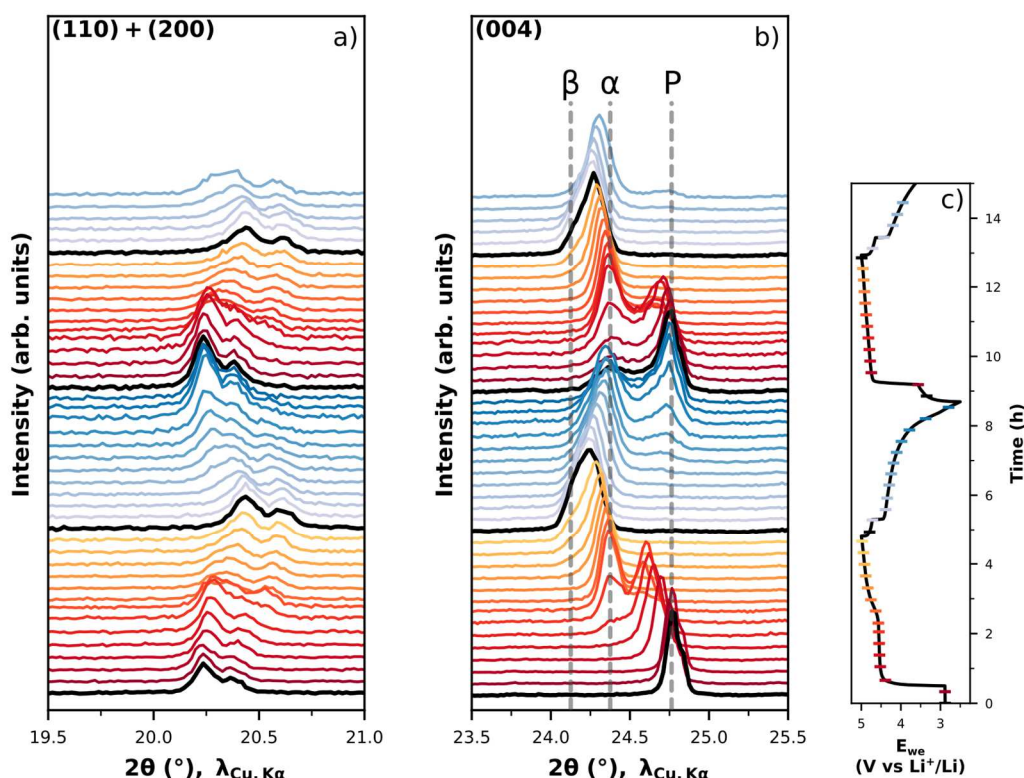


Figure 2.11 – Focus on the (a) (110) + (200) peaks and (b) (004) peaks of an *operando* XRD experiment on $\text{Li}_2\text{Ni}_2\text{W}_2\text{O}_9$. The scans taken during charge are in red; those taken during discharge are in blue. P: peak for pristine $\text{Li}_2\text{Ni}_2\text{W}_2\text{O}_9$. α : peak for $\text{Li}_\alpha\text{Ni}_2\text{W}_2\text{O}_9$. β : peak for $\text{Li}_\beta\text{Ni}_2\text{W}_2\text{O}_9$. (c) Cycling curve (E_{we} against time, 10 $\text{mA}\cdot\text{g}^{-1}$, 20 wt% carbon black) for the *operando* XRD experiment.

Moreover, after removing roughly 0.27 Li^+ equivalents from the material, new peaks start to appear indicating a biphasic system, matching with the first redox plateau. This underlithiated phase crystallizes in the $Pbcn$ space group, similarly to the pristine phase; however, the underlithiated lattice is elongated along the c -axis (Table 2.2). As the peaks for the pristine phase have fully disappeared after removing 0.5 to 0.6 Li^+ , the chemical formula for the underlithiated phase can be written as $\text{Li}_\alpha\text{Ni}_2\text{W}_2\text{O}_9$, with α between 1.4 and 1.5.

Table 2.2 – Lattice parameters calculated by Rietveld refinements of the pristine $\text{Li}_2\text{Ni}_2\text{W}_2\text{O}_9$ XRD pattern (synchrotron powder XRD), and of underlithiated $\text{Li}_\alpha\text{Ni}_2\text{W}_2\text{O}_9$.

	a (Å)	b (Å)	c (Å)	V (Å ³)
$\text{Li}_2\text{Ni}_2\text{W}_2\text{O}_9$	8.69523(8)	5.06407(5)	14.34517(2)	631.928(1)
$\text{Li}_\alpha\text{Ni}_2\text{W}_2\text{O}_9$	8.630(12)	5.0534(6)	14.605(17)	637.0(14)

When more lithium is removed (up to 1.04 Li^+), the peaks of $\text{Li}_\alpha\text{Ni}_2\text{W}_2\text{O}_9$ keep shifting, and new shoulder peaks start to appear at positions matching with the (002) and (004) reflections. These could correspond to another biphasic and an even more underlithiated phase, $\text{Li}_\beta\text{Ni}_2\text{W}_2\text{O}_9$, with $\beta < \alpha < 2$. However, these shoulder peaks are not as defined as for the $\text{Li}_\alpha\text{Ni}_2\text{W}_2\text{O}_9/\text{Li}_2\text{Ni}_2\text{W}_2\text{O}_9$ system. Thus, the existence of this second biphasic is not as clear-cut, even though it would match pretty neatly with the second set of plateaus/peaks observed in Figure 2.8a,b.

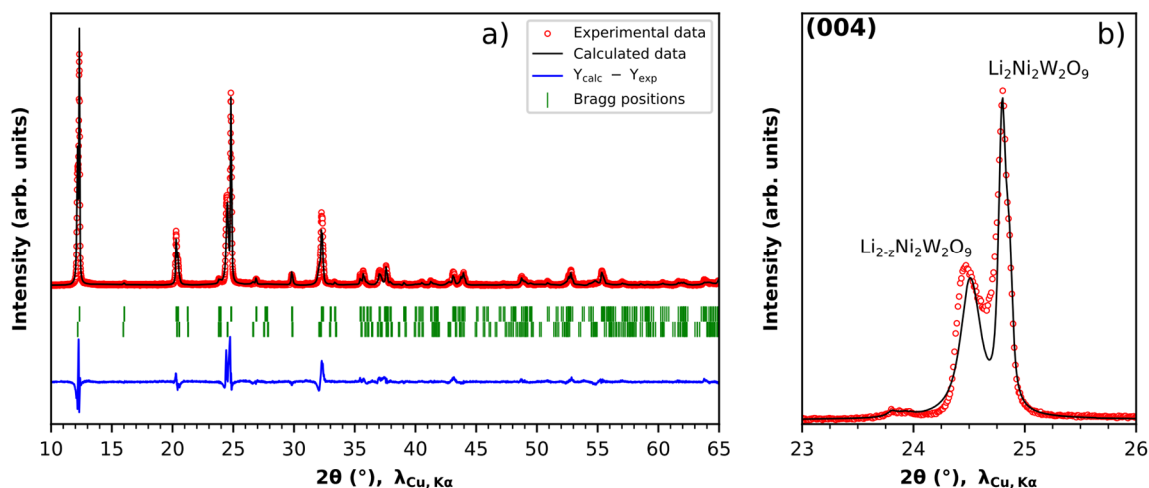


Figure 2.12 – (a) XRD pattern of a discharged (30 cycles, 2.5 to 5.0 V vs Li^+/Li) $\text{Li}_2\text{Ni}_2\text{W}_2\text{O}_9\text{:C}$ (80:20 wt%) powder sample (see Figure 2.10a). The experimental data is in red, the refined pattern is in black (Rietveld refinement), the Bragg positions are in green and the differential curve is in blue. (b) Focus on the (004) reflection of the XRD pattern shown in (a).

An opposite trend in the evolution of the XRD patterns is observed when reinserting lithium, indicating that the structural changes occurring in the $\text{Li}_{2-z}\text{Ni}_2\text{W}_2\text{O}_9$ electrode are

reversible. This reversibility is only partial, however, as the peaks associated to $\text{Li}_\alpha\text{Ni}_2\text{W}_2\text{O}_9$ do not fully disappear at the end of the discharge. This slight structural irreversibility accounts for the 0.2 Li^+ that cannot be inserted back in the material during the first discharge and is responsible for the 7 mA.h.g^{-1} irreversibility in the first cycle. In general, the crystal structure of the material does not appear to deteriorate further past the first cycle (Figure 2.12). This could explain the good reversibility and capacity retention observed for $\text{Li}_2\text{Ni}_2\text{W}_2\text{O}_9$, and it would indicate that structural irreversibilities do not contribute much further to the electrochemical irreversibility after the first couple of cycles.

Electrochemical behavior at lower current densities and lower potentials

The electrochemical behavior shown in Figure 2.8 does not significantly change when (de)lithiating $\text{Li}_2\text{Ni}_2\text{W}_2\text{O}_9$ at a lower current density (Figure 2.13). Going from 10 mA.g^{-1} to 1.5 mA.g^{-1} , the two plateaus still appear both in charge and discharge. This suggests that the biphasic system exposed by the *operando* XRD experiment is not due to kinetic limitation (i.e. cycling the cell too fast). The only significant difference observed when cycling at 1.5 mA.g^{-1} is that the coulombic efficiency decreases, and the slippage in the charge/discharge curves is more significant. This is likely because the slower rate of cycling leaves more time for irreversible electrolyte oxidation to occur.

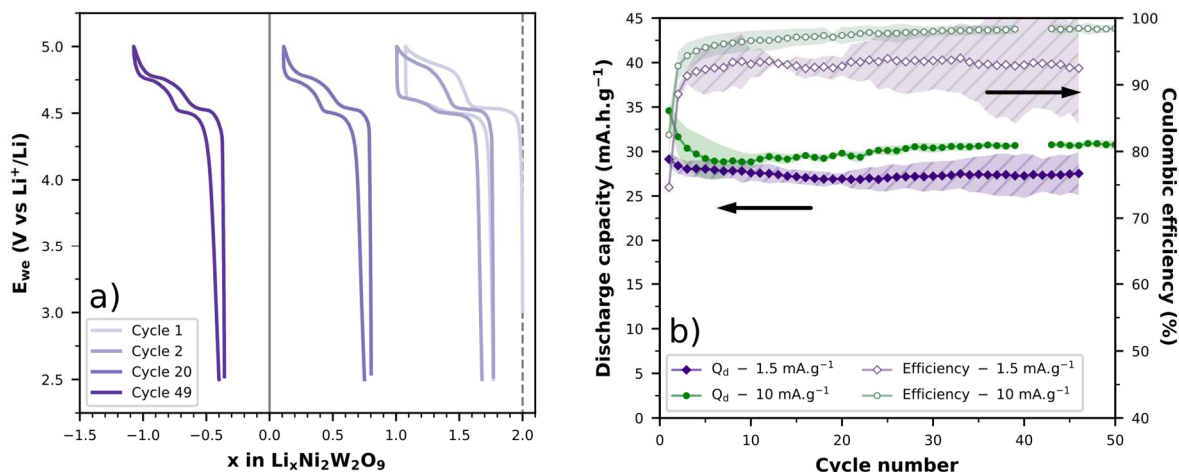


Figure 2.13 – (a) E_{we} vs x curves for $\text{Li}_2\text{Ni}_2\text{W}_2\text{O}_9$ cycled in a coin cell at 1.5 mA.g^{-1} against lithium metal, using 1 M LiPF_6 in EC:PC:DMC (1:1:4 vol) as electrolyte. (b) Discharge capacity (full markers) and coulombic efficiency (empty markers) vs cycle number for $\text{Li}_2\text{Ni}_2\text{W}_2\text{O}_9$ cycled at 10 mA.g^{-1} (green) and 1.5 mA.g^{-1} (purple) against lithium metal.

A similar set of electrochemical characterizations was conducted on $\text{Li}_2\text{Ni}_2\text{W}_2\text{O}_9$ with a lower potential range (1.0 to 3.0 V) to inspect the electrochemical behavior of the phase upon

overlithiation. The results suggest that an irreversible conversion reaction occurs when cycling $\text{Li}_2\text{Ni}_2\text{W}_2\text{O}_9$ in this potential window (Figure 2.14), and the compound is probably transformed into an amorphous mix of different phases after the first discharge to 1.0 V, which is not unheard of for a nickel-tungsten mixed oxide²⁸³.

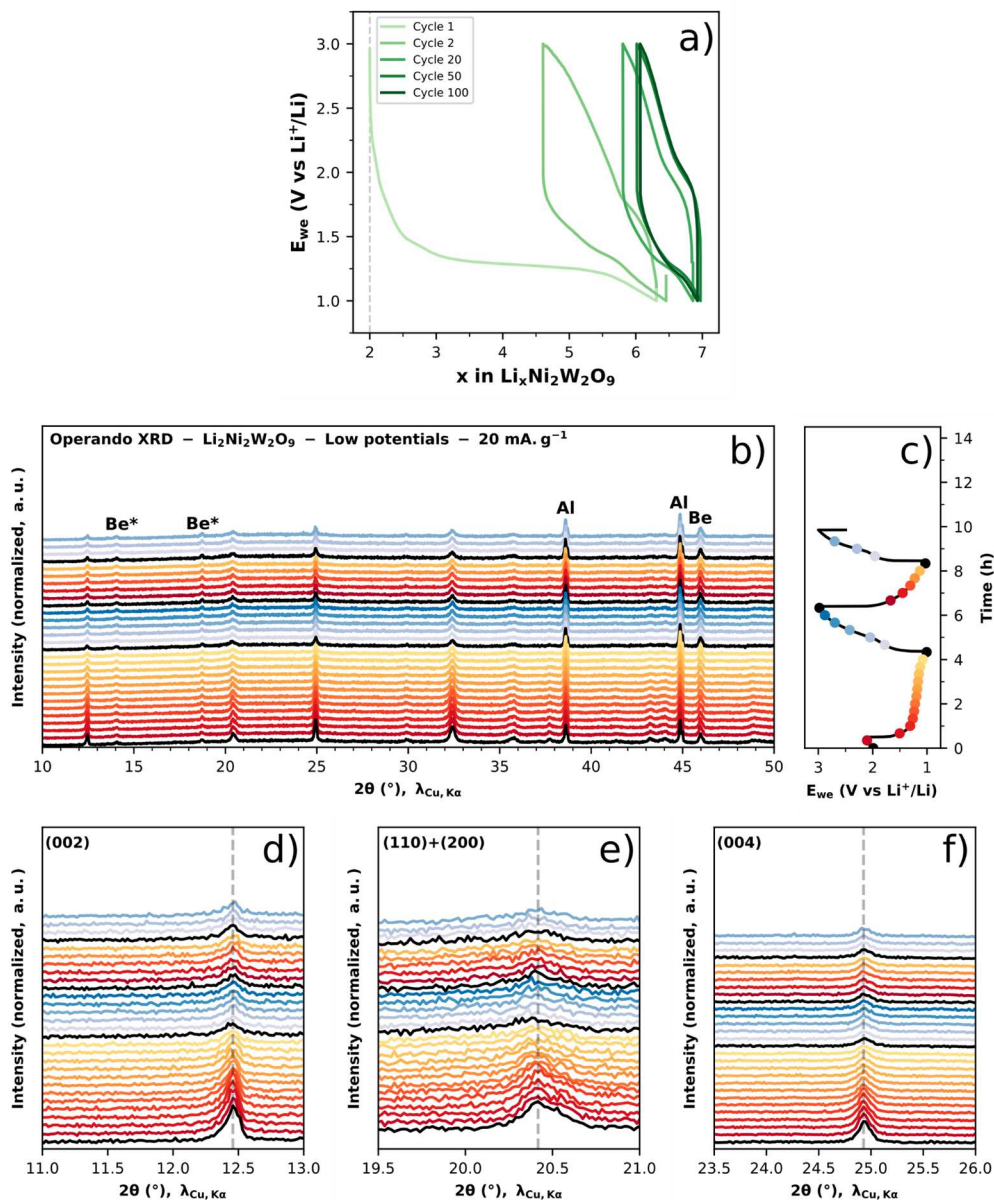


Figure 2.14 – (a) Galvanostatic charge-discharge experiment with $\text{Li}_2\text{Ni}_2\text{W}_2\text{O}_9$ as the working electrode and metallic lithium as the counter-electrode. The current density was of $20 \text{ mA}\cdot\text{g}^{-1}$, the coin cell was cycled at room temperature and the electrolyte was a solution containing 1 M LiPF_6 in a 1:1 (vol) EC:DMC mix. Below: *Operando* XRD experiment in a Be cell with $\text{Li}_2\text{Ni}_2\text{W}_2\text{O}_9$ as the working electrode and metallic lithium as the counter-electrode. Cycling conditions are identical to those used in (a). The discharges are in red and the charges are in blue. (b) XRD scans on the entire $2\theta = 10$ to 50° range. Peaks for the aluminum foil (Al), beryllium window (Be), and impurities on the beryllium window (Be^*) are indicated. (c) E_{we} vs time. (d, e, f) Focus on the (002), (110)+(200), and (004) peaks.

Electrochromism in $\text{Li}_2\text{Ni}_2\text{W}_2\text{O}_9$: insights from *operando* optical reflection microscopy

The *operando* XRD measurements demonstrate that the reversible electrochemical behavior of $\text{Li}_2\text{Ni}_2\text{W}_2\text{O}_9$ at high potentials is also associated to reversible structural changes. Considering this, one might wonder if reversible optical changes are not occurring as well when lithium is inserted or removed from the material.

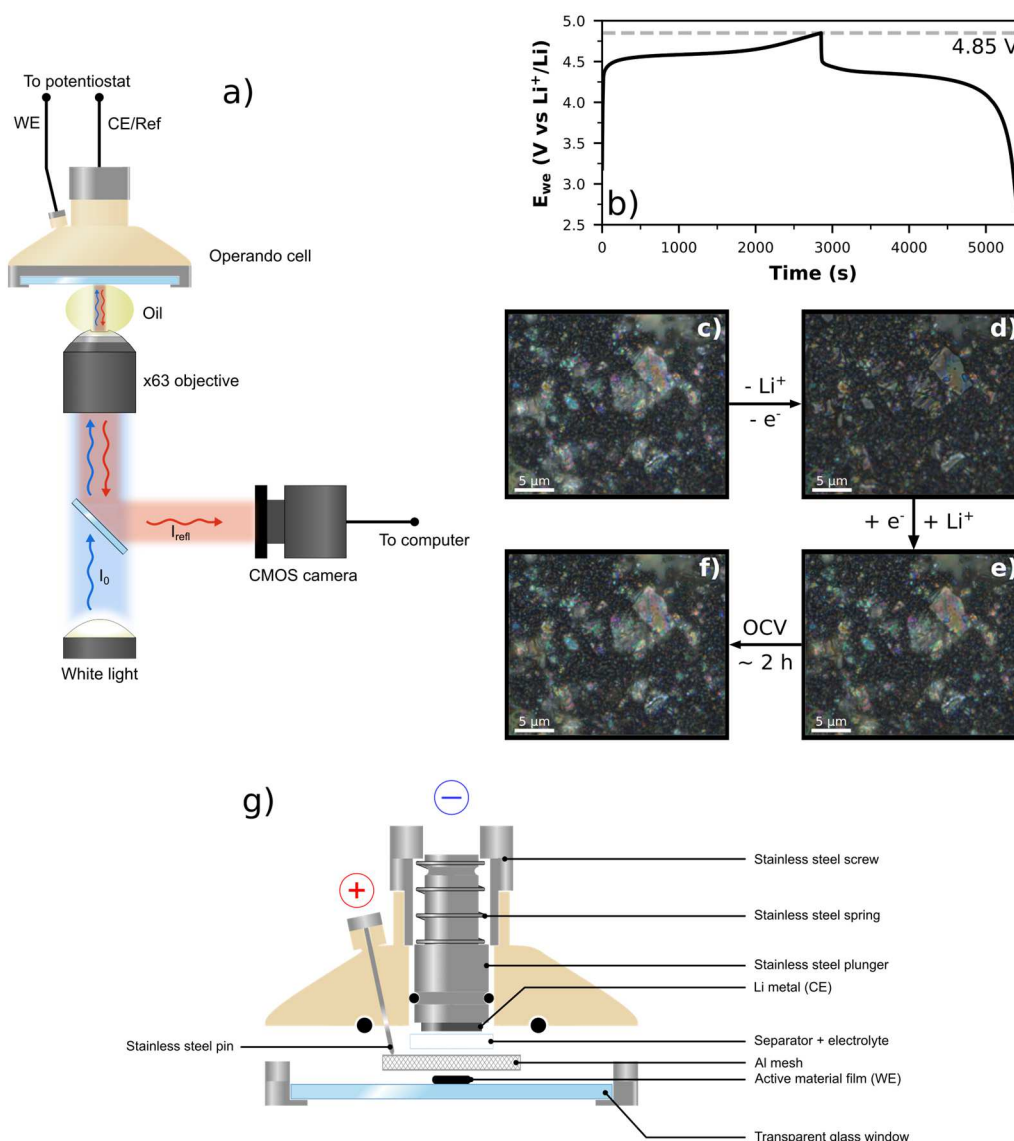


Figure 2.15 – (a) *Operando* optical reflection microscopy setup. (b) Galvanostatic charge-discharge curve (E_{we} vs time, $10 \text{ mA}\cdot\text{g}^{-1}$) for the working electrode during the *operando* optical microscopy experiment. (c, d, e, f):

Optical microscopy pictures taken before the experiment (c), at the end of the charge (d), at the end of the discharge (e), and 2 h hours after the end of the experiment (f), respectively. (g): Detailed representation of the *operando* optical cell.

In order to assess the electrochromic properties of $\text{Li}_2\text{Ni}_2\text{W}_2\text{O}_9$, we performed an *operando* optical reflection microscopy experiment. As shown in the reproduction of the experimental setup (Figure 2.15a), the images were obtained from the collection of light reflected by the imaged sample. A self-standing electrode ($\text{Li}_2\text{Ni}_2\text{W}_2\text{O}_9$: 94.8 wt% / Carbon black Super P: 5 wt% / PTFE: 0.2 wt%) was cycled against lithium metal in a cell designed for this type of experiment (Figure 2.15g)^{284,285}.

The cell was cycled from 2.5 V to 4.85 V vs Li^+/Li (Figure 2.15b), granting an insight into what is happening optically to $\text{Li}_2\text{Ni}_2\text{W}_2\text{O}_9$ during Li^+ (de)insertion, but only for the first redox plateau. The optical microscopy images collected by the CMOS camera (Figure 2.15c, d, e, f) clearly show a general decrease of the reflected intensity (I_{refl}) for the $\text{Li}_2\text{Ni}_2\text{W}_2\text{O}_9$ particles after the removal of lithium cations; the reflected intensity increases back after the reinsertion of Li^+ . Moreover, from transmission-like images of pristine and delithiated $\text{Li}_2\text{Ni}_2\text{W}_2\text{O}_9$ particles acquired *ex situ* (*in situ* experiments in transmission mode are impossible due to the electrode's thickness), we see that the transmitted intensity is also attenuated upon Li^+ deinsertion (Appendix A2.1). Since both reflectance and transmittance decrease during Li^+ deinsertion, this necessarily means that the absorbance of light by the particles increases during the delithiation process. Therefore, it is confirmed that $\text{Li}_2\text{Ni}_2\text{W}_2\text{O}_9$ is an anodic electrochromic material. On top of all this, the electrochromic properties of the material appear to be reversible, at least on a couple of cycles (Figure 2.16).

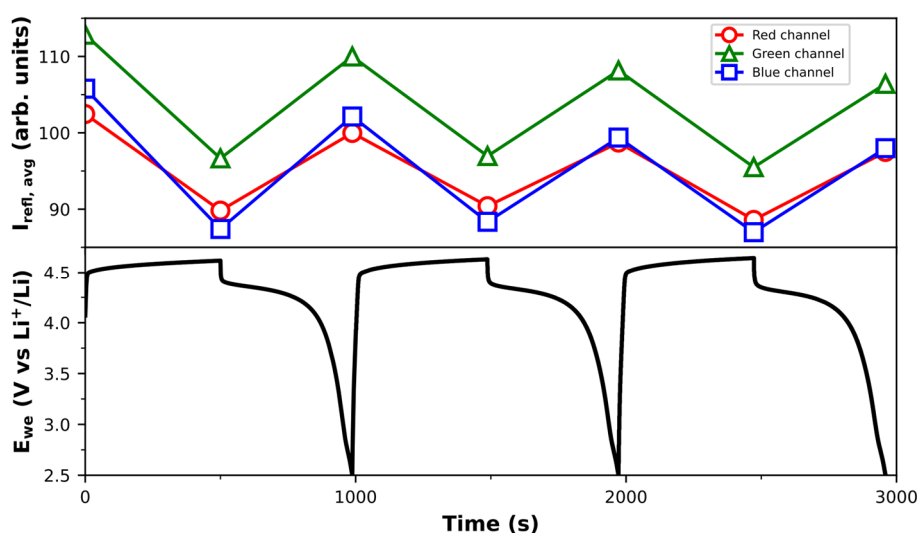


Figure 2.16 – Average reflected intensity (top) and E_{we} (bottom) for the $\text{Li}_2\text{Ni}_2\text{W}_2\text{O}_9$ self-standing electrode in an *operando* optical microscopy experiment. For this experiment, three galvanostatic charge-discharge cycles at $10 \text{ mA} \cdot \text{g}^{-1}$ were performed to confirm that the electrochromic behavior is maintained past the first cycle. The charges lasted 500 s; the discharge were performed until a 2.5 V vs Li^+/Li cut-off voltage was reached.

Quantification of the electrochromic properties: statistical and single particle approaches

The reflection microscopy data was further treated in order to quantify the intensity reflected by each $\text{Li}_2\text{Ni}_2\text{W}_2\text{O}_9$ particle throughout the experiment and to perform a statistical analysis (Figure 2.17).

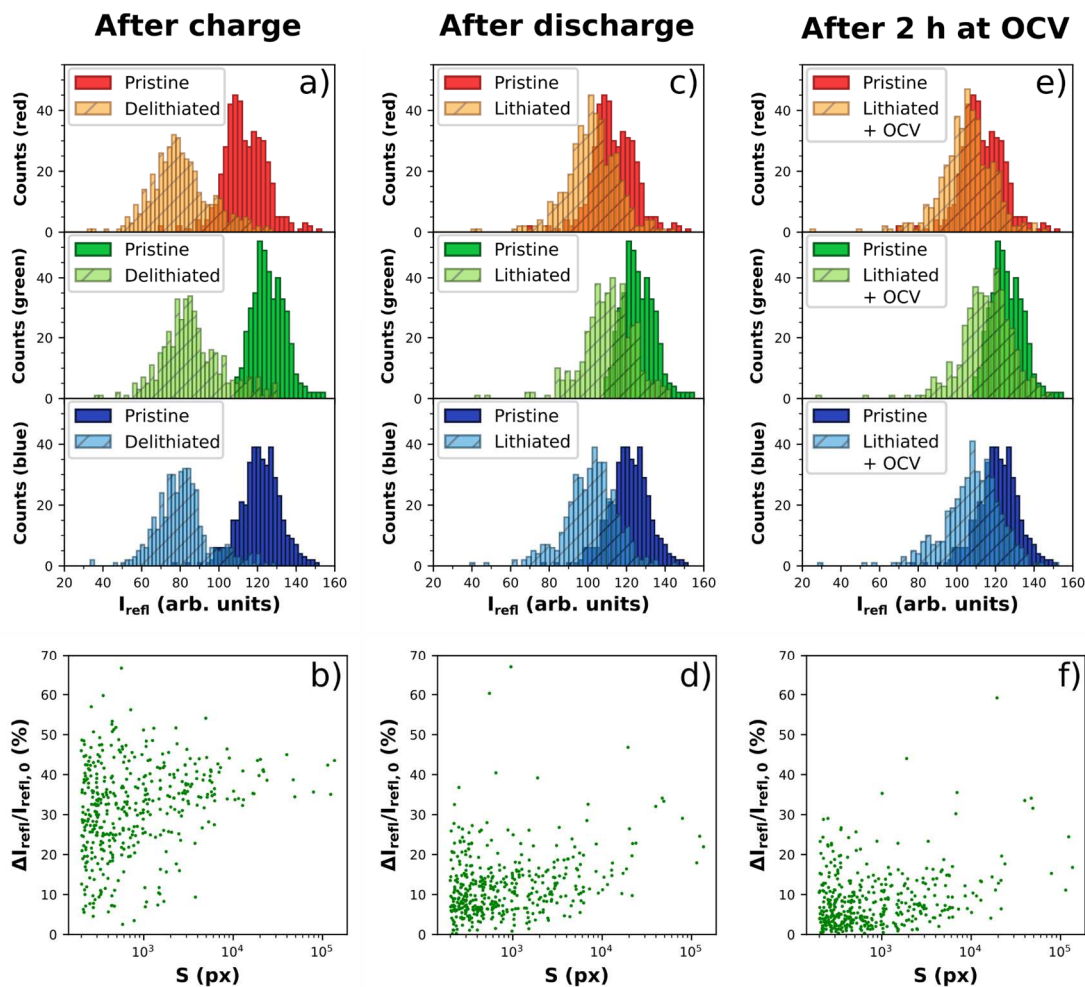


Figure 2.17 – Top: distributions of the intensity reflected by each particle of the optical microscopy picture on the three RGB channels. Bottom: relative variation of the reflected green intensity ($1 - I_{\text{refl}}/I_{\text{refl},0}$) against particle surface S (S is given as the number of pixels required to represent each particle; pixel size = 55 nm). The pristine particles were taken as reference ($I_{\text{refl},0}$). (a, b): Pristine vs delithiated particles. (c, d): Pristine vs lithiated particles. (e, f): Pristine vs lithiated particles after 2 hours at OCV.

The global trend qualitatively observed in Figure 2.15 is confirmed: across all three RGB channels, there is a decrease of reflected intensity after the delithiation and an increase after the lithiation. Interestingly, we can also observe that there is a slight increase of the reflected intensity when leaving the electrode at OCV for two hours after the discharge, compared to what is seen immediately at the end of the discharge (Figure 2.17c,e). This

suggests that the lithium insertion inside the material is kinetically limited, possibly by the contraction of the crystal lattice along the c -axis during lithiation²⁸⁶. Despite this slight increase of I_{refl} after the resting time, the electrode does not fully go back to its original optical state: on all RGB channels, the intensity reflected by the electrode is slightly lower after the experiment compared to the pristine material (Table 2.3). This optical irreversibility matches with the electrochemical (Figure 2.8) and structural irreversibilities (Figure 2.11) displayed by the material when cycled against lithium metal.

Table 2.3 – Results for the gaussian fits of distributions of intensities reflected by each particle, on the three RGB channels, during the first charge-discharge cycle of the *operando* microscopy experiment. μ : expected value. σ : variance. Number of particles (sample size): 425.

Channel	Pristine	Delithiated	Lithiated	Lithiated + OCV
Red	$\mu = 113$	$\mu = 80$	$\mu = 101$	$\mu = 104$
	$\sigma = 11$	$\sigma = 16$	$\sigma = 16$	$\sigma = 17$
Green	$\mu = 126$	$\mu = 85$	$\mu = 110$	$\mu = 114$
	$\sigma = 8$	$\sigma = 16$	$\sigma = 16$	$\sigma = 18$
Blue	$\mu = 121$	$\mu = 81$	$\mu = 100$	$\mu = 107$
	$\sigma = 10$	$\sigma = 14$	$\sigma = 16$	$\sigma = 18$

It is also interesting to see that in terms of optics, not all particles in the electrode behave in the same way. This is especially noticeable when looking at Figure 2.17b: the relative intensity decrease between the particles in their pristine and delithiated states can range from 5.6 % to 67 %, depending on the particle studied and, to some extent, its size. This highlights the importance of looking at what is occurring over time at the single-particle-level, in order to complete the information acquired from the global picture.

Looking at the evolution of the average reflected intensity at the single-particle-level throughout the charge-discharge process (Figure 2.18), the same general trends are observed: a decrease in intensity upon delithiation, an increase upon lithiation. However, some particles can be fully darkened in less than 1000 s (particle *a*, particle *c*), while others require close to the entire charging time to go through the same optical transition (particle *b*). There is not a strong correlation between the electrochromic kinetics and the particle size during the charge (Appendices A2.2, A2.3). It is likely that the coloration rate depends on other properties of the $\text{Li}_2\text{Ni}_2\text{W}_2\text{O}_9$ particles which are difficult to observe with the setup used in this experiment (density, thickness, defects, etc.).

The similarity between the slopes of the I_{refl} curves in charge and discharge suggests that Li^+ cations are inserted, during the discharge, at the same rate as they are deinserted during

the charge. However, irreversibilities in the optical response can be observed, and can be linked to two phenomena: slow-lithium insertion kinetics at the end of the discharge, and a delay in the increase of the optical response during the discharge.

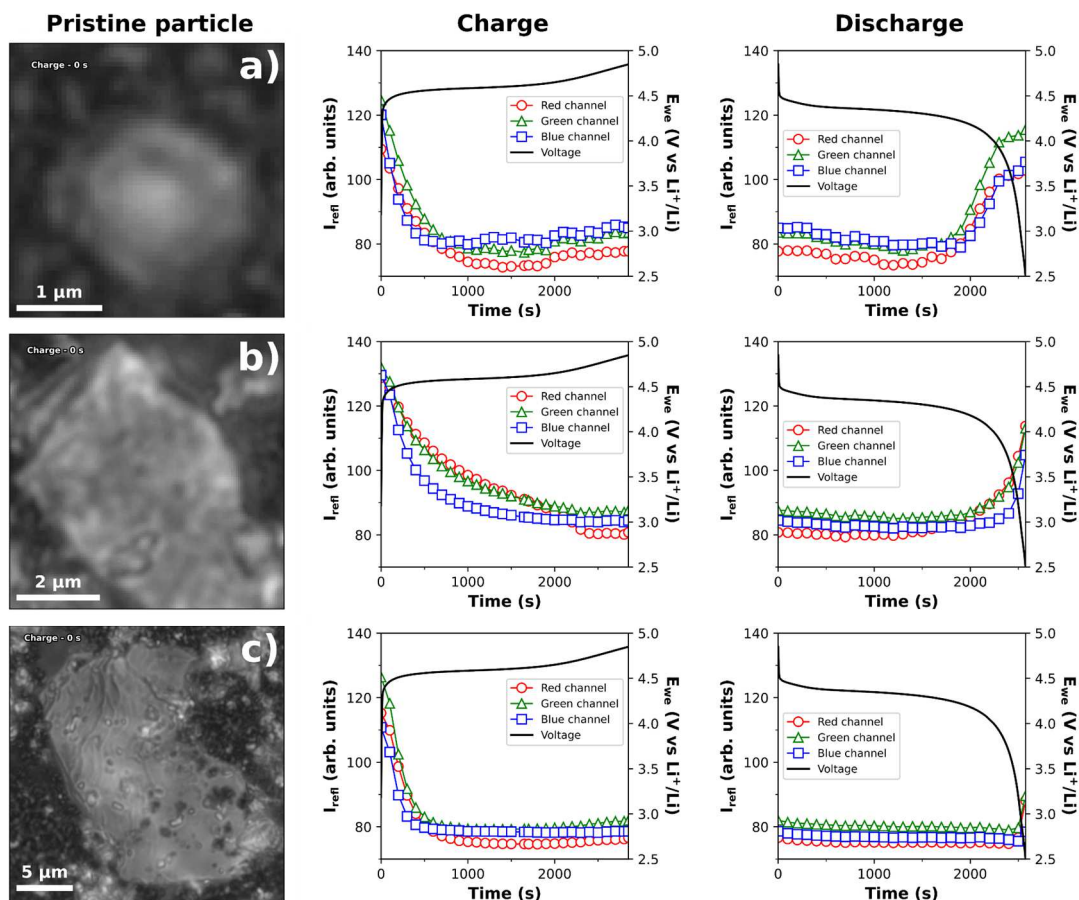


Figure 2.18 – Optical behavior during the galvanostatic charge-discharge for different particles (*a*, *b*, *c*). From left to right: gray-scaled optical microscopy picture in the electrode’s pristine state, I_{refl} and E_{we} vs time during the charge, and I_{refl} and E_{we} vs time during the discharge

In some cases, such as particle *a* (Figure 2.18a), two distinct slopes appear in the curve of I_{refl} vs time during the discharge. The second slope is weaker, indicating slow lithium-insertion kinetics at the end of the discharge leading to some irreversibility in the final reflected intensity (Figure 2.18a). About 29 % of small particles are affected by this two-slope optical increase. In comparison, 22 % of particles with S between 10^3 and 10^4 px show a similar optical behavior during the discharge. The proximity between this two percentages does not allow to conclude on a possible correlation between particle size and this two-slope phenomenon.

As for the “delay” phenomenon mentioned above, it can be observed when increasing the particle size (particles *b* and *c*). More specifically, the recovery of the reflected intensity during discharge happens less and less, and later and later from particle *a* to *c*, and as such, the

optical irreversibilities become larger (Figure 2.18, Figure 2.19); for particle *c*, the reflected intensity barely increases at the very end of the discharge (Figure 2.18c). A t_0 mapping highlights quite well the correlation between the size of a given particle and how late in the discharge its reflected intensity increases (Figure 2.20).

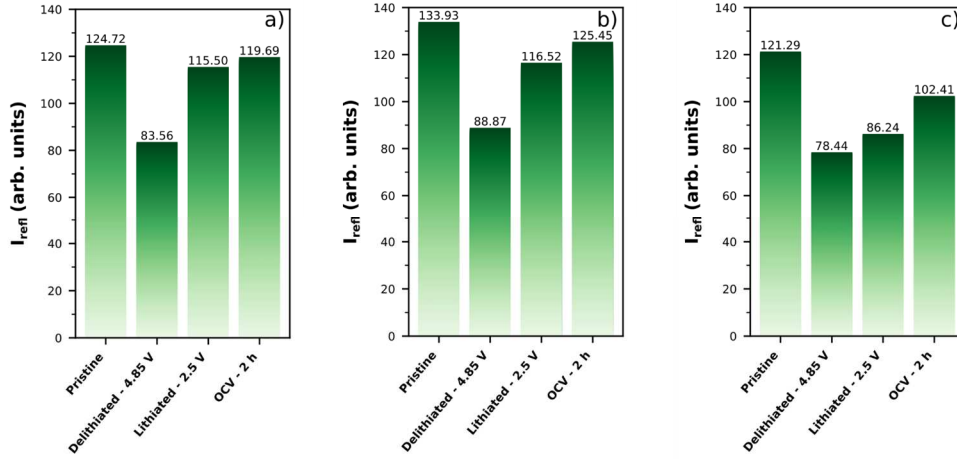


Figure 2.19 – Evolution of the reflected intensity on the green channel for particles *a*, *b* and *c* shown in Figure 2.18. I_{refl} is given for the pristine particles, the particles after charge, the particles after discharge and the particles two hours after the discharge.

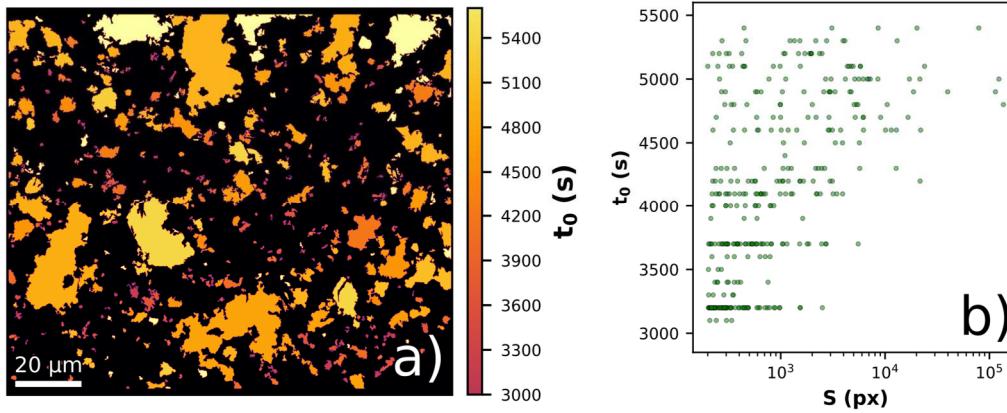


Figure 2.20 – t_0 analysis of the *operando* optical microscopy during the discharge. (a) t_0 mapping of the particles on the optical microscopy image of the $\text{Li}_2\text{Ni}_2\text{W}_2\text{O}_9$ electrode. (b) Plot of t_0 against the size of the particles (S , the size of the particles, is given as the number of pixels required to represent the particle on the microscopy image. 1 px = $0.003025 \mu\text{m}^2$). Number of particles (sample size): 425.

In Figure 2.20, t_0 corresponds to the time for which the variation of the intensity reflected by a given particle increases above a threshold value (Equation 2.6):

$$\left(\frac{dI_{\text{refl}}}{dt}\right)_t > 0.2 * \max\left(\frac{dI_{\text{refl}}}{dt}\right) \quad 2.6$$

It indicates when I_{refl} starts increasing upon lithium insertion. $t = 0$ s is defined as the beginning of the galvanostatic charge; the discharge begins at $t = 2850$ s in Figure 2.20. Overall, it appears that 52 % of small particles ($S < 10^3$ px) start changing color early on during the lithiation of the $\text{Li}_2\text{Ni}_2\text{W}_2\text{O}_9$ electrode, between 3100 and 4000 s. Meanwhile, bigger particles ($S > 10^3$ px) starts changing color after 4000 s, for the most part (Table 2.4).

Table 2.4 – Detailed data of the t_0 mapping for the discharge shown in Figure 2.15b.

t_0 (s)	Size range (px)			
	$[2 \cdot 10^2, 10^3]$	$[10^3, 10^4]$	$[10^4, 10^5]$	$[10^5, 10^6]$
[3100, 3500]	83 (30 %)	3 (2 %)	0	0
[3600, 4000]	60 (22 %)	11 (9 %)	0	0
[4100, 4500]	36 (13 %)	32 (26 %)	2 (11 %)	0
[4600, 5000]	23 (8 %)	39 (31 %)	10 (53 %)	3 (100 %)
[5100, 5500]	17 (6 %)	26 (21 %)	4 (21 %)	0
No bleaching	59 (21 %)	14 (11 %)	3 (16 %)	0
Total	278 part.	125 part.	19 part.	3 part.

This trend can be explained by the poorer Li^+ insertion kinetics of the larger particles during lithiation, which also affects the electrochromic kinetics during discharge as both are related to each other. Worth mentioning is that such limitations of the Li^+ insertion kinetics, which mostly happen during discharge, are actually very common for the layered Ni-containing Li-ion cathode materials^{287–289}. This t_0 mapping also shows that no matter the particle size, a significant number of particles become optically inactive after the first charge, probably due to contact loss. This will also contribute to the general electrochemical, structural, and optical irreversibilities in the $\text{Li}_2\text{Ni}_2\text{W}_2\text{O}_9$ electrode.

The fact that variations in I_{refl} do not occur immediately after the beginning of the discharge for all particles can be explained by a simple top-to-bottom conversion model of the particles (Appendix A2.4). Based on this model, a threshold amount of Li^+ needs to be inserted inside a particle before I_{refl} starts increasing, because changes in I_{refl} can only be observed once a threshold thickness of lithiated phase (< 200 nm) remains in the particle.

Going to higher voltage (above 4.9 V vs Li^+/Li) induces detrimental parasitic reactions in the cell, and therefore, the optical changes related to the second redox plateaus were not studied.

This *operando* optical microscopy experiments proves that $\text{Li}_2\text{Ni}_2\text{W}_2\text{O}_9$ is an electrochromic material, and delivers numerous insights into its electrochemical and optical properties. In particular, it gives several leads into the origin of the electrochemical, structural, and optical irreversibilities occurring in the material upon (de)lithiation.

2.D. Magnetic properties and magnetic structure of $\text{Li}_2\text{Ni}_2\text{W}_2\text{O}_9$

Having described the electrochemical and electrochromic properties of $\text{Li}_2\text{Ni}_2\text{W}_2\text{O}_9$, the rest of this chapter will focus on another property granted by the $3d^8$ electronic configuration of Ni^{2+} : paramagnetism.

A quick reminder on magnetic properties

Magnetic properties in solid materials are often introduced by the presence of paramagnetic ions, which possess at least one unpaired valence electron. This occurs most often in materials containing 3d and 4f elements. An ion with unpaired electrons displays an intrinsic magnetic moment; the magnetic properties of a material are produced by the interactions between these magnetic moments²⁹⁰.

When a paramagnetic material is exposed to an external magnetic field, the moments of the paramagnetic ions will tend to align themselves with the field, leading to a positive magnetization (M) of the material. In usual conditions, this magnetization can be described by Equation 2.7:

$$M = \chi H \tag{2.7}$$

in which H is the applied magnetic field, and χ is the magnetic susceptibility of the material. χ describes the response of a material to a magnetic field: it is positive for paramagnetic materials, and negative (and much less significant) for materials without unpaired electrons (i.e. diamagnetic materials). In this manuscript, the molar susceptibility χ_m , the susceptibility per mole of magnetic cation, will be used to discuss the magnetic properties of $\text{Li}_2\text{Ni}_2\text{W}_2\text{O}_9$.

At high temperatures, in a paramagnetic material, the interactions between magnetic ions are weaker than the thermal energy: the magnetic moments are disordered, and the material is said to be in a “paramagnet” state. By decreasing the temperature, a symmetry-breaking ordering of the magnetic moments can occur. The type of ordering will depend on the structure of the material. There are two main magnetic orders to be expected. Ferromagnetic order, in

which the magnetic moments of the material are parallel to one another, and antiferromagnetic order, in which the magnetic moments are antiparallel to one another. The type of magnetic ordering can be determined by the shape of the curve in a plot of χ_m vs T (Figure 2.21).

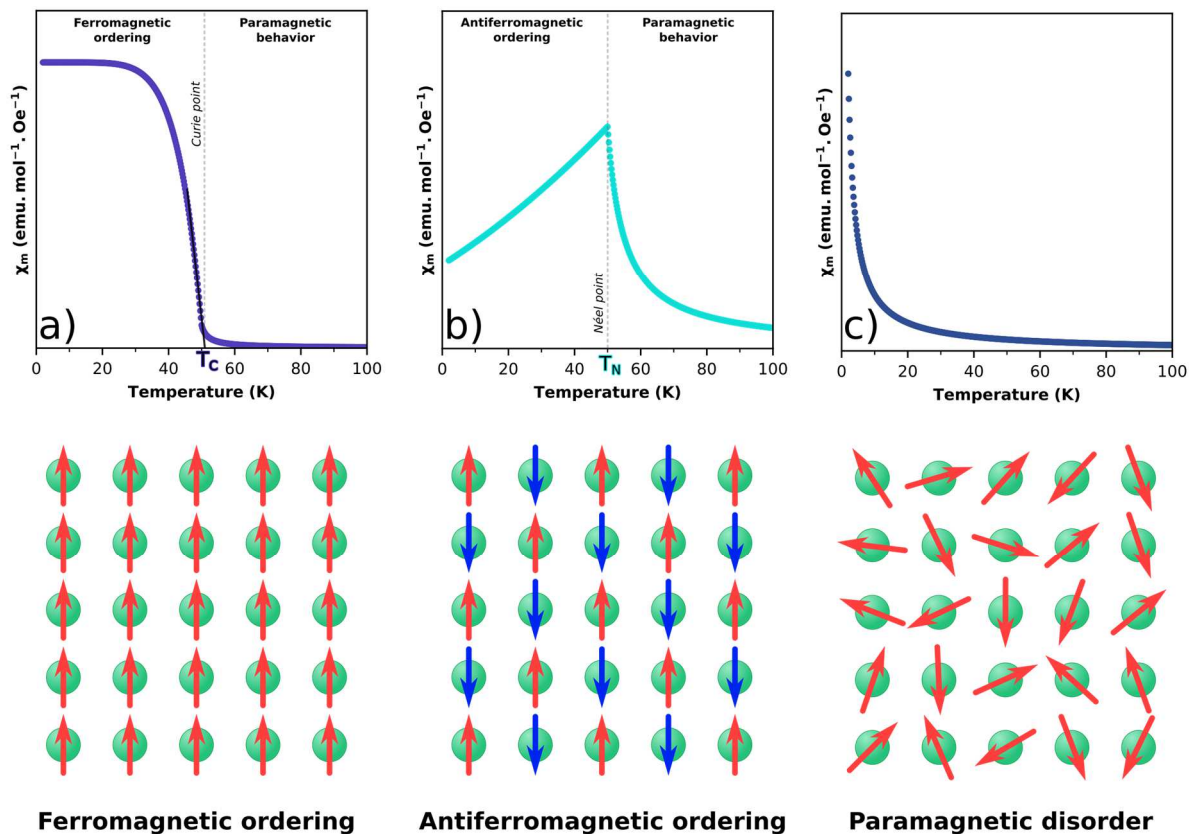


Figure 2.21 – Top: typical χ_m vs T plots for paramagnetic materials displaying (a) a ferromagnetic ordering, (b) an antiferromagnetic ordering, and (c) no magnetic ordering. Bottom: two-dimensional representations of the orientations of magnetic moments in a ferromagnet, an antiferromagnet, and a paramagnet.

When decreasing the temperature below the transition point between paramagnet and ferromagnet (the Curie temperature, T_C), there is a sudden increase in the value of χ_m , followed by a plateau as the temperature keeps decreasing (Figure 2.21a)²⁹¹. On the other hand, when going from a paramagnetic to an antiferromagnetic order, χ_m will sharply decrease below the transition point (the Néel temperature, T_N) leading to a cusp shape (Figure 2.21b)²⁹². In some cases, the magnetic interactions are too weak to ever overcome thermal fluctuations, even at low temperatures; in this case, no magnetic ordering is observed (Figure 2.21c)²⁹³.

Finally, assuming the paramagnetic properties of a material are mostly due to Curie-Weiss paramagnetism, it is possible to fit the $1/\chi_m$ vs T curve obtained from magnetic measurements using Equation 2.8:

$$\chi_m = \chi_0 + \frac{C}{T - \theta_{\text{CW}}} \quad 2.8$$

where χ_0 is a temperature-independent contribution to the magnetic susceptibility in mol^{-1} , C is the Curie constant in $\text{m}^3 \cdot \text{K} \cdot \text{mol}^{-1}$ and θ_{CW} is the Curie-Weiss temperature in K. Results from these fits are extremely useful, as it is possible to calculate the effective moment per magnetic ion, μ_{eff} , using the value of C and Equation 2.9²⁹⁴:

$$\mu_{\text{eff}} = \sqrt{\frac{3k_B}{N_A \mu_0 \mu_B^2}} \sqrt{C} \approx 800 \sqrt{C} \quad 2.9$$

where k_B is the Boltzmann constant ($1.38 \times 10^{-23} \text{ J} \cdot \text{K}^{-1}$), N_A is the Avogadro constant ($6.022 \times 10^{23} \text{ mol}^{-1}$), μ_0 is the magnetic constant ($4\pi \times 10^{-7} \text{ H} \cdot \text{m}^{-1}$), and μ_B is the Bohr magneton ($9.274 \times 10^{-24} \text{ J} \cdot \text{T}^{-1}$). Moreover, the sign of θ_{CW} determines the types of magnetic interactions found in the material: ferromagnetic interactions yield $\theta_{\text{CW}} > 0$, antiferromagnetic interactions yield $\theta_{\text{CW}} < 0$, and for a paramagnet $\theta_{\text{CW}} = 0$ (Figure 2.22).

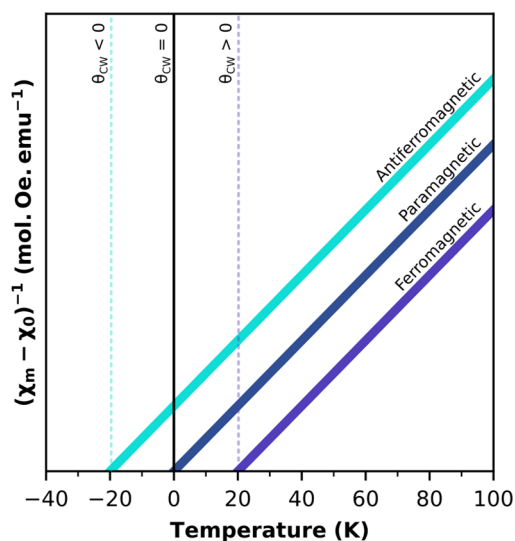


Figure 2.22 – Simplified representations of the linear fits expected for magnetic materials with antiferromagnetic (light blue), paramagnetic (dark blue), and ferromagnetic (purple) interactions, using the modified Curie-Weiss model, for $1/(\chi_m - \chi_0)$ vs T curves.

This quick reminder on the magnetic properties of paramagnets is obviously non-exhaustive: other types of paramagnetism originating from other phenomena exist, and magnetic structures can be far more complex than the ones described in Figure 2.21. However, the notions given in this short paragraph are sufficient to study $\text{Li}_2\text{Ni}_2\text{W}_2\text{O}_9$. On a final note, the international system of units (SI)²⁹⁵ will not be used in this section of the chapter;

centimeter-grams-second (CGS) units²⁹⁶, which are often encountered in the literature on magnetic materials, will be applied instead.

The “429” compounds

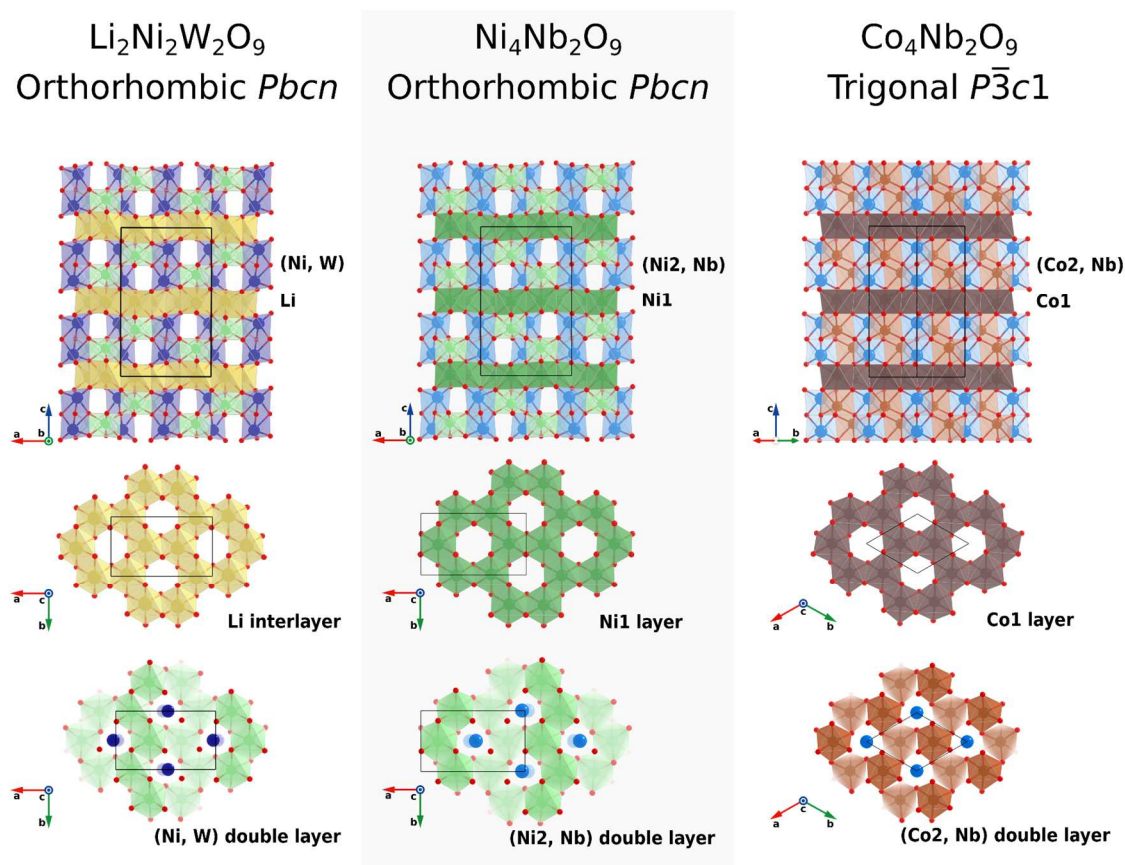


Figure 2.23 – Crystal structures of $\text{Li}_2\text{Ni}_2\text{W}_2\text{O}_9$ (left), $\text{Ni}_4\text{Nb}_2\text{O}_9$ (middle), and $\text{Co}_4\text{Nb}_2\text{O}_9$ (right). Oxygen atoms are red, tungsten atoms are dark blue, and niobium atoms are sky blue; lithium atoms are yellow, nickel atoms in various shades of green, cobalt atoms in various shades of brown. For the double layer view, atoms in a paler color are at lower z-coordinates.

The “429” family is a series of compounds with general formula $M_4A_2O_9$ ($M = \text{Mg}, \text{Mn}, \text{Fe}, \text{Co}, \text{Ni}$; $A = \text{Nb}, \text{Ta}$). Described for the first time by Bertaut et al. in 1961²⁹⁷, these materials sparked interest in recent years because of their magnetic properties; especially their magnetoelectric properties^{298–302}. The linear magnetoelectric effect is a coupling between the electric and magnetic responses of a material: an electric polarization of the material can be induced by a magnetic field, and its magnetization can be induced by an electric field. It has been demonstrated that the existence of this effect in a material relies on its magnetic structure, and particularly its magnetic point symmetry^{303–307}. Most 429-compounds crystallize in the trigonal space group $P\bar{3}c1$, in a structure derived from that of corundum ($\alpha\text{-Al}_2\text{O}_3$)^{297,308}. This often leads to magnetic structures with point symmetries compatible with the magnetoelectric

effect, such as $2/m'$ in $\text{Co}_4\text{Nb}_2\text{O}_9$ ^{261,309–311}, $2/m'$ and $2'/m$ in $\text{Fe}_4\text{Nb}_2\text{O}_9$ ³¹², or $\bar{3}'m'$ in $\text{Mn}_4\text{Nb}_2\text{O}_9$ ²⁹⁷, to give a few examples.

$\text{Ni}_4\text{Nb}_2\text{O}_9$ is an outcast in the 429 family. Although its crystal structure is very similar to corundum, slight differences in the Ni and Nb positions make it crystallize in the orthorhombic $Pbcn$ space group³¹³, instead of the usual trigonal $P\bar{3}c1$ seen in other 429-compounds. $\text{Ni}_4\text{Nb}_2\text{O}_9$ displays interesting magnetic properties originating from the $3d^8$ electronic configuration of Ni^{2+} ; specifically, it has been studied for its ferrimagnetism^{314,315} and magnetization reversal effects^{316–318}. However, the magnetic space group of this material is $Pb'cn'$ with magnetic point group $m'm'm$ (#8.4.27), and thus, it does not allow a magnetoelectric coupling²⁶⁷.

A few studies have been conducted on exotic magnetic materials based on $\text{Ni}_4\text{Nb}_2\text{O}_9$. These materials are usually prepared through the partial substitution of the Ni^{2+} cations by another divalent cation. Tarakina et al. reported on compounds with the general formula $\text{Mg}_{4-x}\text{Ni}_x\text{Nb}_2\text{O}_9$ ($0 \leq x \leq 4$), showing that for $x > 2.75$, the $Pbcn$ structure and the magnetic properties of $\text{Ni}_4\text{Nb}_2\text{O}_9$ were maintained, although planar defects were introduced in the structure²⁶⁶. Later, Bolleta et al. worked on tuning the magnetization reversal effect in $\text{Ni}_4\text{Nb}_2\text{O}_9$ through partial substitution of nickel with zinc, showing significant changes of magnetic properties in $\text{Ni}_{4-x}\text{Zn}_x\text{Nb}_2\text{O}_9$ compounds, from $x = 0$ to $x = 0.75$ ³¹⁶. More recently, Jiongo-Dongmo et al. studied the $\text{Co}_4\text{Nb}_2\text{O}_9 - \text{Ni}_4\text{Nb}_2\text{O}_9$ phase diagram ($\text{Ni}_{4-x}\text{Co}_x\text{Nb}_2\text{O}_9$), aiming to combine the linear magnetoelectric effect of the former with the magnetization reversal of the latter. They showed a nice transition from the $Pbcn$ structure to the $P\bar{3}c1$ structure for x between 2.2 and 2.5. However, the linear magnetoelectric effect could not be observed in the $Pbcn$ structure for this series of compounds³¹⁷.

Similarly to $\text{Ni}_4\text{Nb}_2\text{O}_9$, $\text{Li}_2\text{Ni}_2\text{W}_2\text{O}_9$ crystallizes in a corundum-like $Pbcn$ structure. However, because Li^+ cations are arranged in a honeycomb configuration in-between the (Ni, W) layers (Figure 2.23), the magnetic interactions between Ni^{2+} cations change radically in $\text{Li}_2\text{Ni}_2\text{W}_2\text{O}_9$ compared to $\text{Ni}_4\text{Nb}_2\text{O}_9$.

Antiferromagnetism in $\text{Li}_2\text{Ni}_2\text{W}_2\text{O}_9$

Molar magnetic susceptibility measurements performed on $\text{Li}_2\text{Ni}_2\text{W}_2\text{O}_9$ powder, in zero-field cooled (ZFC) and field cooled (FC) modes, are shown in Figure 2.24.

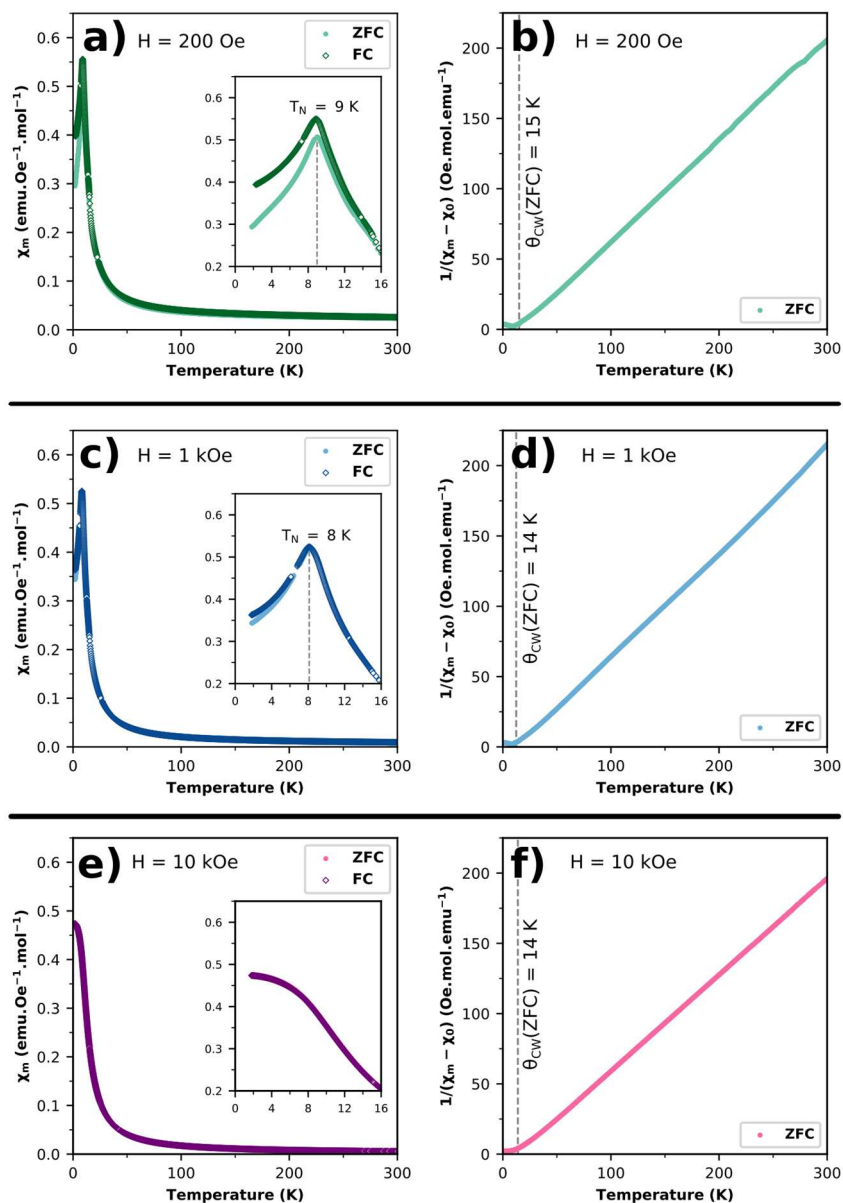


Figure 2.24 – Molar magnetic susceptibility (χ_m) vs T curves and $1/(\chi_m - \chi_0)$ vs T curves for (a, b) $H = 200$ Oe, (c, d) $H = 1$ kOe, and (e, f) $H = 10$ kOe.

For an applied magnetic field H of 200 Oe or 1 kOe, the material displays a paramagnetic behavior down to a temperature T_N of roughly 8 to 9 K. At this Néel point, a cusp can be observed, characteristic of an antiferromagnetic transition. However, such a transition is no longer apparent when the applied field is increased to 10 kOe, suggesting that the magnetic properties of the material are field-dependent. Magnetization measurements were performed to confirm this observation, and are displayed in Figure 2.25.

At 100 K, the magnetization curve is linear, indicating a fully paramagnetic behavior, which does not seem impacted by the applied magnetic field. In contrast, at 2 K, below T_N , inflexion points can be observed in the magnetization curve for $|H| \approx 8$ kOe, indicating a change

in magnetic behavior. This behavior could be associated to a metamagnetic transition³¹⁹, but this needs to be confirmed through neutron diffraction measurements in an applied magnetic field, which were not conducted in this study.

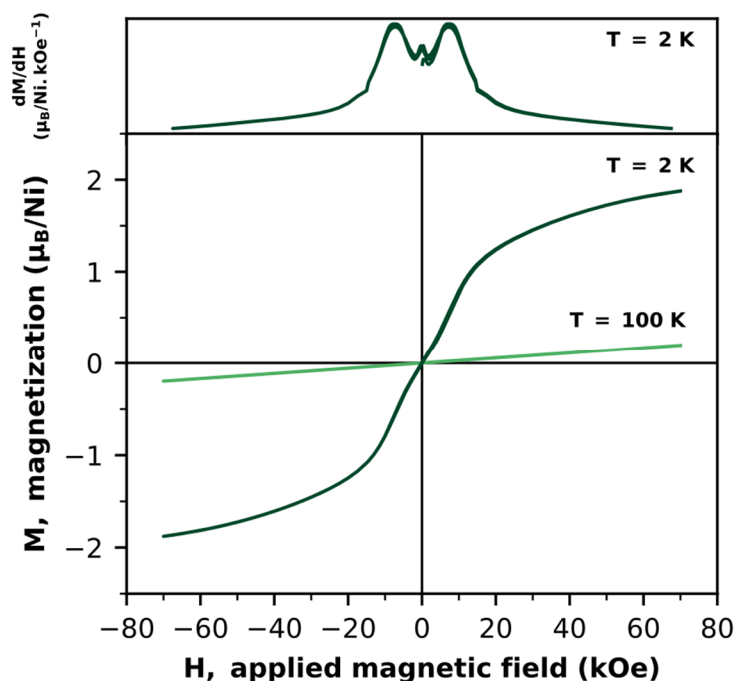


Figure 2.25 – Magnetization curves for $\text{Li}_2\text{Ni}_2\text{W}_2\text{O}_9$ powder at $T = 2$ K (dark green) and $T = 100$ K (light green). The derivative curve for $T = 2$ K is displayed on the upper part of the figure.

The curves for $1/\chi_m$ vs T were fitted with a modified Curie-Weiss law (Equation 2.8). Results of the fits are shown in Table 2.5. The fitting range had to be adapted from one measurement to the next to account for deviations from the model due to magnetic impurities. Interestingly, even though the shape of the susceptibility curves clearly proves that $\text{Li}_2\text{Ni}_2\text{W}_2\text{O}_9$ goes through an antiferromagnetic ordering at low temperatures (for $H < 8$ kOe), the values of θ_{CW} are all positive, which indicates that there are strong ferromagnetic interactions in the material. Values of μ_{eff} were calculated using Equation 2.9.

Table 2.5 – Results of the modified Curie-Weiss fits for the $1/\chi_m$ vs T curves.

		θ_{CW} (K)	C ($10^{-5} \text{ m}^3 \cdot \text{K} \cdot \text{mol}^{-1}$)	μ_{eff} (μ_{B})	Fitting range (K)
H = 200 Oe	ZFC	15.09(2)	1.7228(9)	3.32(8)	[50; 300]
	FC	8.8(1)	2.208(6)	3.8(2)	[50; 200]
H = 1 kOe	ZFC	13.68(3)	1.680(1)	3.28(8)	[50; 250]
	FC	12.85(4)	1.731(1)	3.33(8)	[50; 250]
H = 10 kOe	ZFC	13.99(3)	1.8303(4)	3.42(5)	[50; 300]
	FC	13.98(1)	1.8196(4)	3.41(5)	[50; 300]

Aside from the aberrant $3.8 \mu_B$ value calculated for the FC curve at $H = 200$ Oe (which is probably related to impurities in the sample), the calculated values of μ_{eff} for the Ni^{2+} cations in $\text{Li}_2\text{Ni}_2\text{W}_2\text{O}_9$ range from 3.3 to $3.4 \mu_B$. These experimental values land between the theoretical values for Ni^{2+} in an octahedral coordination, with and without orbital angular momentum (4.47 and $2.83 \mu_B$, respectively); thus, there must be some weak contribution from the orbital angular momentum to the magnetic moment. This matches quite well with empirical values previously reported in the literature^{267,320}.

The frustration index for $\text{Li}_2\text{Ni}_2\text{W}_2\text{O}_9$, f , characterizes competing interactions and geometric frustration in the magnetic lattice. It can be calculated from θ_{CW} and T_N , using Equation 2.10:

$$f = \left| \frac{\theta_{\text{CW}}}{T_N} \right| \quad 2.10$$

Estimating that T_N is roughly equal to 8 K leads to values of f ranging from 1.1 to 1.9: the magnetic structure is not heavily frustrated.

Magnetic structure of $\text{Li}_2\text{Ni}_2\text{W}_2\text{O}_9$

To obtain a better understanding of the results obtained from the bulk magnetic measurements, the magnetic structure of $\text{Li}_2\text{Ni}_2\text{W}_2\text{O}_9$ was solved using low temperature powder neutron diffraction experiments. Neutron diffraction scans were performed between 15 K and 3.5 K, above and below the Néel point (Figure 2.26).

Starting at 7 K, a peak appears at $2\theta = 16.06^\circ$; this peak is not present in the diffractogram for $T = 15$ K, and it keeps increasing as the temperature gets lower. This confirms that there is indeed a magnetic ordering below 8 K. Similarly, another peak seems to increase in intensity as the temperature is decreased, at $2\theta = 9.55^\circ$. Aside from these changes, there is no significant shift in positions or intensities for the nuclear Bragg peaks upon the sample's cooling down, indicating that the nuclear crystal structure remains the same below the magnetic transition temperature.

$\text{Li}_2\text{Ni}_2\text{W}_2\text{O}_9$ crystallizes in the orthorhombic $Pbcn$ space group. The positions of the noticeable magnetic reflections at $2\theta = 9.55^\circ$ and $2\theta = 16.06^\circ$ in the neutron diffraction patterns match with the (001) and (100) Bragg positions for the parent space group, in the same unit

cell as the nuclear structure. Therefore, the propagation vector for the magnetic structure is $\mathbf{k} = (0, 0, 0)$, as the magnetic and nuclear unit cells are identical.

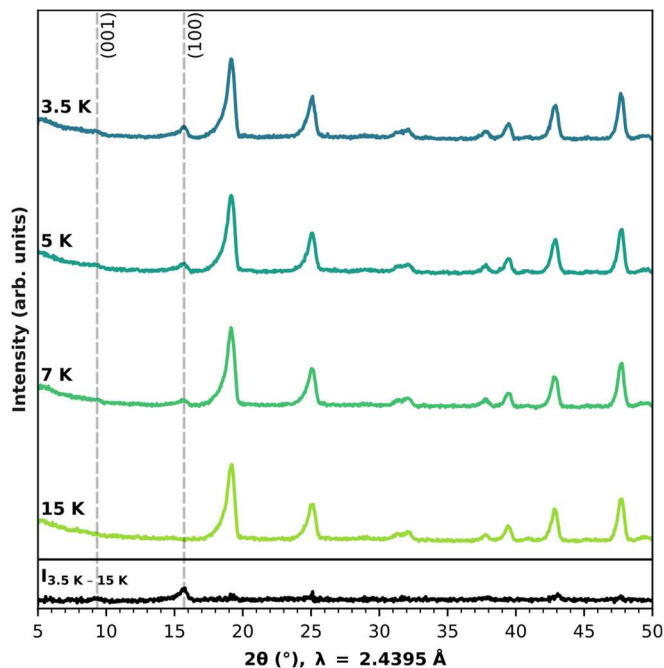


Figure 2.26 – Powder neutron diffraction scans for $\text{Li}_2\text{Ni}_2\text{W}_2\text{O}_9$ powder, from $T = 15$ K (light green) to $T = 3.5$ K (blue). The difference between the diffractograms for $T = 3.5$ K and $T = 15$ K is plotted in black at the bottom of the figure.

Based on the Miller indexes for the magnetic peaks, (001) and (100), it can be ascertained that components of the nickel cations' magnetic moments are perpendicular to the reciprocal space basis vectors \mathbf{c}^* and \mathbf{a}^* ; for an orthorhombic space group, \mathbf{c}^* and \mathbf{a}^* are collinear to the real space vectors \mathbf{c} and \mathbf{a} , respectively. Simulations, based on the nuclear structure of $\text{Li}_2\text{Ni}_2\text{W}_2\text{O}_9$, were performed using the FullProf software³²¹ in the eight Shubnikov magnetic space groups ($Pbcn$, $Pb'cn$, $Pbc'n$, $Pbcn'$, $Pbc'n'$, $Pb'cn'$, $Pb'c'n$, and $Pb'c'n'$), which are compatible with $\mathbf{k} = (0, 0, 0)$ and a magnetic atom in the $8d$ (x,y,z) site. Only two magnetic space groups lead to the appearance of the (001) and (100) diffraction peaks (Figure 2.27, Figure 2.28, Appendix A2.5)³²²: $Pbcn$, with two magnetic components along \mathbf{a} and \mathbf{b} (Figure 2.27a), and $Pb'c'n'$, with two magnetic components along \mathbf{b} and \mathbf{c} (Figure 2.27b, Figure 2.28)³²². However, the best Rietveld²⁵⁴ refinement was obtained when using the latter as the model for the calculations (Figure 2.29, Figure 2.30)³²².

The symmetry of $Pb'c'n'$ allows all three magnetic moment components for the Ni site, but the data showed no evidence of \mathbf{m}_a and it was fixed to zero in the final refinement. The results of this refinement can be found in Table 2.6, and the resulting magnetic structure in Figure 2.31.

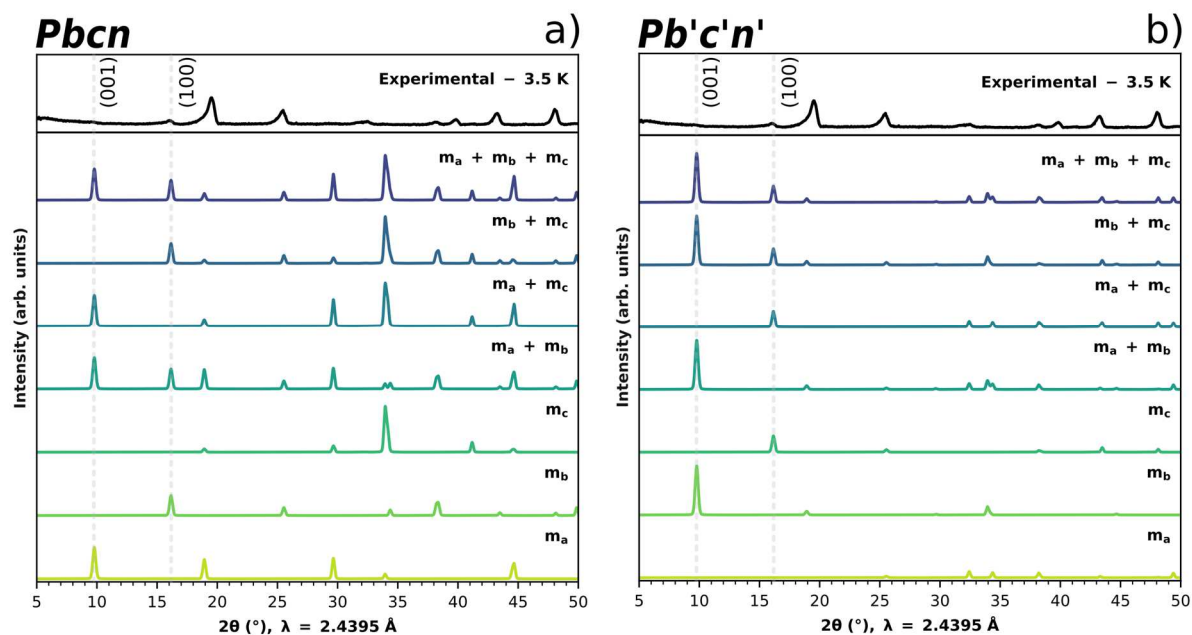


Figure 2.27 – Experimental neutron powder diffraction data at $T = 3.5$ K for $\text{Li}_2\text{Ni}_2\text{W}_2\text{O}_9$ (black, top), and simulated patterns for $k = (0, 0, 0)$ in the (a) $Pbcn$ and (b) $Pb'c'n'$ Shubnikov space groups (colored, bottom). For each simulation, each magnetic component is either equal to $0 \mu_B$ or to $1 \mu_B$; the non-zero components for a given simulation are annotated above its corresponding pattern. Note that in (a), the (001) and (100) peaks appear for two magnetic components along a and b , while in (b) the same peaks appear for two magnetic components along b and c .

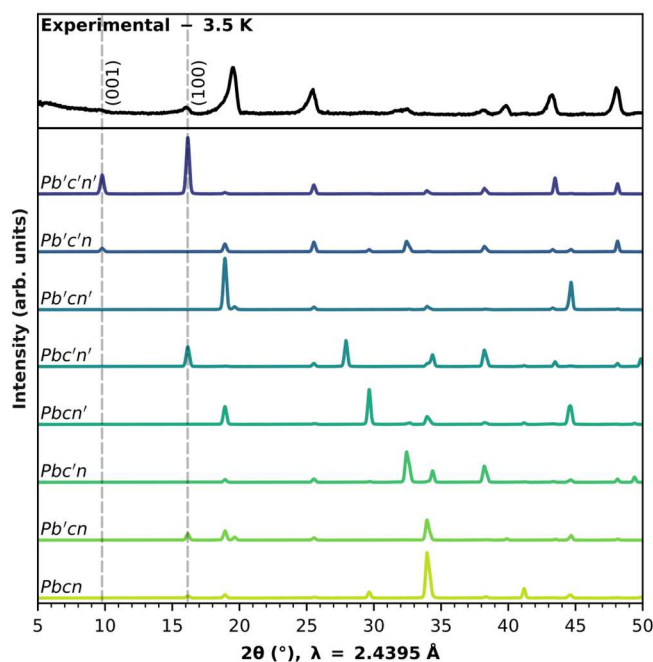


Figure 2.28 – Experimental (black curve, top) and simulated (colored curves) diffraction patterns of $\text{Li}_2\text{Ni}_2\text{W}_2\text{O}_9$. The simulated curves were plotted with $m_b = 0.5 \mu_B$ and $m_c = 1.5 \mu_B$. Theoretical data for the 8 magnetic space groups were taken from the MAXMAGN software³⁰³ of the Bilbao Crystallographic Server^{304–306}.

All nickel cations have a small component along the b -axis ($m_b = 0.51(6) \mu_B$) and a larger component along the c -axis ($m_c = 1.49(5) \mu_B$), for a total magnetic moment of $1.58(5)$

μ_B per nickel cation. This is in reasonable agreement with the expected $2 \mu_B$ for Ni^{2+} , with $S = 1$ in a d^8 electronic configuration. The spin-sequence along **b** is (+ - + - - + - +), and it is (+ + - - - + +) along **c**. This leads to a canted, antiferromagnetic structure, in accordance with the antiferromagnetic transition observed in the bulk magnetic measurements. Moreover, the nickel cations can be paired in such a way that the magnetic components of each cation in a pair are reversed, and their coordinate systems are opposite to one another. Such pairs are Ni(1)/Ni(5), Ni(2)/Ni(6), Ni(3)/Ni(7), and Ni(4)/Ni(8). This indicates that the magnetic structure contains a time reversal center, as well as an inversion center; the combination of these two symmetry elements is required in linear magnetoelectric materials.

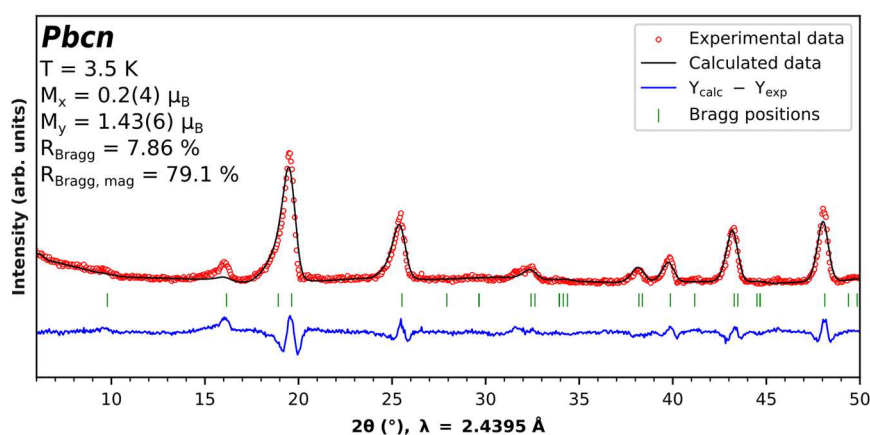


Figure 2.29 – Rietveld refinement of the neutron diffraction pattern of $\text{Li}_2\text{Ni}_2\text{W}_2\text{O}_9$ powder at $T = 3.5$ K, using the *Pbcn* Shubnikov space groups for the calculations.

To get into more details, the magnetic structure of $\text{Li}_2\text{Ni}_2\text{W}_2\text{O}_9$ can be broken down into three different scales: chain, layer, and stack of layers. Inside a Ni-Ni chain, a parallel alignment of the magnetic moments is observed. Meanwhile, inside a Ni-W layer, the magnetic moments of two neighboring chains display weak parallel alignment along the *b*-axis, and a comparatively stronger antiparallel alignment along the *c*-axis. Finally, these layers are piled into stacks along the *c*-axis; the resulting magnetic moments of two neighboring layers in a stack are antiparallel to one another along the *b*-axis (Figure 2.32).

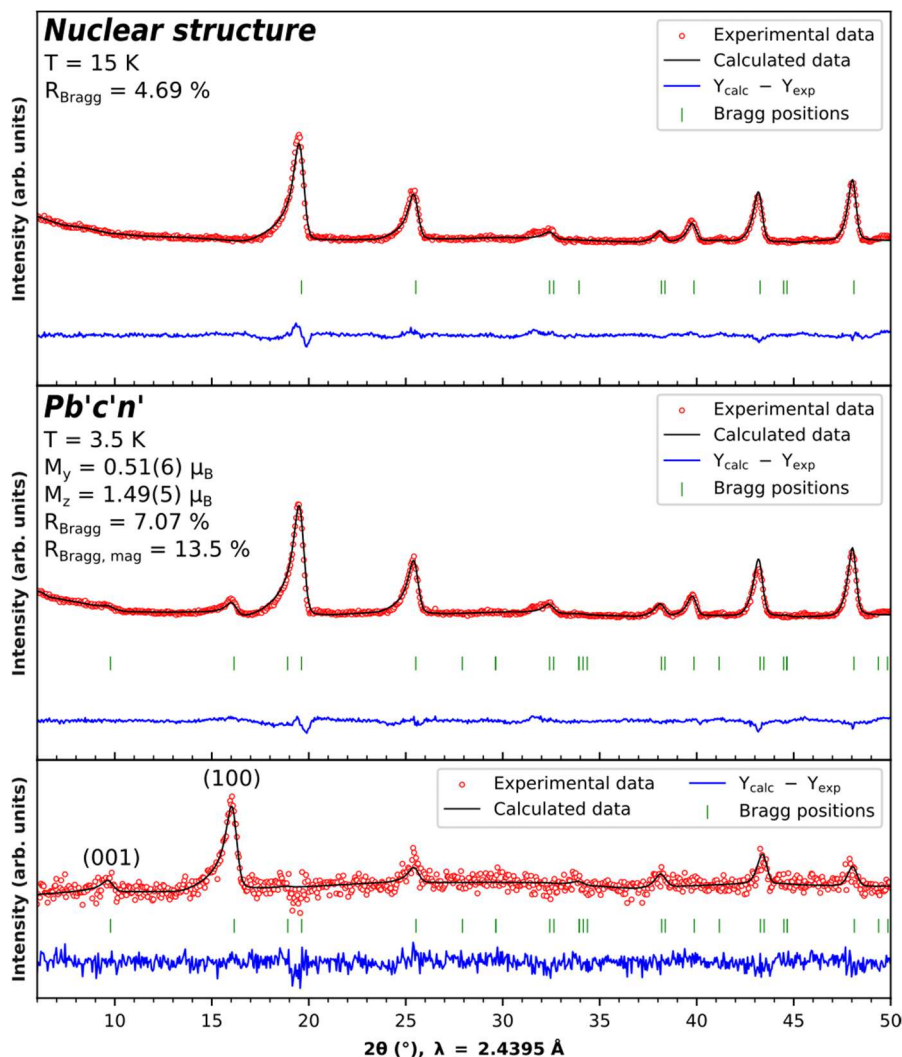


Figure 2.30 – Rietveld refinement for the neutron powder diffraction data of $\text{Li}_2\text{Ni}_2\text{W}_2\text{O}_9$ at $T = 15$ K in the $Pbcn$ nuclear space group (top) and at $T = 3.5$ K in the $Pb'c'n'$ Shubnikov space group (#60.425) (middle). Bottom: Rietveld refinement against the difference curve between the neutron powder diffraction data of $\text{Li}_2\text{Ni}_2\text{W}_2\text{O}_9$ at $T = 3.5$ K and $T = 15$ K.

Table 2.6 – Magnetic structure of $\text{Li}_2\text{Ni}_2\text{W}_2\text{O}_9$ as deduced from the Rietveld refinement of the neutron diffraction pattern measured at 3.5 K.

Shubnikov magnetic space group: $Pb'c'n' / k = (0, 0, 0) / R_{\text{Bragg}} = 7.07\% / R_{\text{Bragg, mag}} = 13.5\% / \chi^2 = 10.2$						
Cation	Coordinates	x/a	y/b	z/c	m_b (μ_B)	m_c (μ_B)
Ni(1)	x, y, z	0.6648(5)	0.512(11)	0.8136(18)	+0.51(6)	+1.49(5)
Ni(2)	$\bar{x}+1/2, \bar{y}+1/2, z+1/2$	0.8352(5)	0.988(11)	0.3136(18)	-0.51(6)	+1.49(5)
Ni(3)	$\bar{x}, y, \bar{z}+1/2$	0.3352(5)	0.512(11)	0.6864(18)	+0.51(6)	-1.49(5)
Ni(4)	$x+1/2, \bar{y}+1/2, \bar{z}$	0.1648(5)	0.988(11)	0.1864(18)	-0.51(6)	-1.49(5)
Ni(5)	$\bar{x}, \bar{y}, \bar{z}$	0.3352(5)	0.488(11)	0.1864(18)	-0.51(6)	-1.49(5)
Ni(6)	$x+1/2, y+1/2, \bar{z}+1/2$	0.1648(5)	0.012(11)	0.6864(18)	+0.51(6)	-1.49(5)
Ni(7)	$x, \bar{y}, z+1/2$	0.6648(5)	0.488(11)	0.3136(18)	-0.51(6)	+1.49(5)
Ni(8)	$\bar{x}+1/2, y+1/2, z$	0.8352(5)	0.012(11)	0.8136(18)	+0.51(6)	+1.49(5)

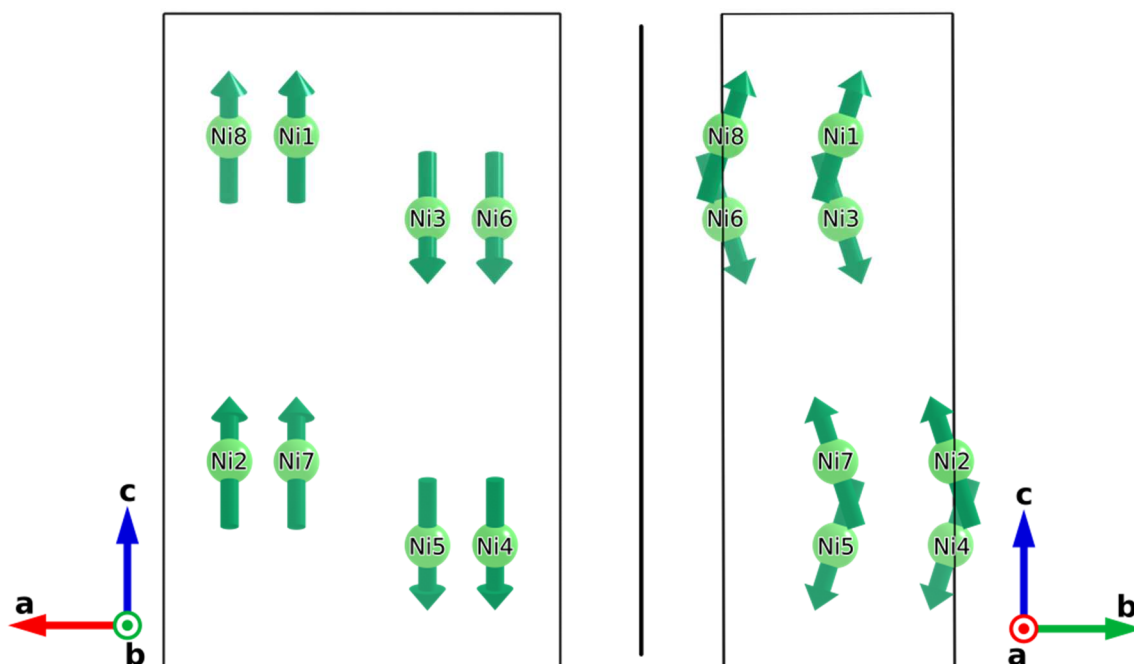


Figure 2.31 – Magnetic structure of $\text{Li}_2\text{Ni}_2\text{W}_2\text{O}_9$. Magnetic moments are represented by green arrows. For the sake of clarity, only nickel atoms are shown in the figure.

Relationships between magnetic structure and magnetic properties in $\text{Li}_2\text{Ni}_2\text{W}_2\text{O}_9$

Table 2.7 – Geometric characteristics of the super-exchange (Ni-O-Ni) and super-super-exchange (Ni-O-O-Ni) paths for exchange interactions J_1 , J_2 , and J_3 . Ni-O-O-Ni is the dihedral angle in degrees for the super-super-exchange path.

Path	Distances (Å)			
	d(Ni-Ni)	d(Ni-O)	d(O-O)	d(O-Ni)
J_1 - Path 1 - super	2.935(6)	1.982(7)	-	2.047(6)
J_1 - Path 2 - super	2.935(6)	2.104(5)	-	2.118(7)
J_2 - super	3.384(10)	2.033(6)	-	2.033(6)
J_3 - super-super	6.051(8)	2.108(5)	3.19738(5)	2.108(5)
Path	Angles (deg.)			
	$\widehat{\text{Ni-O-Ni}}$	$\widehat{\text{Ni-O-O}}$	$\widehat{\text{O-O-Ni}}$	Ni-O-O-Ni
J_1 - Path 1 - super	93.51(17)	-	-	-
J_1 - Path 2 - super	88.07(16)	-	-	-
J_2 - super	112.7(4)	-	-	-
J_3 - super-super	-	108.64(16)	108.64(16)	180.00

$\text{Li}_2\text{Ni}_2\text{W}_2\text{O}_9$'s crystal structure leads to both super-exchange (Ni-O-Ni) and super-super-exchange (Ni-O-O-Ni) interactions in the material. As the magnetic structure is long-range ordered, three distinct isotropic exchange interactions need to be considered: an intrachain double interaction J_1 (2.93 Å), an interchain interaction J_2 (3.40 Å), and an interlayer interaction J_3 (6.05 Å) (Figure 2.32).

Between two closest neighbors in a NiO_6 chain (J_1), two super-exchange paths exist. The super-exchange paths are characterized by a $\sim 90^\circ$ Ni-O-Ni angle (Table 2.7), leading to ferromagnetic interactions in accordance to the Goodenough-Kanamori-Anderson rules^{323–325}. Similarly, for interchain interaction J_2 , the orientation of the magnetic moments of the nickel cations (\mathbf{m}_b components parallel and \mathbf{m}_c components antiparallel) suggest some competition between ferromagnetic and antiferromagnetic interactions. The former could be coming from J_2 's super-exchange path, as the 112.01° Ni-O-Ni angle is closer to 90° than 180° , probably below the ferromagnetic-to-antiferromagnetic critical angle described by Goodenough³²³; but again, this is mostly speculative, and an analysis based solely on geometry might miss some other important factors influencing the magnetic structure. J_3 's super-super-exchange path leads to antiferromagnetic interactions between the (Ni, W) layers without too much ambiguity; this can be explained quite well, again, by the Goodenough-Kanamori-Anderson rules, and by the 180° Ni-O-O-Ni dihedral angle.

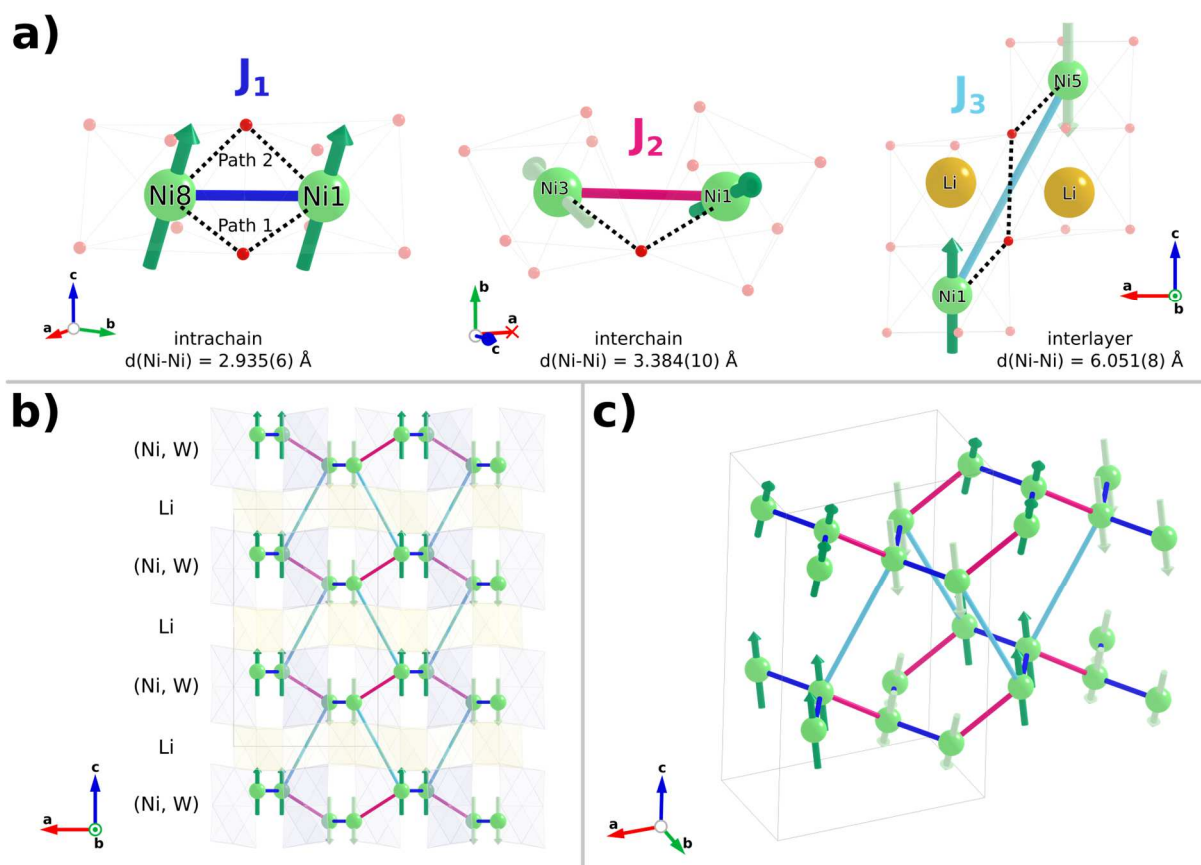


Figure 2.32 – Magnetic interaction paths in $\text{Li}_2\text{Ni}_2\text{W}_2\text{O}_9$. In (a), super-exchange and super-super-exchange paths are shown as black dotted lines. Nickel atoms are shown in green, lithium atoms in yellow and oxygen atoms in red. In (b), WO_6 and LiO_6 octahedra are respectively shown in pale blue and in pale yellow. Magnetic moments with a positive \mathbf{m}_c component are shown in dark green, while those with a negative \mathbf{m}_c component are shown in light green.

In any case, the nature of these magnetic interactions explains the unusual behavior observed in the magnetization measurements: although the structure is antiferromagnetic overall, the Curie-Weiss temperature for $\text{Li}_2\text{Ni}_2\text{W}_2\text{O}_9$ is positive because of the intrachain and interchain ferromagnetic interactions. Moreover, looking at the topology of J_1 , J_2 , and J_3 (Figure 2.32b,c), it is interesting to observe that the magnetic connectivity of the nickel cations leads to hexagonal magnetic loops; as there are no odd-sided loops, the magnetic structure is not geometrically frustrated. This observation matches well with the low values of the frustration index calculated earlier.

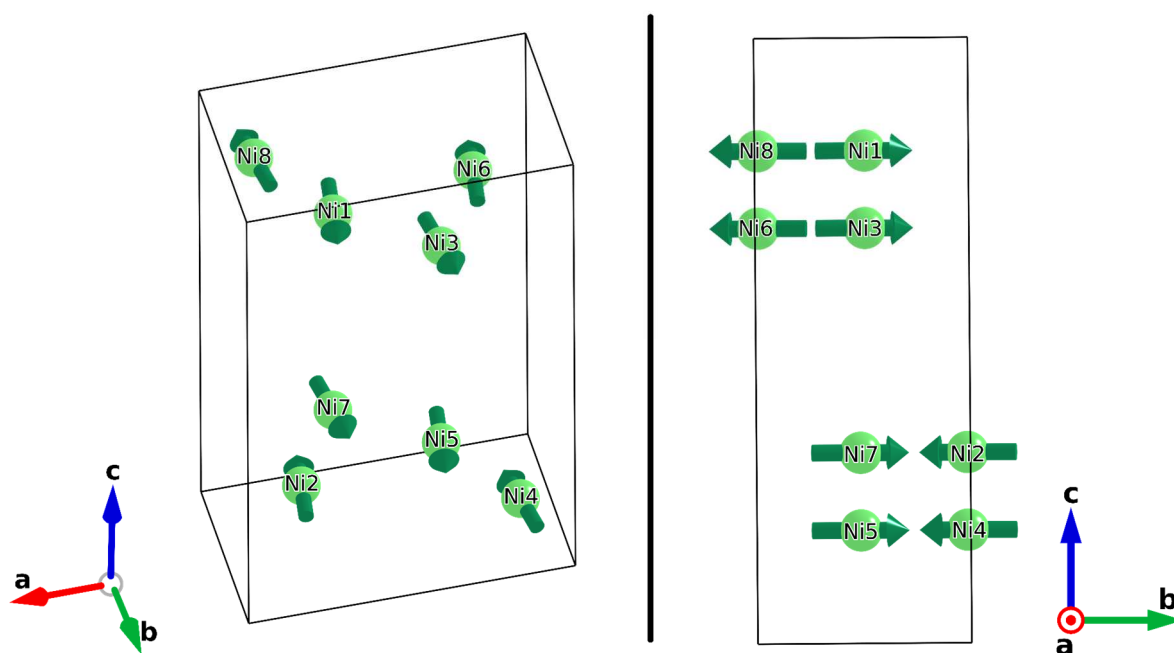


Figure 2.33 – Magnetic structure that would be displayed by $\text{Li}_2\text{Ni}_2\text{W}_2\text{O}_9$ at $T < T_N$ if its Shubnikov space group was $Pbcn$. For the sake of clarity, only the nickel atoms are shown. The green arrows represent the magnetic moments.

These considerations not only fit with the $Pb'c'n'$ space group, they also make it rather unlikely that $\text{Li}_2\text{Ni}_2\text{W}_2\text{O}_9$'s magnetic space group is $Pbcn$, the other possibility mentioned earlier in this chapter. Looking at the theoretical magnetic structure associated with the $Pbcn$ Shubnikov space group (Figure 2.33), one can notice that the magnetic moments of two neighboring Ni cations in a chain would be mostly antiparallel to one another (strong antiparallel alignment along **b**, very weak parallel alignment along **a**). Not only would this go against the Goodenough-Kanamori-Anderson rules, it would also go against the experimental results, namely the high ferromagnetic interactions observed in the magnetic measurements. Considering said measurements, and taking into account that J_1 , as the shortest magnetic interaction path is also likely to be the strongest, it can be confidently ascertained that the

intrachain interactions in $\text{Li}_2\text{Ni}_2\text{W}_2\text{O}_9$ have to be ferromagnetic. Thus, the $Pbcn$ magnetic space group is ruled out, and only $Pb'c'n'$ remains.

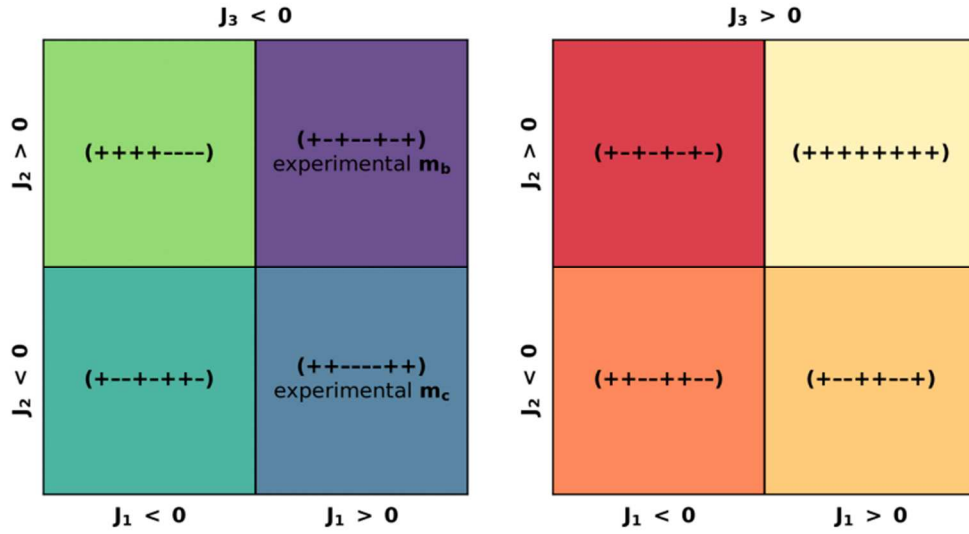


Figure 2.34 – Phase diagram showing the possible magnetic ground states of $\text{Li}_2\text{Ni}_2\text{W}_2\text{O}_9$ below T_N as a function of the values of the exchange integrals J_1 , J_2 and J_3 . $\mathbf{k} = (0, 0, 0)$ in all ground-states. The ground-state magnetic structures observed experimentally from the neutron diffraction data shown in Figure 2.26 are indicated in the purple and blue parts of the diagram.

In Figure 2.34 is displayed a phase diagram showing the possible ground-state magnetic structures of $\text{Li}_2\text{Ni}_2\text{W}_2\text{O}_9$, depending on the values of the propagation vector \mathbf{k} and of the exchange integrals J_1 , J_2 , and J_3 .

This phase diagram was calculated by using the programs SIMBO and ENERMAG; El Khayati et al. gave a full description of these programs and the theory behind them in other works^{326–330}. The magnetic ground state (or first-ordered state) is obtained, as a function of \mathbf{k} and the exchange integrals J_{ij} ; it is the eigenvector corresponding to the lowest eigenvalue of the negative Fourier transform of the exchange integral matrix (Equation 2.11):

$$\xi_{ij}(\mathbf{k}) = - \sum_{\mathbf{m}} J_{ij}(\mathbf{R}_m) e^{-2\pi i \mathbf{k} \cdot \mathbf{R}_m} \quad 2.11$$

where $J_{ij}(\mathbf{R}_m)$ is the isotropic exchange interaction between the spins of atoms i and j in unit cells separated by the lattice vector \mathbf{R}_m . As a convention, a negative value of the exchange interaction J_{ij} means that there is an antiparallel coupling between the spins \mathbf{S}_i and \mathbf{S}_j , leading to the expression of the pair interaction energy shown in Equation 2.12:

$$E_{ij} = -J_{ij} \mathbf{S}_i \cdot \mathbf{S}_j \quad 2.12$$

To build the phase diagram, we used a procedure which was applied to several magnetic structures in the past^{320,331–336}. In a few words, the exchange integral matrixes $\xi(\mathbf{k}, J_1, J_2, J_3)$ were calculated for values of J_1, J_2, J_3 ranging from -100 to 100, and for each set of values (J_1, J_2, J_3), the magnetic structure of lowest energy was selected. For all regions of the phase diagram, the lowest energy was obtained for $\mathbf{k} = (0, 0, 0)$; thus, only the spin sequence vary from one magnetic structure to the other.

The magnetic ground state of $\text{Li}_2\text{Ni}_2\text{W}_2\text{O}_9$ is split between two parts of the phase diagram. Although it is clear that $J_1 > 0$ and $J_3 < 0$, the value of J_2 is not the same depending on the component of the magnetic moments which is considered: indeed, $J_2 > 0$ for \mathbf{m}_b , and $J_2 < 0$ for \mathbf{m}_c . This, again, highlights the dual nature of the J_2 interaction, both ferromagnetic and antiferromagnetic.

Another point to comment on relates to the magnetic space group of $\text{Li}_2\text{Ni}_2\text{W}_2\text{O}_9$, its nuclear structure, and potential magnetoelectric properties. It has been shown that the existence of this property in a material is dependent on the point symmetry of its magnetic structure^{303–307}. In particular, the $m'm'm'$ point group allows for the magnetoelectric effect to manifest, as the diagonal components of the associated magnetoelectric tensor are non-zero^{305,306}. This means that this effect could be present in $\text{Li}_2\text{Ni}_2\text{W}_2\text{O}_9$ because of its $Pb'cn'$ magnetic space group. This is interesting because, as said earlier, the corundum-like structure of $\text{Li}_2\text{Ni}_2\text{W}_2\text{O}_9$ is very similar to that of "429" magnetic compounds²⁹⁷, especially $\text{Ni}_4\text{Nb}_2\text{O}_9$, which crystallizes in the same orthorhombic nuclear space group³¹³. However, ferrimagnetic ordering in $\text{Ni}_4\text{Nb}_2\text{O}_9$ occurs in the $Pb'cn'$ magnetic space group^{267,314}, corresponding to the magnetic point group $m'm'm$ (#8.4.27) which is not compatible with the linear magnetoelectric effect. Meanwhile, 429 compounds crystallizing in a trigonal space group $P\bar{3}c1$ ($\text{Co}_4\text{Nb}_2\text{O}_9$, $\text{Co}_4\text{Ta}_2\text{O}_9$, $\text{Mn}_4\text{Nb}_2\text{O}_9$, $\text{Mn}_4\text{Ta}_2\text{O}_9$, etc.) usually display linear magnetoelectric coupling^{298,309,337,338}. Thus, $\text{Li}_2\text{Ni}_2\text{W}_2\text{O}_9$ might be the gateway to the exploration of a magnetoelectric effect based on Ni^{2+} in a corundum-like orthorhombic structure.

Compared to members of the 429 family, the magnetic transition temperature for $\text{Li}_2\text{Ni}_2\text{W}_2\text{O}_9$ ($T_N \approx 8$ K) is much lower. $\text{Fe}_4\text{Nb}_2\text{O}_9$ displays two temperatures of transition, $T_{N1} \approx 90$ K and $T_{N2} \approx 80$ K^{301,312}. In $\text{Co}_4\text{Nb}_2\text{O}_9$, the Néel point has been reported at $T_N = 27$ K^{261,339}; meanwhile, in $\text{Co}_4\text{Ta}_2\text{O}_9$, various studies find $T_N \approx 20$ K^{337,340,341}. Even $\text{Ni}_4\text{Nb}_2\text{O}_9$, a material

with Ni^{2+} as the paramagnetic cation, displays a Curie temperature T_C equal to 76 K^{267,314,315}. These major differences suggest that the magnetic interactions are weaker in $\text{Li}_2\text{Ni}_2\text{W}_2\text{O}_9$ than in the 429 compounds. This could be due to a number of factors. First of all, the lower amount of magnetic cations per formula unit could introduce some sort of "diamagnetic dilution" effect. Such a phenomenon was reported by Tarakina et al. in $\text{MgNi}_3\text{Nb}_2\text{O}_9$ ²⁶⁶. Another factor, related to the one described above, is the difference in crystal structure between $\text{Li}_2\text{Ni}_2\text{W}_2\text{O}_9$ and the $M_4A_2O_9$ compounds. Whereas $\text{Ni}_4\text{Nb}_2\text{O}_9$, for instance, displays two types of magnetic layers (the (Ni2, Nb) double layer and the Ni1 single layer), paramagnetic Ni^{2+} cations in $\text{Li}_2\text{Ni}_2\text{W}_2\text{O}_9$ are only present in the (Ni, W) double layers, separated by diamagnetic Li^+ interlayers (Figure 2.23). As such, the distance along the c -axis between two paramagnetic Ni^{2+} cations is much longer in $\text{Li}_2\text{Ni}_2\text{W}_2\text{O}_9$ ($d_{J3}(\text{Ni-Ni}) = 6.051(8) \text{ \AA}$) than in $\text{Ni}_4\text{Nb}_2\text{O}_9$ ($d(\text{Ni1-Ni2}) = 2.659(3) \text{ \AA}$)²⁶⁷. This means that the magnetic interactions are likely much weaker between two successive paramagnetic layers in $\text{Li}_2\text{Ni}_2\text{W}_2\text{O}_9$ than in other 429 compounds. Finally, one may wonder whether or not replacing the $\text{Nb}^{5+}/\text{Ta}^{5+}$ cations by W^{6+} cations has an impact on the magnetic properties, even though NbO_6 , TaO_6 , and WO_6 are all distorted by the same second-order Jahn-Teller effect^{258,259}.

It is also interesting to observe that, although it displays the same antiferromagnetic ordering as many of the 429 compounds^{297,301,302,340}, $\text{Li}_2\text{Ni}_2\text{W}_2\text{O}_9$ distinguishes itself by displaying a positive Curie-Weiss temperature $\theta_{\text{CW}} \approx 14 \text{ K}$, whereas all 429 compounds show $\theta_{\text{CW}} < 0$. Even $\text{Ni}_4\text{Nb}_2\text{O}_9$ displays a strongly negative Curie-Weiss temperature ($\theta_{\text{CW}} = -233 \text{ K}$), although it is distinct from other 429 compounds for having a parallel alignment of the Ni^{2+} magnetic moments in its Ni1 single layer, and of those in its (Ni2, Nb) double layer^{267,314}. This again shows how the introduction of the Li^+ interlayer changes the magnetic interactions in $\text{Li}_2\text{Ni}_2\text{W}_2\text{O}_9$. Compared to $\text{Ni}_4\text{Nb}_2\text{O}_9$, for which the Ni1-Ni2 antiferromagnetic interactions are the strongest in the material, the intrachain ferromagnetic Ni-Ni interactions dominate in $\text{Li}_2\text{Ni}_2\text{W}_2\text{O}_9$. Meanwhile, the $P\bar{3}c1$ structure of other 429 compounds usually leads to strong antiferromagnetic intralayer interactions and weak ferromagnetic interlayer interactions^{311,312,340,342}. As such, the crystal structure of $\text{Li}_2\text{Ni}_2\text{W}_2\text{O}_9$ introduces favored ferromagnetic interactions in the antiferromagnetic order usually found in 429 compounds.

2.E. Conclusion of the chapter

$\text{Li}_2\text{Ni}_2\text{W}_2\text{O}_9$ was synthesized through solid-state synthesis, and its structural, electrochromic, and magnetic properties were characterized.

The general crystal structure of this new compound is not completely unheard of: it is very similar to corundum, and matches exactly with the ramsayite structure reported previously in other materials ($\text{Ni}_4\text{Nb}_2\text{O}_9$, $\text{MgNi}_3\text{Nb}_2\text{O}_9$...). However, $\text{Li}_2\text{Ni}_2\text{W}_2\text{O}_9$ stands out by its lithium interlayer, its ordered structure, and its electrochemically active Ni^{2+} cations. This opens a wide array of possibilities for the synthesis of new materials to use as cathodes for the electrochemical (de)insertion of lithium. For instance, replacing the divalent nickel in $\text{Li}_2\text{Ni}_2\text{W}_2\text{O}_9$ with another divalent transition metal, or tungsten with another, lighter element, would make for interesting synthesis prospects. As it is a quaternary oxide, it might be possible to tune the electrochemical and optical properties of the material by changing one or more elements in the composition.

On top of this, playing with the nature of the transition metals could open the door to a new family of electrochromic materials. However, a proper assessment of the electrochromic performances of $\text{Li}_2\text{Ni}_2\text{W}_2\text{O}_9$ still needs to be done. In order to do this, the compound must be prepared as a thin film, and a quantitative study of its optical properties will be required.

As it stands, $\text{Li}_2\text{Ni}_2\text{W}_2\text{O}_9$ displays a reversible specific capacity of roughly $31 \text{ mA}\cdot\text{h}\cdot\text{g}^{-1}$ past its initial capacity fade, which is much too low to compete with other Li-ion battery cathode materials. This low specific capacity stems mainly from its very high molar mass ($642.89 \text{ g}\cdot\text{mol}^{-1}$). LiFePO_4 ³⁴³ and $\text{LiNi}_{1/3}\text{Mn}_{1/3}\text{Co}_{1/3}\text{O}_2$ ³⁴⁴ typically display specific capacities between 160 and $175 \text{ mA}\cdot\text{h}\cdot\text{g}^{-1}$ when cycled in their standard potential windows. Trying to find materials with a similar structure to $\text{Li}_2\text{Ni}_2\text{W}_2\text{O}_9$, but with lighter constituting elements, could be a path to the discovery of new interesting electrochemically active materials.

Finally, at low temperatures (below 8 K), $\text{Li}_2\text{Ni}_2\text{W}_2\text{O}_9$ also displays the interesting combination of an antiferromagnetic ordering with strong ferromagnetic interactions. Its magnetic structure, ordered in the $Pb'c'n'$ Shubnikov space group, should grant it magnetoelectric properties; this possibility calls for further experimentations, to determine the strength of this magnetoelectric effect in $\text{Li}_2\text{Ni}_2\text{W}_2\text{O}_9$.

Even though this work on $\text{Li}_2\text{Ni}_2\text{W}_2\text{O}_9$ does not deliver direct information on the Li-Ni-W-O thin films on which this manuscript focus, it was worthwhile for two reasons. First, to unveil the intrinsic peculiarities of $\text{Li}_2\text{Ni}_2\text{W}_2\text{O}_9$. Second, for the completion of the Li_2O -NiO- WO_3 ternary phase diagram, which will be a very useful tool for the comprehension of Li-Ni-W-O thin films, used in the following chapter.

Chapter 3 – Understanding Li-Ni-W-O nanocomposite thin films

3.A. Motivations

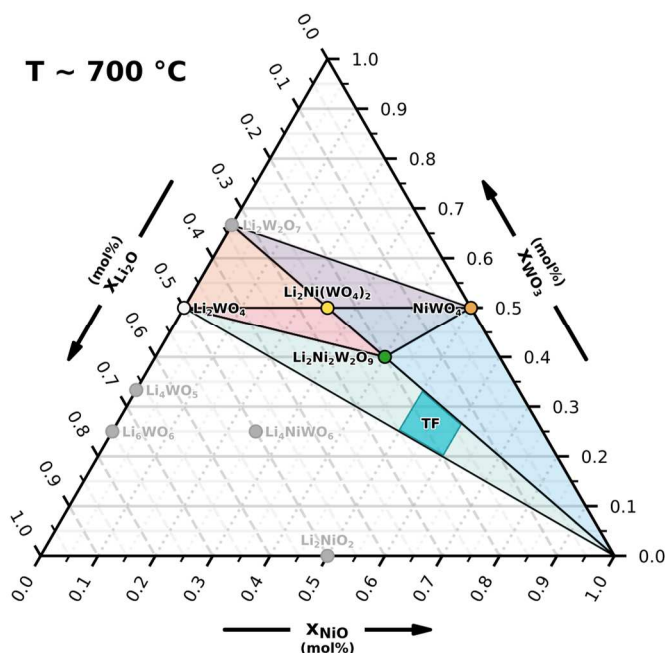


Figure 3.1 – Li_2O - NiO - WO_3 ternary phase diagram at roughly $700\text{ }^\circ\text{C}$. The teal zone corresponds to the composition range of the Li-Ni-W-O thin films (TF). Colored areas have been explored experimentally. Phases that are grayed out have not been studied in this manuscript.

Orthorhombic *Pbcn* $\text{Li}_2\text{Ni}_2\text{W}_2\text{O}_9$, described in depth in the previous chapter, completes the Li_2O - NiO - WO_3 ternary phase diagram (Figure 3.1). This diagram describes the Li-Ni-W mixed oxide phases that can crystallize at high temperature (600 to $700\text{ }^\circ\text{C}$).

The general goal of this thesis is to understand the relationships between the composition, the structure, and the electrochromic properties of the magnetron sputtered Li-Ni-W-O thin films described in Chapter 1. However, the nanocomposite structure of those films makes it difficult to study them. For example, the amorphous matrix, which constitutes a significant part of the films' structure, cannot be observed by XRD due to a lack of structural long-range order. Consequently, it is difficult to track how this matrix may change upon (de)lithiation and thus, it is challenging to conclude on its electrochemical activity between 1.0 and 4.5 V vs Li^+/Li .

A roundabout way to glean information on the matrix and on these mixed oxide thin films in general is to look at similar systems that are easier to characterize. For example, high crystallinity powders can easily be studied by XRD. This is where the ternary phase diagram described in Figure 3.1 comes in. Knowing an approximate atomic composition for the

Li-Ni-W-O thin films, other phases in the diagram can be selected based on their proximity with the thin films' area (TF).

Following this strategy, four phases were selected (Figure 3.2):

- Trigonal $R\bar{3}$ Li_2WO_4 ³⁴⁵, which is one of the vertices of the area containing the thin films' composition (pale green triangle in Figure 3.1).
- Orthorhombic $Pbcn$ $\text{Li}_2\text{Ni}_2\text{W}_2\text{O}_9$ ²⁴⁶, another vertex of the area containing TF.
- Triclinic $P\bar{1}$ $\text{Li}_2\text{Ni}(\text{WO}_4)_2$ ³⁴⁶, an impurity that can often appear in case of inhomogeneous mixing in the solid-state synthesis of $\text{Li}_2\text{Ni}_2\text{W}_2\text{O}_9$.
- Monoclinic $P2/c$ NiWO_4 ³⁴⁷, another impurity that can form in the synthesis of $\text{Li}_2\text{Ni}_2\text{W}_2\text{O}_9$.

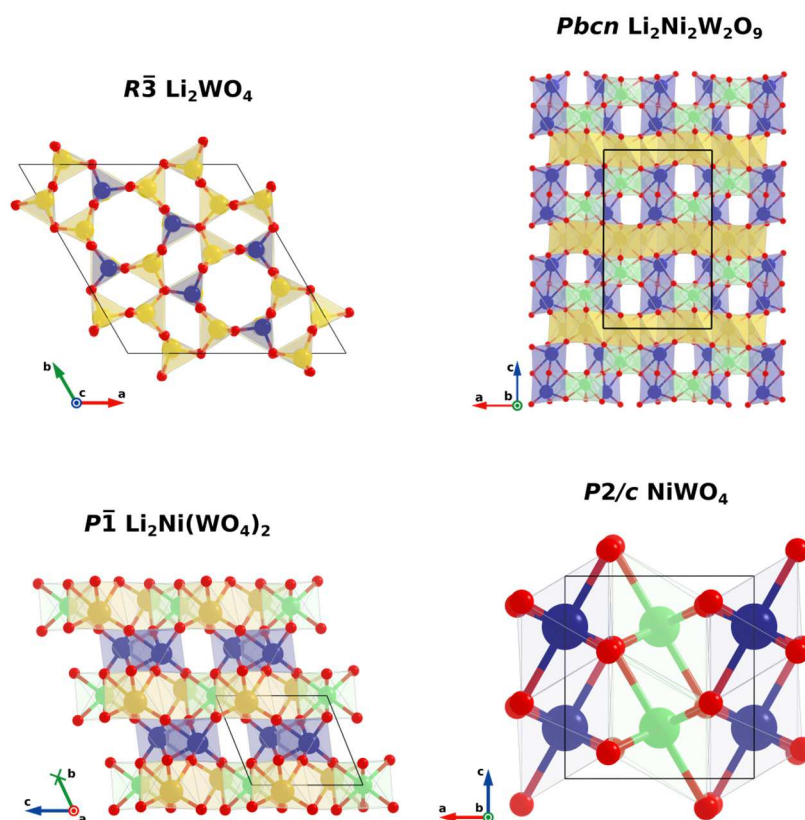


Figure 3.2 – Crystal structures of $R\bar{3}$ Li_2WO_4 , $Pbcn$ $\text{Li}_2\text{Ni}_2\text{W}_2\text{O}_9$, $P\bar{1}$ $\text{Li}_2\text{Ni}(\text{WO}_4)_2$, and $P2/c$ NiWO_4 . Lithium atoms are in yellow, nickel atoms in green, tungsten atoms in blue, and oxygen atoms in red.

In the first sections of this chapter, the electrochemical behavior of these four compounds in Li^+ -conducting electrolytes will be studied and compared to the behavior of the nanocomposite Li-Ni-W-O thin films. Then, the results of *post-mortem* XPS experiments on

cycled Li-Ni-W-O thin films will be presented and analyzed to obtain more information on the secondary reactions occurring when these materials are discharged at low potentials.

3.B. Electrochemical behaviors of the $\text{Li}_x\text{Ni}_y\text{W}_z\text{O}_n$ powders in Li^+ -conducting electrolyte

The four $\text{Li}_x\text{Ni}_y\text{W}_z\text{O}_n$ powders were synthesized by solid-state synthesis. Their purity was assessed by powder XRD (Appendices A3.1, A3.2, A3.3), and they were studied by galvanostatic charge-discharge in coin cells, using a half-cell configuration. For the electrochemical study, each powder was mixed with carbon Super P (20 wt%) in order to prepare the working electrode material. A Li^+ -conducting electrolyte was used in each case, usually 1 M LiPF_6 in EC:DMC (1:1 vol). The counter-electrode in the cells was Li metal.

The behavior of the $\text{Li}_x\text{Ni}_y\text{W}_z\text{O}_n$ at high and low potentials

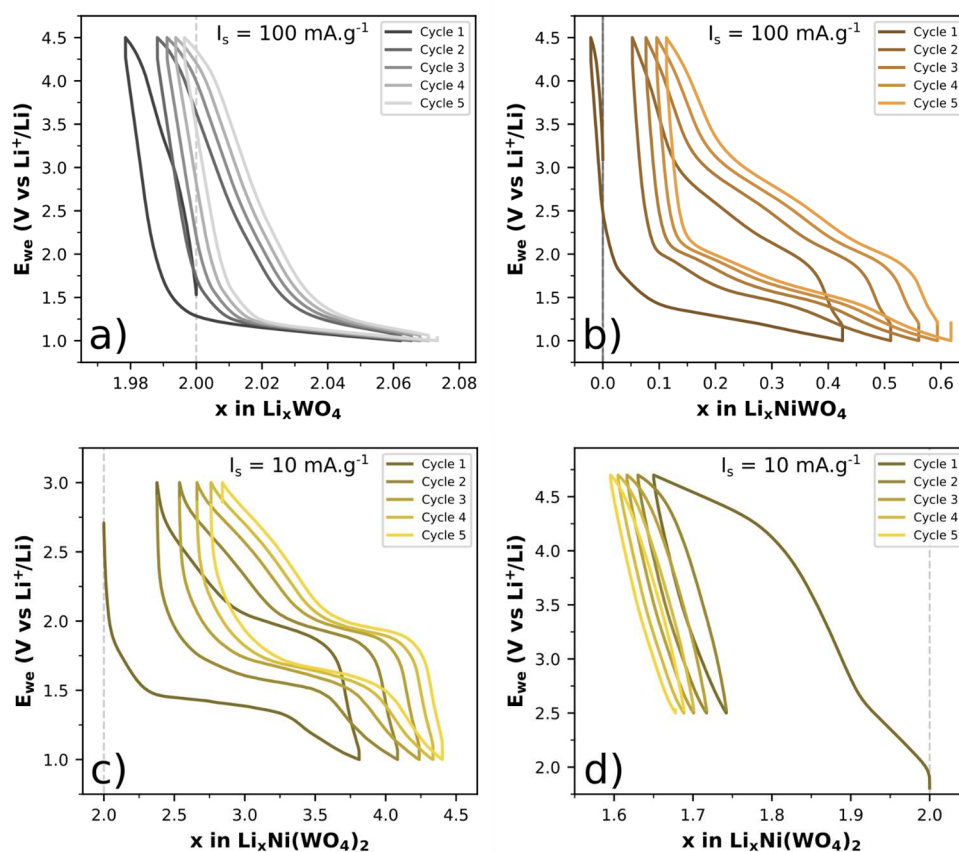


Figure 3.3 – E_{we} vs x curves for galvanostatic charge-discharge experiments using the $\text{Li}_x\text{Ni}_y\text{W}_z\text{O}_n$ powders as working electrodes. (a) Li_2WO_4 , 100 mA.g^{-1} , 1.0 to 4.5 V vs Li^+/Li . (b) NiWO_4 , 100 mA.g^{-1} , 1.0 to 4.5 V vs Li^+/Li . (c) $\text{Li}_2\text{Ni}(\text{WO}_4)_2$, 10 mA.g^{-1} , 1.0 to 3.0 V vs Li^+/Li . (d) $\text{Li}_2\text{Ni}(\text{WO}_4)_2$, 10 mA.g^{-1} , 2.0 to 4.7 V vs Li^+/Li .

Figure 3.3 shows the E_{we} vs x curves for the galvanostatic charge-discharge experiments performed on Li_2WO_4 , NiWO_4 , and $\text{Li}_2\text{Ni}(\text{WO}_4)_2$ powder electrodes. When cycled against Li

metal at 100 mA.g^{-1} , pure Li_2WO_4 (Figure 3.3a) does not display electrochemical activity at high potentials ($> 2.0 \text{ V vs Li}^+/\text{Li}$). However, a small plateau appears in reduction between 1.5 and 1.0 V vs Li^+/Li ; its counterpart manifests in a similar potential range during the oxidation sweep, but delivers less capacity. The reduction reaction seems to be incomplete, as the end of the plateau is not reached with a lower cutoff voltage of 1.0 V. This low potential redox couple accounts for the reversible (de)insertion of around $0.07 \text{ Li}^+ \text{ eq.}$, and a capacity of 7.6 mAh.g^{-1} , much lower than what can be found for WO_3 ³⁴⁸. There is a slight slippage toward higher x values through the cycles, possibly because of parasitic reactions. Otherwise, the electrochemical behavior of Li_2WO_4 is quite reversible.

The low capacity of Li_2WO_4 is not surprising. It has been reported that the deep electrochemical lithiation of tungsten trioxide leads to the irreversible formation of Li_2WO_4 , which then acts as a lithium trap^{349,350}. The low reversible activity measured likely comes from the redox of a small amount of W sites.

Similarly to Li_2WO_4 , pure monoclinic nickel(II) tungstate (Figure 3.3b) displays faradaic activity at low potentials only ($< 3.5 \text{ V vs Li}^+/\text{Li}$); Ni^{2+} cannot be oxidized as there is no lithium to remove from the material. There is a significant slippage through the cycles, due to irreversible reactions occurring during the discharges.

The amount of charges reversibly inserted in NiWO_4 during the cycling process is higher than for Li_2WO_4 . About 0.45 Li^+ equivalents are inserted in the first discharge (39.1 mA.h.g^{-1}), of which 0.37 Li^+ equivalents are deinserted in the following charge (32.6 mA.h.g^{-1}). These values are too low to correspond to a complete reduction of nickel or tungsten to another oxidation state: the conversion reaction of Ni^{2+} to Ni^0 requires the exchange of $2 \text{ Li}^+ \text{ eq.}$, while the reduction of W^{6+} to W^{5+} would require $1 \text{ Li}^+ \text{ eq.}$ Thus, although a reduction of the NiWO_4 electrode occurs, it here again remains incomplete when using a lower cutoff voltage of 1.0 V vs Li^+/Li . Based on previous studies on NiO ^{351,352} and NiWO_4 ²⁸³ anodes, the electrochemical activity observed in Figure 3.3b could be attributed to the beginning of the reversible conversion reaction of NiO to Ni^0 . *Operando* XRD on the same potential window does not show anything of note, beside a very slight decrease in the overall intensity of the NiWO_4 peaks during lithiation, which would match with the beginning of a conversion reaction (Appendix A3.4).

Similarly to NiWO_4 and Li_2WO_4 , when cycled at low potentials, the E_{we} vs x curves of lithium nickel bitungstate ($\text{Li}_2\text{Ni}(\text{WO}_4)_2$) (Figure 3.3c) show significant slippage due to a slight

irreversibility between the charge and the discharge. Again, this is probably because of parasitic reactions during the discharge. After 5 cycles, around 1.56 Li^+ eq. can be reversibly (de)inserted in the material, a number which is more than four times higher than for NiWO_4 . The reaction associated to the low-potential reactivity of $\text{Li}_2\text{Ni}(\text{WO}_4)_2$ is unclear: an *operando* XRD experiment on this material cycled between 1.0 and 3.0 V vs Li^+/Li does not show any variation in the crystal structure of the material, at any point during cycling (Appendix A3.5). Results shown by Ge et al. suggest that, by going at lower potentials (0.5 V vs Li^+/Li), a conversion reaction occurs. Besides these observations, the material displays almost no faradaic activity at a higher potential range (2.5 – 4.7 V vs Li^+/Li) (Figure 3.3d).

Comparison with the electrochemical behavior of the nanocomposite Li-Ni-W-O thin films

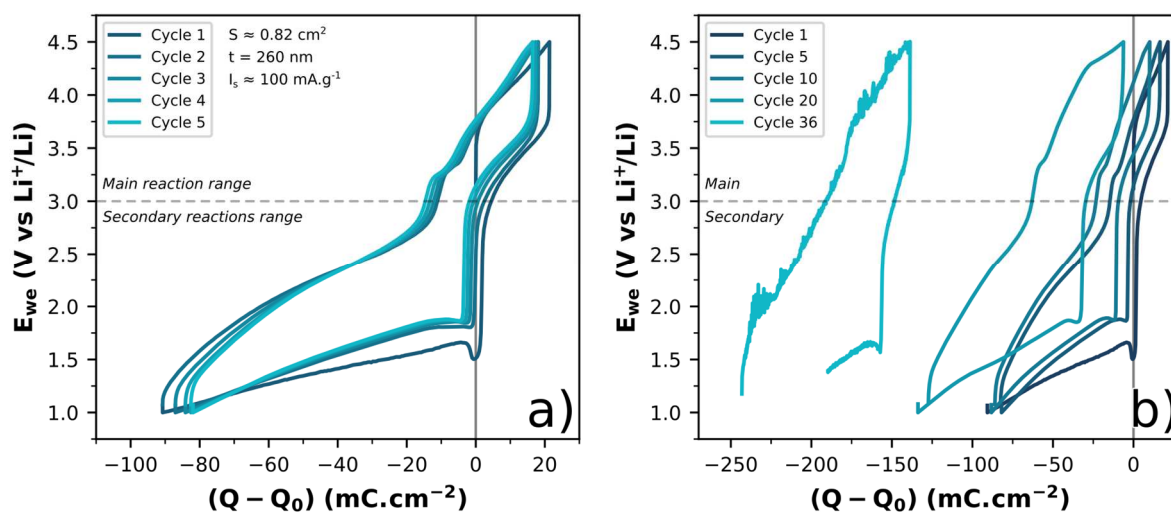


Figure 3.4 – Galvanostatic charge-discharge curves for a sputtered Li-Ni-W-O thin film electrode cycled against Li metal in a 1 M LiPF_6 in EC:DMC (1:1 vol) electrolyte. The cell was cycled at $\sim 100 \text{ mA.g}^{-1}$ (assuming a film density of $\sim 7 \text{ g.cm}^{-3}$). (a) First five cycles; (b) evolution of the cycling behavior from the launch to the death of the cell.

There are some strong similarities among the $\text{Li}_x\text{Ni}_y\text{W}_z\text{O}_n$ powders when it comes to their electrochemistry.

Firstly, none of them are electrochemically active between 3.0 and 4.5 V vs Li^+/Li . $\text{Li}_2\text{Ni}_2\text{W}_2\text{O}_9$ does show electrochemical activity at high potentials due to the reversible redox of the $\text{Ni}^{3+}/\text{Ni}^{2+}$ couple (see Chapter 2), but it only occurs between 4.5 and 5.0 V vs Li^+/Li . This is above the potential range of the main reaction in the magnetron sputtered Li-Ni-W-O thin films (Figure 3.4).

Secondly, all of the powders containing nickel are electrochemically active on the 1.0-3.0 V vs Li⁺/Li voltage window. Li₂WO₄ is distinct from the nickel-based compounds, as it only displays a weak faradaic activity at very low potentials (< 1.5 V vs Li⁺/Li). This might indicate that nickel is required in order to display strong electrochemical activity in the “secondary reactions” potential range.

Finally, in the three Ni-based compounds (NiWO₄, Li₂Ni(WO₄)₂, Li₂Ni₂W₂O₉), the first reduction sweep against a lithium metal counter-electrode is characterized by a conversion reaction. In general, following this initial conversion reaction, the behavior of the powder materials becomes quite reversible in the subsequent cycles. More experiments (such as XPS, XAS, or Raman spectroscopy) are required to obtain more details on the exact conversion mechanism.

The study of the powders do not bring much information about the main reaction in the magnetron sputtered Li-Ni-W-O thin films. The main reaction between 2.0 and 4.5 V vs Li⁺/Li seems to be a phenomenon intrinsically related to the thin film structure. Reports on similar Li-Ni-W-O nanocomposite systems suggest that this high-potential reaction is likely due to the oxidation of the NiO-like nanocrystallites contained in the amorphous matrix^{243,244,344}.

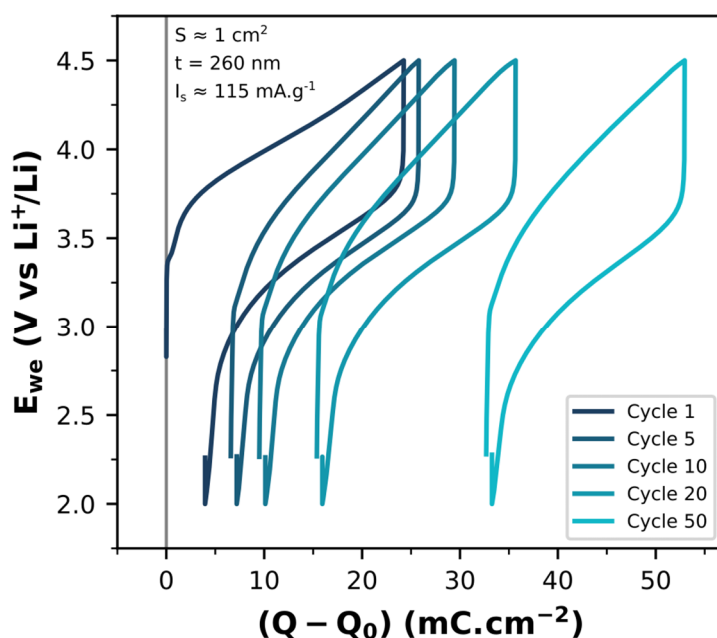


Figure 3.5 – E_{we} vs $(Q - Q_0)$ curves for a galvanostatic charge-discharge experiment on a Li-Ni-W-O film||Li metal cell. The electrolyte used was 1 M LiPF₆ in EC:DMC (1:1 vol), and the current density was roughly 115 mA.g⁻¹.

Despite this lack of knowledge on the main reaction, the low-potential behavior of the Li_xNi_yW_zO_n powders brings valuable information to grasp the secondary reactions in

Li-Ni-W-O thin films. The sputtered films' behavior in the first reduction sweep is distinct from their behavior in subsequent cycles (Figure 3.4a). This could, here again, point to a conversion reaction, similar to the ones observed in NiWO_4 , $\text{Li}_2\text{Ni}(\text{WO}_4)_2$, or $\text{Li}_2\text{Ni}_2\text{W}_2\text{O}_9$.

It is also interesting to quantify the charge associated to the secondary reactions in Li-Ni-W-O thin films. The exact amount of material contained in the thin films is impossible to determine exactly without a proper density measurement; the capacities reported in Figure 3.4 were calculated by assuming that the film has a density close to that of NiO ($\sim 7 \text{ g}\cdot\text{cm}^{-3}$). Nonetheless, it is clear that, in the first cycle, the capacity associated to the secondary reactions in the film is 4 to 4.5 times higher than the capacity associated to the main reaction. Let us assume that the $\text{Ni}^{3+}/\text{Ni}^{2+}$ redox at the NiO nanocrystallites is responsible for the capacity of the main reaction. If the secondary reactions were solely due to the NiO nanocrystallites and the $\text{Ni}^{2+}/\text{Ni}^0$ redox couple, the capacity associated to the secondary reactions would only be twice as high as the capacity of the main reaction. Since the secondary reactions' capacity is much higher than that, the amorphous matrix has to contribute to the low-potential activity of the thin film.

In any case, the secondary reactions in the Li-Ni-W-O thin films quickly leads to the deterioration of the films. As is shown in Figure 3.4b, after a few cycles, new plateaus appear in the cycling profile of the film, and the voltage measured starts to become unstable after 36 cycles. Such a deterioration is not observed in the $\text{Li}_x\text{Ni}_y\text{W}_z\text{O}_n$ powders, or when cycling the Li-Ni-W-O films between 2.0 and 4.5 V vs Li^+/Li to avoid the secondary reaction (Figure 3.5).

3.C. XPS study of Li-Ni-W-O thin films

To support the information obtained from the electrochemistry, a series of XPS experiments were performed on the four reference $\text{Li}_x\text{Ni}_y\text{W}_z\text{O}_n$ powders and on a pristine Li-Ni-W-O thin film. Then, this technique was used *post-mortem* to track the evolution of the valence states in the Li-Ni-W-O thin films as the state of charge (SOC) varies.

Comparison between $\text{Li}_x\text{Ni}_y\text{W}_z\text{O}_n$ powders and a pristine Li-Ni-W-O thin film

When looking at the Li1s and O1s XPS peaks (Figure 3.6), it appears clearly that the pristine Li-Ni-W-O thin film is very different from the $\text{Li}_x\text{Ni}_y\text{W}_z\text{O}_n$ powders. The Li1s peaks for $\text{Li}_2\text{Ni}_2\text{W}_2\text{O}_9$, $\text{Li}_2\text{Ni}(\text{WO}_4)_2$, and Li_2WO_4 appear at binding energies of 55.0, 54.7, and 55.5 eV, respectively. These values can be attributed to lattice Li^{+353} . Meanwhile, for the

pristine Li-Ni-W-O thin film, the binding energy for the Li1s peak is slightly higher, at 56.3 eV. This value matches more closely to lithium fluoride (LiF)³⁵⁴. This is unexpected considering that the thin film is not supposed to contain fluorine. Likewise, when looking at the O1s peak, the binding energy for the four $\text{Li}_x\text{Ni}_y\text{W}_z\text{O}_n$ powders ranges from 530.3 eV ($\text{Li}_2\text{Ni}_2\text{W}_2\text{O}_9$) to 531.0 eV (Li_2WO_4); these values match well with what is reported for lattice oxygen³⁵³. Although the pristine Li-Ni-W-O thin film displays a peak at 530.7 eV that can be associated to lattice oxygen as well, it also displays two other peaks in the O1s region: one at 532.3 eV, and the other at 533.4 eV. Those two peaks can be attributed respectively to the C-O and the C=O bonds in alkyl carbonates species^{355,356}. The presence of the peak of LiF in the Li1s region, and of those alkyl carbonates peak in the O1s region, indicate that the surface of the pristine thin film was contaminated prior to the XPS measurements. This is not unrealistic, as the sample was stored in a glovebox used to prepare Li-ion batteries: LiF and alkyl carbonates are common species that can be found in liquid electrolytes for Li-ion systems. Despite this impurity layer at the surface of the film, the presence of a peak associated to lattice oxygen means that other elements in the Li-Ni-W-O thin film proper could be detected by XPS; thus, the experiments continued undisturbed.

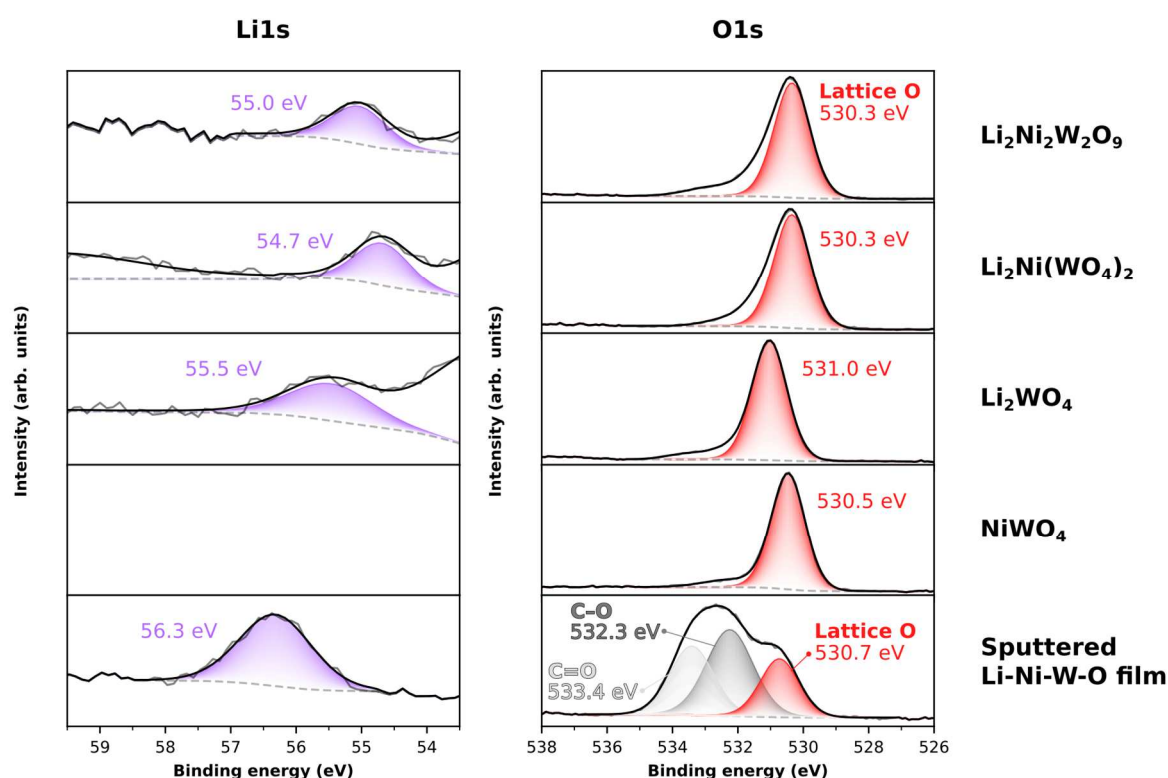


Figure 3.6 – Li1s (left) and O1s (right) regions of the XPS spectra for $\text{Li}_2\text{Ni}_2\text{W}_2\text{O}_9$ powder, $\text{Li}_2\text{Ni}(\text{WO}_4)_2$ powder, trigonal Li_2WO_4 powder, NiWO_4 powder, and a pristine magnetron sputtered Li-Ni-W-O thin film. Contribution from lattice oxygen are shown in red in the O1s region.

This surface contamination of the pristine Li-Ni-W-O thin film is also characterized by the overlap of the Auger KLL peaks of fluorine with the peaks of Ni2p_{3/2} (Figure 3.7). In spite of this overlap, it is still quite clear that the position of the main Ni2p_{3/2} peak is shifted to slightly higher binding energies compared to Li₂Ni₂W₂O₉, Li₂Ni(WO₄)₂, and NiWO₄ powders; this is also the case for the Ni3p peaks of the film in the Ni3p region. Moreover, the Ni2p_{3/2} peak appears to be wider for the film than for the powders. These differences in binding energies and width could stem from a higher amount of Ni³⁺ species in the film, introduced by the oxidizing atmosphere used during the magnetron sputtering process. Furthermore, the positions of the Ni2p_{3/2} peaks for all Ni-containing samples are closer to those reported for NiWO₄ (~ 856.2 eV)³⁵⁷ than for other Ni²⁺ species reported in the literature, such as pure or hydroxylated nickel oxide (~ 855.0 eV)³⁵⁸.

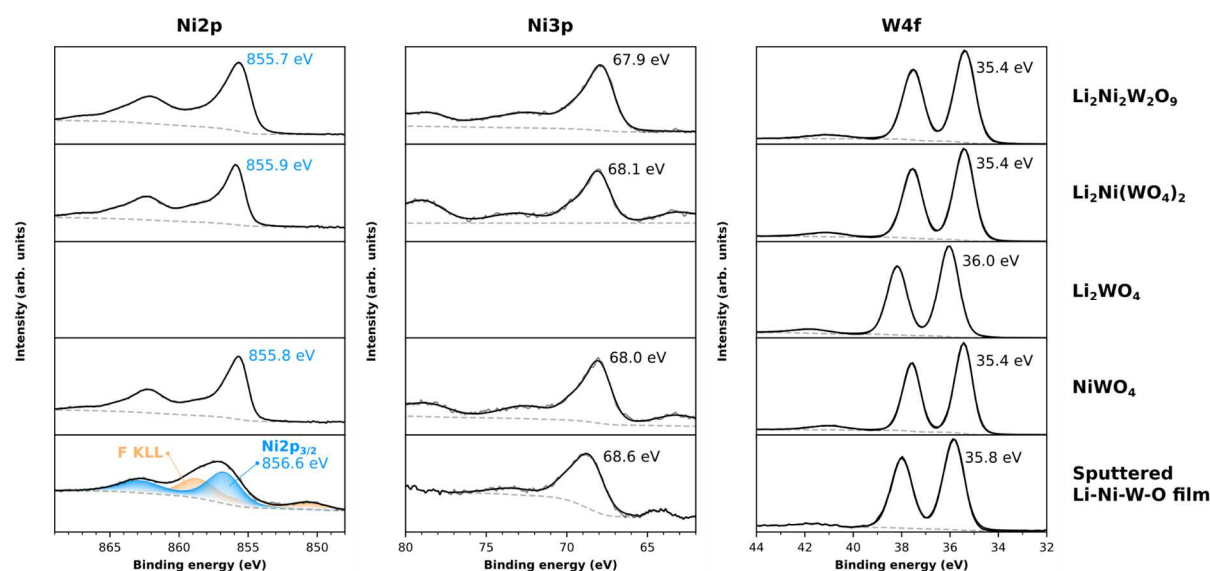


Figure 3.7 – Ni2p (left), Ni3p (middle) and W4f (right) regions of the XPS spectra for Li₂Ni₂W₂O₉ powder, Li₂Ni(WO₄)₂ powder, trigonal Li₂WO₄ powder, NiWO₄ powder, and a pristine magnetron sputtered Li-Ni-W-O thin film. Contributions from the Auger KLL electrons of fluorine and from the Ni2p_{3/2} peaks are respectively shown in orange and in blue in the Ni2p region for the Li-Ni-W-O thin film.

This could indicate that there are weak electronic transfer from the Ni to the W cations in the Ni-W mixed oxides. This is further supported by the binding energies of the W4f_{7/2} and W4f_{5/2} peaks for the Li_xNi_yW_zO_n powders and the Li-Ni-W-O thin film. The shape and position of the peaks correspond to W⁶⁺ in an octahedral configuration (i.e. WO₃-like) for all the samples. However, there is a significant shift of the peak to higher binding energy for Li₂WO₄, which may originate from the lack of Ni²⁺ in the material, and thus the lack of Ni-W electronic transfer. The position of the W4f_{7/2} peak (35.8 eV) in the thin film to a slightly higher binding energy compared to NiWO₄, Li₂Ni(WO₄)₂, and Li₂Ni₂W₂O₉ (35.4 eV) could indicate that there are weaker Ni-W electronic transfer in the film than in the powders.

The exclusivity of the 6+ valence state of tungsten in the sputtered Li-Ni-W-O thin film is also noteworthy. In a previous study by Green et al. on the XPS spectra of Ni-W mixed oxide thin films prepared by reactive DC magnetron co-sputtering, the binding energies of the W4f peaks were reported to be much lower (< 35.0 eV), and the peaks themselves to be wider, for Ni/W ratios above 1³⁵⁹. The authors attributed those observations to the formation of W^{5+} states in the thin films for high amounts of nickel; but the Ni/W ratio in the magnetron sputtered thin film studied here is roughly equal to 2, and no W^{5+} was detected. Hence, the lack of W^{5+} states in the pristine Li-Ni-W-O thin film may come from the significant amount of lithium in the film, or the heat treatment that follows the sputtering process.

To summarize, the comparison of the XPS results for $Li_xNi_yW_zO_n$ powders and the pristine Li-Ni-W-O thin film tells us that the thin film probably contains a mix of Ni^{2+} and Ni^{3+} , and W^{6+} -O octahedra with a slightly different environment from what can be found in the powders.

Post-mortem XPS on Li-Ni-W-O thin films at various states of charge

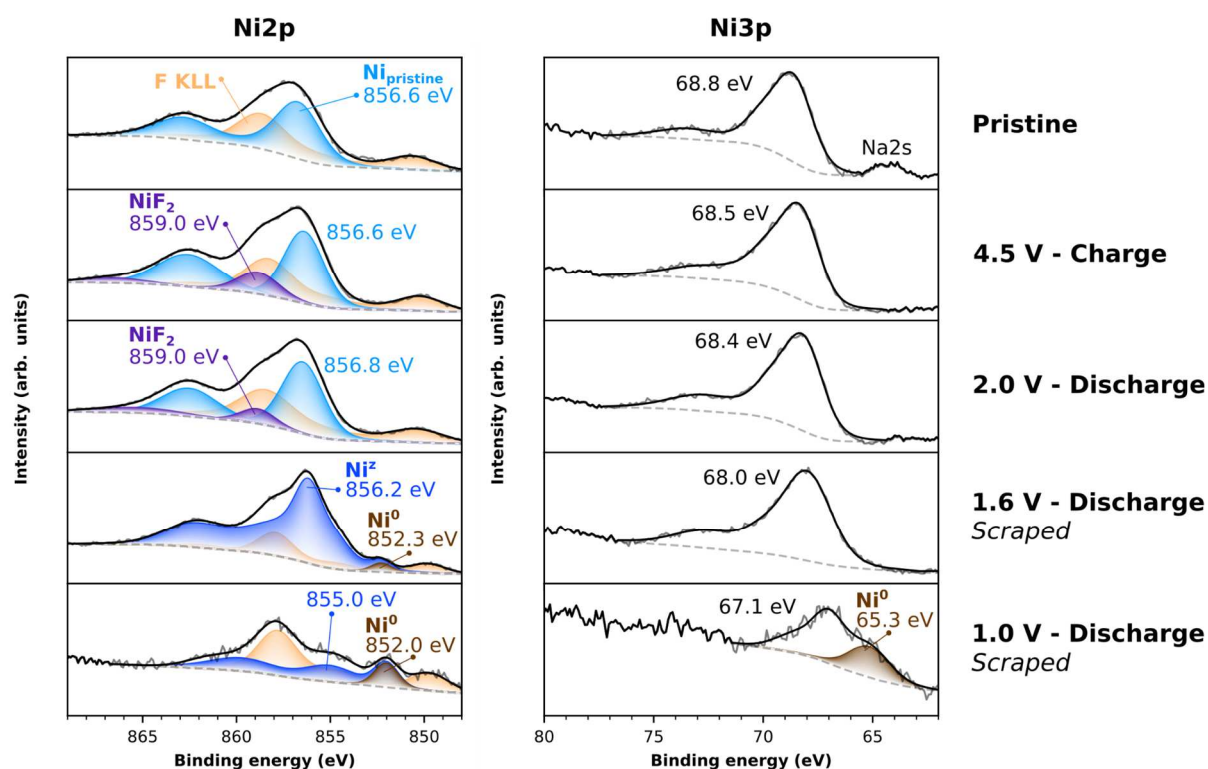


Figure 3.8 – Ni2p (left) and Ni3p (right) regions of the XPS spectra for a pristine Li-Ni-W-O thin film and Li-Ni-W-O thin films in various states of charge. Contribution from the Auger KLL peaks of fluorine are in orange, those from the nickel in the pristine film are in light blue, and those from NiF_2 formed during the charge are in purple. In the low potential samples, the total contribution of all nickel centers in the samples is in dark blue, and the specific contribution of Ni^0 is in dark brown.

Next, XPS was used to see how the electrochemical reactions occurring in the film during Li⁺ (de)insertion affects the valence states of nickel and tungsten.

To accomplish this, four different Li-Ni-W-O thin film samples were cycled at different states of charge ($\sim 100 \text{ mA}\cdot\text{g}^{-1}$, 1 M LiPF₆ in EC:DMC 1:1 vol). All four samples were charged up to 4.5 V vs Li⁺/Li. Then, one sample was discharged down to 2.0 V vs Li⁺/Li, another to 1.6 V vs Li⁺/Li, and another to 1.0 V vs Li⁺/Li. The final sample was not discharged at all and taken out of its cell directly after the initial charge. XPS measurements were performed on all these samples *post-mortem*. In the cases of the samples discharged to 1.6 and 1.0 V vs Li⁺/Li, a CEI layer had started to form at the surface of the samples. It was gently scraped away with a spatula in order to detect the surface of the Li-Ni-W-O thin film (Appendix A3.6).

The pristine thin film is characterized by a Ni2p_{3/2} peak at 856.6 eV and a Ni3p peak at 68.8 eV (Figure 3.8). In the charged sample, a small shoulder peak appears next to the Ni2p_{3/2} peak, at roughly 859.0 eV. This peak contributes to about 21 % of the Ni2p_{3/2} signal. The peak does not disappear during the discharge: it still represents 16 % of the total Ni2p_{3/2} signal after a discharge at 2.0 V vs Li⁺/Li. Since the cycling behavior of the thin film is quite reversible at high potentials (Figure 3.5), this peak cannot be attributed to the reversible formation of Ni³⁺ centers, as it should become much smaller in the sample discharged at 2.0 V if that were the case. Moreover, a binding energy of 859.0 eV is very high for a nickel oxide species, even a nickel(III) oxide³⁶⁰, which suggest that the nickel cations contributing to this peak are coordinated by ligands of higher electronegativity than oxygen. Considering that the samples were cycled in a fluorinated electrolyte, the presence of this peak may be due to the formation of NiF₂ on the surface of the electrode³⁶¹. The formation of this phase on the surface of Ni-based cathode materials in LiPF₆ electrolytes was reported by Li et al.^{362,363} and is likely the result of a reaction with a decomposition product of the electrolyte at high potential (HF)³⁶⁴.

Aside from the apparition of this NiF₂ peak at 859.0 eV, there are no major differences between the Ni2p_{3/2} peaks in the pristine sample and those in the charged sample or the sample discharged at 2.0 V vs Li⁺/Li. The same can be said for the Ni3p area of the spectra. This suggests that the structure of the film remains unchanged during the main reaction at high potentials: this reaction is not associated to phase transitions in the film.

Looking next at what happens in overlithiated samples, their most striking feature is the apparition in the Ni2p region of a small peak at 852.3 eV and 852.0 eV for the samples discharged at 1.6 V and 1.0 V, respectively. These peaks clearly match with values reported in

the literature for the Ni $2p_{3/2}$ peak of metallic nickel^{360,365}. The peak is also much more prominent for the sample with the deepest lithiation: the Ni 0 peak represents 26 % of the total Ni $2p_{3/2}$ signal for the 1.0 V sample, whereas it is only 2.9 % of the total signal for the 1.6 V sample. This proves what has been observed for Li $_x$ Ni $_y$ W $_z$ O $_n$ powders: the overlithiation process of the Li-Ni-W-O thin film is associated to the reduction of Ni $^{2+}$ into Ni 0 . It also seems that this reduction is incomplete at 1.0 V, like in the Li $_x$ Ni $_y$ W $_z$ O $_n$ powders. The formation of Ni 0 is also characterized by the apparition of a small peak at 65.3 eV in the Ni3p region for the sample discharged at 1.0 V, and the apparition of a peak at ~ 0 eV in the valence band for the sample discharged at 1.6 V (Figure 3.9).

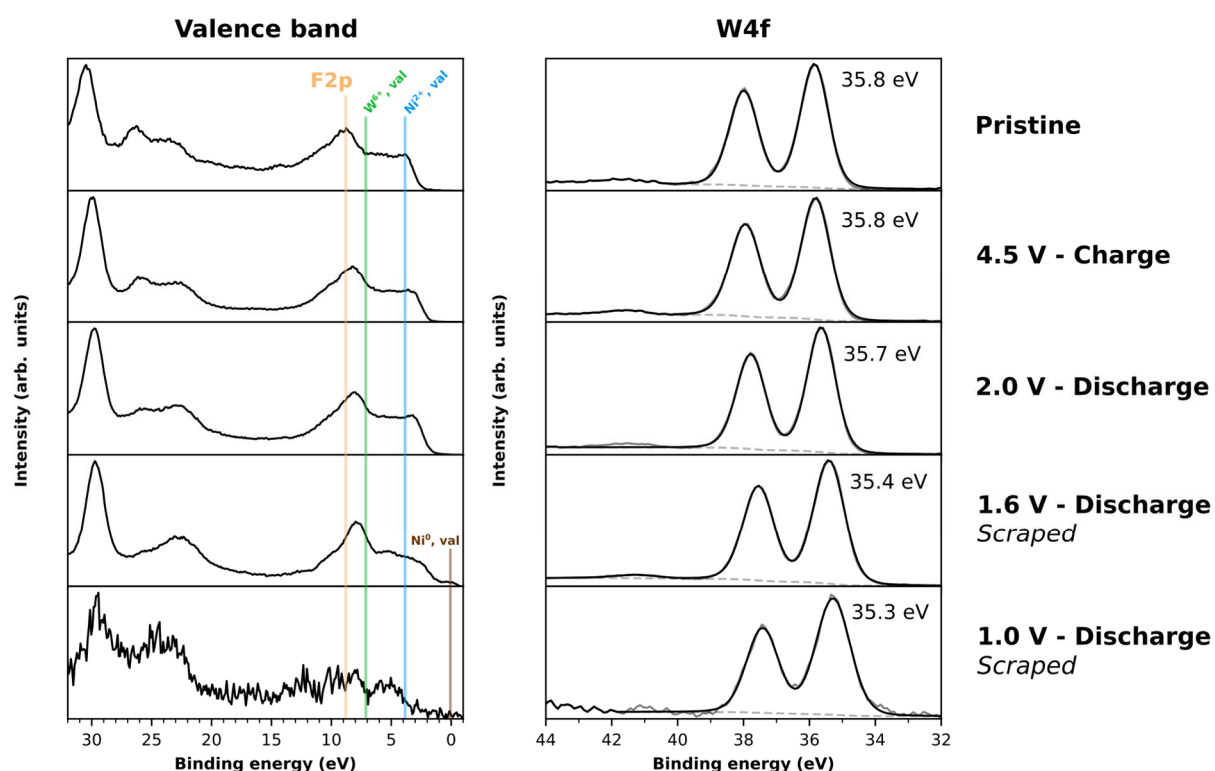


Figure 3.9 – Valence band (left) and W4f (right) regions of the XPS spectra for a pristine Li-Ni-W-O thin film and Li-Ni-W-O thin films in various states of charge.

Finally, the W4f peaks remain essentially the same for all states of charge of the Li-Ni-W-O thin films. As detailed before, the positions and shapes of the W4f $_{7/2}$ and W4f $_{5/2}$ peaks can be attributed to W $^{6+}$, coordinated by oxygen and in an octahedral configuration. There is a slight shift to lower binding energies for the overlithiated thin film samples, but it probably stems from the drastic change in environment due to the reduction of Ni $^{2+}$ to Ni 0 . Indeed, since no new peaks appear, it is unlikely that a subpopulation of reduced W centers is formed on the secondary reactions potential window. This means that tungsten plays a

structural role in the magnetron sputtered Li-Ni-W-O thin films, and is not electrochemically active on the 1.0 V-4.5 V vs Li⁺/Li potential window.

3.D. Preparation of spin-coated Li_xNi_yW_zO_n thin films

Why study thin films and why use spin coating?

In the previous sections of this chapter, the electrochemical properties of powders in the Li₂O-NiO-WO₃ ternary phase diagram were compared to those of the magnetron sputtered Li-Ni-W-O thin film this manuscript focuses on.

Although some useful pieces of information could be obtained from that comparison, one must admit that there are restrictive differences between the two systems. On one hand, the Li_xNi_yW_zO_n powders are monophasic, highly crystallized systems; on the other, the sputtered Li-Ni-W-O thin films are biphasic, and mostly amorphous.

To find more information on the relationships between composition, structure, and electro-optical properties in Li-Ni-W-O thin films, it is necessary to compare them to similar systems. This is particularly important to understand the high-potential main reaction in the nanocomposite films. However, the magnetron sputtering process described at the end of Chapter 1 is adapted to prepare thin films with only one definite atomic composition. It would be very time-consuming to figure out the correct sputtering parameters to prepare thin films with various compositions, and then to perform the right characterizations (for example, ICP) to ensure that said compositions are correct.

To circumvent this issue, spin coating was used to prepare Li_xNi_yW_zO_n thin films. Spin coating is a wet coating method, meaning that it uses a solution prepared ahead of the coating process. The final composition of the spin-coated film depends solely on the stoichiometry of the coating solution, and thus on the amount of each precursor put in the solution. Therefore, in the context of this study, it is much easier to control the composition of spin-coated films than magnetron sputtered films. This allows a smooth exploration of the Li₂O-NiO-WO₃ ternary phase diagram, and an easy study of the impact of composition on the structure and the electro-optical properties.

This rest of this chapter will first give a brief description of the spin coating process used to prepare Li_xNi_yW_zO_n thin films, and the different parameters that had to be optimized to do so. Then, the compositions of the various thin films prepared this way will be detailed,

and their microstructure will be described using SEM and optical reflection microscopy images, as well as profilometry measurements. Finally, the electrochromic properties of these thin films will be studied using results from an *operando* UV-Visible spectroscopy electrochemical experiment.

General description of the spin coating process

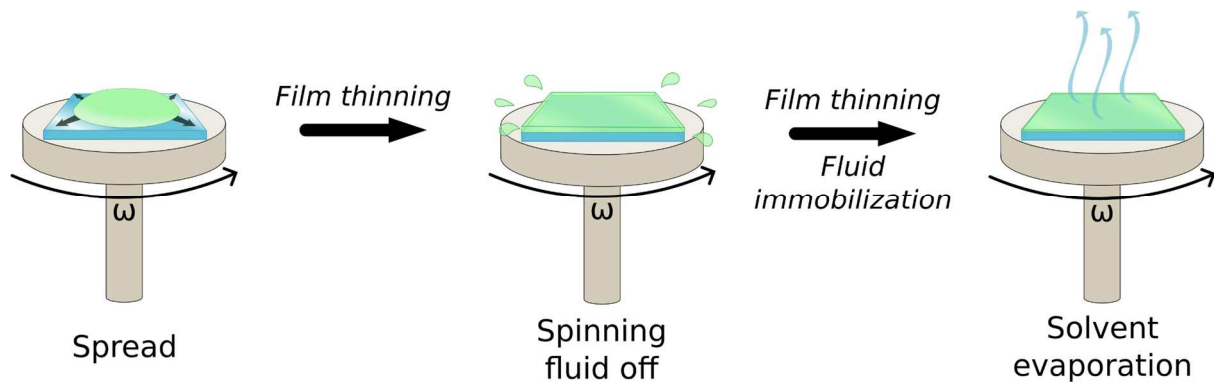


Figure 3.10 – Simplified representation of the spin coating process.

The spin coating process is based on the thinning of a fluid on the surface of a substrate by fast rotation^{366,367}. The substrate is placed on a rotating plate and is held by a vacuum chuck or a groove to avoid being thrown off the plate during the spinning process. The coating solution is dispensed on the substrate, which is then spun by switching the rotating plate on. The film is formed in three steps (Figure 3.10):

- The coating solution spreads evenly on the substrate due to the centrifugal force.
- Once the solution has spread across the entire surface of the substrate, it becomes thinner as the centrifugal force throws some of the fluid off the substrate.
- Once enough liquid has been spun off, the remaining fluid becomes highly viscous and is immobilized on the substrate. At this point, excess solvent starts evaporating, leading to the final thickness of the film.

The film's thickness after spin coating, h_f , can be estimated using Meyerhofer's equation³⁶⁸ (Equation 3.1):

$$h_f = c_0 \sqrt[3]{\frac{3}{2} \frac{v_0 e}{(1 - c_0)\omega^2}} \quad 3.1$$

in which v_0 is the initial kinematic viscosity of the coating solution, e is the evaporation rate of the solvent, and ω the angular speed of the rotating plate. c_0 represents the concentration of

precursors in the solution, and can be expressed using the initial volume occupied by the solvent (L_0) and the volume occupied by solid matter if all the initial solvent were to evaporate (S_0) (Equation 3.2):

$$c_0 = \frac{S_0}{S_0 + L_0} \quad 3.2$$

The main takeaway of Equation 3.1 is that the thickness of the film will increase for slower outflow rates, and for higher precursor concentrations in the spinning solution. However, it relies on the hypothesis that there is a significant outflow of liquid at the beginning of the spin coating process; this hypothesis can be translated by $S_0 \geq 2h_f$.

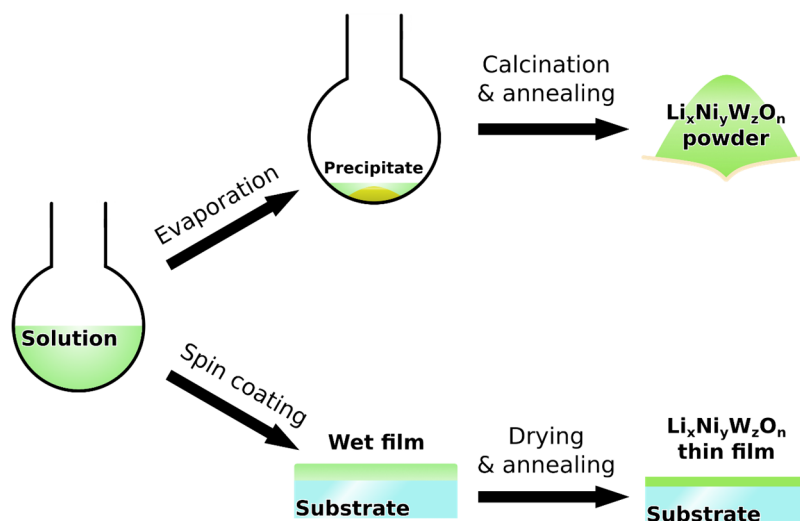


Figure 3.11 – Simplified scheme for the preparation of densified $\text{Li}_x\text{Ni}_y\text{W}_z\text{O}_n$ thin films and $\text{Li}_x\text{Ni}_y\text{W}_z\text{O}_n$ powders from a spin coating solution.

The process used for the preparation of the standard magnetron sputtered Li-Ni-W-O thin films (see Chapter 2) includes a heat treatment step after magnetron sputtering. To get as close as possible to these standard film, the spin coated $\text{Li}_x\text{Ni}_y\text{W}_z\text{O}_n$ thin films are dried at $100\text{ }^\circ\text{C}$ to remove excess solvent, and annealed in a muffled furnace, both to burn away the organic component of the film and to densify it (Figure 3.11). In order to get a similar nanocomposite structure to the standard film, the spin coated films were annealed at similar temperatures (between $380\text{ }^\circ\text{C}$ and $450\text{ }^\circ\text{C}$), for 5 to 30 minutes.

Once a film has been synthesized by spin coating, the remaining solution can be used to indirectly check the composition of the film. The solvent is evaporated, at which point a wet precipitate is formed; this precipitate is then calcined and annealed at high temperatures to obtain a crystallized $\text{Li}_x\text{Ni}_y\text{W}_z\text{O}_n$ powder (Figure 3.11). This powder can then be scanned by powder XRD in order to identify which phases it contains, and what is its elemental

composition. Finally, this elemental composition can be compared with the expected stoichiometry for the spin coating solution and the spin-coated thin film.

This brief description of the spin coating process shows that there are many parameters to take into account when preparing thin films with this method. The optimization of some of these parameters will be detailed in the following paragraphs.

Choice of the reactants

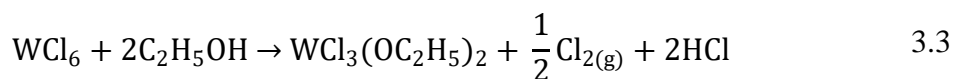
To prepare a spin coating solution for the synthesis of $\text{Li}_x\text{Ni}_y\text{W}_z\text{O}_n$ thin films, three reactants are required: a source of lithium, a source of nickel, and a source of tungsten. Oxygen is provided by the organic solvent, or the atmosphere, as the annealing of the thin films takes place in air. Ethanol was used as solvent, as it is relatively harmless, evaporates easily, and displays good flow capabilities.

Hence, the initial criterion used to select the precursors was their solubility in ethanol. Another point to consider was the possibility to easily remove parasite species from the film during the heat treatment. The candidates for the preparation of the spin coating solution are usually salts. However, only one ion from each salt precursor is of interest for the composition of the thin film; it is important that the counter-ions are decomposed during the thermal treatment.

For the Li(I) and Ni(II) precursors, several candidates are available in terms of solubility: nitrates, chlorides, and acetates, as well as nickel sulfate heptahydrate³⁶⁹. There are less options when it comes to the W(VI) precursor: only tungsten(VI) chloride (WCl_6), and tungsten(VI) oxochloride (WOCl_4) are commercially available and soluble in ethanol.

In this study, WCl_6 was selected as the tungsten source. This restricted the choice of the Li(I) and Ni(II) precursors. Neither lithium chloride (LiCl) nor nickel chloride hexahydrate ($\text{NiCl}_2 \cdot 6\text{H}_2\text{O}$) would dissolve in a solution containing WCl_6 , as the Cl^- concentration was too high. Of the remaining possibilities, lithium nitrate (LiNO_3) and nickel nitrate hexahydrate ($\text{Ni}(\text{NO}_3)_2 \cdot 6\text{H}_2\text{O}$) were arbitrarily chosen as the lithium and nickel sources. They were picked to limit the number of distinct counter-ion species in the solution.

The use of WCl_6 as a tungsten source also requires the addition of another compound to the solution: citric acid. Indeed, without citric acid, WCl_6 readily reacts with ethanol to form a dark blue tungsten(V) alkoxychloride precipitate^{370,371} (Equation 3.3):



By adding citric acid to the solution, WCl_6 should instead form a stable derivative of WOCl_4 in solution³⁷², according to Equation 3.4:



The formation of a WOCl_4 derivative can be observed by attenuated total reflectance infrared spectroscopy (ATR-IR). It is characterized by the apparition of a small absorption peak around 950 cm^{-1} (Figure 3.12). This peak is attributed to the stretching of the $\text{W}=\text{O}$ bond in WOCl_4 ³⁷¹.

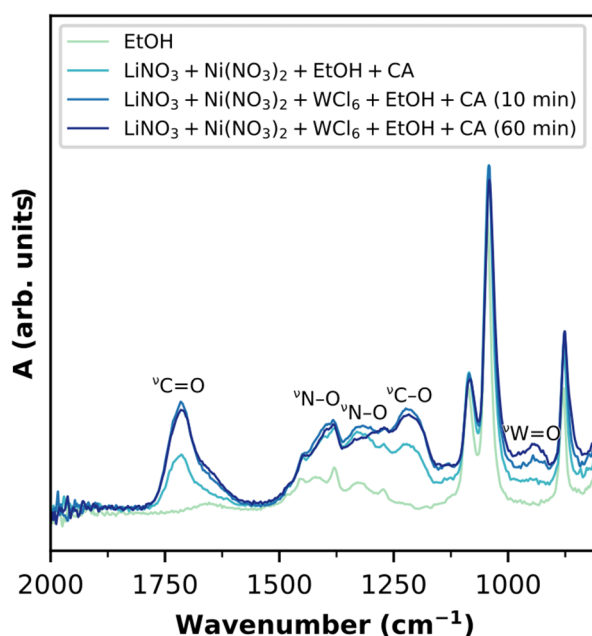


Figure 3.12 – ATR-IR spectra for ethanol absolute (light green), an ethanol solution containing LiNO_3 , $\text{Ni}(\text{NO}_3)_2 \cdot 6\text{H}_2\text{O}$, and citric acid monohydrate (0.3 M, 0.3 M, 1.2 M) (light blue), and an ethanol solution containing LiNO_3 , $\text{Ni}(\text{NO}_3)_2 \cdot 6\text{H}_2\text{O}$, WCl_6 and citric acid monohydrate (0.3 M, 0.3 M, 0.3 M, 1.8 M) 10 minutes (blue) and 60 minutes (dark blue) after adding the WCl_6 to the solution.

The formation of this stable WOCl_4 species is essential to avoid the immediate apparition of a precipitate in the coating solution. Precipitates can disturb the outflow of liquid during the spin coating process, and yield non-uniform films³⁶⁷.

However, it has been observed that citric acid alone is not enough to prevent the reduction and precipitation of the W(V) species. Empirically, an ethanol solution containing only WCl_6 and citric acid monohydrate ($\text{C.A.}/\text{M}^z = 2:1$) will also precipitate. The precipitation of W(V) species can only be prevented if a nitrate salt (LiNO_3 or $\text{Ni}(\text{NO}_3)_2 \cdot 6\text{H}_2\text{O}$) and citric

acid are present in the solution with WCl_6 . This suggests that the stabilization of W(VI) occurs through a mechanism slightly more complex than the one described in Equation 3.4.

Citric acid to metallic cation ratio

The addition of citric acid, on top of the Li(I), Ni(II), and W(VI) precursors, will lead to a stable solution. However, its lifespan will depend on the amount of citric acid added. Empirically, a citric acid to metallic cation ratio (C.A./ M^z) of at least 2:1 yields a solution that do not precipitate for seven days. After this period of time, a yellow precipitate will form; the solution then becomes unusable for spin coating. The nature of this precipitate is unknown, although it is clearly related to the addition of WCl_6 in the solution, as it does not form for solutions containing only LiNO_3 , $\text{Ni}(\text{NO}_3)_2 \cdot 6\text{H}_2\text{O}$, and citric acid monohydrate (Figure 3.13).

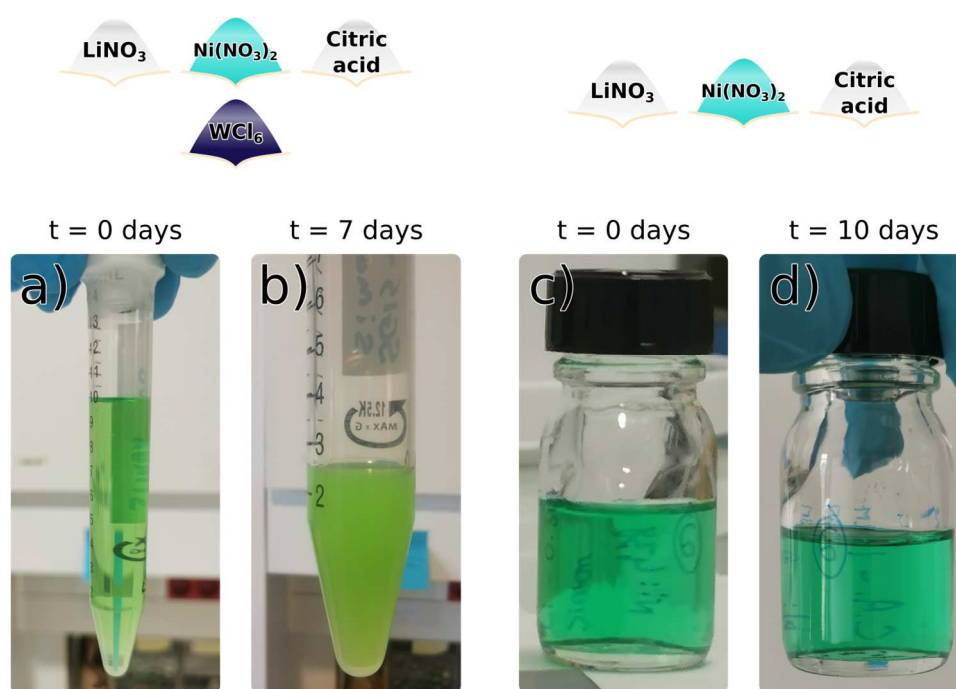


Figure 3.13 – (a, b): Ethanolic solution containing 0.2 M LiNO_3 , 0.2 M $\text{Ni}(\text{NO}_3)_2 \cdot 6\text{H}_2\text{O}$, 0.2 M WCl_6 , and 1.2 M citric acid monohydrate, (a) 0 days and (b) 7 days after complete dissolution/reaction of all the reactants. (c, d): Ethanolic solution containing 0.3 M LiNO_3 , 0.3 M $\text{Ni}(\text{NO}_3)_2 \cdot 6\text{H}_2\text{O}$, and 1.2 M citric acid monohydrate, (c) 0 days and (d) 10 days after complete dissolution/reaction of all the reactants.

For solutions with $\text{C.A.}/M^z = 1:1$, the formation of the yellow precipitate starts in less than a day; $\text{C.A.}/M^z > 2:1$ yield solution with longer lifespans, but also higher viscosities.

Nature of the substrate

Beside the reactants contained in the solution, the substrate used for the preparation of the thin films is also important, for two reasons.

The first one is the risk of contamination. Elements contained in the substrate should not diffuse inside the thin film. This is a significant point to consider, especially because the spin coating process used in this study is followed by a heat treatment step, which can favor diffusion of cations from the substrate to the film³⁷³. For example, thin films with $\text{Li}_2\text{Ni}_2\text{W}_2\text{O}_9$ as the target composition that were directly deposited on glass were contaminated by sodium during the heat treatment (450 °C, 30 min, air). This was observed by a XRD measurement of the films in Bragg-Brentano configuration: peaks associated to cubic $Fd\bar{3}m$ Na_2WO_4 ³⁷⁴ are clearly visible in the diffractogram (Figure 3.14b). This contamination can lead to heterogeneous and non-uniform coatings (Figure 3.14a), and can deviate the thin films from their target composition.

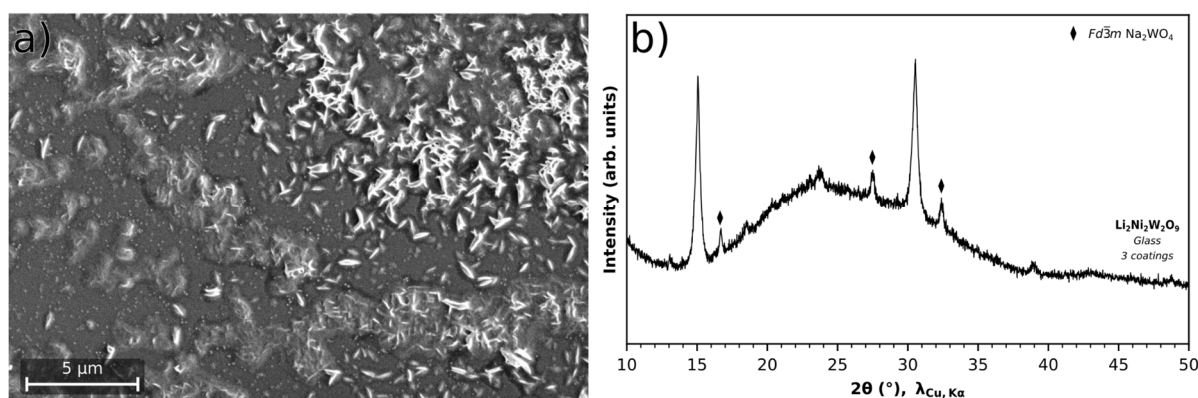


Figure 3.14 – (a) Top view SEM image of a thin film (composition: $\text{Li}_2\text{Ni}_2\text{W}_2\text{O}_9$) spin coated on a glass substrate. (b) XRD pattern for the thin film shown in (a). Peaks associated to cubic Na_2WO_4 are clearly visible. Other peaks could not be attributed.

The second reason why the nature of the substrate is important in the context of this study relates to the type of measurements that need to be conducted on the thin film samples. Different types of measurements may call for different types of substrates; herein, the optical and electrochemical properties of the thin films need to be characterized. Thus, the substrate has to be transparent, and has to be an electronic conductor: a transparent conductive oxide immediately comes to mind.

The substrate selected for the preparation of the spin-coated $\text{Li}_x\text{Ni}_y\text{W}_z\text{O}_n$ thin films was an ITO/ SiO_x / NbO_x /Glass stack, prepared by magnetron sputtering. It is the same substrate as those used for the standard magnetron sputtered Li-Ni-W-O nanocomposite films. The transparent conductive layer, ITO, is 400 nm in thickness. SiO_x and NbO_x are anti-glare layers, no more than 50 nm in total thickness. Finally, the glass pane is 2.2 mm in thickness. For the sake of simplicity, this substrate will simply be called “ITO/Glass” in the rest of the manuscript.

Other parameters to consider and final description of the spin-coating process

There are numerous parameters to consider when performing spin coating. The few detailed prior to this point were specific to the compositions and the properties studied in this paper. However, other aspects of the process were also considered and optimized, such as:

- the concentration of metallic cations, which impacts the viscosity of the solution, and which cannot be too high as it could lead to the spontaneous formation of a yellow precipitate.
- the rotation speed, rotation acceleration, and duration of rotation for the spinning plate of the spin-coater.
- the number of successive coatings on the same substrate, which can slightly impact the thickness of the densified film (Figure 3.15).

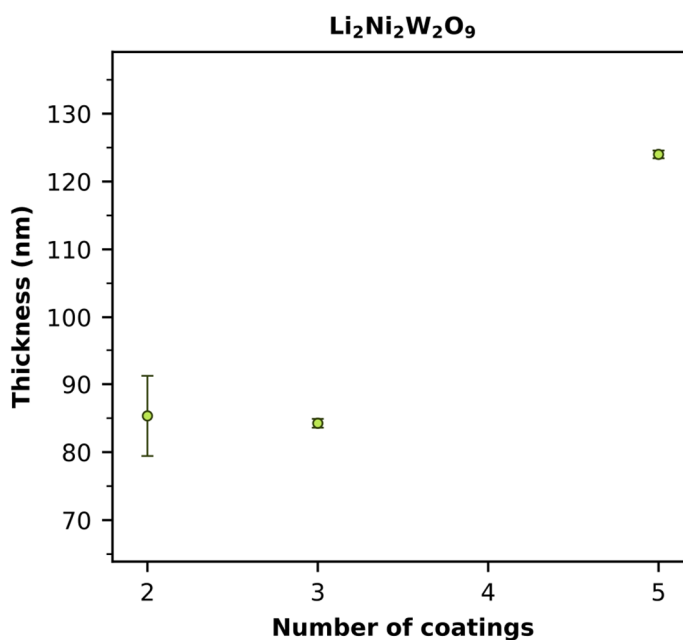


Figure 3.15 – Impact of the number of successive coatings on the final thickness of three different thin film samples. Composition: $\text{Li}_2\text{Ni}_2\text{W}_2\text{O}_9$. Concentrations: $[\text{Li}^+] = [\text{Ni}^{2+}] = [\text{W}^{6+}] = 0.2 \text{ M}$. C.A./ $M^z = 2:1$. Substrate: ITO/Glass. Thicknesses were measured using a Dektak profilometer; each data point is the average of at least three measurements on the same sample.

- the annealing temperature and annealing duration, which have a strong influence on the crystallinity and the density of a film, and by extension on its optical and electrochemical properties. Thermogravimetric analysis measurements (TGA) on the calcined precipitate obtained from a spin coating solution suggest that temperatures as high as $400 \text{ }^\circ\text{C}$ are required to remove all organic, nitrated, and chlorinated impurities from the films (Figure 3.16).

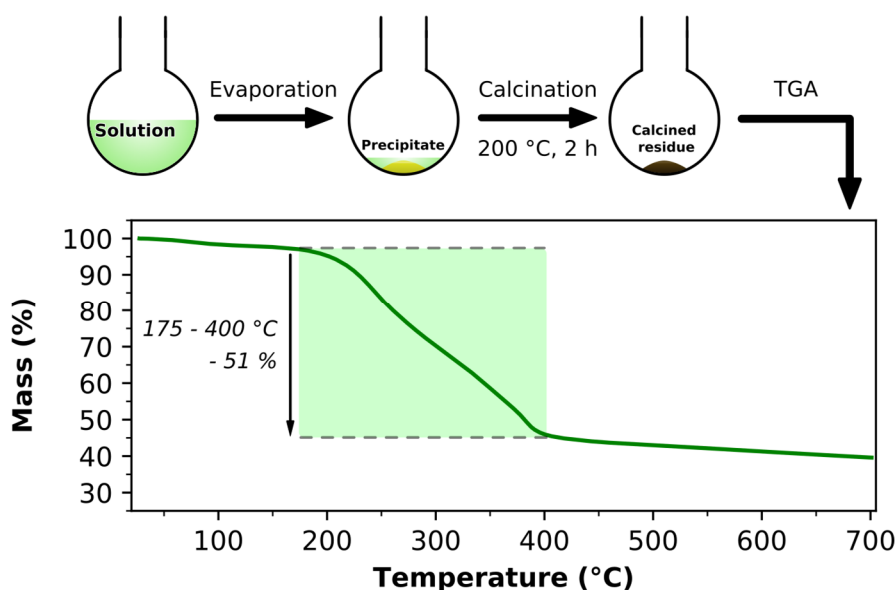


Figure 3.16 – Evaporation/calcination process leading to the formation of a calcined residue from a spin coating solution (top), and TGA curve for the calcined residue of a spin coating solution with composition $\text{Li}_2\text{Ni}_2\text{W}_2\text{O}_9$ (concentrations: $[\text{Li}^+] = [\text{Ni}^{2+}] = [\text{W}^{6+}] = 0.2 \text{ M}$; C.A./ $M^z = 2:1$).

The optimization of all these parameters led to the general spin coating process used for the preparation of $\text{Li}_x\text{Ni}_y\text{W}_z\text{O}_n$ thin films. These parameters are fully described in Table 3.1.

Table 3.1 – General parameters used for the preparation of spin-coated $\text{Li}_x\text{Ni}_y\text{W}_z\text{O}_n$ thin films.

Solvent	Ethanol absolute
Reactants	LiNO_3 , $\text{Ni}(\text{NO}_3)_2 \cdot 6\text{H}_2\text{O}$, WCl_6 , citric acid monohydrate
Concentrations	The concentration for the majority cation was set to 0.2 M; other concentrations were adapted to match the desired stoichiometry.
C.A./M^z	2:1; M^z corresponds to the total metal cation concentration ($[\text{Li}^+] + [\text{Ni}^{2+}] + [\text{W}^{6+}]$)
Substrate	ITO/Glass, 5 x 5 cm
Rotation speed	3000 rpm
Rotation acceleration	1000 rpm.s ⁻¹
Rotation duration	30 s
Number of successive coatings	2; the second coating is performed after drying the first one
Drying parameters	100 °C, ~ 10 min
Annealing parameters	380 °C to 450 °C, 5 to 30 min, + 5 °C.min ⁻¹ , air

Having described the optimization of the spin coating process, the rest of this chapter focuses on the synthesis of various $\text{Li}_x\text{Ni}_y\text{W}_z\text{O}_n$ thin films, and on the impact of the composition on the structure and properties of said films.

3.E. Compositions of the $\text{Li}_x\text{Ni}_y\text{W}_z\text{O}_n$ thin films studied

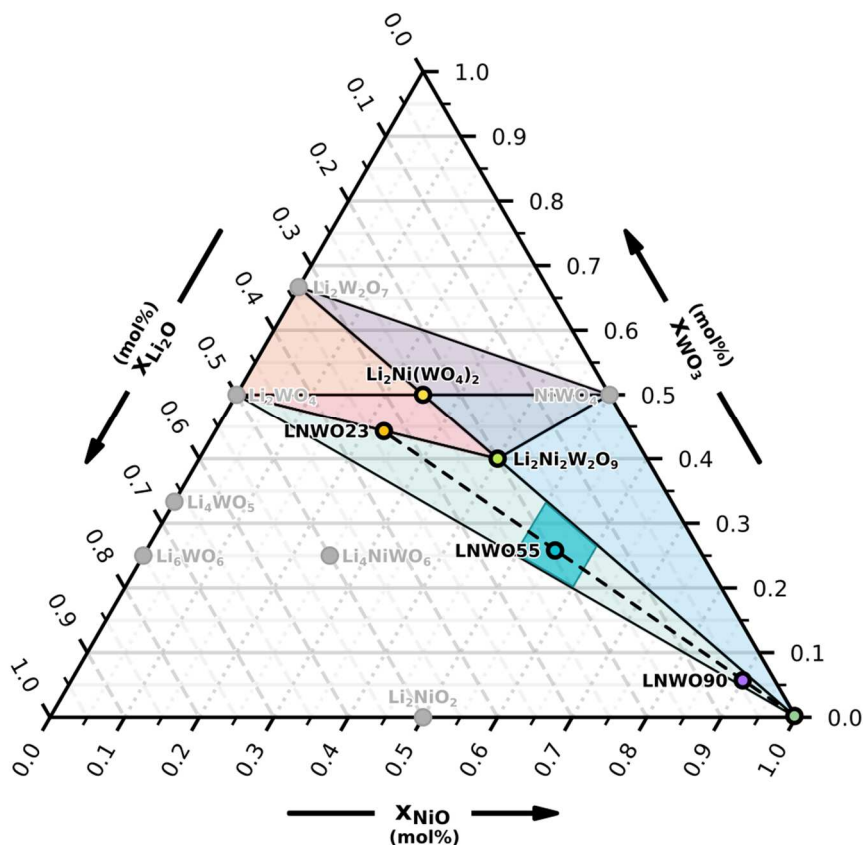


Figure 3.17 – Li_2O - NiO - WO_3 ternary phase diagram showing the different compositions tested for the spin-coated $\text{Li}_x\text{Ni}_y\text{W}_z\text{O}_n$ thin films. Compositions that are grayed out were not studied as thin films in this manuscript.

Several thin film compositions were explored in this study (Figure 3.17). Films with compositions $\text{Li}_2\text{Ni}_2\text{W}_2\text{O}_9$ and $\text{Li}_2\text{Ni}(\text{WO}_4)_2$ were prepared to match with the powders presented in Chapter 3. Besides these two, four other compositions were considered. Those were selected by plotting a straight line between NiO (lower right vertex of the ternary) and an arbitrary composition in the composition range of the magnetron sputtered Li-Ni-W-O thin films (cyan area). The four compositions were picked on that line (dashed line in Figure 3.17), which is mathematically described by Equations 3.5 and 3.6:

$$x_{\text{NiO}} = -2.33x_{\text{Li}_2\text{O}} + 1 \quad 3.5$$

$$x_{\text{NiO}} + x_{\text{Li}_2\text{O}} + x_{\text{WO}_3} = 1 \quad 3.6$$

in which x_{NiO} , $x_{\text{Li}_2\text{O}}$, and x_{WO_3} are the molar fractions of NiO, Li₂O, and WO₃.

To simplify the discussions on these thin films, the following naming conventions will be used in the rest of this chapter:

- NiO, Li₂Ni₂W₂O₉, and Li₂Ni(WO₄)₂ will be called as such.
- Films on the dashed line of the ternary will be named “LNWOX”, where X is the desired value of x_{NiO} for this sample.
- The standard magnetron sputtered Li-Ni-W-O thin film, that will be used as a reference, will be called MS-LNWO.

The complete list of all compositions studied is shown in Table 3.2:

Table 3.2 – Names and compositions of the thin film studied in Chapter 3.

Short name	Elemental composition
MS-LNWO	Magnetron sputtered Li-Ni-W-O (formula not given)
NiO	NiO
Li ₂ Ni(WO ₄) ₂	Li ₂ Ni(WO ₄) ₂
Li ₂ Ni ₂ W ₂ O ₉	Li ₂ Ni ₂ W ₂ O ₉
LNWO23	Li _{0.66} Ni _{0.23} W _{0.44} O _{1.88}
LNWO55	Li _{0.38} Ni _{0.55} W _{0.26} O _{1.52}
LNWO90	Li _{0.08} Ni _{0.90} W _{0.06} O _{1.12}

The spin-coated films discussed in the rest of this chapter were all annealed at 450 °C for 30 minutes during the heat treatment step.

3.F. Microstructural characterization of the Li_xNi_yW_zO_n thin films

Film surface

The surface quality of the spin-coated thin films was characterized by optical reflection microscopy. Microscopy images for the various compositions can be seen in Figure 3.18.

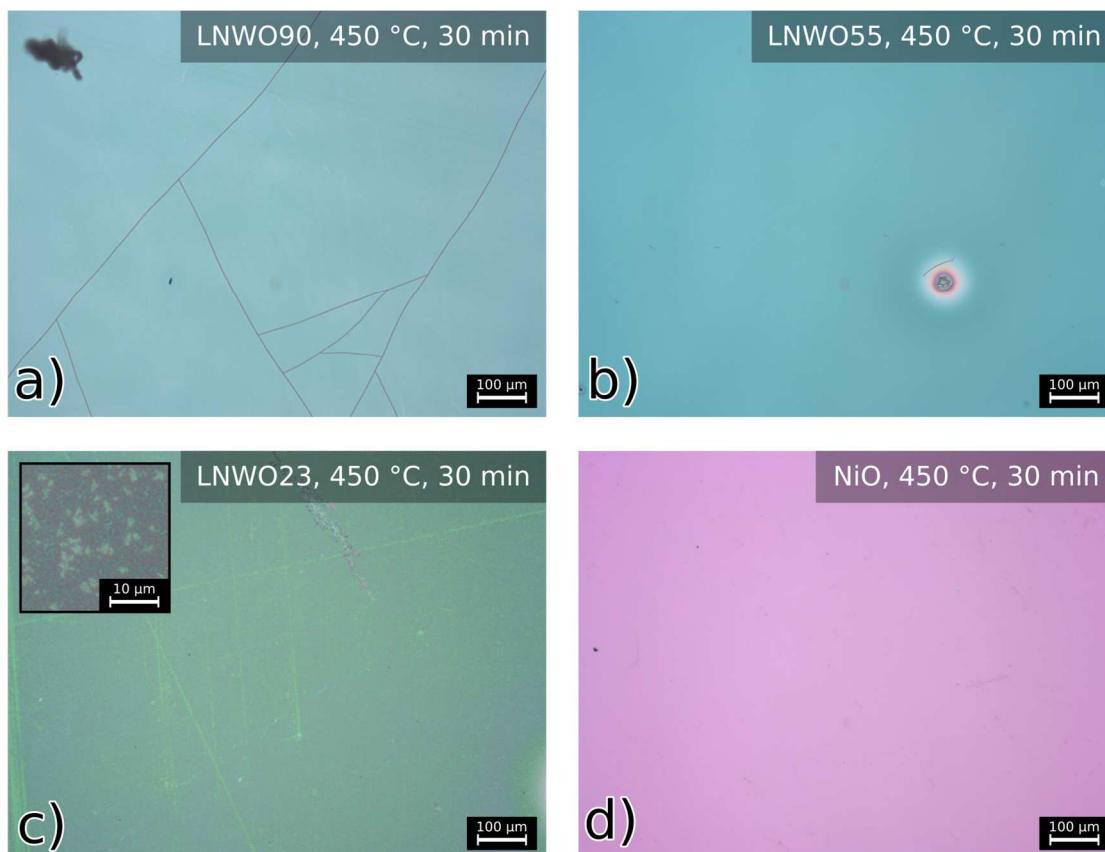


Figure 3.18 – Optical microscopy images for spin coated (a) LNWO90, (b) LNWO55, (c) LNWO23, and (d) NiO thin films.

Overall, spin-coated $\text{Li}_x\text{Ni}_y\text{W}_z\text{O}_n$ thin films display a continuous surface. However, some defects can be observed. A network of cracks is clearly visible in LNWO90 (Figure 3.18a). Nonetheless, these cracks should not be detrimental to the electrochemical performances of the films; this is also the case for other punctual defects, such as pinholes (Figure 3.18b).

In the case of LNWO23, small microcrystals seem to have formed across the entire surface of the film during the annealing process (Figure 3.18c). Such crystalline features are absent from the other films.

Top-view SEM images of LNWO55 and MS-LNWO were taken to confirm that the microstructure of the spin-coated film is similar to that of the standard magnetron sputtered film (Figure 3.19).

Both films seem to have a smooth, continuous surface, with no significant micrometric feature, besides some dust particles and, in the case of LNWO55, isolated cracks. All in all, with the noticeable exception of LNWO23, the spin-coated $\text{Li}_x\text{Ni}_y\text{W}_z\text{O}_n$ thin films are

continuous and do not display any significant micrometric feature aside from cracks and pinholes, which are likely related to the spin-coating/heating process.

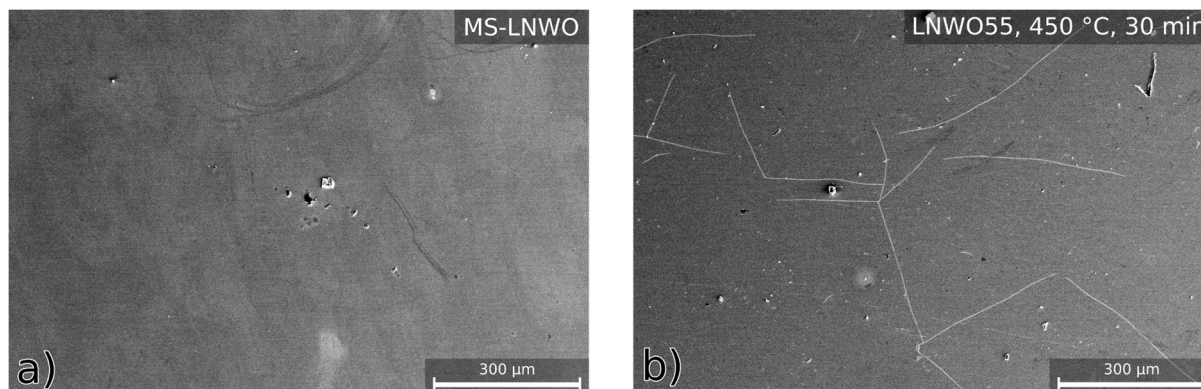


Figure 3.19 – Top-view SEM images of (a) MS-LNWO and (b) spin-coated LNWO55.

Profilometry

Thickness measurements were performed on the different $\text{Li}_x\text{Ni}_y\text{W}_z\text{O}_n$ thin films, using a Dektak profilometer. The results are listed in Table 3.3. The coating parameters are the same for all the films. Hence, the variations in thickness could be explained by a shift in the viscosity of the solutions, due to their different compositions. In particular, the coating solution for the NiO thin film, which did not require the addition of WCl_6 and citric acid, was evidently less viscous than the others, leading to a thinner film.

Table 3.3 – Average thicknesses measured for different spin coated thin films using a Dektak profilometer. The thicknesses are averaged over at least three different measurements on the same sample.

Short name	Average film thickness (nm)
NiO _z	20 ± 10
Li ₂ Ni(WO ₄) ₂	120 ± 20
Li ₂ Ni ₂ W ₂ O ₉	80 ± 20
LNWO23	76 ± 9
LNWO55	60 ± 9
LNWO90	82 ± 9

3.G. Electrochemical and optical properties of the $\text{Li}_x\text{Ni}_y\text{W}_z\text{O}_n$ thin films

Operando UV-Visible electrochemistry setup

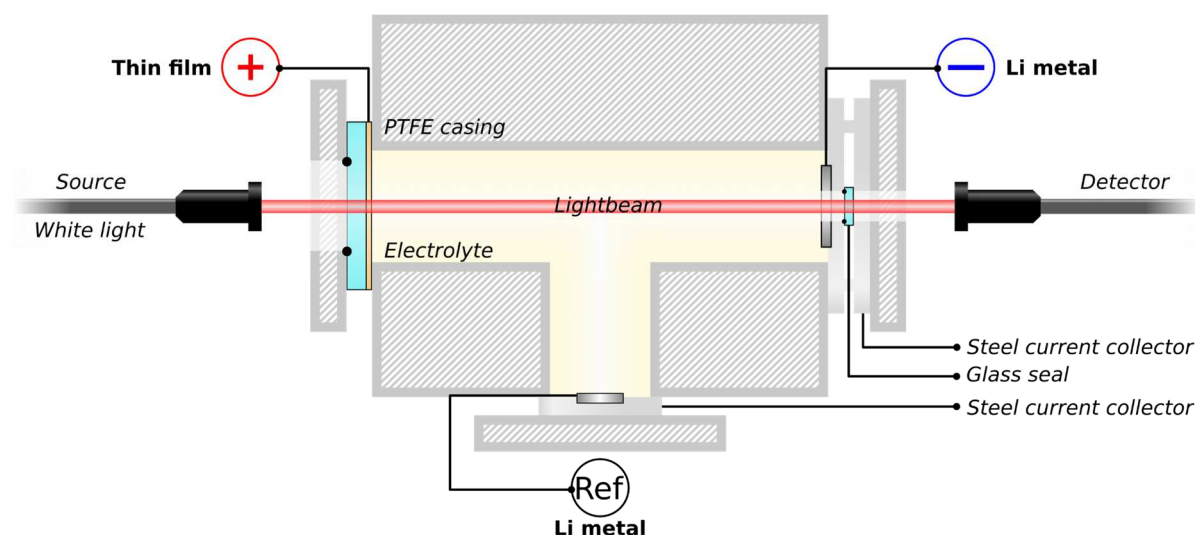


Figure 3.20 – Experimental setup for an *operando* UV-Visible spectroscopy electrochemical measurement.

The quality of the spin-coated $\text{Li}_x\text{Ni}_y\text{W}_z\text{O}_n$ thin films was deemed good enough to study their electrochemical and optical properties. To do so, a specific *operando* setup was used (Figure 3.20). It allows the simultaneous collection of UV-Visible spectra and electrochemical data for a thin film sample.

This setup takes the form of a three-electrode liquid cell. The positive electrode is a thin film deposited on a transparent substrate, the negative electrode is a lithium metal ring, and the reference electrode is a lithium metal disk. The liquid electrolyte, which is also transparent, is 1 M LiClO_4 in PC, a very common electrolyte used in the study of electrochromic systems. Pierced polytetrafluoroethylene (PTFE) plates and pierced steel plates hold the positive and negative electrodes into place. Thus, the cell is designed in such a way that an incident beam of white light can travel through the thin film and its substrate, the electrolyte, the sealing glass pane at the negative electrode, and be collected after exiting the cell. Specifically, the transmitted light beam is collected by an optical fiber leading to a UV-Visible spectrometer.

The UV-Visible spectra thus collected are theoretically due to the entire (substrate + thin film + electrolyte + glass pane) system. However, upon electrochemical exchange of Li^+ , the only part of the system that is expected to optically change is the electrochromic thin film. Consequently, by performing a blank measurement with the cell in its initial state, one can

obtain the relative variations of transmission for the thin film during cycling. Eventually, by collecting a *post-mortem* UV-Visible transmission spectrum of the thin film, the absolute transmission variations of the thin film during cycling can be calculated.

Electrochemical responses of $\text{Li}_x\text{Ni}_y\text{W}_z\text{O}_n$ thin films

Using the *operando* UV-Visible electrochemical setup, galvanostatic charge-discharge experiments were performed on the $\text{Li}_x\text{Ni}_y\text{W}_z\text{O}_n$ thin films. First, the cycling curves for MS-LNWO are shown in Figure 3.21.

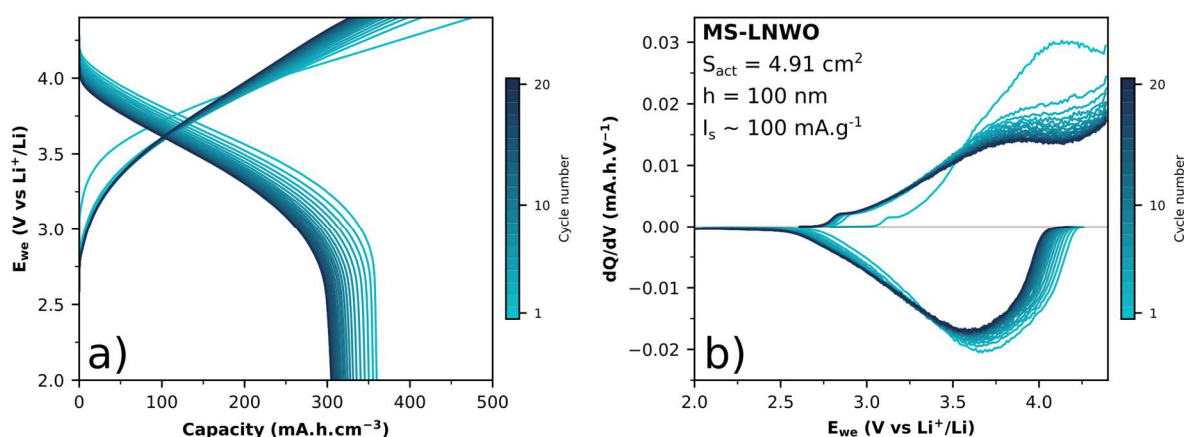


Figure 3.21 – (a) E_{we} vs capacity and (b) dQ/dV curves for a galvanostatic charge-discharge experiment using a 100-nm MS-LNWO thin film as the working electrode. The active surface area (S_{act}) is equal to 4.91 cm^2 , the density of the film was assumed to be $\sim 7 \text{ g.cm}^{-3}$, and the current density (I_s) was set to be $\sim 100 \text{ mA.g}^{-1}$.

Focusing only on the main reaction at high potentials (2.0 to 4.4 V vs Li^+/Li), the magnetron sputtered thin film displays a single pair of redox peaks between 2.5 and 4.4 V vs Li^+/Li . As explained before, these peaks are assumed to come from the $\text{Ni}^{3+}/\text{Ni}^{2+}$ redox couple. The electrochemical behavior of MS-LNWO is quite reversible over 20 cycles, although there is a slight difference between the redox peak of the first oxidation sweep compared to those of the subsequent cycles. Finally, the film displays a reversible capacity of roughly 360 mA.h.cm^{-3} in its first cycle, which fades to 305 mA.h.cm^{-3} in cycle 20.

Next, the cycling curves for the LNWOX thin films are shown in Figure 3.22. The first thing to notice is that the electrochemical behavior is very similar from one spin-coated film to another, despite significant differences in composition. All the films display redox activity at high potentials, between 3.25 and 4.4 V vs Li^+/Li (LNWO23, LNWO55) or 3.0 and 4.4 V vs Li^+/Li (LNWO90). Based on the shape of the E_{we} vs capacity curves (Figure 3.22a,c,e) and the peaks in the dQ/dV curves (Figure 3.22b, d, f), most of the reversible capacity is likely due to

a single redox couple. For this reaction, all spin-coated thin films show a low polarization. There is also a significant irreversibility between charge and discharge, probably stemming from electrolyte decomposition. Similarly, the onset of an irreversible electrochemical reaction is visible below 2.5 V vs Li⁺/Li in discharge for the three compositions.

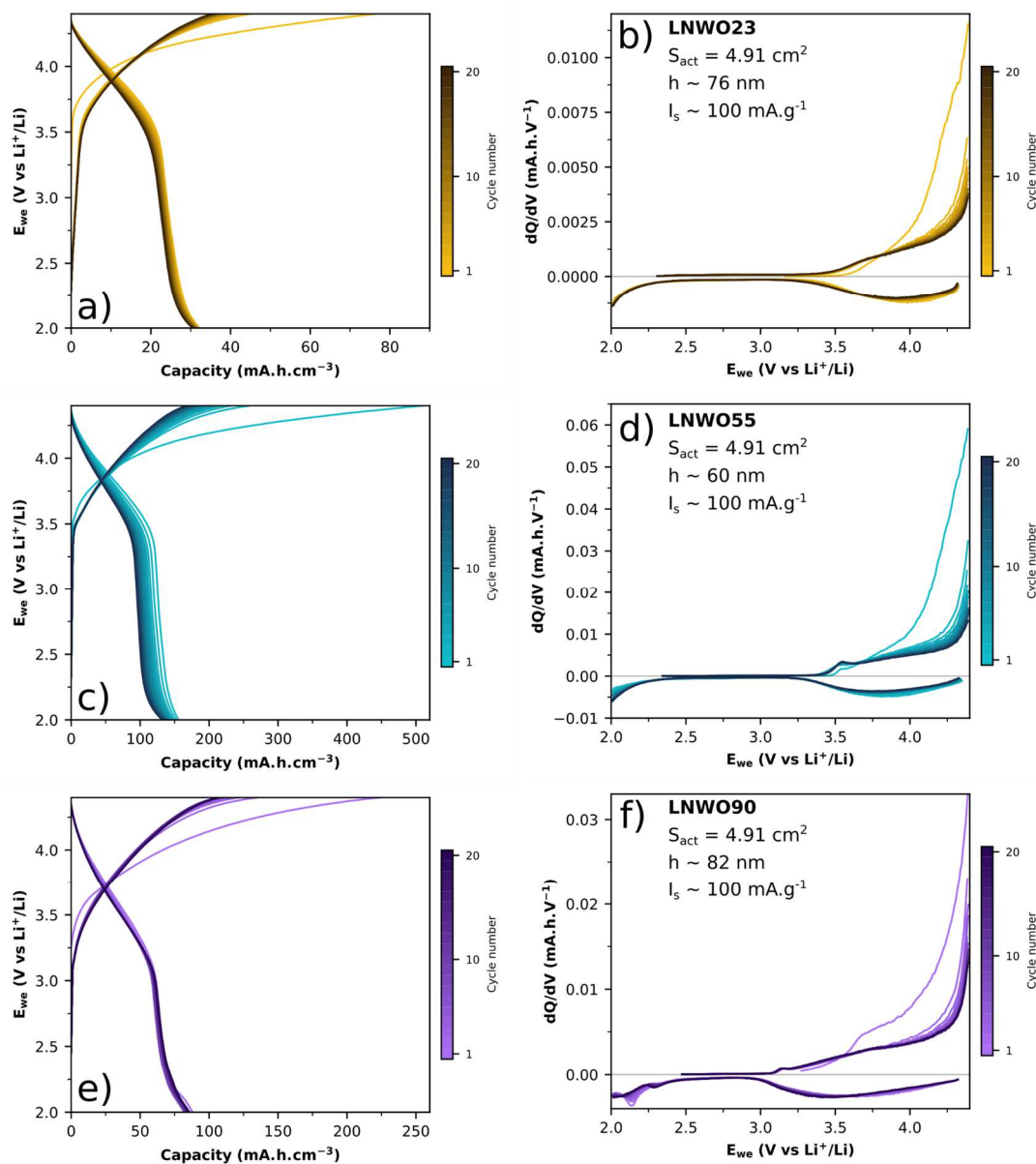


Figure 3.22 – E_{we} vs capacity curves (left) and dQ/dV curves (right) for LNWO23 (a, b), LNWO55 (c, d), and LNWO90 (e, f) spin-coated thin films. The films were cycled against Li metal using a 1 M LiClO₄ in PC electrolyte.

The strong similarity between the cycling behaviors of LNWOX thin films suggest that, regardless of composition, the same phase plays the role of active material in all samples. However, the capacity varies greatly with the composition: the discharge capacities in the first

cycle for LNWO23, LNWO55, and LNWO90 are of 32, 156, and 88 mA.h.cm⁻³, respectively. These variations suggest that the composition has an impact on the amount of active material.

Another interesting detail is the fact that, although the specific capacity is more than two times higher in MS-LNWO compared to LNWOX films, the cycling behavior for the high-potential reaction is very similar between the two types of samples (Figure 3.21). The deposition method has a great impact on the electrochromic performance, but the active species involved in spin-coated LNWOX and in magnetron sputtered MS-LNWO thin films might be the same. Thus, it becomes very important to try to pinpoint what phase is responsible for the high potential reaction. In order to figure this out, the electrochemical behaviors of two other spin-coated thin films are considered: a pure NiO_z thin film, and a Li₂Ni(WO₄)₂ thin film (Figure 3.23).

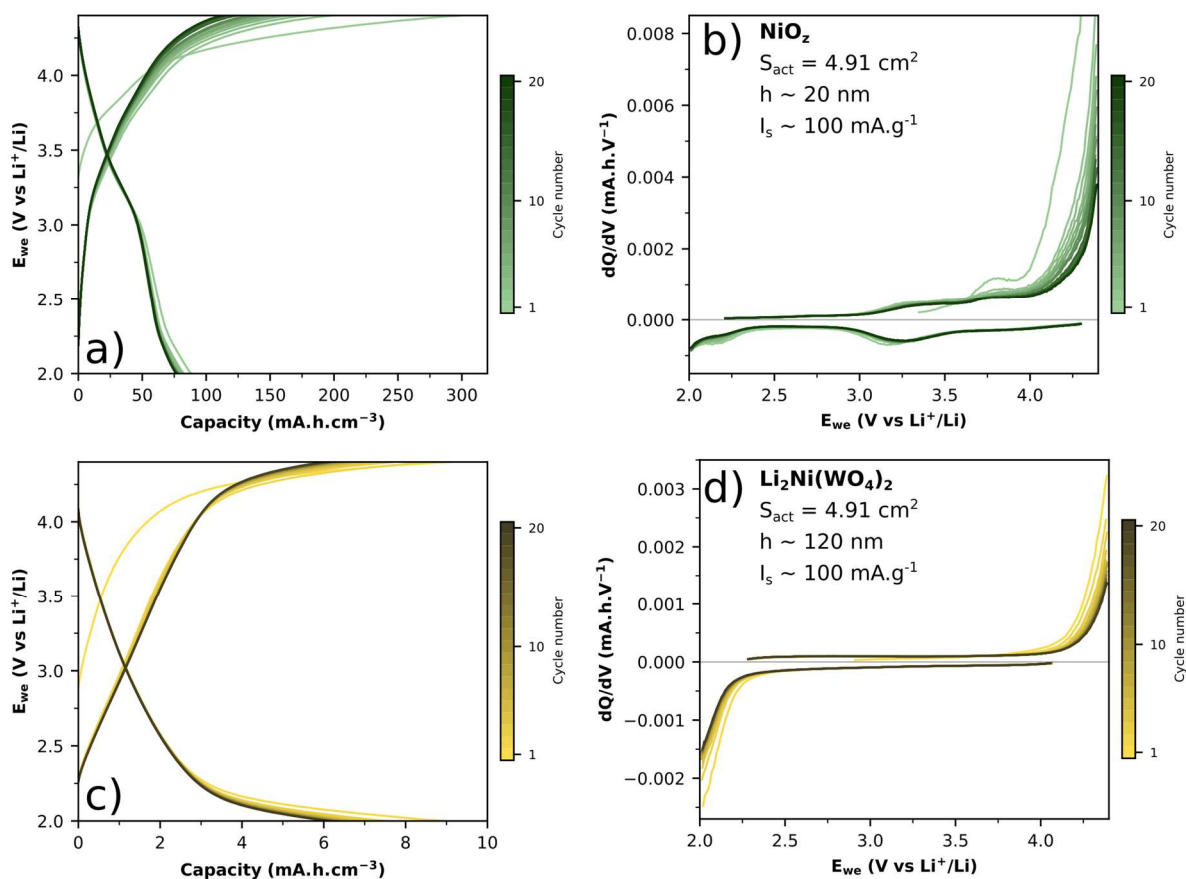


Figure 3.23 – E_{we} vs capacity curves (left) and dQ/dV curves (right) for NiO_z (a, b), and Li₂Ni(WO₄)₂ (c, d) spin-coated thin films. The films were cycled against Li metal using a 1 M LiClO₄ in PC electrolyte.

Looking at the cycling behavior for the NiO_z thin film, a reversible electrochemical activity is observed in the same potential range as for the MS-LNWO and LNWOX thin films (between 2.5 and 4.4 V vs Li^{+/Li}). The main difference is that this electrochemical activity is

characterized by two peaks in the dQ/dV curves (Figure 3.23b), rather than one. Parasitic reactions at high potentials in oxidation and low potentials in reduction are also occurring. On the other hand, the spin-coated $\text{Li}_2\text{Ni}(\text{WO}_4)_2$ thin film does not display the same redox activity as all the other films previously described (Figure 3.23c,d). In fact, its weak activity stems only from the parasitic reactions previously mentioned. Thus, the reversible electrochemical activity in MS-LNWO and LNWOX thin films likely comes from a NiO-like phase, which is apparently not present in the $\text{Li}_2\text{Ni}(\text{WO}_4)_2$ thin film.

XRD on $\text{Li}_x\text{Ni}_y\text{W}_z\text{O}_n$ powders synthesized from spin coating solutions

To further confirm that a NiO-like phase is responsible for the electrochemical activity of Li-Ni-W mixed oxide thin films, it is useful to go back to the study of powders. Indeed, as mentioned earlier in this chapter, the excess solution remaining after a spin coating process can be evaporated, calcined, and annealed in order to synthesize a $\text{Li}_x\text{Ni}_y\text{W}_z\text{O}_n$ powder with the same elemental composition as the spin-coated film (Figure 3.11). These powders can then very easily be characterized by powder XRD. Although bulk and thin film materials are evidently different systems, the phases crystallizing in a powder compound can give some insights into the phase composition of its thin film counterpart.

This powder synthesis process was performed on the coating solutions for the LNWO55, LNWO90, and $\text{Li}_2\text{Ni}(\text{WO}_4)_2$ thin films, using the heating program described in Figure 3.24.

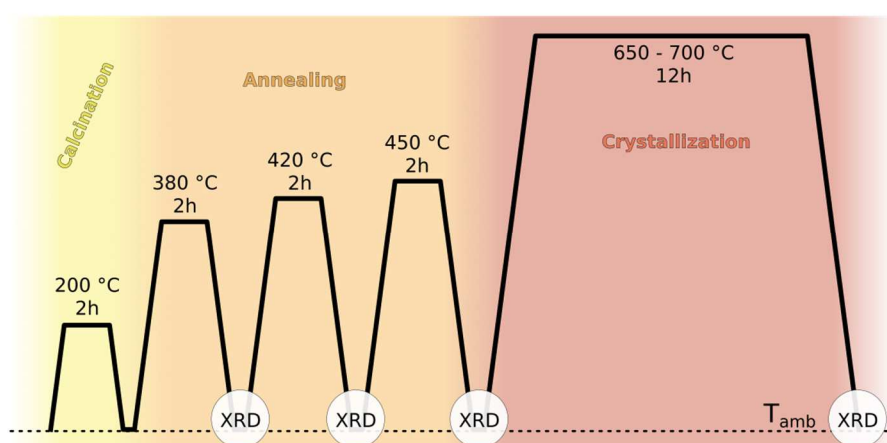


Figure 3.24 – Heating process for the XRD study of phases in $\text{Li}_x\text{Ni}_y\text{W}_z\text{O}_n$ powders synthesized from spin coating solutions.

The XRD patterns for the LNWO55 and LNWO90 powders in Figure 3.25 show that in the typical annealing temperature range used after spin coating (380 to 450 °C), cubic rocksalt NiO crystallizes. The width of the NiO peaks at these temperatures would even tend to indicate that the crystallites are nanosized; this can be confirmed by using Scherrer's equation^{375,376} (Equation 3.7):

$$s = \frac{K\lambda}{\beta\cos(\theta)} \quad 3.7$$

in which s is the crystallite size, K is a shape factor characterizing the crystallites' shape ($K \sim 0.9$ for spherical particles), λ is the wavelength of the X-rays used for the XRD measurement, β is the full width at half-maximum in radians of the peak of interest, and θ is the Bragg angle associated to the peak of interest. Applying this equation to the (111) and (200) peaks of NiO for LNWO55 annealed at 450 °C (Figure 3.25a) yields $s \sim 20$ nm. Applying it to the same peaks in the XRD pattern of LNWO90 annealed at 450 °C (Figure 3.25b) yields $s \sim 11$ nm.

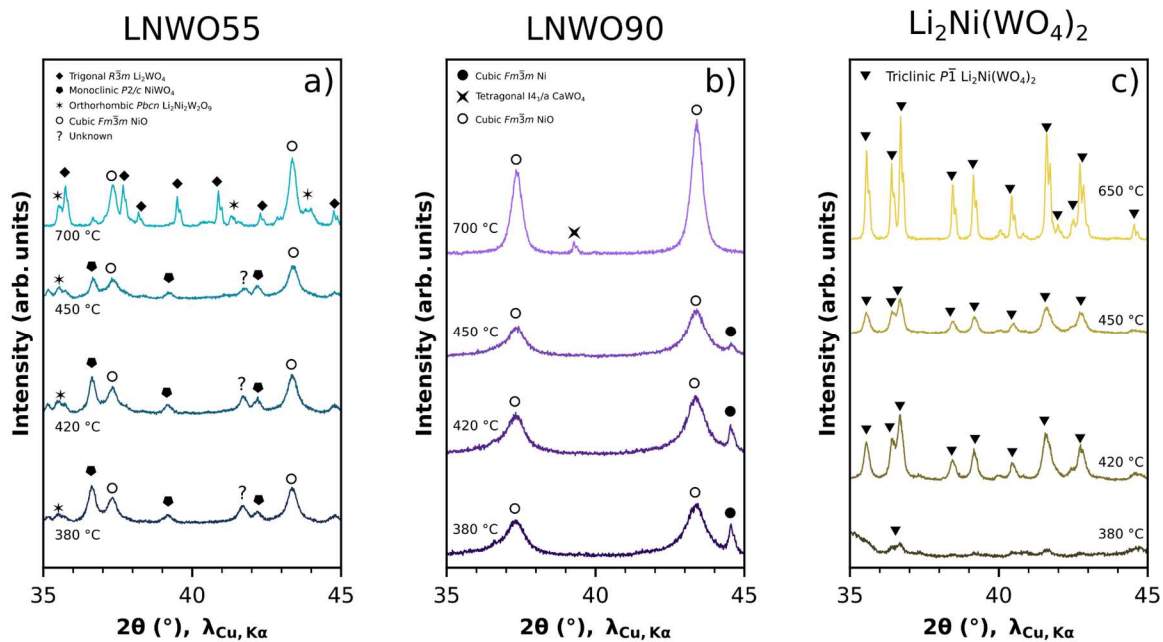


Figure 3.25 – XRD patterns between $2\theta = 35^\circ$ and $2\theta = 45^\circ$ for powders synthesized from spin coating solutions. (a) LNWO55 powder annealed at 380 °C, 420 °C, 450 °C, and 700 °C. (b) LNWO90 powder annealed at 380 °C, 420 °C, 450 °C, and 700 °C. (c) $Li_2Ni(WO_4)_2$ powder annealed at 380 °C, 420 °C, 450 °C, and 650 °C.

On the other hand, the XRD patterns for the powder obtained from the $Li_2Ni(WO_4)_2$ solution (Figure 3.25c) show that NiO never crystallizes, no matter the temperature. In fact, the

only phase that appears, for temperatures as low as 420 °C, is triclinic $\text{Li}_2\text{Ni}(\text{WO}_4)_2$, which is not electrochemically active at high potentials (see Chapter 3).

These results show that the spin coated thin films displaying electrochemical activity are also those whose elemental composition yields NiO nanocrystallites upon evaporation, calcination, and annealing of the coating solution. This further supports the idea that the electrochemically active phase in Li-Ni-W mixed oxide thin films is a NiO-like phase.

Electrochromic performances of the MS-LNWO and LNWOX thin films

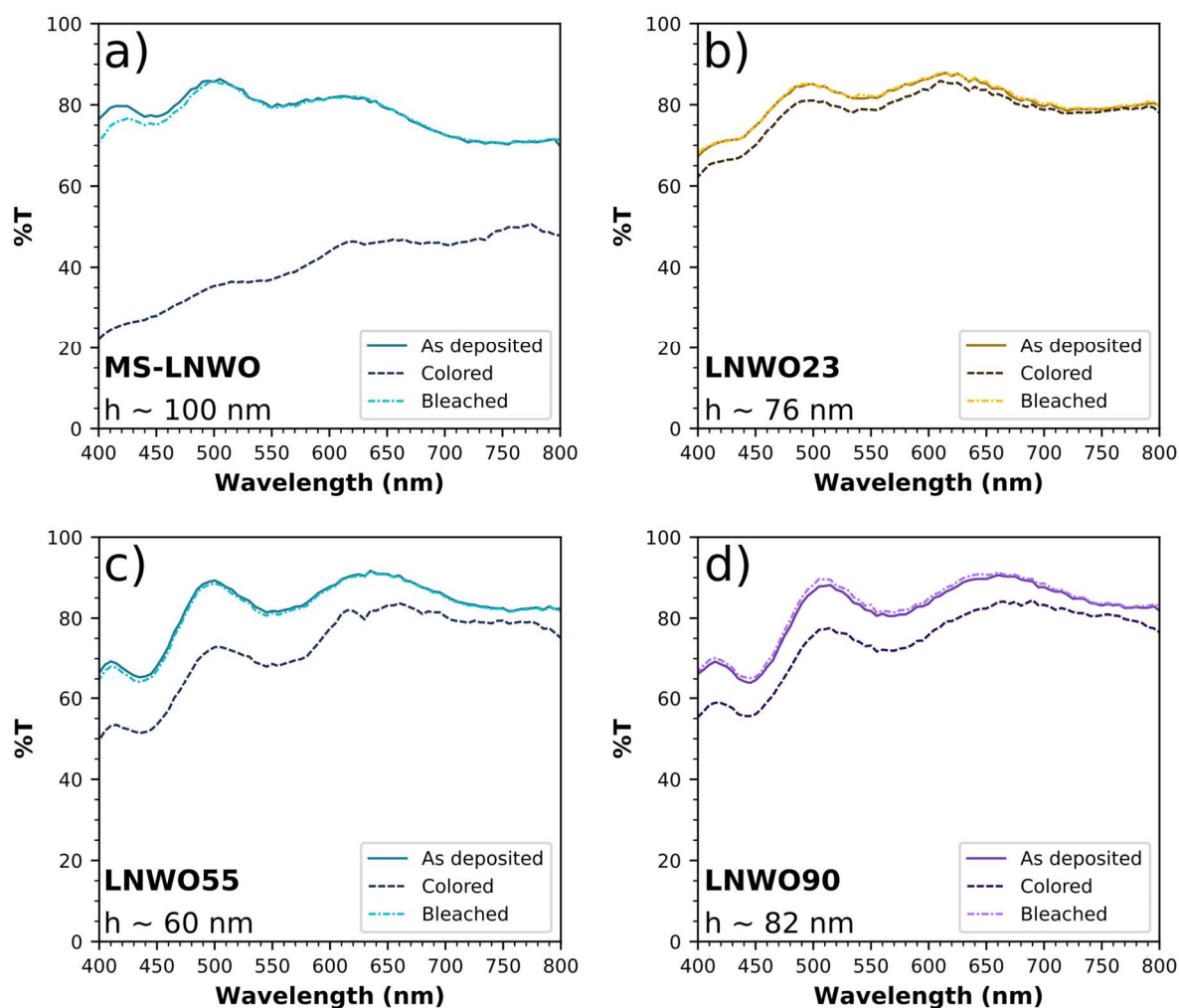


Figure 3.26 – Transmission spectra for as-deposited (solid line), colored (dashed line), and bleached (dashdotted line) Li-Ni-W mixed oxide thin films in their first charge-discharge cycle. (a) MS-LNWO. (b) Spin-coated LNWO23. (c) Spin-coated LNWO55. (d) Spin-coated LNWO90.

Figure 3.26 shows the evolution of the transmission spectra of the MS-LNWO and the spin-coated LNWOX thin films during the first cycle of their galvanostatic charge-discharge in the *operando* UV-Visible electrochemical cell. All four films presented display an anodic

electrochromic behavior: their transmission decrease upon oxidation (colored state) and increases back to its original state upon reduction (bleached state). However, it is obvious that the optical modulation for the magnetron sputtered thin film is much higher than for the spin-coated thin films (Table 3.4), even LNWO55 which is supposed to have a similar composition. Although part of this improved optical modulation can be explained by a slightly higher thickness, it is the superior reversible capacity of MS-LNWO that grants it good electrochromic performances (Figure 3.21). Similarly, when comparing the three spin-coated LNWOX films, LNWO55 has the highest optical modulation and LNWO23 the lowest optical modulation; this can again be correlated to the fact that the LNWO55 thin film has the highest reversible capacity of the spin-coated films, and LNWO23 the lowest reversible capacity (Figure 3.22).

Table 3.4 – Optical transmittance modulations at 450 nm, 550 nm, 630 nm and optical luminous transmittance modulation for MS-LNWO and the spin-coated LNWOX thin films. Standard error on the measurements is estimated to be ± 0.2 %.

Short name	ΔT_{450} (%)	ΔT_{550} (%)	ΔT_{630} (%)	ΔT_L (%)
MS-LNWO	47.0	42.7	36.2	42.4
LNWO23	4.4	3.3	2.4	3.3
LNWO55	13.5	12.5	10.4	12.3
LNWO90	9.5	10.1	9.2	10.1

When comparing the LNWOX thin films, it is interesting to observe that LNWO55 appears to be the optimal composition to get the best optical modulation. This likely comes from a compromise between two competing aspects: the number of electrochemically active sites and how easily ions can diffuse to these sites. Because it contains a relatively small fraction of nickel, the number of NiO_z sites in LNWO23 may be too low for it to display a good electrochemical capacity. On the other hand, in LNWO90, the amount of NiO_z sites in the material may be too high, to the point that it becomes too difficult for Li^+ to diffuse to certain parts of the film. Indeed, cubic rocksalt NiO_z is notoriously bad for the diffusion of ions^{46,377}. The stoichiometry of LNWO55, and by extension of MS-LNWO, probably leads to a sufficient number of electrochemically active NiO_z sites, and to enough amorphous matrix for Li^+ ions to diffuse to and from these sites^{243,244}.

The reversibility of the electrochromic behavior for the MS-LNWO and the LNWOX thin films over 20 cycles is shown in Figure 3.27.

There are some signs of irreversibility, such as a hysteresis in the b^* value of the light transmitted through MS-LNWO (b^*_T). Nonetheless, the electrochromic behavior of the four thin films is quite reversible. The general color variation is also the same for the four thin films: the light transmitted becomes less green and redder during oxidation (a^*_T increases), and it also becomes more yellow (b^*_T increases). During reduction, the opposite behavior is observed. However, as the transmittance modulation is higher for MS-LNWO, the contrast in color between its bleached state and its colored state is also much more significant compared to the LNWOX thin films (Figure 3.28).

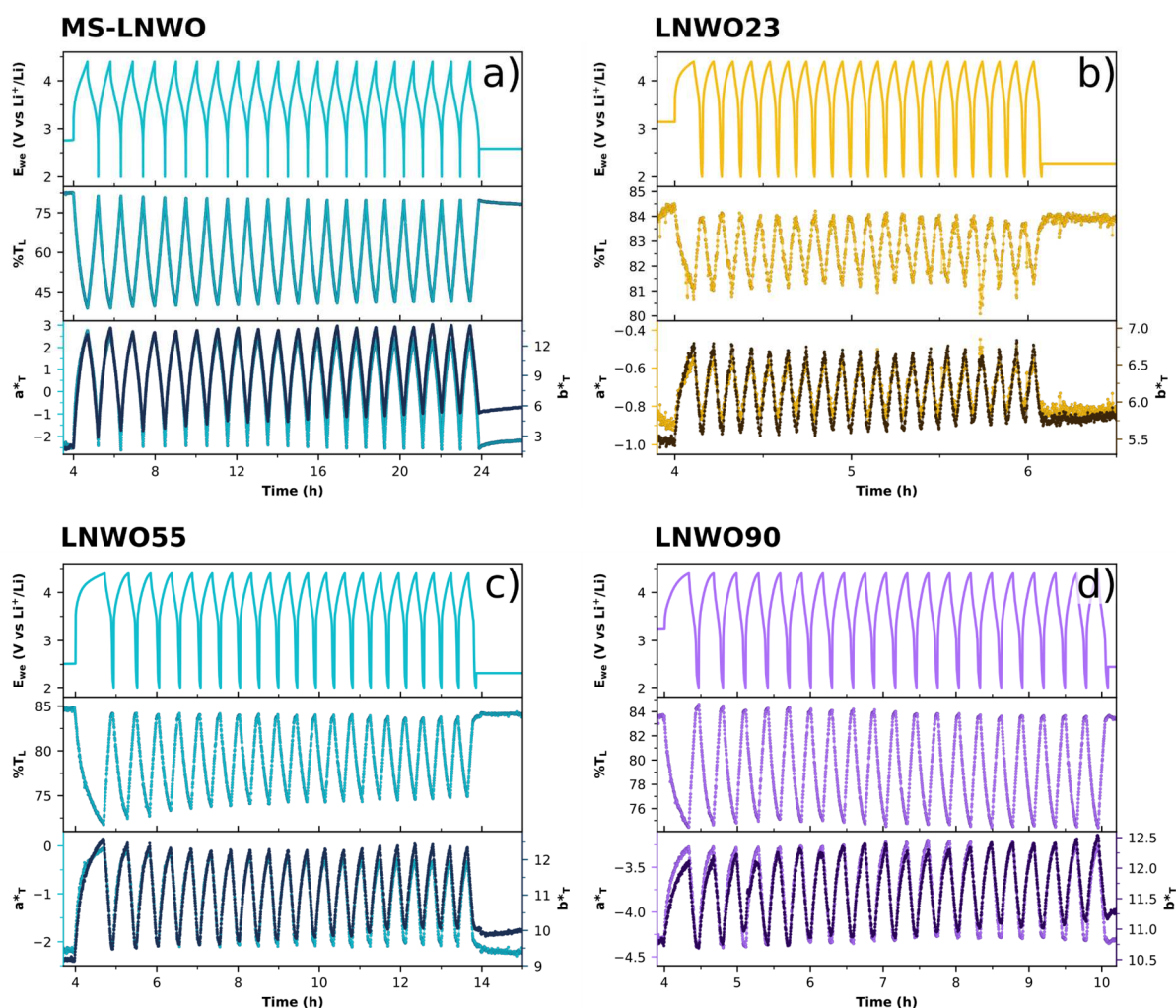


Figure 3.27 – Evolution of E_{we} , T_L , a^*_T , and b^*_T for (a) MS-LNWO, (b) LNWO23, (c) LNWO55, and (d) LNWO90 during 20 cycles of a galvanostatic charge-discharge experiment. The curve of b^*_T is plotted in a darker color in each graph.

Finally, the coloration efficiency values are rather close between MS-LNWO, LNWO23, LNWO55, LNWO90. This can be seen in Figure 3.29: the coloration efficiency for the four films remains between 17 and 24 $\text{cm}^2 \cdot \text{C}^{-1}$. Considering that it can reach much higher values in other electrochromic materials (174.3 $\text{cm}^2 \cdot \text{C}^{-1}$ at 600 nm for a PEDOT/halloysite

composite for example¹⁹⁰), the close proximity in coloration efficiency between the four films studied here suggest again that they follow the same electrochemical mechanism.

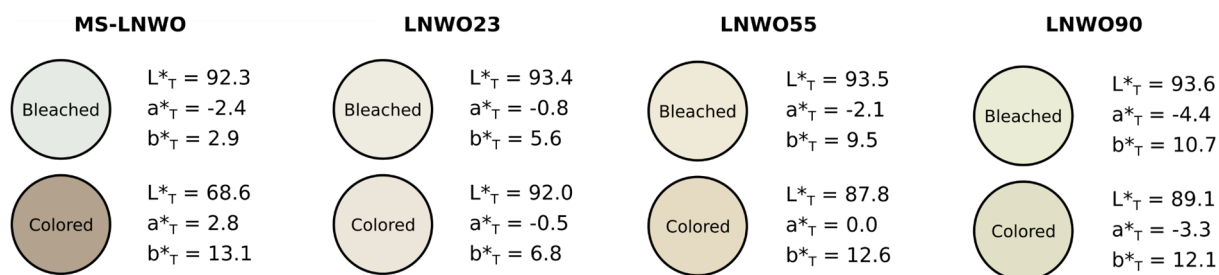


Figure 3.28 – Colors and CIELAB coordinates for the MS-LNWO and LNWOX thin films in their bleached and their colored states, in transmission. Data taken from the first charge-discharge cycle of the experiment shown in Figure 3.27.

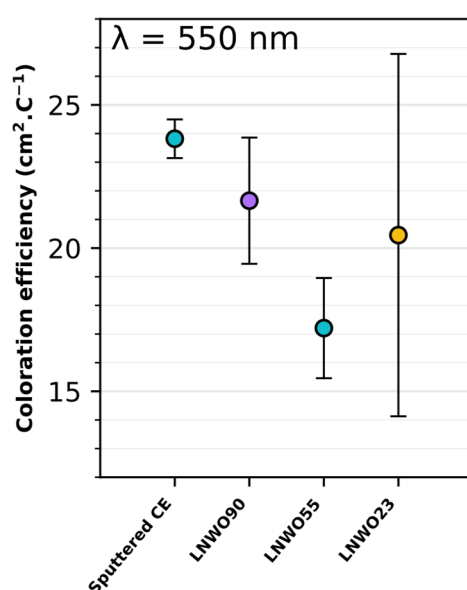


Figure 3.29 – Coloration efficiency of the MS-LNWO and LNWOX thin films at 550 nm. Values calculated from data collected during the first cycle of the galvanostatic charge-discharge experiments.

Electrochemical mechanism in Li-Ni-W mixed oxide thin films

Looking back at the electrochemical activity for the spin-coated NiO_z thin film (Figure 3.23a,b), it can be noticed that despite containing no lithium in its initial state, the material is active during the initial charge/delithiation. This suggest that the activity of the NiO_z thin film is not based on a Li⁺ (de)insertion process, but rather on an adsorption process, as it has been discussed in previous studies^{181,216–218,377}. This initial electrochemical activity could thus be due to the desorption of surface protons, initially adsorbed by contact with atmospheric water, and/or to the adsorption of anions from the electrolyte (ClO₄⁻).

It is more difficult to reach such a conclusion about the Li-Ni-W mixed oxide thin films. Indeed, as lithium is present in the pristine material, one could argue that the activity of these films during the initial charge (Figure 3.21) comes from Li^+ (de)insertion. In order to gain a little bit more insight into the electrochemical mechanism of these nanocomposite systems, a CV experiment was run using the *operando* UV-Visible cell. The CV response of the standard magnetron sputtered MS-LNWO thin film at different scan rates was studied, from 2 to 100 $\text{mV}\cdot\text{s}^{-1}$, between 2.0 and 4.4 V vs Li^+/Li . The resulting curves are shown in Figure 3.30.

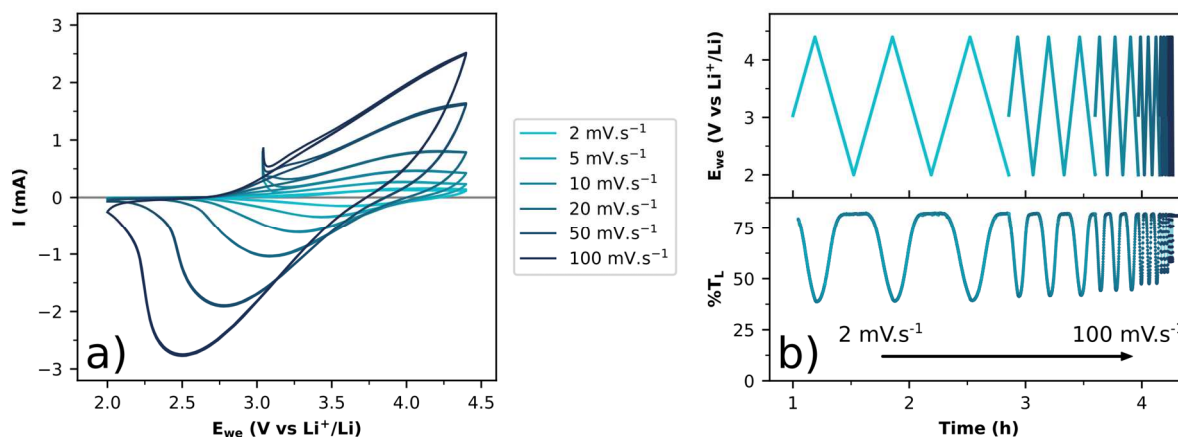


Figure 3.30 – (a) CV curves and (b) E_{we} vs time and T_L vs time curves for a MS-LNWO||1 M LiClO_4 :PC||Li electrochemical system, cycled at different scan rates (2 to 100 $\text{mV}\cdot\text{s}^{-1}$).

At every scan rate, the MS-LNWO thin film is characterized by a broad peak in oxidation and its counterpart in reduction, due to the activity of the $\text{Ni}^{3+}/\text{Ni}^{2+}$ couple. At 2 $\text{mV}\cdot\text{s}^{-1}$, the oxidation of the film occurs above 2.5 V and leads to a T_L of roughly 39 % in the colored state; the reduction brings the film back to its original optical state ($T_L \sim 83$ %) and ends around 2.7 V. As the scan rate increases, the oxidation peak shifts to higher potentials, and the reduction to lower potentials. In oxidation, the peak's apex shifts from 4.1 to more than 4.4 V when going from 2 $\text{mV}\cdot\text{s}^{-1}$ to 100 $\text{mV}\cdot\text{s}^{-1}$, whereas it shifts from 3.6 to 2.5 V in reduction. Moreover, the film does not become as dark in its colored state when increasing the scan rate; its bleached state luminous transmittance remains the same, however (Figure 3.30b).

These observations indicate that the electrochemical mechanism in MS-LNWO is kinetically limited, likely by mass transport. As the scan rates increase, ionic species such as Li^+ do not have enough time to diffuse out of the film and allow the redox of the $\text{Ni}^{3+}/\text{Ni}^{2+}$ couple, hence explaining the strong overpotentials and lower optical modulation at faster scan rates. This behavior is in direct opposition with what was reported by Da Rocha et al.³⁷⁷ and

Wen et al.¹⁸¹ for pure NiO_z thin films: they did not notice a strong increase in the overpotential or a decrease in the optical modulation with faster scan rates.

It is probable that the kinetic limitation in MS-LNWO thin films comes from the amorphous matrix. Although it allows the diffusion of Li⁺ to and from the NiO active sites and grants its electrochemical activity to the film, the Li⁺ diffusion coefficient of the matrix may be lower than that of the liquid electrolyte. Thus, although it is difficult to know whether or not Li⁺ is (de)inserted in the NiO nanocrystallites during the coloration/bleaching process, it is still, in a way, “deinserted” from the amorphous matrix of the film (Figure 3.31). As a consequence, and regardless of what is happening at the nanocrystallites, the overall behavior of the MS-LNWO thin film is more akin to that of an insertion material than to the capacitive response seen for pure NiO_z thin films.

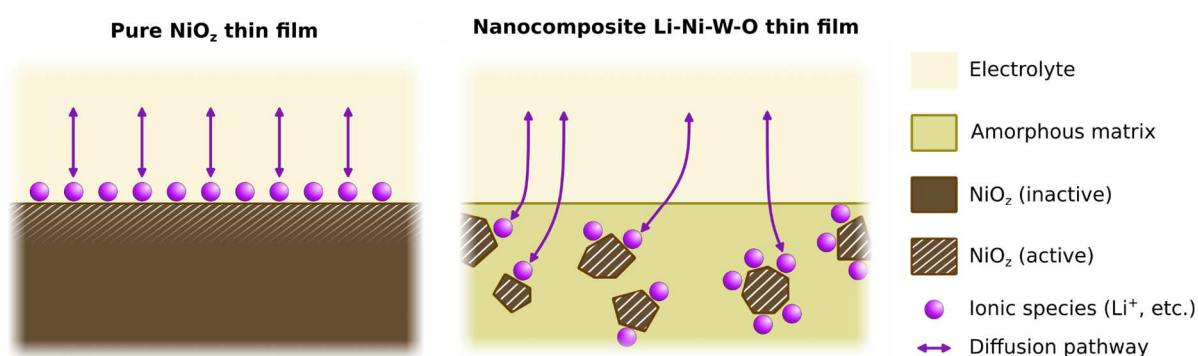


Figure 3.31 – Schematic representation of the diffusion pathways of ionic species (namely Li⁺) during electrochemical charge-discharge of a pure NiO_z thin film (left) and of nanocomposite Li-Ni-W-O thin film (right).

3.H. Perspectives on spin-coated Li_xNi_yW_zO_n thin films

The challenges of spin coating

The synthesis and the study of the LNWOX thin films were very useful to understand the nanocomposite MS-LNWO thin film. However, the electrochromic performances of these spin-coated thin films are lacking compared to their magnetron sputtered counterpart. This is clearly due to the major differences between the magnetron sputtering and the spin coating process. Is it possible to decrease the gap between these two techniques and, at the same time, to decrease the performance gap between the films they yield?

A significant difference between the two methods is the control of the oxidation state of nickel. During the magnetron sputtering process, an Ar/O₂ gas mix is used to realize the reactive deposition of the initial Ni-W-O layer (see Chapter 1). By modifying the fraction of

O₂ in the mix, one can control the oxidation state of nickel^{378,379}, from Ni²⁺ to Ni³⁺. Following the deposition of this first layer, the addition of a layer of Li⁰ on top and/or the subsequent thermal treatment reduces the Ni³⁺ sites to Ni²⁺; this is supported by the almost identical optical properties of MS-LNWO between its as-deposited and fully reduced bleached states (Figure 3.26a). It is likely that the electrochemically active sites in the film correspond to the Ni³⁺ sites formed during the reactive sputtering of the initial Ni-W-O layer.

Thus, a good control of the number of Ni³⁺ sites may be essential to obtain good electrochromic performances, and in particular, good optical contrast in Li-Ni-W-O nanocomposite thin films. However, the oxidation state of nickel cannot be controlled so easily during the spin coating process. Indeed, there does not seem to exist commercial Ni(III) precursors for the coating solutions. It may be possible to introduce Ni³⁺ sites in a spin-coated film by performing the heat treatment of the film in an oxidative atmosphere (i.e. O₂), but literature on this specific aspect seems to be scarce.

This facilitated control of the oxidation state of nickel is another reason in favor of magnetron sputtering when it comes to the preparation of commercial ECDs.

High-crystallinity Li₂Ni₂W₂O₉ thin films

As mentioned in Chapter 2, to properly quantify the electrochromic performances of Li₂Ni₂W₂O₉, it must first be obtained as a thin film. This endeavor comes with its own set of challenges.

As explained at the beginning of Chapter 2, Li₂Ni₂W₂O₉ fully crystallizes at high temperatures (~ 700 °C). This means that Li₂Ni₂W₂O₉ thin films can only be prepared on substrates that do not degrade at these temperatures. For example, the ITO/Glass substrates used for the LNWOX thin films is not a suitable candidate, as the glass transition temperature (the transition temperature above which a glass becomes viscous) ranges from 500 to 700 °C for standard soda-lime silicate glasses^{380–382}.

To avoid this issue, spin-coated Li₂Ni₂W₂O₉ thin films were prepared on fused silica substrates (SiO₂); this substrate material possesses a higher glass transition temperature (~ 1200 °C) and can withstand the crystallization temperature of Li₂Ni₂W₂O₉. However, optical reflection microscopy and SEM images (Figure 3.32) of Li₂Ni₂W₂O₉/SiO₂ samples show that coatings prepared in these conditions are not continuous. Instead, there is a severe dewetting of the film, leading to the formation of isolated particles on the surface of the SiO₂

substrate. Since the film takes the form of a dispersion of small particles, it scatters light and is hazy at the macroscopic scale, which is detrimental to the characterization of the optical properties of the material. The same observations can be made for a $\text{Li}_2\text{Ni}_2\text{W}_2\text{O}_9$ film spin-coated on an ITO/ SiO_2 substrate.

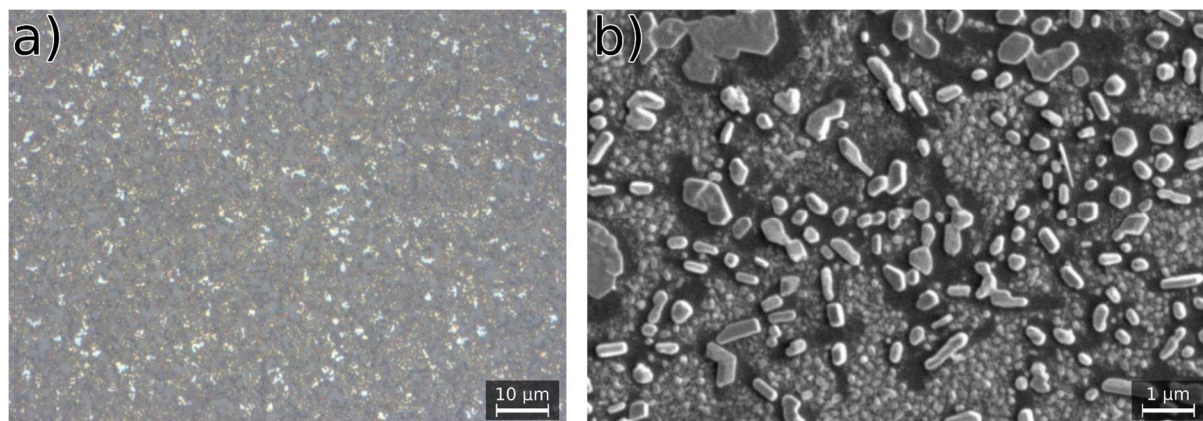


Figure 3.32 – Top-view (a) optical reflection microscopy and (b) SEM images of the surface of a $\text{Li}_2\text{Ni}_2\text{W}_2\text{O}_9$ thin film prepared by spin coating on a fused SiO_2 substrate. Prepared from a solution with $[\text{Li}^+] = [\text{Ni}^{2+}] = [\text{W}^{6+}] = 0.1 \text{ M}$, with C.A./ $\text{M}^z = 2:1$. Only one coating, annealed at $700 \text{ }^\circ\text{C}$ for 30 minutes.

Formation of high-crystallinity oxide thin films by spin coating is not heavily reported in the literature³⁸³, so the origin of this dewetting phenomenon in $\text{Li}_2\text{Ni}_2\text{W}_2\text{O}_9$ remains uncertain. It may be that the removal of the organic component of the film by combustion and the significant densification of the material due to the heat treatment lead to a non-uniform spread of the Li, Ni, W, O atoms on the surface of the substrate. In that case, it may be required to play with the solvent, the amount of citric acid, or the use of other additives in the coating solution, in order for the densification of the film to be less severe. There are many parameters left to be played with in the spin coating process. They would warrant a deeper study of the process developed in this chapter.

It may also be interesting to play with the nature of the substrate in order to try to form the crystallized $\text{Li}_2\text{Ni}_2\text{W}_2\text{O}_9$. For example, in the case of blue light-emitting diodes (LEDs) based on crystallized gallium nitride (GaN) thin films, Nakamura et al.^{384,385} first had to conceive an “amorphous” GaN buffer layer in order to obtain continuous, crystallized GaN thin films. The buffer layer is meant to accommodate the crystal structure of the high-crystallinity layer; maybe a similar approach could be used in the case of $\text{Li}_2\text{Ni}_2\text{W}_2\text{O}_9$. However, in the case of Nakamura, a chemical vapor deposition method was used, which allowed to control the temperature of the substrate during the coating of the GaN layers. This permitted the successive deposition of the buffer layer and the crystallized GaN layer. To adapt

this to the spin coating process described in this manuscript, one would need to perform two spin coating steps and two heat treatments at different temperatures. This raise the question: is it possible to obtain crystallized $\text{Li}_2\text{Ni}_2\text{W}_2\text{O}_9$ thin films using spin coating, or is another deposition method (magnetron sputtering, chemical vapor deposition, etc.) required? In any case, the formation of high-crystallinity $\text{Li}_2\text{Ni}_2\text{W}_2\text{O}_9$ thin films and the quantification of their electrochromic performances are challenges waiting to be tackled.

Absorbance spectra of $\text{Li}_x\text{Ni}_y\text{W}_z\text{O}_n$ systems

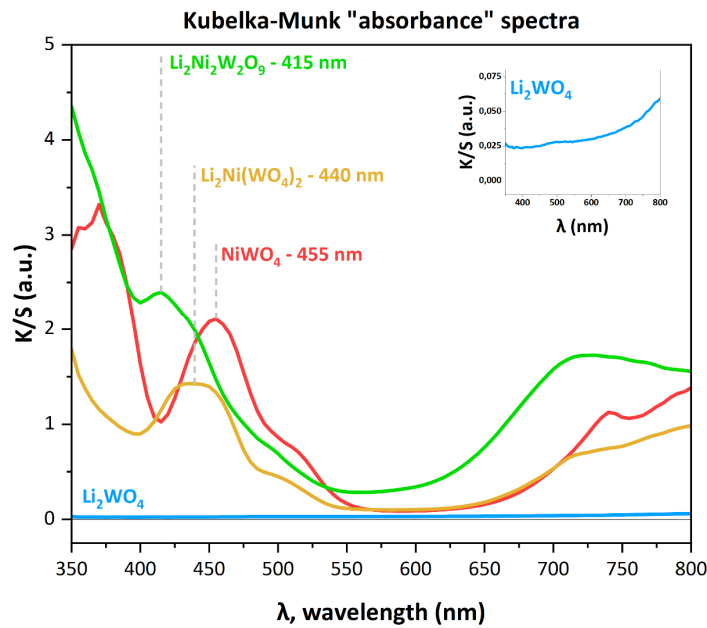


Figure 3.33 – Shape of the absorbance spectra of $\text{Li}_x\text{Ni}_y\text{W}_z\text{O}_n$ powders, obtained using the Kubelka-Munk equations^{386–388}. Orthorhombic $\text{Li}_2\text{Ni}_2\text{W}_2\text{O}_9$ (green), triclinic $\text{Li}_2\text{Ni}(\text{WO}_4)_2$ (orange), monoclinic NiWO_4 (455 nm), trigonal Li_2WO_4 (blue).

Using the Kubelka-Munk equations^{386–388} (Equation 3.8) and UV-Visible reflection measurements on thick powder layers, it is possible to obtain the shape of the absorbance spectra for compounds in powder form.

$$\frac{K}{S} = \frac{(1 - R_\infty^2)}{2R_\infty} \sim kA \quad 3.8$$

In Equation 3.8, K and S are the linear absorption and scattering coefficients of the powder sample, R_∞ is the reflection of the sample, A is the absorbance of the material, and k is a proportion coefficient. The Kubelka-Munk equations rely on the hypotheses that the layer of powder used for the reflection measurements is thick enough to have a null transmission, and that the scattering coefficient, S , is independent of the wavelength.

These equations were applied to reflection measurements performed on powder layers made from the four reference compounds described at the beginning of the chapter (Figure 3.33).

The Kubelka-Munk model is useful, because it allows the determination of the shape of the absorbance spectra (and thus, the color) of materials without knowing their refractive index. Such is not the case for thin film systems, which usually require ellipsometry measurements and UV-Visible reflection/transmission spectroscopy in order to perform calculations leading back to their absorbance. An interesting idea, which could not come to fruition during this project, was to use the absorbance spectra of the reference powders shown in Figure 3.33 as “optical fingerprints” in order to identify the origin of the color of $\text{Li}_x\text{Ni}_y\text{W}_z\text{O}_n$ thin films. By collecting optical data on the thin films (ellipsometry, UV-Visible spectroscopy, etc.) and knowing their thickness, it is possible to determine their refractive index and simulate their absorption spectra. Then, a comparison of the absorption spectra of the thin films with those of crystalline powders could deliver some insights into the phases present in the films, and their effect on the films' color.

3.I. Conclusions of the chapter

In this chapter, the electrochemical activity of several $\text{Li}_x\text{Ni}_y\text{W}_z\text{O}_n$ powders was studied using galvanostatic charge-discharge experiments. Three phases were considered, on top of the $\text{Li}_2\text{Ni}_2\text{W}_2\text{O}_9$ compound described in Chapter 2: trigonal Li_2WO_4 , monoclinic NiWO_4 , and triclinic $\text{Li}_2\text{Ni}(\text{WO}_4)_2$. In general, the nickel-containing species go through a partial conversion reaction when cycled at low potentials, down to 1.0 V vs Li^+/Li ; and at higher potentials, up to 4.5 V vs Li^+/Li , none of the crystalline phases considered are electrochemically active. These experiments, and the literature on the low-potential redox of Li-Ni-W mixed oxides, introduce the idea that the $\text{Ni}^{2+}/\text{Ni}^0$ redox couple might also be responsible for the secondary reactions happening in the magnetron sputtered Li-Ni-W-O thin film.

To confirm this idea, a series of XPS experiments were performed on Li-Ni-W-O thin film samples. A comparison of the XPS spectra of a pristine Li-Ni-W-O thin film and of the four $\text{Li}_x\text{Ni}_y\text{W}_z\text{O}_n$ powders proves that the thin film contains W^{6+} , and a mix of Ni^{2+} and Ni^{3+} , with some weak electronic transfer between the two elements. Then, the evolution of the XPS spectrum of the Li-Ni-W-O thin film with its state of charge shows that the $\text{Ni}^{2+}/\text{Ni}^0$ redox couple is indeed involved in the secondary reaction. Meanwhile the tungsten centers maintain

their 6+-valence state on the entire 1.0-4.5 V vs Li⁺/Li potential range, and solely play a structural role in the film.

Unfortunately, neither the electrochemical study of the Li_xNi_yW_zO_n powders, nor the XPS study of the Li-Ni-W-O thin film samples grant much insight into the main reaction occurring at high potentials. It seems clear that the Ni³⁺/Ni²⁺ redox couple is involved, and the XPS results suggest that the film remains structurally unaffected by the main reaction at high potentials. To push this study further, the electrochemical behavior of the standard nanocomposite Li-Ni-W-O thin film was compared to other thin films with various compositions in the Li₂O-NiO-WO₃ ternary phase diagram.

To prepare these thin films, a spin coating/annealing method was elaborated, based on the use of LiNO₃, Ni(NO₃)₂·6H₂O, WCl₆, and citric acid precursors in an ethanolic solution. The optimization of the solution and of the spin coating parameters led to continuous thin films of good quality. Yet, some questions remain, mostly in regards to the reactions occurring in the spin coating solution after the addition of the WCl₆ precursor. It is clear that the stability of the solution relies on the simultaneous presence of citric acid and nitrate species in the medium when the WCl₆ is added, but further experiments are required to understand what keeps precipitates from forming immediately.

The electrochemical behaviors of the spin-coated LNWOX thin films are very similar among themselves, but also quite similar to that of the standard magnetron sputtered MS-LNWO thin film. This was made clearer by looking at the behavior of spin-coated NiO and Li₂Ni(WO₄)₂ thin films, but also at the phases formed in powders obtained from the LNWOX spin coating solutions. The MS-LNWO and LNWOX thin films are electrochemically active on the same potential range as the NiO thin films. Meanwhile, the Li₂Ni(WO₄)₂ thin film, the only one to not display a strong electrochemical response, is also the only sample whose spin coating solution does not yield cubic rocksalt NiO after a calcination/annealing process. Thus, the presence of NiO particles is required for a Li-Ni-W-O thin film to display electrochemical activity at high potentials. To further confirm this trend, it might be interesting to look at the electrochemical behavior of other compositions with high amounts of W ($x_{\text{WO}_3} > 50$ mol%).

When comparing the electrochromic responses of the spin-coated LNWOX thin films, collected thanks to an *operando* UV-Visible electrochemical cell, it seems that there is an optimal composition in terms of optical modulation, LNWO55. This composition might be a good compromise between a high amount of active NiO sites, and a sufficient amount of

amorphous matrix for ionic species to diffuse to these active sites. TEM experiments showing the nanostructure of the thin films could support this hypothesis, and looking at more compositions along the NiO/MS-LNWO straight line of the ternary phase diagram may further confirm the trends observed here.

Finally, the electrochemical behavior of the MS-LNWO thin film at high potentials, when cycled at various scan rates in a CV experiment, is similar to that of an insertion material, and not to the pseudocapacitive behavior previously reported for pure NiO_z thin films. This might come from the fact that Li⁺ has to be “deinserted” from the amorphous matrix to oxidize the electrochemically active NiO nanocrystallites, which introduces kinetic limitations related to mass transport. All in all, a lot of work remains to be done in order to fully understand the electrochemical mechanism of nanocomposites Li-Ni-W-O thin films, and especially what is happening at the NiO nanocrystallites.

Conclusions and perspectives

The endeavor undertaken throughout this PhD project was the exploration and the study of materials in the $\text{Li}_2\text{O-NiO-WO}_3$ ternary phase diagram, in order to get a better understanding of the electrochromic properties observed in lithium-nickel-tungsten mixed oxide thin films. In particular, the goal was to uncover the relationships between the composition, the structure, and the electrochromism of magnetron sputtered, nanocomposite Li-Ni-W-O thin films, comprised of an amorphous matrix surrounding NiO-like nanocrystallites.

This initiative started with the solid-state synthesis of $\text{Li}_x\text{Ni}_y\text{W}_z\text{O}_n$ powders, which led to the fortuitous discovery of orthorhombic *Pbcn* $\text{Li}_2\text{Ni}_2\text{W}_2\text{O}_9$. The crystal structure of this new material was solved, and found to match with a ramsayite structure previously described for other mixed oxides. To take it a step further, and because the lamellar structure of the phase was reminiscent of the layered structure of other cathode materials used in Li-ion batteries, the electrochemical properties of $\text{Li}_2\text{Ni}_2\text{W}_2\text{O}_9$ were studied. Conventional galvanostatic charge-discharge experiments were performed, showing the reversible redox of the $\text{Ni}^{3+}/\text{Ni}^{2+}$ couple above 4.5 V vs Li^+/Li . Although the capacities displayed by $\text{Li}_2\text{Ni}_2\text{W}_2\text{O}_9$ are far too low to compete with regular Li-ion battery cathodes, its reversible behavior and the activity of nickel prompted the investigation of its electrochromic properties, using an *operando* optical microscopy setup. This experiment confirmed that $\text{Li}_2\text{Ni}_2\text{W}_2\text{O}_9$ is an anodic electrochromic material, and an in-depth image treatment highlighted the impact of particle size on the reversibility of Li^+ (de)insertion in a $\text{Li}_2\text{Ni}_2\text{W}_2\text{O}_9$ electrode.

The study of this new phase brings forth several fascinating prospects. From a materials synthesis standpoint, although the pseudocorundum structure of $\text{Li}_2\text{Ni}_2\text{W}_2\text{O}_9$ has been observed in other inorganic compounds before, the fact that it is a quaternary oxide calls for the search of other isostructural materials. One can wonder what the partial or total substitution of one of the three cations in $\text{Li}_2\text{Ni}_2\text{W}_2\text{O}_9$ would yield. A first path to follow would be the substitution of nickel by other 3d transition metals, namely cobalt or iron. It could be interesting to see how the substitution of nickel by one of these elements affects the crystal structure of the material. For example, $\text{Li}_2\text{Zn}_2\text{W}_2\text{O}_9$ crystallizes in the $P\bar{3}c1$ space group³⁸⁹, and $\text{Li}_2\text{Mg}_2\text{W}_2\text{O}_9$ displays strong cationic mixing between the Mg and Li sites²⁶⁴. As for the field of electrochromics, the discovery of a quaternary electrochromic oxide opens new possibilities. Indeed, most inorganic electrochromic oxides that have been uncovered and studied so far are binary oxides, or doped/substituted materials derived from binary oxides. This has obviously restricted the field to a few efficient transition metal oxides. The fact that $\text{Li}_2\text{Ni}_2\text{W}_2\text{O}_9$ displays electrochromic properties suggest that there are more electrochromic oxides to unveil. Whether

these hypothetical materials display good electrochromic *performances* and are able to compete with WO_3 , NiO_z , and IrO_z is another question. In the case of $\text{Li}_2\text{Ni}_2\text{W}_2\text{O}_9$, answering that question requires preparing the material as a thin film, a process that will likely come with its own set of challenges, since the crystal structure of the material, only formed at high temperatures ($> 700\text{ }^\circ\text{C}$) seems essential to its electrochemical properties. Finally, the *operando* optical microscopy setup used in the study of $\text{Li}_2\text{Ni}_2\text{W}_2\text{O}_9$ also offers interesting ideas that could be applied to the investigation of cathode materials in batteries. Indeed, *operando* optical microscopy has not been used often in the field of battery materials. Moreover, the few reports made on the use of this technique are often limited to the scale of a single particle^{284,286}. Although this approach delivers significant insights into the electrochemical mechanisms of cathode material, looking at an area comprising several hundred particles allows for a statistical data treatment, which highlighted interesting trends in the case of $\text{Li}_2\text{Ni}_2\text{W}_2\text{O}_9$. Applying this statistical method to other cathode materials could maybe shed light on the general effects of particle size and particle morphology on electrochemical performance in batteries.

On top of its electrochromic properties, the magnetic properties and magnetic structure of $\text{Li}_2\text{Ni}_2\text{W}_2\text{O}_9$ were characterized and solved. The material displays strong ferromagnetic interactions in an antiferromagnetic lattice, both introduced by paramagnetic $3d^8$ nickel cations. Furthermore, the point symmetry of the magnetic structure in $\text{Li}_2\text{Ni}_2\text{W}_2\text{O}_9$ allows the occurrence of a linear magnetoelectric effect, which will need to be properly characterized in the future. In the same way that it brings a fresh outlook on the study of inorganic electrochromic oxides, the discovery of $\text{Li}_2\text{Ni}_2\text{W}_2\text{O}_9$ may shake up the research on “429” magnetic compounds ($M_4A_2O_9$; $M = \text{Fe, Co, Mn, Ni, etc.}$; $A = \text{Ta, Nb}$), which also possess a corundum-like or pseudocorundum crystal structure.

Once the study of $\text{Li}_2\text{Ni}_2\text{W}_2\text{O}_9$ was completed, the electrochemical behaviors and XPS spectra of this powder compound and of three others ($R\bar{3}$ Li_2WO_4 , $P2/c$ NiWO_4 , $P\bar{1}$ $\text{Li}_2\text{Ni}(\text{WO}_4)_2$) were compared to the data collected for the magnetron sputtered, nanocomposite Li-Ni-W-O thin film. From the comparison, it appears that the main reaction seen at high potentials in the thin film (2.0 V to 4.4 V vs Li^+/Li) does not manifest in any of the powder compounds. This reaction can only occur in the film, but based on the XPS results, it is not related to any strong changes in local structure in the material. At low potentials, however (1.0 V to 3.0 V vs Li^+/Li), the secondary reactions observed in the film and in all the nickel-containing powders could be associated to conversion reactions leading to the formation of Ni^0 . In the case of the thin film, the secondary reaction probably involves both the amorphous matrix

and the NiO-like nanocrystallites. The *post-mortem* XPS results on thin film samples cycled at different states of charge also proved that Ni is the only electrochemically active element in the Li-Ni-W-O thin films, between 1.0 and 4.5 V vs Li⁺/Li. W solely plays a structural role in the material.

To complete this study based on a comparison with Li_xNi_yW_zO_n powders, a spin coating process was developed to prepare Li_xNi_yW_zO_n thin films, which can be compared more easily to the magnetron sputtered Li-Ni-W-O thin film. Several compositions were tested, and the spin-coated films were characterized using an *operando* UV-Visible electrochemical setup. The results show that the presence of NiO nanocrystallites is required for the main reaction at high potentials to occur in Li_xNi_yW_zO_n thin films. This indicates that, for this high-potential reaction, the nanocrystalline NiO-like particles are the electrochemically active phase in the magnetron sputtered Li-Ni-W-O thin film. Moreover, by comparing the electrochromic performances of spin-coated films with different compositions, it appears clearly that a balance has to be found between having too few and too many NiO-like active sites in a nanocomposite thin film. This balance can be reached by playing with a film's elemental composition. This also suggest that the amorphous matrix plays an important role, as it may allow Li⁺ cations to diffuse inside and out of the thin film, to and fro the NiO-like nanoparticles. In fact, the electrochemical behavior of the magnetron sputtered nanocomposite Li-Ni-W-O is reminiscent of an insertion material, while several pure NiO_z thin film described in the literature display a pseudocapacitive behavior.

A characterization that is unfortunately missing in this study is the TEM imaging of the spin-coated Li_xNi_yW_zO_n thin films. Indeed, it has been assumed that the spin-coated films were nanocomposites, just like the magnetron sputtered Li-Ni-W-O thin film; TEM images, showing the nanostructure of the films, would be a direct proof of this hypothesis. Moreover, it would be interesting to support the trends observed for the spin-coated thin films, by studying more compositions in the appropriate areas of the ternary phase diagram.

The spin-coating process describes in this manuscript works well, although the reactions involved in the preparation of the coating solution remain uncertain, and might make for an interesting subject of research. Nonetheless, there are still strong differences between the films prepared by spin-coating and the magnetron sputtered Li-Ni-W-O thin film. These are made obvious by the differences in electrochromic performances between the spin-coated and magnetron sputtered systems. Ideally, to reach more reliable conclusions, the exploration of the Li₂O-NiO-WO₃ ternary phase diagram should be performed using samples prepared with

the same magnetron sputtering process as the standard Li-Ni-W-O thin film. This way, the only variation in the synthesis conditions would be the composition of the samples, and the comparison with the standard material would be more robust. It would also be interesting to prepare a thin film made of the amorphous matrix, devoid of any NiO-like nanocrystallite. Such a sample would allow direct measurements of the ionic conductivity and diffusion properties of the amorphous matrix, and confirm its role in the nanocomposite Li-Ni-W-O thin film.

Overall, although there is still a lot to be done to fully grasp the relationships between composition, structure, and electrochromism in the nanocomposite magnetron sputtered thin films, the work presented in this manuscript represents a good starting point to develop the research on nanocomposite Li-Ni-W-O electrochromic systems

Abbreviations and symbols

ΔT : Transmission modulation

η : Coloration efficiency

θ_{CW} : Curie-Weiss temperature

χ : Magnetic susceptibility

χ_0 : Temperature-independent contribution to the molar magnetic susceptibility

χ_m : Molar magnetic susceptibility

3D: Three-dimensional

a, b, c: Lattice vectors of a direct lattice

a*, b*, c*: Lattice vectors of a reciprocal lattice

L^* , a^* , b^* : Coordinates in the CIELAB color space

B_{iso} : Debye-Waller factor

BVS: Band valence sum

C: Curie constant

CA: Citric acid monohydrate

C.A./ M^z : Molar ratio of citric acid monohydrate to cations in solution

CEI: Cathode-electrolyte interphase

Chem.: Chemical

CV: Cyclic voltammetry

DC: Direct current

DMC: Dimethyl carbonate

dDPC-STEM: Differentiated differential phase contrast scanning transmission electron microscopy

E_F : Fermi level

E_g : Bandgap

E_{we} : Potential of the working electrode

EC: Ethylene carbonate

ECD: Electrochromic device

EDX: Energy dispersive X-ray spectroscopy

EtOH: Ethanol

eq.: Equivalents

EXAFS: Extended X-ray absorption fine structure

FC: Field-cooled

h: Thickness

HAADF-STEM: High-angle annular dark field scanning transmission electron microscopy

ICP-MS: Inductively coupled plasma mass spectrometry

ITO: Indium-doped tin oxide

I_{refl} : Reflected optical intensity

$I_{refl,0}$: Initial reflected optical intensity

$I_{refl,avg}$: Average reflected optical intensity

I_s : Current density

k: Propagation vector

m_i: Component collinear to any lattice vector **i** for a given magnetic moment

NIR: Near infrared

OCV: Open circuit voltage

Q: Capacity

Q_d : Discharge capacity

PANI: Polyaniline

PBA: Prussian blue analogues

PC: Propylene carbonate

PCD: Photochromic device

PEDOT: Poly(3,4-ethylenedioxythiophene)

PPy: Polypyrrole

PTFE: Polytetrafluoroethylene

rf: radiofrequency

S_{act} : Active surface area

SEM: Scanning electron microscopy

SOC: State of charge

T_C : Curie temperature

T_L : Luminous transmission

T_N : Néel temperature

T_{vis} : Visible light transmission

TCD: Thermochromic device

TEM: Transmission electron microscopy

TGA: Thermogravimetric analysis

UME: Ultra micro-electrode

UV: Ultraviolet

XANES: X-ray absorption near-edge structure

XAS: X-ray absorption spectroscopy

XPS: X-ray photoelectron spectroscopy

ZFC: Zero field-cooled

Experimental methods

Experimental methods in Chapter 2

Reagents – $\text{Li}_2\text{Ni}_2\text{W}_2\text{O}_9$ powder was synthesized from nickel oxide powder (NiO, Sigma-Aldrich, 99 %), tungsten trioxide powder (WO_3 , Alfa Aesar, 99.8 %), and lithium carbonate powder (Li_2CO_3 , Sigma-Aldrich, ≥ 99.0 %). The $\text{Li}_2\text{Ni}_2\text{W}_2\text{O}_9$ self-standing film was made from the prepared $\text{Li}_2\text{Ni}_2\text{W}_2\text{O}_9$ powder, carbon black Super P (C, Alfa Aesar, ≥ 99 %), and a 60 wt% polytetrafluoroethylene dispersion in water (PTFE, Sigma-Aldrich).

Synthesis – $\text{Li}_2\text{Ni}_2\text{W}_2\text{O}_9$ was obtained through solid-state synthesis. For a typical batch of 2 g, NiO powder (435 mg, 2 eq.), WO_3 powder (1350 mg, 2 eq.), and Li_2CO_3 powder (215 mg, 1 eq.) were hand-ground together in an agate mortar; acetone was used to ensure an homogeneous mix. The mix was then ground for 30 minutes in a stainless steel jar containing two stainless steel balls using a SPEX SamplePrep 8000M Mixer/Mill. The resulting mix was then poured in an alumina crucible and heated in a Carbolite CWF 1200 muffle furnace. It was first heated in air at 650 °C (heating rate: 5 °C/min) for 12 h to ensure the decarbonation of Li_2CO_3 , then to 700 °C (heating rate: 2 °C/min) for 24 h. The resulting powder was ball milled for 30 minutes and was then heated again at 700 °C in air (heating rate: 5 °C/min) for 24 h, yielding a green powder.

Structural characterization – Synchrotron powder X-ray diffraction (XRD) experiments were performed at the 11-BM beamline of the Advanced Photon Source (APS) ($\lambda = 0.45898$ Å), at Argonne National Laboratory, USA³⁹⁰. The measurements were realized in transmission mode. The $\text{Li}_2\text{Ni}_2\text{W}_2\text{O}_9$ powder was mixed with crushed glass (1:1 volume ratio) to decrease the absorption of the X-ray beam by tungsten. The samples were poured in borosilicate capillaries (0.7 mm in diameter), and sealed in Kapton tubes.

Neutron powder diffraction patterns were obtained from the Echidna diffractometer³⁹¹ ($\lambda = 1.6220$ Å) at the Open Pool Australian Lightwater (OPAL) reactor of Australia's Nuclear Science and Technology Organisation (ANSTO). The measurements were performed at room temperature using roughly 2 g of pristine $\text{Li}_2\text{Ni}_2\text{W}_2\text{O}_9$ powder placed in a vanadium cylindrical can.

All powder diffraction patterns were refined following the Rietveld method²⁵⁴, in the FullProf software suite³²¹.

Samples for the transmission electron microscopy (TEM) were prepared by grinding the powder in an agate mortar with methanol and depositing drops of the resulting suspension

on a copper TEM grid with a holey carbon layer. Electron diffraction patterns (ED), high-angle annular dark field scanning transmission electron microscopy (HAADF-STEM) images, and energy dispersive X-ray spectra in STEM-mode (STEM-EDX) were collected with a probe-corrected Titan Themis Z electron microscope operated at 200 kV and equipped with a Super-X EDX detector.

Electrochemistry – Galvanostatic charge-discharge experiments were performed using coin cells in a half-cell configuration. The working electrode was $\text{Li}_2\text{Ni}_2\text{W}_2\text{O}_9$ mixed with carbon black Super P (20 wt%), and the counter electrode was lithium metal. Aluminum foil and a stainless steel plate were used as current collectors at the positive and negative electrodes, respectively. Two layers of Whatman GF/D glass fiber filters were used as separator between the two electrodes. The electrolyte was a 1 M solution of lithium hexafluorophosphate (LiPF_6) in a 1:1:4 vol% mix of ethylene carbonate (EC), propylene carbonate (PC) and dimethyl carbonate (DMC).

The measurements were carried out using a BioLogic BCS-805 battery cycler, and the data was acquired using EC-Lab. The cells were cycled between 2.5 and 5.0 V vs Li^+/Li , at a current density of $10 \text{ mA}\cdot\text{g}^{-1}$, at room temperature. Three coin cells were cycled in the same conditions to verify the repeatability of the electrochemical behavior, and to get some statistical dispersion on these measurements.

X-ray Absorption Spectroscopy – X-ray absorption spectroscopy (XAS) measurements were performed at the ROCK beamline³⁹² of SOLEIL synchrotron (France). A Si (111) quick-XAS monochromator with an oscillation frequency of 2 Hz was used to select the incident energy across the Ni K-edge. The quick-XAS spectra were collected in transmission mode using a Ni foil to ensure the energy calibration, and averaged over 10 minutes.

Samples were prepared by mixing 3 mg of active material with cellulose and pressing the resulting powder into 5-mm-wide pellets. In the case of electrochemically (de)lithiated materials, those were retrieved as quickly as possible from their electrochemical cells after cycling, centrifugated three time in clean DMC (6000 rpm, 2 minutes) and dried in vacuum, before being pressed into pellets inside an argon-filled glovebox. The resulting pellets were sealed in plastic film to avoid air exposure during XAS measurements. The energy calibration and normalization of the XAS data was performed using the DEMETER package³⁹³. The k^2 -weighted EXAFS oscillations were extracted at Ni K-edge using a sine windows in the k -range of $[2.2-16.3] \text{ \AA}^{-1}$ and the refinement was done in the R -range of $[1,3.25] \text{ \AA}$. The E_0 , S_0^2 and

coordination number N_i were kept fixed, only the radial distance R_i and the mean-square relative displacements σ_i^2 were allowed to vary. To refine the EXAFS oscillations, we have used the starting model obtained by the structure reported in Table 2.1. The refined structural parameters obtained by EXAFS analysis are reported in Appendix A2.6.

Operando XRD – *Operando* XRD measurements were performed in reflection mode by using $\text{Li}_2\text{Ni}_2\text{W}_2\text{O}_9$ powder mixed with carbon black Super P (20 wt%) as the working electrode in a specialized *operando* cell, sealed with a Be window (Figure A2.7). The counter-electrode was metallic lithium. Thin Al foil (thickness: 0.003 mm) and a stainless steel plate were used as current collectors at the positive and negative electrodes, respectively. Two layers of Whatman GF/D glass fiber filters were used as separators between the two electrodes. The electrolyte was a 1 M solution of lithium hexafluorophosphate (LiPF_6) in a 1:1:4 vol% mix of ethylene carbonate (EC), propylene carbonate (PC) and dimethyl carbonate (DMC). The cell was cycled between 2.5 and 5.0 V vs Li^+/Li , at a current density of $10 \text{ mA}\cdot\text{g}^{-1}$, at room temperature. Electrochemical measurements were carried out using a BioLogic SP-50 potentiostat, and the electrochemical data was collected with EC-Lab.

The XRD scans were performed with a Bruker D8 Advance lab diffractometer, equipped with a Cu $K\alpha$ source ($\lambda_1 = 1.54056 \text{ \AA}$ and $\lambda_2 = 1.54439 \text{ \AA}$) and a LynxEye-2 detector. The measurements were performed in reflection mode, in the Bragg-Brentano configuration.

Optical microscopy – *Operando* optical microscopy measurements were performed by using a $\text{Li}_2\text{Ni}_2\text{W}_2\text{O}_9$ self-standing film as a working electrode in an ECC-Opto-Std optical test cell from EL-Cell (Figure A2.8). The working electrode was prepared by carefully mixing the components (94.8 wt% $\text{Li}_2\text{Ni}_2\text{W}_2\text{O}_9$, 5 wt% Carbon Super P, 0.2 wt% PTFE) in ethanol, using an agate mortar and an agate pestle. The resulting powder was poured on a clean glass surface and repeatedly flattened with a glass cylinder until a $\sim 0.5 \text{ mm}$ film was obtained. This film was then dried at $80 \text{ }^\circ\text{C}$ in vacuum overnight.

The counter electrode was metallic lithium. The current collector on the working electrode's side was an Al mesh, and one layer of Whatman GF/D glass fiber filter was used as a separator between the two electrodes. The electrolyte was a 1 M solution of lithium hexafluorophosphate (LiPF_6) in a 1:1:4 vol% mix of ethylene carbonate (EC), propylene carbonate (PC) and dimethyl carbonate (DMC). The cell was mounted on an inverted microscope (Axio Observer 7, Zeiss) and illuminated from the backside through a 63x oil immersion objective (Plan Apochromat, Zeiss, NA = 1.4) by means of an unpolarized white

light source. A CMOS color camera (Axiocam 705 color, Zeiss) collected the reflected light through the same objective. Each image was taken manually, every 100 s, in order to maintain the focus on the working electrode through the experiment. The cell was cycled between 2.5 and 4.85 V vs Li⁺/Li at a current density of 10 mA.g⁻¹, at room temperature, using a CHI 760E potentiostat from CH Instruments.

Transmission-like images (Appendix A2.1) of pristine and delithiated LNWO particles were obtained by dispersing the electrode material (carbon + LNWO, see *Electrochemistry*) with a droplet of DMC on a glass coverslip, and by positioning a 25 μm-diameter Pt ultramicroelectrode (UME) above the particle, 10 μm above the glass surface, using an ElProScan scanning electrochemical probe microscope from HEKA. The Pt UME acts as a mirror reflecting the light transmitted by the particle towards the microscope objective.

The image analysis was carried out using homemade Python routines. For the statistical analysis, the images were first thresholded and then segmented into the different particles using the `skimage.measure.label` function from the `scikit-image` library³⁹⁴. From there, the average reflected intensity, I_{refl} , and the surface area in terms of pixels (pixel size = 55 nm), S , were extracted for each particle. The same method was used to extract I_{refl} over time for a given particle, in the single-particle-scale study. Lateral drift was corrected using the `trackpy` library³⁹⁵. Due to the nature of the data treatment, a few particle agglomerates were identified as “single particles”; this is especially true for the biggest agglomerates ($S > 10^5$ px).

Magnetic properties – The magnetic properties of Li₂Ni₂W₂O₉ were assessed using a Quantum Design MPMS3 Superconducting QUantum Interference Device (SQUID). A few milligrams of Li₂Ni₂W₂O₉ powder were compressed in a plastic capsule and placed in a brass sample holder for the measurements.

Longitudinal magnetic moment (M) measurements were performed in a DC magnetic field ($H = 200$ Oe, 1 kOe or 10 kOe), with temperatures ranging from 1.8 K to 300 K; the measurements were performed in field-cooled (FC) and zero-field-cooled (ZFC) modes. Magnetization curves were obtained for $T = 2$ K and $T = 100$ K, with H ranging from -70 to 70 kOe.

Neutron diffraction (magnetic structure) – Neutron powder diffraction measurements were performed using the Echidna diffractometer³⁹¹ ($\lambda_{\text{LT}} = 2.4395$ Å or $\lambda_{\text{RT}} = 1.6220$ Å) at the Open Pool Australian Lightwater (OPAL) reactor of Australia’s Nuclear Science and Technology Organisation (ANSTO). The measurements were performed at room temperature

($\lambda = \lambda_{RT}$), then at $T = 15$ K, 7 K, 5 K, and 3.5 K ($\lambda = \lambda_{LT}$), using roughly 2 g of $\text{Li}_2\text{Ni}_2\text{W}_2\text{O}_9$ powder placed in a vanadium can.

The powder diffraction patterns were analysed according to the Rietveld method²⁵⁴ with the FullProf suite³²¹. The magnetic form factor of Ni^{2+} was used to solve and refine the magnetic structure.

Experimental methods in Chapter 3

Reagents (powder synthesis) – Li_2WO_4 , NiWO_4 , and $\text{Li}_2\text{Ni}(\text{WO}_4)_2$ powders were synthesized from nickel oxide powder (NiO, Sigma-Aldrich, 99 %), tungsten trioxide powder (WO_3 , Alfa Aesar, 99.8 %), and lithium carbonate powder (Li_2CO_3 , Sigma-Aldrich, ≥ 99.0 %). The magnetron sputtered nanocomposite Li-Ni-W-O thin film was provided by Saint-Gobain Research Paris.

Synthesis – Li_2WO_4 , NiWO_4 , and $\text{Li}_2\text{Ni}(\text{WO}_4)_2$ powders were obtained through solid-state synthesis. For each compound, stoichiometric amounts of NiO powder, WO_3 powder, and Li_2CO_3 powder were hand-ground together in an agate mortar; acetone was used to ensure an homogeneous mix. The mix was then ground for 30 minutes in a stainless steel jar containing two stainless steel balls using a SPEX SamplePrep 8000M Mixer/Mill. The resulting mix was then poured in an alumina crucible and heated in a Carbolite CWF 1200 muffle furnace. It was heated in air at 600 °C (Li_2WO_4), 650 °C ($\text{Li}_2\text{Ni}(\text{WO}_4)_2$) or 700 °C (NiWO_4) (heating rate: 5 °C/min) for 12 h. The resulting powder was ball milled for 30 minutes and was then heated again at the same temperature as before (heating rate: 5 °C/min) for 12 h, in air.

Electrochemistry – Galvanostatic charge-discharge experiments on the Li_2WO_4 , NiWO_4 , and $\text{Li}_2\text{Ni}(\text{WO}_4)_2$ powders were performed using coin cells in a half-cell configuration. The working electrode was made by mixing the studied powder with carbon black Super P (20 wt%), and the counter electrode was lithium metal. Aluminum foil and a stainless steel plate were used as current collectors at the positive and negative electrodes, respectively. Two layers of Whatman GF/D glass fiber filters were used as separator between the two electrodes. The electrolyte was a 1 M solution of lithium hexafluorophosphate (LiPF_6) in a 1:1 vol% mix of ethylene carbonate (EC) and dimethyl carbonate (DMC).

The measurements were carried out using a BioLogic BCS-805 or VMP-3 battery cycler, and the data was acquired using EC-Lab. The cells were cycled at a current density of 100 mA.g^{-1} (for Li_2WO_4 and NiWO_4) or 10 mA.g^{-1} (for $\text{Li}_2\text{Ni}(\text{WO}_4)_2$), at room temperature.

For the magnetron sputtered Li-Ni-W-O thin film, the galvanostatic charge-discharge experiment was performed in a Swagelok cell. The thin film served as working electrode, and contact with the aluminum current collector at the positive electrode was provided by a strip of aluminum mesh. The counter electrode was lithium metal; its current collector was a stainless steel plate. A single layer of Whatman GF/D glass fiber filter was used as a separator between the two electrodes. The electrolyte was a 1 M solution of lithium hexafluorophosphate (LiPF_6) in a 1:1 vol% mix of ethylene carbonate (EC) and dimethyl carbonate (DMC).

The measurements were carried out using a VMP-3 battery cycler, and the data was acquired using EC-Lab. The cells were cycled at a current density of roughly $100 \text{ mA}\cdot\text{g}^{-1}$ (assuming a film density of $7 \text{ g}\cdot\text{cm}^{-3}$) at room temperature. This experimental setup was also used to prepare the charged and discharged thin film samples for the XPS experiments.

XPS – X-ray photoemission spectroscopy (XPS) was performed with a THERMO Escalab spectrometer, using focused Al $K\alpha$ monochromatic radiation ($h\nu = 1486.6 \text{ eV}$). The samples were entered through an argon-filled glovebox in order to avoid exposure to air and moisture. Peaks were recorded with a constant pass energy of 20 eV. The C1s peak at 285.0 eV was used to calibrate the binding energy scale. The curve fits for core peaks were obtained using a minimum number of components. Prior to the measurements, cycled thin film samples were carefully washed with DMC in an argon-filled glovebox, in order to remove electrolyte residue.

Reagents (spin coating) – The spin coating solutions were prepared from lithium nitrate powder (LiNO_3 , Alfa Aesar, $\geq 98.5 \%$), nickel(II) nitrate hexahydrate ($\text{Ni}(\text{NO}_3)_2\cdot 6\text{H}_2\text{O}$, Alfa Aesar, 99.9985 %), tungsten hexachloride powder (WCl_6 , Sigma-Aldrich, $\geq 99.9 \%$), citric acid monohydrate powder ($\text{C}_6\text{H}_8\text{O}_7\cdot\text{H}_2\text{O}$, Sigma-Aldrich, $\geq 99.0 \%$), and ethanol absolute ($\text{C}_2\text{H}_6\text{O}$ or EtOH, VWR chemicals). The magnetron sputtered nanocomposite Li-Ni-W-O thin film, ITO/Glass substrates, and glass substrates were provided by Saint-Gobain Research Paris. Fused SiO_2 substrates were obtained from Neyco; ITO/ SiO_2 were prepared by magnetron sputtering of 400 nm of ITO on a fused SiO_2 substrate.

Solution preparation – A typical spin-coating solution was prepared by adding first $\text{Ni}(\text{NO}_3)_2\cdot 6\text{H}_2\text{O}$ and citric acid monohydrate to $\sim 8 \text{ mL}$ of ethanol absolute, in a polypropylene bottle. The solution was magnetically stirred until the solids were almost completely dissolved. Then, the desired amounts of LiNO_3 and WCl_6 were taken out of an argon-filled glovebox and added to the solution, which was left under continuous magnetic stirring for a few hours (in

general, 6 to 16 hours). The resulting solution was collected with a syringe, filtered using a Whatman syringe filter (polypropylene, pore diameter: 0.2 μm) and completed to 10 mL with ethanol absolute. It was then stored in a polypropylene tube and used for spin-coating in the following 24 h. LiNO_3 , $\text{Ni}(\text{NO}_3)_2 \cdot 6\text{H}_2\text{O}$, and WCl_6 were added in stoichiometric amounts to the solution, based on the desired elemental composition. For any given solution, the concentration of the majority metal cation was set to 0.2 M, and the concentrations of the other precursors were adapted to fit the stoichiometry. The citric acid monohydrate to total metal cation ratio (C.A./ M^2) was 2:1 in every solution.

Spin coating process – Prior to the spin-coating process, substrates were cut to be about 5 by 5 cm and washed by sonication in diluted detergent (RBS 50, Sigma-Aldrich), deionized water, and isopropanol.

Spin-coating was performed using a Polos Spin150i spin-coater. For a typical thin film sample, the substrate was held into place by vacuum, using a pump and a vacuum chuck. The coating solution was dispensed by a syringe equipped with a Whatman syringe filter (polypropylene, pore diameter: 0.2 μm). About 40 drops (~ 1 mL) were dispensed on the substrate, which was then spun for 30 s, at 3000 rpm, with an acceleration/deceleration rate of 1000 $\text{rpm}\cdot\text{s}^{-1}$. After the first coating, the sample was dried on a heating plate at 100 $^\circ\text{C}$, for roughly 10 minutes. It was then coated again through the same process, and dried again at 100 $^\circ\text{C}$ for 10 minutes.

Following spin-coating and drying, the thin film sample was then heated in an AAF 1100 muffle furnace from Carbolite at 450 $^\circ\text{C}$ (heating rate: 5 $^\circ\text{C}/\text{min}$), for 30 minutes, in air.

Structural characterization – Scanning electron microscopy (SEM) images of the thin films were collected using a FEI Magellan Microscope. Optical reflection microscopy images were collected using a Zeiss AxioScope 5 microscope, equipped with an AxioCam 105 camera. Profilometry measurements were performed using a DektakXT profilometer from Bruker.

Operando UV-Visible electrochemistry measurements – Electro-optical measurements were performed on the thin film samples using a custom three-electrode electrochemical cell described in Figure 3.20. It was designed in such a way that a beam of white light could cross the entirety of the cell, including the thin film sample. The light source was an AvaLight-CAL-Neon from Avantes, emitting on a spectral range from 337 to 1084.5 nm. The light exiting the custom electrochemical cell was analyzed with an AvaSpec-ULS4096CL-EVO from Avantes. Incident light was delivered to the cell by a silica optical

fiber; light exiting the cell was collected by the same type of fiber. The blank measurement for the transmitted optical signal was performed with the assembled cell placed in the optical pathway, prior to the electrochemical measurement. A *post-mortem* UV-Visible transmission spectroscopy measurement was performed on the cycled thin film with a PerkinElmer Lambda950S spectrometer to calculate the absolute values of transmittance throughout the *operando* experiment.

The working electrode in the electrochemical cell was the studied thin film sample (4.91 cm² were electrochemically active); an aluminium strip was soldered to the film and the ITO/Glass substrate to ensure the electrical connection to the potentiostat. The counter-electrode was a lithium metal ring, and the reference electrode was a lithium metal disk. The electrolyte was 1 M LiClO₄ in PC. Due to the high volume of electrolyte required to fill the cell, it was not changed between experiments.

For the galvanostatic charge-discharge experiments, the films were cycled between 2.0 and 4.4 V vs Li⁺/Li, with a current density of roughly 100 mA.g⁻¹ (assuming a film density of ~ 7 g.cm⁻³, or ~ 6 g.cm⁻³ for the Li₂Ni(WO₄)₂ thin film), for 20 cycles. For the cyclic voltammetry experiment, the MS-LNWO thin film was cycled successively at 2, 5, 10, 20, 50, and 100 mV.s⁻¹, with three cycles per scan rate. All experiments were performed at room temperature. The measurement were carried out by a VMP-3 potentiostat from BioLogic, and the data was collected by EC-Lab.

Powder synthesis from spin-coating solutions – For a given solution, a powder was synthesized by first evaporating the solvent with a rotavapor. The resulting wet precipitate was calcined at 200 °C (heating rate: 2 °C/min), for 2 h, in air, using an AAF 1100 muffle furnace from Carbolite. Then, the calcined black mass was crushed and ground in an agate mortar, poured inside an alumina crucible, and successively annealed at 380 °C, 420 °C, 450 °C, and 700 °C (or 650 °C for the solution used for the Li₂Ni(WO₄)₂ thin film) in the same muffle furnace as the calcination step. For each intermediate step, the powder was annealed for 2 h in air, with a heating rate of 5 °C/min. For the final high-temperature crystallization step, the powder was annealed for 12 h, in air, with a heating rate of 5 °C/min.

XRD scans of the powders were performed with a Bruker D8 Advance lab diffractometer, equipped with a Cu K α source ($\lambda_1 = 1.54056 \text{ \AA}$ and $\lambda_2 = 1.54439 \text{ \AA}$) and a LynxEye-XE-T detector. The measurements were performed in reflection mode, in the Bragg-Brentano configuration.

TGA measurements were performed on the calcined black powders using a STARe TGA/DSC 3+ system from Mettler-Toledo. The measurement was performed by placing the calcined powder in an alumina crucible and heating it up to 700 °C with a heating rate of +10 °C/min.

UV-Visible spectroscopy measurements on powders – UV-Visible spectroscopy measurements on $\text{Li}_2\text{Ni}_2\text{W}_2\text{O}_9$, $\text{Li}_2\text{Ni}(\text{WO}_4)_2$, NiWO_4 , and Li_2WO_4 powder sample were performed with a PerkinElmer Lambda950 spectrometer. The samples were prepared by filling a quartz groove with powder and sealing it with another quartz slide. The resulting powder layers had thicknesses of 10, 20, or 50 μm ; the thickness was selected to ensure a null transmission of the samples.

Appendix

Part of the results presented in this appendix were published in the following articles: Redor et al. *J. Am. Chem. Soc.* **2023**, *145* (23), 12823–12836 and Redor et al. *Phys. Rev. B* **2024**, *109* (5), 054105.

A2. Appendix to Chapter 2

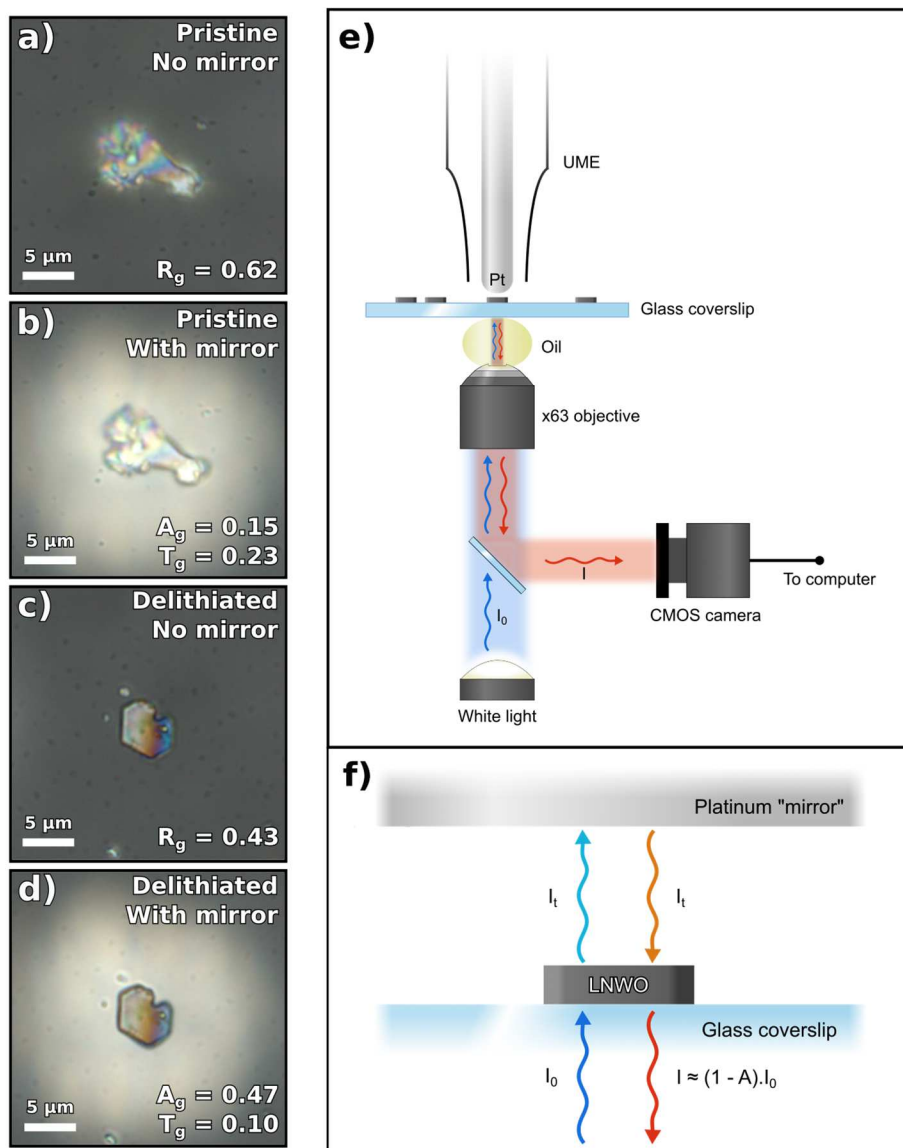


Figure A2.1 – Optical microscopy images of pristine (a,b) and delithiated (c,d) LNWO particles. Images (a) and (c) were taken without Pt mirror (reflection microscopy), while (b) and (d) were taken with a Pt mirror behind the particle (“transmission-like” microscopy). The values of the reflectance on the green channel (R_g) are indicated on the bottom right of (a) and (c). The values of the transmittance and absorbance on the green channel (T_g and A_g) are indicated on the bottom right of (b) and (d). (e) “Transmission-like” optical microscopy setup (not to scale). (f) Optical model used for the calculations of R, T and A (not to scale).

Figure A2.1 compares the reflection and the transmission of a double travel of light (back and forth) for two different particles: a pristine $\text{Li}_2\text{Ni}_2\text{W}_2\text{O}_9$ particle, and a delithiated one. The images of the pristine particle by reflection in Figure A2.1a and back-and-forth transmission in Figure A2.1b show that the particle, even if partly reflecting light, is quite transparent to the light beam. The same comparison for the delithiated particle show that the reflected or transmitted images are very similar, suggesting that the particle is not able to

transmit as much light in its delithiated state, most likely because it absorbs more of the incoming light. Based on Figure A2.1, the values of the reflectance (R), transmittance (T), and absorbance (A) are defined as the fractions of the incident light intensity (I_0) which are reflected, transmitted, and absorbed by the particle in this optical configuration. Particularly the light transmitted corresponds to light that passes back and forth through the particle and is collected through the microscope. R, T, and A are defined by the following equations:

$$R = \frac{I_{refl}}{I_0} \quad T = \frac{I_{trans}}{I_0} \quad A = \frac{I_{abs}}{I_0} \quad \begin{array}{l} \text{A2.1, A2.2,} \\ \text{A2.3} \end{array}$$

$$R + T + A = 1 \quad \text{A2.4}$$

I_{refl} , I_{trans} and I_{abs} are the reflected, transmitted, and absorbed intensities, respectively. The system defined in Figure A2.1f contains the $\text{Li}_2\text{Ni}_2\text{W}_2\text{O}_9$ particle and the Pt mirror behind it. This system is based on the approximation that 100 % of the light reaching the Pt mirror is reflected. As such, the transmittance and absorbance of the system do not match with the transmittance and absorbance of the $\text{Li}_2\text{Ni}_2\text{W}_2\text{O}_9$ particle alone. It is because, in our case, the beam of light coming out of the entire system (I) has crossed the $\text{Li}_2\text{Ni}_2\text{W}_2\text{O}_9$ particle twice. The reflectance should be the same for the $\text{Li}_2\text{Ni}_2\text{W}_2\text{O}_9 + \text{Pt}$ system and the $\text{Li}_2\text{Ni}_2\text{W}_2\text{O}_9$ particle alone, however.

Therefore, the values of transmittance and absorbance on the green channel ($\lambda = 532 \text{ nm}$) reported on Figure A2.1b,d are the values for the $\text{Li}_2\text{Ni}_2\text{W}_2\text{O}_9 + \text{Pt}$ system. However, the only difference between the optical systems in Figure A2.1b and Figure A2.1d is the lithiation state of the $\text{Li}_2\text{Ni}_2\text{W}_2\text{O}_9$ particle. Therefore, the decrease in transmittance (increase in absorbance) observed for the $\text{Li}_2\text{Ni}_2\text{W}_2\text{O}_9 + \text{Pt}$ system can be correlated to a decrease in transmittance (increase in absorbance) of the $\text{Li}_2\text{Ni}_2\text{W}_2\text{O}_9$ particle when it is electrochemically delithiated. Unfortunately, the absorbance and transmittance of the $\text{Li}_2\text{Ni}_2\text{W}_2\text{O}_9$ particle alone cannot be easily quantified.

The trend observed on the green channel can also be observed on the red ($\lambda = 632 \text{ nm}$) and blue ($\lambda = 450 \text{ nm}$) channels.

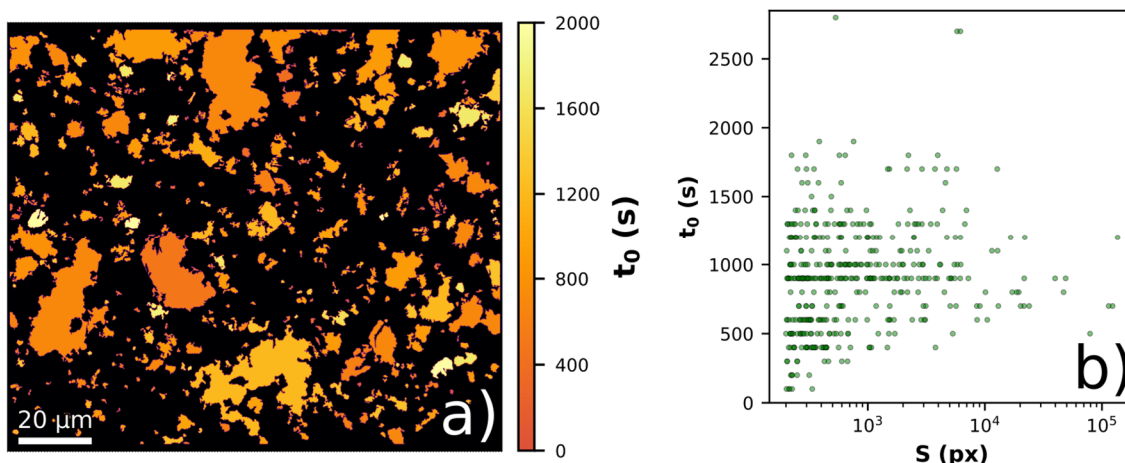


Figure A2.2 – t_0 analysis of the *operando* optical microscopy during the charge. (a) t_0 mapping of the particles on the optical microscopy image of the $\text{Li}_2\text{Ni}_2\text{W}_2\text{O}_9$ electrode. (b) Plot of t_0 against the size of the particles (S , the size of the particles, is given as the number of pixels required to represent the particle on the microscopy image. 1 px = $0.003025 \mu\text{m}^2$). Number of particles (sample size): 425.

Table A2.3 – Detailed data of the t_0 mapping for the charge shown in Figure A2.2.

t_0 (s)	Particle size (px)			
	$[2 \cdot 10^2, 10^3]$	$[10^3, 10^4]$	$[10^4, 10^5]$	$[10^5, 10^6]$
[0, 500]	68 (24 %)	9 (7 %)	1 (5 %)	0
[600, 1000]	133 (48 %)	71 (57 %)	13 (68 %)	2 (67 %)
[1100, 1500]	63 (23 %)	32 (26 %)	4 (21 %)	1 (33 %)
[1600, 2000]	13 (5 %)	10 (8 %)	1 (5 %)	0
[2100, 2500]	0	0	0	0
No plateau	1 (< 1 %)	3 (2 %)	0	0
Total	278 part.	125 part.	19 part.	3 part.

In Figure A2.2 and Table A2.3, t_0 corresponds to the time at which the variation of the intensity reflected by a given LNWO particle decreases above a threshold value:

$$\left(\frac{dI}{dt}\right)_t < 0.2 * \max\left(\frac{dI}{dt}\right)$$

It indicates at which time I_{refl} reaches a plateau or a sudden slower rate of lithium deinsertion for a given particle. $t = 0$ s is defined as the beginning of the galvanostatic charge in this specific figure; the discharge begins at $t = 2850$ s. In Table A2.3, the row “No plateau” corresponds to particles that do not reach a plateau or a sudden slope change in the evolution of I_{refl} against time during the charge.

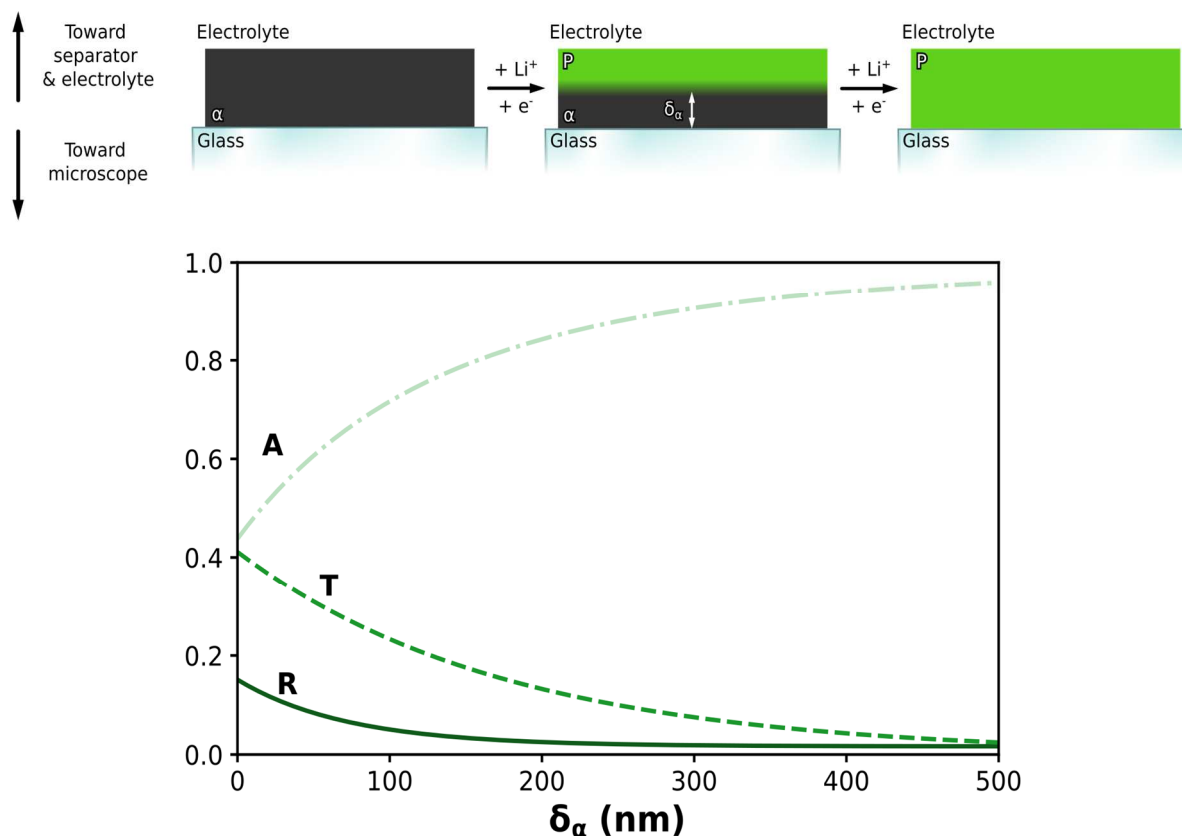


Figure A2.4 – Top: “top-to-bottom” model for the transformation of $\text{Li}_\alpha\text{Ni}_2\text{W}_2\text{O}_9$ to $\text{Li}_2\text{Ni}_2\text{W}_2\text{O}_9$ upon electrochemical lithium insertion in a Li-metal cell. Bottom: simulated reflectance (R), transmittance (T) and absorbance (A) curves plotted against the thickness of the $\text{Li}_\alpha\text{Ni}_2\text{W}_2\text{O}_9$ layer, based on the top-to-bottom model. The thickness of the entire particle is set to 500 nm.

In the “top-to-bottom” model described in Figure A2.4, it is assumed that during the *operando* optical microscopy experiment, and after the electrochemical removal of lithium from a $\text{Li}_2\text{Ni}_2\text{W}_2\text{O}_9$ particle, the material will have fully transformed into $\text{Li}_\alpha\text{Ni}_2\text{W}_2\text{O}_9$. Upon lithium reinsertion, since the Li^+ ions are coming from the electrolyte, the Li^+ cations are going to be inserted in the side of the particle closer to the separator first. This would lead to a transformation of the particle from the side closest to the separator (“top”) to the side closest to the cell’s glass window (“bottom”). This also assumes that the particle edges are less well connected to the conducting paste than its top face and/or the thickness of the particle is smaller than its lateral size.

Based on this model, and on the work of Byrnes on thick non-coherent films³⁹⁶, the evolution of the reflectance, transmittance, and absorbance as the underlithiated phase is transformed back to the original fully lithiated phase were calculated. For these calculations, the refractive indexes of glass and the electrolyte were set to 1.5 and 1.4, respectively. The refractive index (1.3) and extinction coefficient (0.3) of Ni_2O_3 were used for the underlithiated

phase (α)³⁹⁷. For the original, fully lithiated phase (P), the refractive index (2.6) and extinction coefficient (0.06) of NiO were used³⁹⁸. Although these values are not very reliable, they were considered sufficient, as the variations of the reflectance, transmittance and absorbance are what is most interesting in this specific case.

In particular, it can be seen that the reflectance remains constant even after the transformation of $\text{Li}_x\text{Ni}_2\text{W}_2\text{O}_9$ into $\text{Li}_2\text{Ni}_2\text{W}_2\text{O}_9$, and it starts increasing only when the underlithiated layer of the particle becomes very thin (< 200 nm). This could explain why increases in reflectance for single particles (Figure 2.18) can only be seen at the end of the discharge during the *operando* optical microscopy experiment: even though lithium is inserted into the particle, if the underlithiated layer in the particle is too thick, the reflectance remains constant. As such, the t_0 mapping for the discharge shown in Figure A2.2 can be interpreted as a qualitative thickness mapping: the thinner a particle is, the smaller t_0 will be, as less lithium needs to be inserted in the particle to reach the threshold thickness that can be probed through a measurement of I_{refl} .

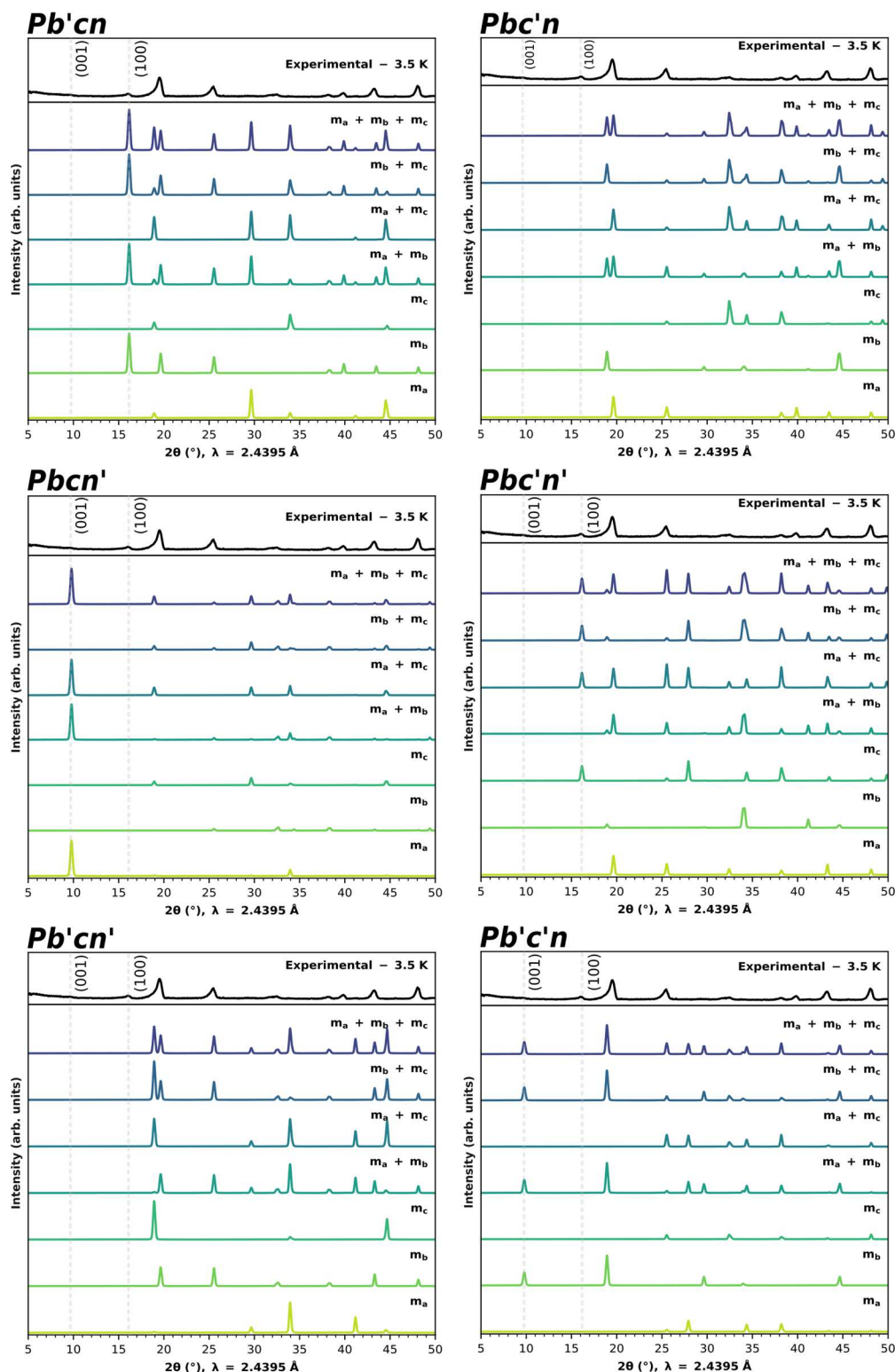


Figure A2.5 – Experimental neutron powder diffraction data at $T = 3.5$ K for $\text{Li}_2\text{Ni}_2\text{W}_2\text{O}_9$ (black, top), and simulated patterns for $\mathbf{k} = (0, 0, 0)$ in the $Pb'cn$ (top left), $Pbc'n$ (top right), $Pbcn'$ (middle left), $Pbc'n'$ (middle right), $Pb'cn'$ (bottom left), and $Pb'c'n$ (bottom right) Shubnikov space groups (colored, bottom). For each simulation, each magnetic component is either equal to $0 \mu_B$ or to $1 \mu_B$; the non-zero components for a given simulation are annotated above its corresponding pattern.

Appendix

Table A2.6 – Results for the refinements of the EXAFS oscillations. E_0 is the photoelectron energy origin, $d_{\text{avg}}(\text{Ni-O})$ the average Ni-O bond length, N is the coordination number, R the radial distance, and σ^2 is the correlated Debye-Waller factor.

	O₁	O₂	Ni₁	W₁	W₃	O₃	Ni₂
Pristine LNWO ($E_0 = -1.681$ eV / $d_{\text{avg}}(\text{Ni-O}) = 2.05$ Å / Reduced χ^2 : 129.208 / R-factor: 0.0085998)							
N	3	3	2	2	1	3	1
R (Å)	1.99385	2.10228	2.93942	3.05905	3.12913	3.39878	3.46758
σ^2 (Å²)	0.00109	0.00109	0.00366	0.00380	0.00380	0.00109	0.00366
Charged LNWO – 1 st cycle ($E_0 = -2.130$ eV / $d_{\text{avg}}(\text{Ni-O}) = 2.00$ Å / Reduced χ^2 : 131.593 / R-factor: 0.0094653)							
N	1	3	2	2	1	1	3
R (Å)	2.02725	2.05870	2.93002	3.05335	3.15630	3.47182	3.37637
σ^2 (Å²)	0.00253	0.00253	0.00395	0.00477	0.00477	0.00395	0.00253
Discharged LNWO – 1 st cycle ($E_0 = -0.606$ eV / $d_{\text{avg}}(\text{Ni-O}) = 2.06$ Å / Reduced χ^2 : 210.266 / R-factor: 0.0162799)							
N	4	2	2	2	1	3	1
R (Å)	2.02319	2.12651	2.94569	3.06477	3.14698	3.42347	3.46692
σ^2 (Å²)	0.00191	0.00191	0.00334	0.00287	0.00287	0.00191	0.00334
Charged LNWO – 50 th cycle ($E_0 = -1.401$ eV / $d_{\text{avg}}(\text{Ni-O}) = 2.02$ Å / Reduced χ^2 : 139.697 / R-factor: 0.0097308)							
N	1	3	2	2	1	3	1
R (Å)	2.08547	2.05459	2.93700	3.06094	3.16052	3.39198	3.48530
σ^2 (Å²)	0.00251	0.00251	0.00392	0.00402	0.00402	0.00251	0.00392

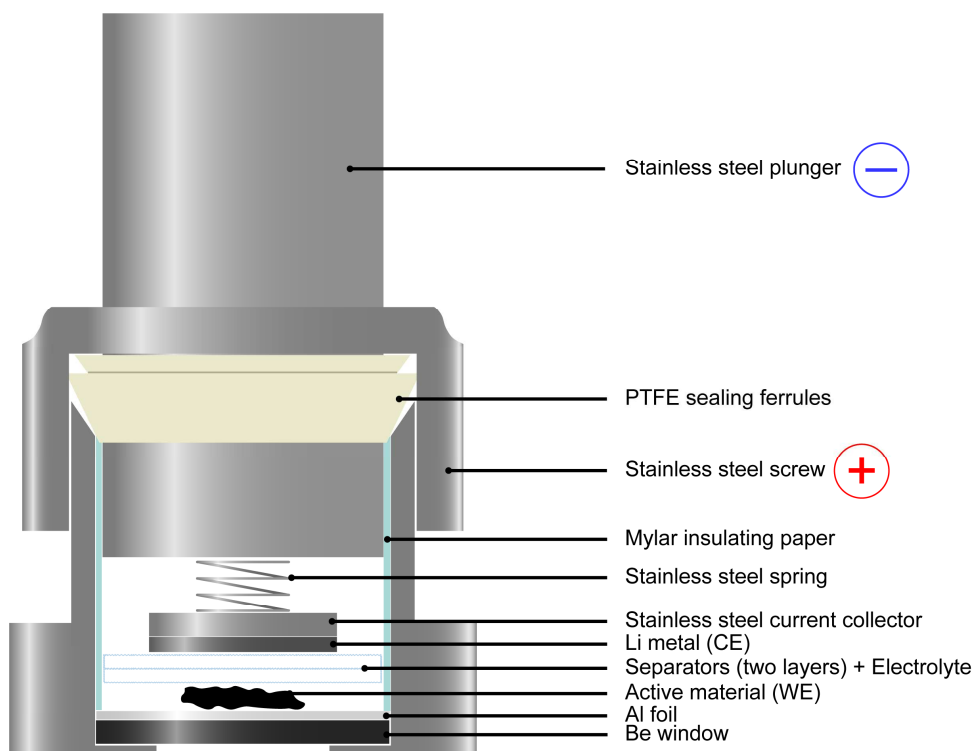


Figure A2.7 – Schematic representation of an *operando* XRD cell.

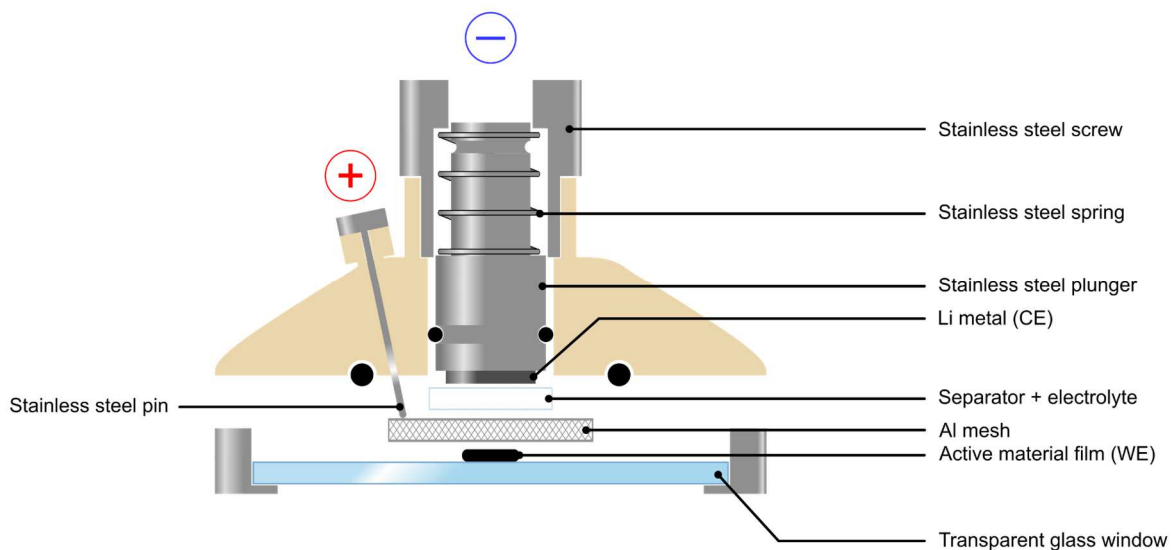
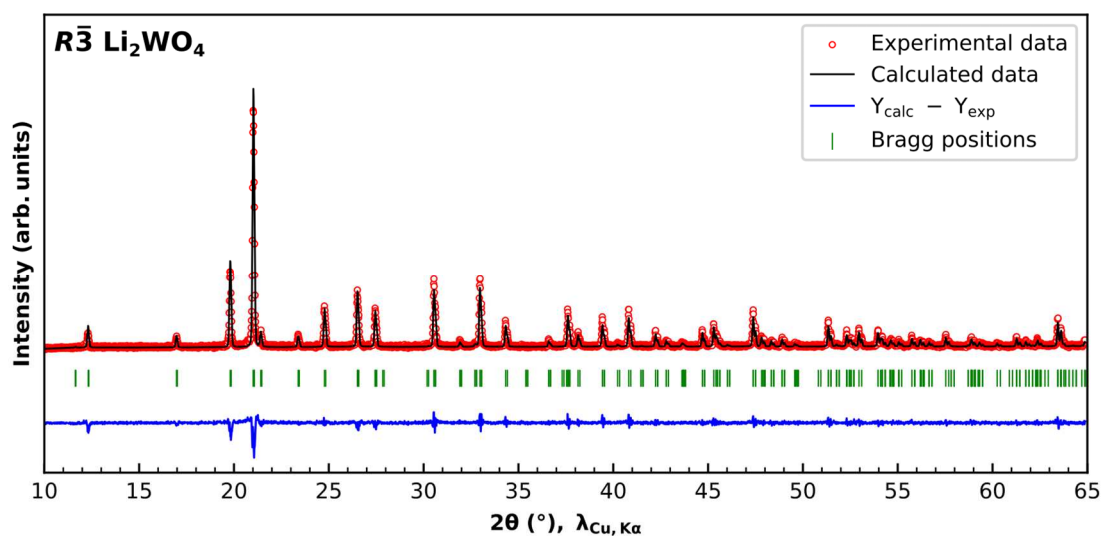
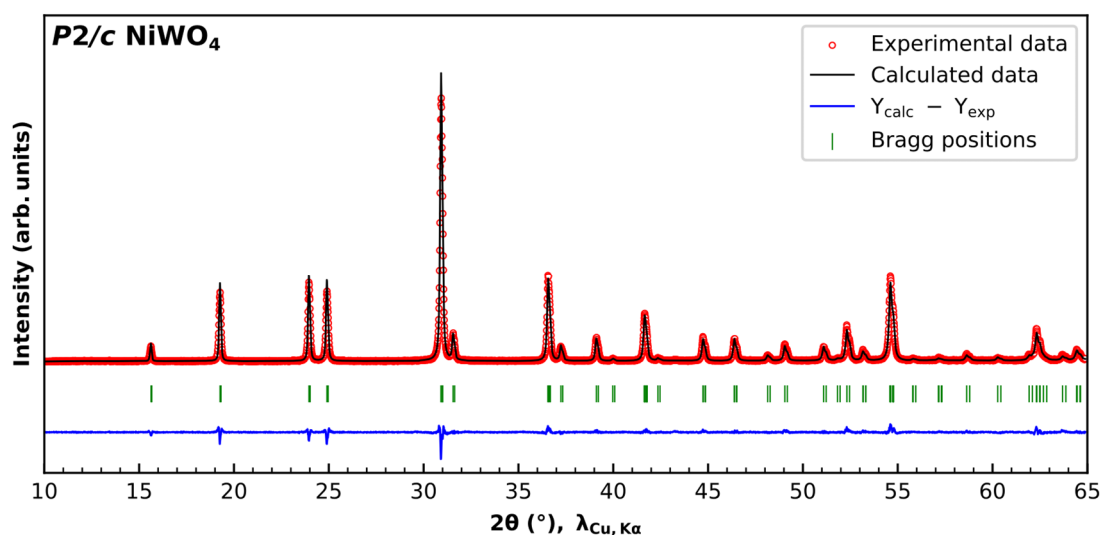


Figure A2.8 – Schematic representation of the *operando* reflection optical microscopy cell.

A3. Appendix to Chapter 3

Figure A3.1 – XRD pattern and Rietveld refinement for Li_2WO_4 powder sample. $R_{Bragg} = 17.8\%$.Figure A3.2 – XRD pattern and Rietveld refinement for $NiWO_4$ powder sample. $R_{Bragg} = 2.97\%$.

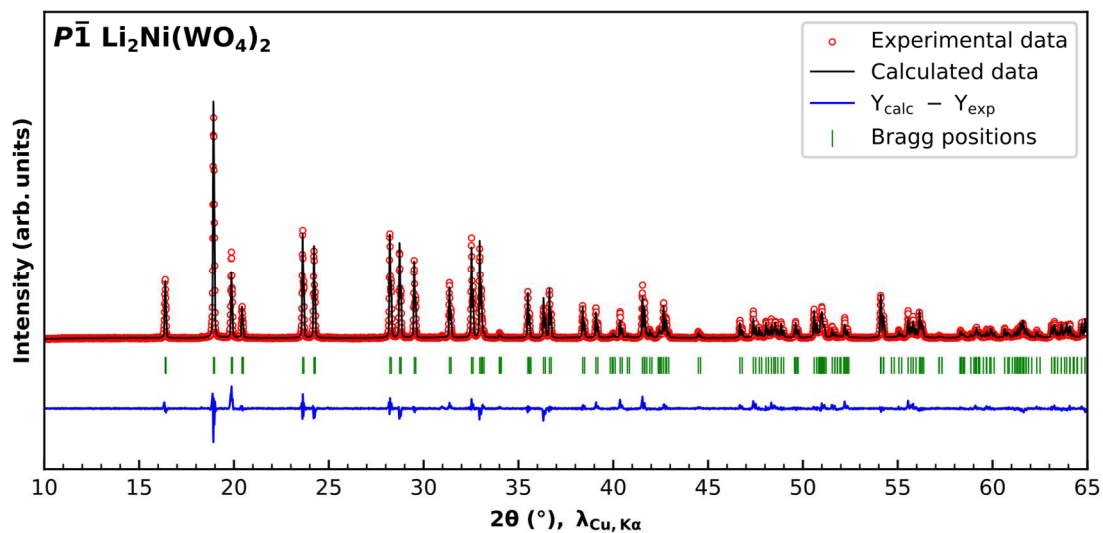


Figure A3.3 – XRD pattern and Rietveld refinement for $\text{Li}_2\text{Ni}(\text{WO}_4)_2$ powder sample. $R_{\text{Bragg}} = 7.97\%$.

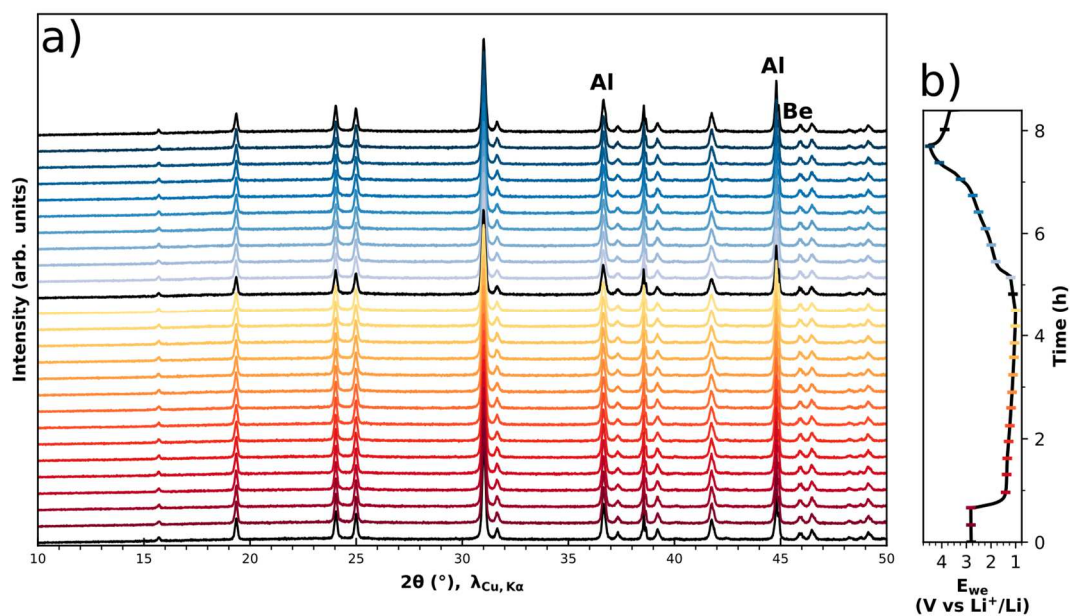


Figure A3.4 – (a) XRD patterns and (b) E_{we} vs time curve for an *operando* XRD galvanostatic charge-discharge experiment in a $\text{NiWO}_4:\text{C}||\text{Li}$ cell, using a 1 M LiPF_6 in EC:DMC (1:1 vol) electrolyte.

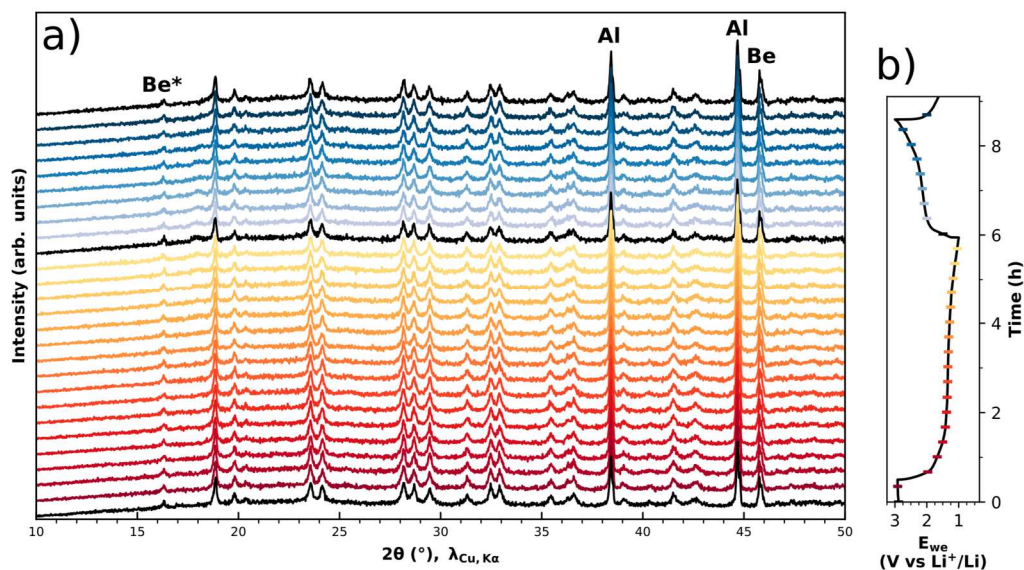


Figure A3.5 - (a) XRD patterns and (b) E_{we} vs time curve for an *operando* XRD galvanostatic charge-discharge experiment in a $Li_2Ni(WO_4)_2:C||Li$ cell, using a 1 M $LiPF_6$ in EC:DMC (1:1 vol) electrolyte.

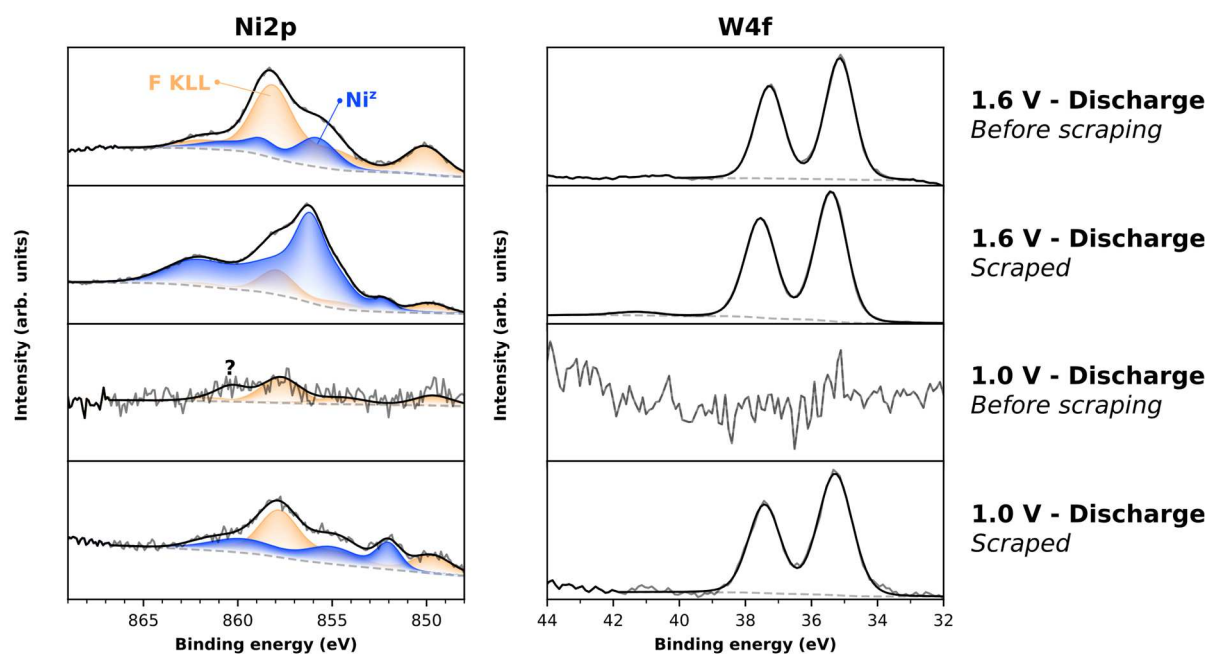


Figure A3.6 – Ni2p (left) and W4f (right) regions of the XPS spectra for magnetron sputtered Li-Ni-W-O thin film samples discharged to 1.6 V and 1.0 V vs Li^+/Li , before and after scraping the CEI layer off the samples. In the Ni2p region, the contribution of the Auger peaks of fluorine is in orange, while the total contribution of the $Ni2p_{3/2}$ peaks for all nickel species is in blue.

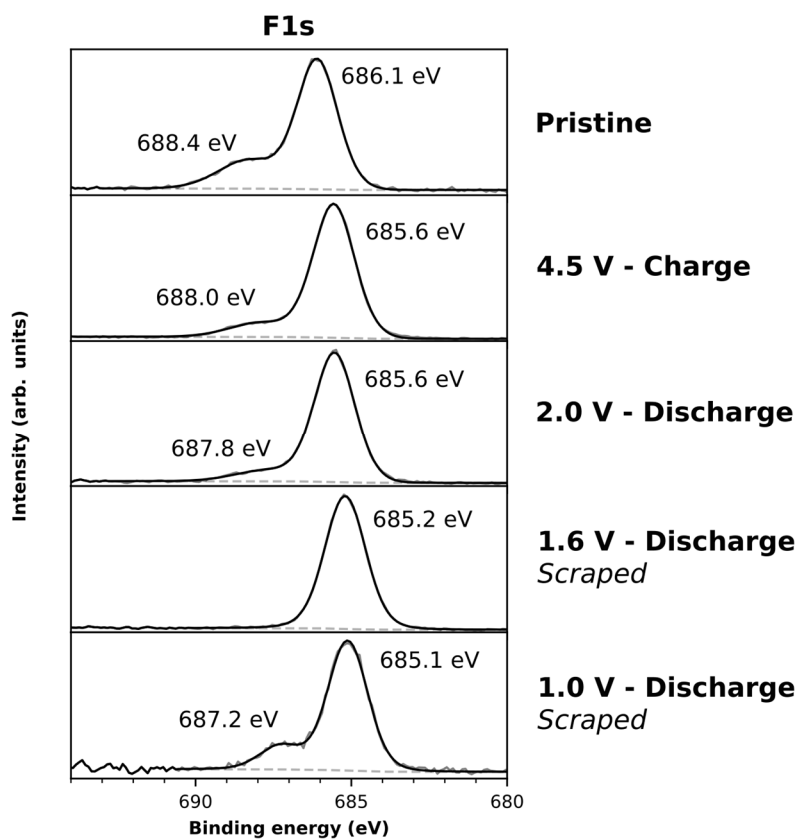


Figure A3.7 – F1s region for the XPS spectra of Li-Ni-W-O thin film samples at different states of charge.

Résumé en français de la thèse

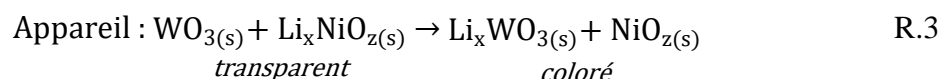
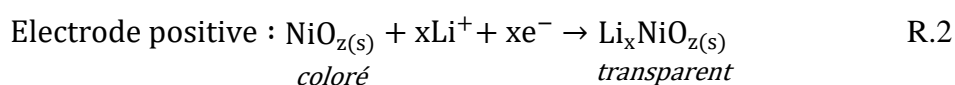
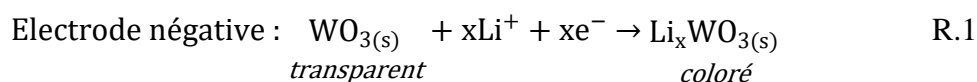
Cette thèse s'inscrit dans le contexte du réchauffement climatique global. Les rapports alarmants du GIEC appellent à une diminution immédiate des émissions de gaz à effet de serre, afin d'éviter une hausse de la température moyenne mondiale au-dessus de 2,0 °C entre la période 1850-1900 et 2100. Le franchissement de cette limite risquerait de causer des événements climatiques extrêmes, et aurait des conséquences désastreuses sur la santé humaine, la sécurité alimentaire, les infrastructures, la biodiversité, etc. Or, en 2019, le secteur du bâtiment était responsable de 21 % des émissions de gaz à effet de serre mondiales. Il s'agit donc d'un secteur-clé pour la lutte contre le réchauffement climatique¹.

Une bonne stratégie pour diminuer les émissions des bâtiments à long terme est l'utilisation de matériaux à haute efficacité énergétique. En outre, il faut que ces matériaux soient adaptés au climat futur, qui sera caractérisé par de fortes températures ; il sera donc nécessaire d'assurer des températures intérieures raisonnables pour les habitants des bâtiments de demain². Les vitrages électrochromes apparaissent alors comme des candidats pertinents pour remplir ces deux critères. Ces vitrages dynamiques ont la capacité de changer d'état optique (notamment de transparence) lorsqu'on leur applique une tension ou un courant électrique. Cela permet de contrôler la quantité d'émissions solaires visibles et infrarouges entrant dans un bâtiment, et donc de contrôler sa température intérieure. Cette technologie repose sur la présence d'une pile de couches minces placée dans le vitrage, qui présente une architecture similaire à celle qu'on pourrait trouver dans une batterie Li-ion : deux électrodes (positive et négative), séparées par un électrolyte, et derrière lesquelles se trouve un collecteur de courant transparent.

Les matériaux d'électrodes dans ces appareils électrochromes sont critiques pour obtenir de bonnes performances, notamment en termes de contraste optique : en effet, ce sont ces matériaux d'électrode, dits matériaux électrochromes, qui changent de couleur lors de l'application d'une tension ou d'un courant électrique, grâce à des changements de degré d'oxydation. L'objectif de ce projet de thèse est d'apporter une compréhension fondamentale des propriétés électrochimiques et optiques présentées par un matériau électrochrome pour électrode positive : une couche mince d'un oxyde mixte lithium-nickel-tungstène (Li-Ni-W-O).

Historiquement, les premiers rapports sur des matériaux présentant des changements de couleur dues à des changements de degrés d'oxydation remontent à 1706 et 1815, au sujet du Bleu de Prusse ($\text{Fe}_4^{\text{III}}[\text{Fe}^{\text{II}}(\text{CN})_6]_3$)¹² et du trioxyde de tungstène (WO_3)¹⁴, respectivement. Au

cours des siècles qui suivirent, les recherches sur ce genre de matériaux et leurs applications ont progressé doucement. Mais en 1969, la recherche sur les matériaux et les appareils électrochromes a été propulsée en avant grâce à la mise au point par Deb de ce qui est souvent considéré comme le premier appareil électrochrome, conçu sous la forme d'une pile de couches minces²³. Après la publication des travaux de Deb, de nombreux laboratoires de recherche et entreprises se sont penchés sur la technologie des appareils électrochromes. Le design en « pile » ou en « sandwich » proposé par Deb a mené à l'une des structures les plus utilisées pour les appareils électrochromes aujourd'hui, la structure en 5 couches : collecteur de courant – électrode positive – électrolyte – électrode négative – collecteur de courant. Ce type d'appareil électrochrome réalise son changement de couleur par l'échange de petits cations (souvent H⁺ ou Li⁺) et d'électrons d'une électrode à l'autre. Un exemple est donné dans les Équations R.1, R.2, R.3 :



Le changement d'état d'oxydation va permettre un changement simultané d'état optique aux deux électrodes. À l'électrode positive, on retrouve un matériau électrochrome anodique, qui se colore lorsqu'on l'oxyde ; à l'électrode négative, se trouve un matériau électrochrome cathodique, qui se colore lorsqu'on le réduit. La combinaison des deux permet à l'appareil électrochrome complet de passer de transparent à coloré en échangeant des ions et des électrons d'une électrode à l'autre.

Cette technologie électrochromes a permis de nombreuses innovations dans différents domaines : les vitrages^{3,33-35} mais aussi les affichages dynamiques⁷⁸⁻⁸³, les rétroviseurs automobiles⁸⁴, des dispositifs de vision⁸⁵⁻⁸⁸, etc. Ce manuscrit se concentre tout particulièrement sur les matériaux électrochromes utilisés dans les vitrages intelligents. Parmi tous les types de matériaux électrochromes qui ont été découverts et développés au cours des dernières décennies (Bleu de Prusse¹³⁸⁻¹⁴⁰, viologènes¹¹⁵, polymères conducteurs¹²⁵⁻¹²⁸, etc.),

ce sont les oxydes de métaux de transition qui sont les plus utilisés dans les vitrages électrochromes, car ils peuvent facilement être produits sous formes de couches minces à l'échelle industrielle grâce à des techniques de pulvérisation magnétron^{47,48,61,62}. En particulier, WO_3 est très souvent utilisé pour l'électrode négative des vitrages électrochromes, car il présente d'excellentes performances en tant que matériau électrochrome, et les mécanismes à l'origine de ses propriétés électrochimiques et optiques sont bien compris. Pour l'électrode positive, l'oxyde d'iridium (IrO_z) et l'oxyde de nickel (NiO_z) sont de bons candidats, là encore grâce à leurs bonnes performances¹⁷⁵. L'oxyde de nickel est cependant moins cher, et est donc plus souvent choisi par les industriels pour leurs vitrages électrochromes¹⁸⁸.

Toutefois, les mécanismes derrière l'électrochromisme de NiO_z sont beaucoup plus controversés que pour WO_3 . Ils sont d'autant plus compliqués à élucider que ces mécanismes changent selon le type d'électrolyte utilisé dans l'appareil électrochrome étudié. Dans les électrolytes aqueux conducteurs de protons, il y a des incertitudes sur les phases formées au cours du processus d'oxydation-réduction de NiO_z ^{202,203,206,207,209}; dans les électrolytes aprotiques conducteurs d'ions lithium (Li^+), la question est plutôt de savoir si l'oxydoréduction repose sur l'insertion ou l'adsorption des ions Li^+ à l'électrode^{181,210,214,216,377}.

En dépit de ce manque de clarté sur le mécanisme électrochrome de NiO_z , de nombreuses recherches sont menées pour améliorer les performances du matériau, notamment en termes de contraste optique et d'efficacité de coloration. Deux types de stratégie se démarquent pour accomplir cet objectif : nanostructurer NiO_z , ou le doper avec d'autres éléments. Situés à l'interface entre ces deux approches, quelques articles présentent des oxydes mixtes lithium-nickel-tungstène, dotés d'une structure nanocomposite : des nanocristaux d'oxyde de nickel entourés d'une matrice amorphe^{243,244}. Ces systèmes nanocomposites sont intéressants car, contrairement à d'autres films nanostructurés décrits dans la littérature, ils peuvent être préparés par pulvérisation magnétron. Ainsi, ils sont faciles à produire à l'échelle industrielle.

Ce manuscrit est ainsi dédié à une étude assez générale des propriétés électrochromes des oxydes mixtes lithium-nickel-tungstène, mais plus spécifiquement à celles d'une de ces couches minces nanocomposites susmentionnées, et aux relations entre la composition, la structure et les propriétés électrochimiques et optiques de cette couche mince. Le système étudié ici est préparé en trois étapes : la pulvérisation magnétron d'une cible métallique Ni-W sous atmosphère Ar/O_2 sur un substrat d'ITO, puis la pulvérisation magnétron d'une couche de Li métallique sous atmosphère inerte d'argon, et enfin un traitement thermique entre 300 et

500 °C, pendant plusieurs minutes, sous air. La couche mince ainsi préparée présente un ratio Li/Ni de 0,7 et un ratio Ni/W ~ 2. Des mesures de microscopie électronique en transmission prouvent qu'elle présente bien une structure nanocomposite, avec des nanoparticules semblables à du NiO cubique (~ 3 nm) prises dans une matrice amorphe. Au niveau de ses propriétés électrochromes, lorsqu'elle est cyclée dans une cellule électrochimique avec du lithium métallique comme contre-électrode, la couche mince réagit sur deux plages de potentiels : à hauts potentiels (2,0 à 4,5 V vs Li⁺/Li), et à bas potentiels (1,0 à 3,0 V vs Li⁺/Li). La première plage de potentiels est associée à la « réaction principale », qui est d'intérêt pour l'application de la couche mince dans des vitrages électrochromes, tandis que la seconde plage de potentiels est associée à des « réactions secondaires », moins utiles pour une application commerciale. Lorsqu'elle est oxydée à haut potentiel, la couche mince passe, de façon réversible, d'un état jaune transparent à un état brun foncé plus opaque. Lorsqu'elle est réduite à bas potentiel, la couche mince devient aussi brun foncé et plus opaque.

Une première stratégie adoptée pour essayer de comprendre un peu mieux les mécanismes de coloration-décoloration dans cette couche mince nanocomposite Li-Ni-W-O a été de synthétiser et d'étudier des poudres de différentes compositions dans le diagramme de phase ternaire Li₂O-NiO-WO₃. Or, au cours de ce processus, un nouveau composé cristallin a été identifiée à l'issue d'une synthèse par voie céramique. Ce composé, Li₂Ni₂W₂O₉, a été synthétisé à l'état pur, puis sa structure cristalline a été caractérisée par diffraction des rayons X synchrotron et diffraction de neutrons. Un affinement des données par la méthode Rietveld²⁵⁴ a permis de modéliser sa structure cristalline : ce composé cristallise dans le groupe d'espace orthorhombique *Pbcn*, et présente une structure lamellaire, dans laquelle s'alternent des feuillets composés de chaînes linéaires d'octaèdres NiO₆ et de dimères W₂O₉, et des feuillets d'octaèdres LiO₆ en nid d'abeilles. Ce modèle structural a pu être confirmé par des mesures de microscopie électronique à transmission. Grâce à cette structure lamellaire, qui rappelle d'autres matériaux d'insertion couramment étudiés dans le domaine des batteries, Li₂Ni₂W₂O₉ présente une activité électrochimique à très hauts potentiels (4,5 à 5,0 V vs Li⁺/Li). Cette activité est associée au couple rédox Ni³⁺/Ni²⁺ et présente une très bonne réversibilité (84 % de rétention de capacité entre le cycle 1 et le cycle 100 d'une expérience de charge-décharge galvanostatique ; 98 % entre le cycle 50 et le cycle 100). Toutefois, la capacité spécifique réversible du matériau est faible, à seulement 34 mA.h.g⁻¹. En dépit de cette faible capacité spécifique, l'oxydoréduction du couple Ni³⁺/Ni²⁺ étant associée à des propriétés électrochromes dans NiO_z, cette activité électrochimique dans Li₂Ni₂W₂O₉ a mené à l'étude de

ses propres propriétés électrochromes. Pour se faire, un montage de microscopie optique en réflexion *operando* a été mis au point, à l'aide d'une cellule électrochimique spécialement conçue pour le suivi des propriétés optiques de l'électrode de travail. Cette expérience a permis tout d'abord de mettre en évidence que $\text{Li}_2\text{Ni}_2\text{W}_2\text{O}_9$, tout comme NiO_z , est un matériau électrochrome anodique, qui perd en transmittance lorsque le Ni^{2+} qu'il contient est oxydé en Ni^{3+} par désinsertion de Li^+ . En outre, une étude des images collectées, à l'échelle de plusieurs centaines de particules de $\text{Li}_2\text{Ni}_2\text{W}_2\text{O}_9$, révèle que les particules plus petites présentent une meilleure réversibilité optique et électrochimique que les particules de plus grande taille. Enfin, une étude à l'échelle de particules isolées montre que même pour les particules de petites tailles, des limitations cinétiques ont l'air d'empêcher une réinsertion complète du lithium, et introduit donc des irréversibilités électrochimiques et optiques²⁴⁶.

Le cas de $\text{Li}_2\text{Ni}_2\text{W}_2\text{O}_9$ est intéressant pour plusieurs raisons. En ce qui concerne la science des matériaux, ce composé pourrait être le point de départ d'une nouvelle famille de matériaux, qui pourrait être développée en substituant le Ni^{2+} par du Co^{2+} ou du Fe^{2+} , par exemple. Ensuite, le fait qu'un oxyde quaternaire présente des propriétés électrochromes est intéressant car cela ouvre la porte vers la recherche de l'électrochromisme dans une plus vaste sélection de matériaux. En effet, la recherche de propriétés électrochromes dans les oxydes de métaux de transition s'est souvent limitée aux oxydes binaires. Enfin, la méthode de microscopie optique *operando* employée pour étudier $\text{Li}_2\text{Ni}_2\text{W}_2\text{O}_9$ pourrait être employée pour étudier d'autres matériaux électrochromes potentiels, mais aussi pour réaliser des études sur les effets de taille ou de morphologie de particules dans des matériaux de cathode pour batterie Li-ion ou Na-ion.

En plus de ses propriétés électrochromes, les propriétés magnétiques de $\text{Li}_2\text{Ni}_2\text{W}_2\text{O}_9$, dues au $\text{Ni}^{2+} 3d^8$ paramagnétique, ont aussi été caractérisées. Le matériau présente un ordre antiferromagnétique, avec une température de Néel à environ 8 K, mesuré par un magnétomètre SQUID. Cependant, ces mêmes mesures, traitées selon le modèle de Curie-Weiss modifié, donnent une température de Curie-Weiss positive, qui est caractéristique d'interactions ferromagnétiques. Pour résoudre cette apparente contradiction, la structure magnétique de $\text{Li}_2\text{Ni}_2\text{W}_2\text{O}_9$ a été caractérisée par des mesures de diffraction des neutrons à basse température, notamment en dessous de la température de Néel. Un travail de modélisation par affinement Rietveld a permis de définir la structure magnétique de $\text{Li}_2\text{Ni}_2\text{W}_2\text{O}_9$ (groupe d'espace magnétique $Pb'c'n'$), et de comprendre l'origine des propriétés magnétiques. Bien que la maille soit globalement antiferromagnétique en dessous de 8 K, de fortes interactions

ferromagnétiques au sein des chaînes de NiO_6 existent. Les interactions chaîne à chaîne, plus faibles, ont à la fois un caractère antiferromagnétique et ferromagnétique, et les interactions d'un feuillet Ni-W-O à un autre sont globalement antiferromagnétiques. Ces observations sur $\text{Li}_2\text{Ni}_2\text{W}_2\text{O}_9$ sont à mettre en regard avec les propriétés magnétiques des composés de la famille des « 429 » ($M_4A_2O_9$; $M = \text{Fe, Co, Mn, Ni, etc.}$; $A = \text{Nb, Ta}$), d'autant plus que la symétrie ponctuelle magnétique de $\text{Li}_2\text{Ni}_2\text{W}_2\text{O}_9$ est compatible avec un effet magnétoélectrique²⁴⁷.

Ayant complété le diagramme de phases ternaire $\text{Li}_2\text{O-NiO-WO}_3$ par la découverte et la caractérisation de $\text{Li}_2\text{Ni}_2\text{W}_2\text{O}_9$, la comparaison de la couche mince nanocomposite Li-Ni-W-O avec des poudres du diagramme de phases a pu se poursuivre. Quatre poudres ont été sélectionnées et synthétisées par voie céramique pour être comparées avec la couche mince : $R\bar{3}$ Li_2WO_4 , $P2/c$ NiWO_4 , $P\bar{1}$ $\text{Li}_2\text{Ni}(\text{WO}_4)_2$, et $Pbcn$ $\text{Li}_2\text{Ni}_2\text{W}_2\text{O}_9$. Ces poudres ont été sélectionnées pour leur proximité, en termes de compositions élémentaires, avec la couche mince Li-Ni-W-O. Le comportement électrochimique de ces quatre poudres a été caractérisé par des expériences de charge-décharge galvanostatique dans des piles bouton. Elles présentent toutes le même point commun : l'absence d'activité électrochimique sur la plage de potentiels associées à la réaction principale de la couche mince, 2,0 V à 4,5 V vs Li^+/Li . Il semblerait donc que cette réaction soit propre à la couche mince et à sa structure nanocomposite. Toutefois, à bas potentiels (1,0 V à 3,0 V), $\text{Li}_2\text{Ni}_2\text{W}_2\text{O}_9$, $\text{Li}_2\text{Ni}(\text{WO}_4)_2$, et NiWO_4 présentent tous des réactions plus ou moins réversibles qui pourraient être associés à des réactions de conversion liées au couple $\text{Ni}^{2+}/\text{Ni}^0$. Cela a introduit la possibilité que les réactions secondaires observées dans la couche mince Li-Ni-W-O soit elles aussi liées à des réactions de conversion du nickel.

Pour confirmer cette hypothèse, des mesures de spectroscopie de photoémission des rayons X ont été réalisées sur les quatre poudres étudiées, sur la couche mince Li-Ni-W-O intacte, et sur des échantillons de couches minces à différents états de charge (mesures *post-mortem*). Il ressort de ces mesures que, dans les couches minces nanocomposite Li-Ni-W-O, du nickel métallique Ni^0 est en effet formé à bas potentiel ($< 1,6$ V vs Li^+/Li), tandis que l'état d'oxydation du W paraît a priori inchangé, restant à W^{6+} . Par ailleurs, bien que ces mesures ne révèlent pas grand-chose sur la réaction principale à hauts potentiels, il est certain que cette réaction est associée au couple $\text{Ni}^{3+}/\text{Ni}^{2+}$, car ni le tungstène, ni le lithium ne peuvent être oxydés. Ainsi, il semblerait que le nickel soit le seul élément électrochimiquement actif de la couche mince nanocomposite Li-Ni-W-O, tandis que le tungstène ne joue qu'un rôle purement structural. De plus, en comparant les capacités électrochimiques dues à la réaction principale

et aux réactions secondaires (4 à 4,5 fois plus élevées que pour la réaction principale), il semble probable que les réactions secondaires impliquent à la fois la matrice amorphe et les nanocristaux de la couche mince.

La comparaison de poudres $\text{Li}_x\text{Ni}_y\text{W}_z\text{O}_n$ (monophasiques, haute cristallinité) avec la couche mince nanocomposite (biphasique, faible cristallinité) est limitée par les grandes différences structurales entre les deux types de systèmes. Pour réaliser une comparaison un peu plus rigoureuse et plus fiable, des couches minces de différentes compositions dans le diagramme de phase ternaire $\text{Li}_2\text{O-NiO-WO}_3$ ont été synthétisées par une méthode d'enduction centrifuge suivie d'un traitement thermique sous air (450 °C, 30 min). Les différents paramètres de cette méthode ont été optimisés, et bien qu'il reste des zones d'ombre sur les réactions qui ont lieu au cours de la préparation de la solution d'enduction, les films obtenus ont une surface continue et semblent de bonne qualité. Les propriétés électrochromes de ces films ont alors été caractérisées par des mesures de charge-décharge galvanostatique couplées à des mesures *operando* de spectroscopie UV-Visible en transmission, grâce à une cellule électrochimique spécialement conçue pour ces mesures. En comparant les couches minces enduites entre elles et avec la couche mince nanocomposite de référence, et en complétant l'étude par des mesures DRX sur des poudres synthétisées à partir des solutions d'enduction, il apparaît que la présence des nanocristaux de NiO_z soit essentielle à la réaction principale qui a lieu à hauts potentiels. Cela semble indiquer que la phase active pour cette réaction principale est l'ensemble des nanocristaux. Toutefois, il semblerait aussi qu'il y ait un juste milieu à trouver entre une proportion trop faible ou trop forte de nanocristaux. S'il n'y en a pas assez, il y a une faible capacité à cause du faible nombre de sites actifs. Mais s'il y en a trop, il est possible que la diffusion des ions Li^+ soient gênée. Cette hypothèse suppose que le rôle de la matrice amorphe est en effet de faciliter la diffusion des ions, ce qui reste à vérifier. D'un point de vue mécanistique, le mécanisme exact associé à la réaction principale reste incertain ; on peut toutefois noter que le comportement de la couche mince nanocomposite Li-Ni-W-O de référence est bien différent de celui rapportée par Da Rocha et Wen^{181,377} pour des couches minces de NiO_z pur. Là où ces derniers rapportent un comportement plutôt pseudocapacitif, une expérience de voltamétrie cyclique à différentes vitesses de balayage sur la couche mince nanocomposite montre qu'elle présente plutôt un comportement qui s'apparente à un matériau d'insertion. Cela pourrait être dû à la présence de la matrice amorphe, dans laquelle les ions Li^+ doivent être insérés et désinsérés.

Globalement, cette thèse, en plus de compléter le diagramme de phase $\text{Li}_2\text{O-NiO-WO}_3$ grâce à la synthèse de $\text{Li}_2\text{Ni}_2\text{W}_2\text{O}_9$, apporte certains éclaircissements sur l'origine des propriétés électrochromes dans les couches minces nanocomposite Li-Ni-W-O sur lesquelles elle se concentre. L'activité électrochimique de ces couches minces est entièrement due à l'oxydoréduction du nickel, entre 1,0 V et 4,5 V vs Li^+/Li . À hauts potentiels, c'est le couple rédox $\text{Ni}^{3+}/\text{Ni}^{2+}$ qui est électrochimiquement actif, tandis qu'à bas potentiels, une réaction de conversion ($\text{Ni}^{2+}/\text{Ni}^0$) impliquant à la fois la matrice amorphe et les nanocristallites a lieu. Cette réaction de conversion peut, à long terme, être néfaste aux performances de la couche mince, et est donc à éviter. L'activité à haut potentiel est, quant à elle, très probablement due aux nanocristaux NiO_z présents dans la couche mince. Même si ce qu'il se produit exactement au niveau de ces nanocristaux restent incertain, le matériau présente un comportement similaire à d'autres matériaux d'insertion, sans doute à cause de la diffusion du lithium à travers la matrice amorphe.

Il reste de nombreuses questions à élucider sur ces couches minces nanocomposites, et l'étude présentée dans ce manuscrit est perfectible de bien des manières. Une caractérisation de la nanostructure des couches minces enduites par microscopie électronique à transmission permettrait de renforcer la théorie sur le compromis entre quantité de nanoparticules et de matrice amorphe. Idéalement, pour que la comparaison entre la couche mince nanocomposite de référence et d'autres compositions de couches minces $\text{Li}_x\text{Ni}_y\text{W}_z\text{O}_n$ soit parfaitement rigoureuse, il faudrait que ces dernières soient préparées en suivant exactement le même procédé de pulvérisation magnétron que la couche mince originale, et non un procédé d'enduction centrifuge. La différence entre les deux procédés introduit forcément des différences structurales et/ou de degré d'oxydation entre l'échantillon de référence et les autres couches minces, qui se traduisent par de grandes différences dans les performances optiques et électrochimiques. Cela a par exemple empêché d'observer de façon rigoureuse l'impact de la composition sur les propriétés colorimétriques des couches minces.

Il reste donc beaucoup à faire pour pleinement comprendre les mécanismes de coloration-décoloration dans les oxydes mixtes lithium-nickel-tungstène. Mais les résultats présentés dans cette thèse apportent de premières pistes qui pourront s'avérer utiles pour de futures recherches sur ces matériaux essentiels pour le développement de vitrages électrochromes.

References

- (1) Calvin, K. et al. IPCC, 2023: Climate Change 2023: Synthesis Report. Contribution of Working Groups I, II and III to the Sixth Assessment Report of the Intergovernmental Panel on Climate Change [Core Writing Team, H. Lee and J. Romero (Eds.)]. IPCC, Geneva, Switzerland., First.; Intergovernmental Panel on Climate Change (IPCC), 2023. <https://doi.org/10.59327/IPCC/AR6-9789291691647>.
- (2) Cabeza, L. F.; Bai, Q.; Bertoldi, P.; Kihila, J. M.; Lucena, A. F. P.; Mata, E.; Mirasgedis, S.; Novikova, A.; Saheb, Y. Buildings. In *Climate Change 2022 - Mitigation of Climate Change*; Intergovernmental Panel On Climate Change (Ipcc), Ed.; Cambridge University Press, 2023; pp 953–1048. <https://doi.org/10.1017/9781009157926.011>.
- (3) Granqvist, C. Electrochromism and Smart Window Design. *Solid State Ion.* **1992**, 53–56, 479–489. [https://doi.org/10.1016/0167-2738\(92\)90418-O](https://doi.org/10.1016/0167-2738(92)90418-O).
- (4) Granqvist, C. G. Electrochromics for Smart Windows: Oxide-Based Thin Films and Devices. *Thin Solid Films* **2014**, 564, 1–38. <https://doi.org/10.1016/j.tsf.2014.02.002>.
- (5) Azens, A.; Granqvist, C. Electrochromic Smart Windows: Energy Efficiency and Device Aspects. *J. Solid State Electrochem.* **2003**, 7 (2), 64–68. <https://doi.org/10.1007/s10008-002-0313-4>.
- (6) Burdis, M. S.; Weir, D. G. J. Electrochromic Devices and Methods. US 2008/0169185 A1, July 17, 2008.
- (7) Gillaspie, D. T.; Weir, D. G. J. Electrochromic Nickel Oxide Simultaneously Doped with Lithium and a Metal Dopant. US 10,514,581 B2, December 24, 2019.
- (8) Brossard, S.; Giron, J.-C.; Leyder, C.; Abreu, J. Electrochromic Device Including a Means for Preventing Ion Migration and a Process of Forming the Same. US 10,303,032 B2, May 28, 2019.
- (9) Platt, J. R. Electrochromism, a Possible Change of Color Producible in Dyes by an Electric Field. *J. Chem. Phys.* **1961**, 34 (3), 862–863. <https://doi.org/10.1063/1.1731686>.
- (10) Fletcher, S. The Definition of Electrochromism. *J. Solid State Electrochem.* **2015**, 19 (11), 3305–3308. <https://doi.org/10.1007/s10008-015-3039-9>.
- (11) Mortimer, R. J. Electrochromic Materials. *Annu. Rev. Mater. Res.* **2011**, 41 (1), 241–268. <https://doi.org/10.1146/annurev-matsci-062910-100344>.
- (12) Kraft, A. What a Chemistry Student Should Know about the History of Prussian Blue. *ChemTexts* **2018**, 4 (4), 16. <https://doi.org/10.1007/s40828-018-0071-2>.
- (13) Weil, M.; Schubert, W.-D. *The Beautiful Colours of Tungsten Oxides*; 2013.
- (14) Berzelius, J. *Afhandlingar i Fysik. Kemi Och Mineral. No IV* **1815**.
- (15) Monk, P.; Mortimer, R.; Rosseinsky, D. *Electrochromism and Electrochromic Devices*, 1st ed.; Cambridge University Press, 2007. <https://doi.org/10.1017/CBO9780511550959>.
- (16) Wöhler, F. Natriumwolframbronzen. *Ann Phys* **1824**, 2, 350–358.

- (17) Smith, R.; Bain, A. Improvement in Electro-Chemical Telegraphs. US6837A, October 30, 1849.
- (18) Hutchison, M. R. Electrographic Display Apparatus and Method. US1068774A, July 29, 1913.
- (19) Kobosew, N.; Nekrassow, N. Formation of Free Hydrogen Atoms in the Cathode Polarisation of Metals. *Z. Elektrochem. Angew. Phys. Chem.* **1930**, 36, 529–544.
- (20) Talmey, P. Electrolytic Recording Paper. US2281013A, April 28, 1942.
- (21) Talmey, P. Electrolytic Recording. US2319765A, May 18, 1943.
- (22) Brimm, E.; Brantley, J.; Lorenz, J.; Jellinek, M. Sodium and Potassium Tungsten Bronzes. *J. Am. Chem. Soc.* **1951**, 73 (11), 5427–5432.
- (23) Deb, S. K. A Novel Electrophotographic System. *Appl. Opt.* **1969**, 8 (S1), 192. <https://doi.org/10.1364/AO.8.S1.000192>.
- (24) Deb, S. K. Reminiscences on the Discovery of Electrochromic Phenomena in Transition Metal Oxides. *Sol. Energy Mater. Sol. Cells* **1995**, 39 (2–4), 191–201. [https://doi.org/10.1016/0927-0248\(95\)00055-0](https://doi.org/10.1016/0927-0248(95)00055-0).
- (25) Deb, S. K. Optical and Photoelectric Properties and Colour Centres in Thin Films of Tungsten Oxide. *Philos. Mag.* **1973**, 27 (4), 801–822. <https://doi.org/10.1080/14786437308227562>.
- (26) Deb, S. K.; Shaw, R. F. Electro-Optical Device Having Variable Optical Density. US3521941A, July 28, 1970.
- (27) Granqvist, C. G. *Handbook of Inorganic Electrochromic Materials*; Elsevier: Amsterdam ; New York, 1995.
- (28) Granqvist, C. G. Electrochromics for Smart Windows: Oxide-Based Thin Films and Devices. *Thin Solid Films* **2014**, 564, 1–38. <https://doi.org/10.1016/j.tsf.2014.02.002>.
- (29) Kamimori, T.; Nagai, J.; Mizuhashi, M. Electrochromic Devices for Transmissive and Reflective Light Control. *Sol. Energy Mater.* **1987**, 16 (1), 27–38. [https://doi.org/10.1016/0165-1633\(87\)90005-0](https://doi.org/10.1016/0165-1633(87)90005-0).
- (30) Klingler, M.; Chu, W. F.; Weppner, W. Three-Layer Electrochromic System. *Sol. Energy Mater. Sol. Cells* **1995**, 39 (2–4), 247–255. [https://doi.org/10.1016/0927-0248\(95\)00061-5](https://doi.org/10.1016/0927-0248(95)00061-5).
- (31) Percec, S.; Tilford, S. A Single-layer Approach to Electrochromic Materials. *J. Polym. Sci. Part Polym. Chem.* **2011**, 49 (2), 361–368. <https://doi.org/10.1002/pola.24433>.
- (32) Kavanagh, A.; Fraser, K. J.; Byrne, R.; Diamond, D. An Electrochromic Ionic Liquid: Design, Characterization, and Performance in a Solid-State Platform. *ACS Appl. Mater. Interfaces* **2013**, 5 (1), 55–62. <https://doi.org/10.1021/am3018948>.

- (33) Gy, R.; Giron, J.-C.; Yeh, L.-Y.; Letocart, P.; Andreau-Wiedenmaier, A.; Armand, P. Electrochemical Glazing Having Electrically Controllable Optical and Energy-Related Properties. US 2023/0393385 A1, December 7, 2023.
- (34) Rozbicki, R. T.; Kailasam, S. K.; Friedman, R. S.; Gillaspie, D. T.; Pradhan, A. A.; Mehtani, D. Fabrication of Electrochromic Devices. US 2023/0314892 A1, October 5, 2023.
- (35) Karmhag, R.; Gregard, G.; Vogt, R. Electrochromic Devices and Manufacturing Methods Thereof. US 10,012,887 B2, July 3, 2018.
- (36) Jeong, C. Y.; Kubota, T.; Tajima, K.; Kitamura, M.; Imai, H. Complementary Electrochromic Devices Based on Acrylic Substrates for Smart Window Applications in Aircrafts. *Mater. Chem. Phys.* **2022**, *277*, 125460. <https://doi.org/10.1016/j.matchemphys.2021.125460>.
- (37) Laurenti, M.; Bianco, S.; Castellino, M.; Garino, N.; Virga, A.; Pirri, C. F.; Mandracci, P. Toward Plastic Smart Windows: Optimization of Indium Tin Oxide Electrodes for the Synthesis of Electrochromic Devices on Polycarbonate Substrates. *ACS Appl. Mater. Interfaces* **2016**, *8* (12), 8032–8042. <https://doi.org/10.1021/acsami.6b00988>.
- (38) Greer, B. D.; Snyder, M. O. Set of Window Assemblies and a Method of Fabricating the Same. US10666189B2, May 26, 2020.
- (39) Jensen, J.; Hösel, M.; Kim, I.; Yu, J.; Jo, J.; Krebs, F. C. Fast Switching ITO Free Electrochromic Devices. *Adv. Funct. Mater.* **2014**, *24* (9), 1228–1233. <https://doi.org/10.1002/adfm.201302320>.
- (40) Zhao, Y.; Zhang, X.; Li, W.; Li, Z.; Zhang, H.; Chen, M.; Sun, W.; Xiao, Y.; Zhao, J.; Li, Y. High-Performance Electrochromic WO₃ Film Driven by Controllable Crystalline Structure and Its All-Solid-State Device. *Sol. Energy Mater. Sol. Cells* **2022**, *237*, 111564. <https://doi.org/10.1016/j.solmat.2021.111564>.
- (41) Burheim, O. S. Secondary Batteries. In *Engineering Energy Storage*; Elsevier, 2017; pp 111–145. <https://doi.org/10.1016/B978-0-12-814100-7.00007-9>.
- (42) Macêdo, M. A.; Dall'Antonia, L. H.; Valla, B.; Aegerter, M. A. Electrochromic Smart Windows. *J. Non-Cryst. Solids* **1992**, *147–148*, 792–798. [https://doi.org/10.1016/S0022-3093\(05\)80718-5](https://doi.org/10.1016/S0022-3093(05)80718-5).
- (43) Macrelli, G.; Poli, E. Mixed Cerium/Titanium and Cerium/Zirconium Oxides as Thin Film Counter Electrodes for All Solid State Electrochromic Transmissive Devices. *Electrochimica Acta* **1999**, *44* (18), 3137–3147. [https://doi.org/10.1016/S0013-4686\(99\)00031-6](https://doi.org/10.1016/S0013-4686(99)00031-6).
- (44) Berton, M. A. C.; Avellaneda, C. O.; Bulhões, L. O. S. Thin Film of CeO₂-SiO₂: A New Ion Storage Layer for Smart Windows. *Sol. Energy Mater. Sol. Cells* **2003**, *80* (4), 443–449. <https://doi.org/10.1016/j.solmat.2003.08.012>.
- (45) Ottermann, C. R.; Temmink, A.; Bange, K. Comparison of Tungsten and Nickel Oxide Electrochromism in Single Films and in All-Solid-State Devices. *Thin Solid Films* **1990**, *193–194*, 409–417. [https://doi.org/10.1016/S0040-6090\(05\)80051-3](https://doi.org/10.1016/S0040-6090(05)80051-3).

- (46) Da Rocha, M.; Rougier, A. Electrochromism of Non-Stoichiometric NiO Thin Film: As Single Layer and in Full Device. *Appl. Phys. A* **2016**, 122 (4), 370. <https://doi.org/10.1007/s00339-016-9923-z>.
- (47) Giron, J.-C.; Bouzy, L.; Chevallier, T.; Patissier, A.; Mercadier, N. A. Electrochromic Device Including a Means for Mechanical Resistance and a Process of Forming the Same. US2022121077A1, April 21, 2022.
- (48) Nguyen, P. P.; Liu, S. Electrochromic Device and Method for Making Electrochromic Device. US2018307110A1, October 25, 2018.
- (49) Cui, Y.; Wang, Q.; Yang, G.; Gao, Y. Electronic Properties, Optical Properties and Diffusion Behavior of WO₃ with H⁺, Li⁺ and Na⁺ Intercalated Ions: A First-Principles Study. *J. Solid State Chem.* **2021**, 297, 122082. <https://doi.org/10.1016/j.jssc.2021.122082>.
- (50) Fernandes, M.; Leones, R.; Pereira, S.; Costa, A. M. S.; Mano, J. F.; Silva, M. M.; Fortunato, E.; De Zea Bermudez, V.; Rego, R. Eco-Friendly Sol-Gel Derived Sodium-Based Ormolytes for Electrochromic Devices. *Electrochimica Acta* **2017**, 232, 484–494. <https://doi.org/10.1016/j.electacta.2017.02.098>.
- (51) Li, R. et al. Ion-Transport Design for High-Performance Na⁺-Based Electrochromics. *ACS Nano* **2018**, 12 (4), 3759–3768. <https://doi.org/10.1021/acsnano.8b00974>.
- (52) Sivakumar, R.; Shanthakumari, K.; Thayumanavan, A.; Jayachandran, M.; Sanjeeviraja, C. Coloration and Bleaching Mechanism of Tungsten Oxide Thin Films in Different Electrolytes. *Surf. Eng.* **2007**, 23 (5), 373–379. <https://doi.org/10.1179/174329407X247181>.
- (53) Gershinsky, G.; Yoo, H. D.; Gofer, Y.; Aurbach, D. Electrochemical and Spectroscopic Analysis of Mg²⁺ Intercalation into Thin Film Electrodes of Layered Oxides: V₂O₅ and MoO₃. *Langmuir* **2013**, 29 (34), 10964–10972. <https://doi.org/10.1021/la402391f>.
- (54) Bell, J. M.; Matthews, J. P.; Skryabin, I. L.; Wang, J.; Monsma, B. G. Sol-Gel Deposited Electrochromic Devices. *Renew. Energy* **1998**, 15 (1–4), 312–317. [https://doi.org/10.1016/S0960-1481\(98\)00179-7](https://doi.org/10.1016/S0960-1481(98)00179-7).
- (55) Livage, J.; Ganguli, D. Sol–Gel Electrochromic Coatings and Devices: A Review. *Sol. Energy Mater. Sol. Cells* **2001**, 68 (3), 365–381. [https://doi.org/10.1016/S0927-0248\(00\)00369-X](https://doi.org/10.1016/S0927-0248(00)00369-X).
- (56) Rakibuddin, M.; Shinde, M. A.; Kim, H. Sol-Gel Fabrication of NiO and NiO/WO₃ Based Electrochromic Device on ITO and Flexible Substrate. *Ceram. Int.* **2020**, 46 (7), 8631–8639. <https://doi.org/10.1016/j.ceramint.2019.12.096>.
- (57) White, C. M.; Gillaspie, D. T.; Whitney, E.; Lee, S.-H.; Dillon, A. C. Flexible Electrochromic Devices Based on Crystalline WO₃ Nanostructures Produced with Hot-Wire Chemical Vapor Deposition. *Thin Solid Films* **2009**, 517 (12), 3596–3599. <https://doi.org/10.1016/j.tsf.2009.01.033>.

- (58) Yeh, W. Y. W.; Matsumura, M. M. M. Chemical Vapor Deposition of Nickel Oxide Films from Bis- π -Cyclopentadienyl-Nickel. *Jpn. J. Appl. Phys.* **1997**, 36 (11R), 6884. <https://doi.org/10.1143/JJAP.36.6884>.
- (59) El Bachiri, A.; Soussi, L.; Karzazi, O.; Louardi, A.; Rmili, A.; Erguig, H.; El Idrissi, B. Electrochromic and Photoluminescence Properties of Cobalt Oxide Thin Films Prepared by Spray Pyrolysis. *Spectrosc. Lett.* **2019**, 52 (1), 66–73. <https://doi.org/10.1080/00387010.2018.1556221>.
- (60) Romero, R.; Dalchiele, E. A.; Martín, F.; Leinen, D.; Ramos-Barrado, J. R. Electrochromic Behaviour of Nb₂O₅ Thin Films with Different Morphologies Obtained by Spray Pyrolysis. *Sol. Energy Mater. Sol. Cells* **2009**, 93 (2), 222–229. <https://doi.org/10.1016/j.solmat.2008.10.012>.
- (61) Buch, V. R.; Chawla, A. K.; Rawal, S. K. Review on Electrochromic Property for WO₃ Thin Films Using Different Deposition Techniques. *Mater. Today Proc.* **2016**, 3 (6), 1429–1437. <https://doi.org/10.1016/j.matpr.2016.04.025>.
- (62) Song, X.; Dong, G.; Gao, F.; Xiao, Y.; Liu, Q.; Diao, X. Properties of NiO_x and Its Influence upon All-Thin-Film ITO/NiO_x/LiTaO₃/WO₃/ITO Electrochromic Devices Prepared by Magnetron Sputtering. *Vacuum* **2015**, 111, 48–54. <https://doi.org/10.1016/j.vacuum.2014.09.007>.
- (63) Porqueras, I.; Bertran, E. Electrochromic Behaviour of Nickel Oxide Thin Films Deposited by Thermal Evaporation. *Thin Solid Films* **2001**, 398–399, 41–44. [https://doi.org/10.1016/S0040-6090\(01\)01301-3](https://doi.org/10.1016/S0040-6090(01)01301-3).
- (64) Wang, C.-H.; Yen, H.-K.; Yang, S.-M.; Lu, K.-C. Catalyst-Free Synthesis of Tungsten Oxide Nanowires via Thermal Evaporation for Fast-Response Electrochromic Devices. *CrystEngComm* **2022**, 24 (47), 8213–8218. <https://doi.org/10.1039/D2CE01269C>.
- (65) Iida, Y.; Kaneko, Y.; Kanno, Yoshinori. Fabrication of Pulsed-Laser Deposited V₂O₅ Thin Films for Electrochromic Devices. *J. Mater. Process. Technol.* **2008**, 197 (1–3), 261–267. <https://doi.org/10.1016/j.jmatprotec.2007.06.032>.
- (66) Liu, Y.; Jiang, N.; Liu, Y.; Cui, D.; Yu, C.-F.; Liu, H.; Li, Z. Effect of Laser Power Density on the Electrochromic Properties of WO₃ Films Obtained by Pulsed Laser Deposition. *Ceram. Int.* **2021**, 47 (16), 22416–22423. <https://doi.org/10.1016/j.ceramint.2021.04.251>.
- (67) Fu, Z.; Wei, Y.; Liu, W.; Li, J.; Li, J.; Ma, Y.; Zhang, X.; Yan, Y. Investigation of Electrochromic Device Based on Multi-Step Electrodeposited PB Films. *Ionics* **2021**, 27 (10), 4419–4427. <https://doi.org/10.1007/s11581-021-04156-0>.
- (68) Pham, N. S.; Seo, Y. H.; Park, E.; Nguyen, T. D. D.; Shin, I.-S. Implementation of High-Performance Electrochromic Device Based on All-Solution-Fabricated Prussian Blue and Tungsten Trioxide Thin Film. *Electrochimica Acta* **2020**, 353, 136446. <https://doi.org/10.1016/j.electacta.2020.136446>.
- (69) Waits, R. K. Planar Magnetron Sputtering. *J. Vac. Sci. Technol.* **1978**, 15 (2), 179–187. <https://doi.org/10.1116/1.569451>.

- (70) Greene, J. E. Review Article: Tracing the Recorded History of Thin-Film Sputter Deposition: From the 1800s to 2017. *J. Vac. Sci. Technol. Vac. Surf. Films* **2017**, 35 (5), 05C204. <https://doi.org/10.1116/1.4998940>.
- (71) Mattox, D. M. The Low Pressure Plasma Processing Environment. In *Handbook of Physical Vapor Deposition (PVD) Processing*; Elsevier, 2010; pp 157–193. <https://doi.org/10.1016/B978-0-8155-2037-5.00005-8>.
- (72) Zhao, Y.; Zhang, X.; Chen, X.; Li, W.; Wang, L.; Li, Z.; Zhao, J.; Endres, F.; Li, Y. Preparation of Sn-NiO Films and All-Solid-State Devices with Enhanced Electrochromic Properties by Magnetron Sputtering Method. *Electrochimica Acta* **2021**, 367, 137457. <https://doi.org/10.1016/j.electacta.2020.137457>.
- (73) Reddy, A. S.; Uthanna, S.; Reddy, P. S. Properties of Dc Magnetron Sputtered Cu₂O Films Prepared at Different Sputtering Pressures. *Appl. Surf. Sci.* **2007**, 253 (12), 5287–5292. <https://doi.org/10.1016/j.apsusc.2006.11.051>.
- (74) Meng, L.; dos Santos, M. P. Properties of Indium Tin Oxide Films Prepared by Rf Reactive Magnetron Sputtering at Different Substrate Temperature. *Thin Solid Films* **1998**, 322 (1), 56–62. [https://doi.org/10.1016/S0040-6090\(97\)00939-5](https://doi.org/10.1016/S0040-6090(97)00939-5).
- (75) Pooyodying, P.; Ok, J.-W.; Son, Y.; Sung, Y.-M. Electrical and Optical Properties of Electrochromic Device with WO₃:Mo Film Prepared by RF Magnetron Co-Sputtering. *Opt. Mater.* **2021**, 112, 110766. <https://doi.org/10.1016/j.optmat.2020.110766>.
- (76) Liu, Q.; Dong, G.; Xiao, Y.; Gao, F.; Wang, M.; Wang, Q.; Wang, S.; Zuo, H.; Diao, X. An All-Thin-Film Inorganic Electrochromic Device Monolithically Fabricated on Flexible PET/ITO Substrate by Magnetron Sputtering. *Mater. Lett.* **2015**, 142, 232–234. <https://doi.org/10.1016/j.matlet.2014.11.151>.
- (77) Dong, D.; Wang, W.; Dong, G.; Zhou, Y.; Wu, Z.; Wang, M.; Liu, F.; Diao, X. Electrochromic Properties of NiO_x:H Films Deposited by DC Magnetron Sputtering for ITO/NiO_x:H/ZrO₂/WO₃/ITO Device. *Appl. Surf. Sci.* **2015**, 357, 799–805. <https://doi.org/10.1016/j.apsusc.2015.09.056>.
- (78) Chang, I. F.; Gilbert, B. L.; Sun, T. I. Electrochromic Systems for Display Applications. *J. Electrochem. Soc.* **1975**, 122 (7), 955–962. <https://doi.org/10.1149/1.2134377>.
- (79) Goodman, L. Passive Liquid Displays: Liquid Crystals, Electrophoretics, and Electrochromics. *IEEE Trans. Consum. Electron.* **1975**, CE-21 (3), 247–259. <https://doi.org/10.1109/TCE.1975.266744>.
- (80) Chang, I. F.; Howard, W. E. Performance Characteristics of Electrochromic Displays. *IEEE Trans. Electron Devices* **1975**, 22 (9), 749–758. <https://doi.org/10.1109/T-ED.1975.18215>.
- (81) McAtamney, C.; Pichot, F.; O’Flaherty, A.; Leyland, N.; Rao, S. N.; Stobie, N.; Kinsella, M.; Corr, D.; Bach, U. *Electrochromic Paper-Quality Displays*; Glynn, T. J., Ed.; Galway, Ireland, 2003; p 796. <https://doi.org/10.1117/12.481096>.

- (82) Müller, H.; Colley, A.; Häkkinä, J.; Jensen, W.; Löchtfeld, M. Using Electrochromic Displays to Display Ambient Information and Notifications. In Adjunct Proceedings of the 2019 ACM International Joint Conference on Pervasive and Ubiquitous Computing and Proceedings of the 2019 ACM International Symposium on Wearable Computers; ACM: London United Kingdom, 2019; pp 1075–1078. <https://doi.org/10.1145/3341162.3344844>.
- (83) Zhang, W.; Li, H.; Elezzabi, A. Y. Electrochromic Displays Having Two-Dimensional CIE Color Space Tunability. *Adv. Funct. Mater.* **2022**, 32 (7), 2108341. <https://doi.org/10.1002/adfm.202108341>.
- (84) Tonar, W. I.; Forgette, J. A.; Anderson, J. S.; Bechtel, J. H.; Carter, J. W.; Stam, J. S.; Cammenga, D. J. Electrochromic Rearview Mirror Incorporating a Third Surface Reflector. US 2009/0040588 A1, February 12, 2009.
- (85) Buyan, M.; Brühwiler, P. A.; Azens, A.; Gustavsson, G.; Karmhag, R.; Granqvist, C. G. Facial Warming and Tinted Helmet Visors. *Int. J. Ind. Ergon.* **2006**, 36 (1), 11–16. <https://doi.org/10.1016/j.ergon.2005.06.005>.
- (86) Ma, C.; Taya, M.; Xu, C. Smart Sunglasses Based on Electrochromic Polymers. *Polym. Eng. Sci.* **2008**, 48 (11), 2224–2228. <https://doi.org/10.1002/pen.21169>.
- (87) Vasiliev, E. V.; Zalkin, P. A.; Kruglikov, N. V.; Lorentzen, C. Wearable Electro-Optical Device Using Electrochromic Layer. US 2023/0251506 A1, August 10, 2023.
- (88) Larson, C.; Covington, L.; Shi, Z.; Du, L. Glasses with Customizable Tint-Adjusting Experience. US20240142802A1, May 2, 2024.
- (89) Braig, A.; Meisel, T. A Revolution in Thermal Control of Spacecraft. *Dornier Post* **1992**, 2, 29.
- (90) Demiryont, H.; Moorehead, D. Electrochromic Emissivity Modulator for Spacecraft Thermal Management. *Sol. Energy Mater. Sol. Cells* **2009**, 93 (12), 2075–2078. <https://doi.org/10.1016/j.solmat.2009.02.025>.
- (91) Teissier, A.; Dudon, J.-P.; Aubert, P.-H.; Vidal, F.; Remaury, S.; Crouzet, J.; Chevrot, C. Feasibility of Conducting Semi-IPN with Variable Electro-Emissivity: A Promising Way for Spacecraft Thermal Control. *Sol. Energy Mater. Sol. Cells* **2012**, 99, 116–122. <https://doi.org/10.1016/j.solmat.2011.06.017>.
- (92) Dusk. Ampere. <https://ampere.shop/products/dusk-electrochromic-smart-sunglasses> (accessed 2024-05-28).
- (93) Data center MRS2 | SageGlass. <https://www.sageglass.com/fr/%C3%A9tudes-de-cas/data-center-mrs2> (accessed 2024-05-28).
- (94) Solutions with Printed E-Paper | Ynvisible. <https://www.ynvisible.com/solutions> (accessed 2024-05-28).
- (95) Germid auto dimming rear view mirror. http://www.germid.cn/10_inch_auto_dimming_rear_view_mirror_compass_temperature_ad_10dct.html (accessed 2024-08-20).

- (96) Tällberg, R.; Jelle, B. P.; Loonen, R.; Gao, T.; Hamdy, M. Comparison of the Energy Saving Potential of Adaptive and Controllable Smart Windows: A State-of-the-Art Review and Simulation Studies of Thermochromic, Photochromic and Electrochromic Technologies. *Sol. Energy Mater. Sol. Cells* **2019**, 200, 109828. <https://doi.org/10.1016/j.solmat.2019.02.041>.
- (97) Piccolo, A.; Marino, C.; Nucara, A.; Pietrafesa, M. Energy Performance of an Electrochromic Switchable Glazing: Experimental and Computational Assessments. *Energy Build.* **2018**, 165, 390–398. <https://doi.org/10.1016/j.enbuild.2017.12.049>.
- (98) Dussault, J.-M.; Gosselin, L. Office Buildings with Electrochromic Windows: A Sensitivity Analysis of Design Parameters on Energy Performance, and Thermal and Visual Comfort. *Energy Build.* **2017**, 153, 50–62. <https://doi.org/10.1016/j.enbuild.2017.07.046>.
- (99) Casini, M. Active Dynamic Windows for Buildings: A Review. *Renew. Energy* **2018**, 119, 923–934. <https://doi.org/10.1016/j.renene.2017.12.049>.
- (100) Kato, K.; Song, P. K.; Odaka, H.; Shigesato, Y. Study on Thermochromic VO₂ Films Grown on ZnO-Coated Glass Substrates for “Smart Windows.” *Jpn. J. Appl. Phys.* **2003**, 42 (Part 1, No. 10), 6523–6531. <https://doi.org/10.1143/JJAP.42.6523>.
- (101) Bechinger, C.; Ferrere, S.; Zaban, A.; Sprague, J.; Gregg, B. A. Photoelectrochromic Windows and Displays. *Nature* **1996**, 383 (6601), 608–610. <https://doi.org/10.1038/383608a0>.
- (102) Mäkitalo, J. Simulating Control Strategies of Electrochromic Windows: Impacts on Indoor Climate and Energy Use in an Office Building., 2013.
- (103) Feng, W.; Zou, L.; Gao, G.; Wu, G.; Shen, J.; Li, W. Gasochromic Smart Window: Optical and Thermal Properties, Energy Simulation and Feasibility Analysis. *Sol. Energy Mater. Sol. Cells* **2016**, 144, 316–323. <https://doi.org/10.1016/j.solmat.2015.09.029>.
- (104) Llordés, A.; Garcia, G.; Gazquez, J.; Milliron, D. J. Tunable Near-Infrared and Visible-Light Transmittance in Nanocrystal-in-Glass Composites. *Nature* **2013**, 500 (7462), 323–326. <https://doi.org/10.1038/nature12398>.
- (105) Mukherjee, S.; Hsieh, W. L.; Smith, N.; Goulding, M.; Heikenfeld, J. Electrokinetic Pixels with Biprimary Inks for Color Displays and Color-Temperature-Tunable Smart Windows. *Appl. Opt.* **2015**, 54 (17), 5603–5609. <https://doi.org/10.1364/AO.54.005603>.
- (106) Shian, S.; Clarke, D. R. Electrically Tunable Window Device. *Opt. Lett.* **2016**, 41 (6), 1289–1292. <https://doi.org/10.1364/OL.41.001289>.
- (107) Dussault, J.-M.; Gosselin, L.; Galstian, T. Integration of Smart Windows into Building Design for Reduction of Yearly Overall Energy Consumption and Peak Loads. *Sol. Energy* **2012**, 86 (11), 3405–3416. <https://doi.org/10.1016/j.solener.2012.07.016>.
- (108) DeForest, N.; Shehabi, A.; Selkowitz, S.; Milliron, D. J. A Comparative Energy Analysis of Three Electrochromic Glazing Technologies in Commercial and Residential Buildings. *Appl. Energy* **2017**, 192, 95–109. <https://doi.org/10.1016/j.apenergy.2017.02.007>.
- (109) Lee, E. S.; DiBartolomeo, D. L.; Selkowitz, S. E. Daylighting Control Performance of a Thin-Film Ceramic Electrochromic Window: Field Study Results. *Energy Build.* **2006**, 38 (1), 30–44. <https://doi.org/10.1016/j.enbuild.2005.02.009>.

- (110) Hunt, R. W. G.; Pointer, M. *Measuring Colour*, 4th ed.; The Wiley-IS & T series in imaging science and technology; Wiley: Hoboken, NJ, 2011.
- (111) International Commission On Illumination (Cie). CIE Standard Illuminant D65, 2022. <https://doi.org/10.25039/CIE.DS.hjfjmt59>.
- (112) Vos, J. J. Colorimetric and Photometric Properties of a 2° Fundamental Observer. *Color Res. Appl.* **1978**, 3 (3), 125–128. <https://doi.org/10.1002/col.5080030309>.
- (113) International Commission On Illumination (Cie). CIE Spectral Luminous Efficiency for Photopic Vision, 2019. <https://doi.org/10.25039/CIE.DS.dktna2s3>.
- (114) *Colorimetry*, 4th edition.; Internationale Beleuchtungskommission, Ed.; Technical report; Commission Internationale de l’Eclairage: Vienna, 2018.
- (115) Michaelis, L.; Hill, E. S. THE VIOLOGEN INDICATORS. *J. Gen. Physiol.* **1933**, 16 (6), 859–873. <https://doi.org/10.1085/jgp.16.6.859>.
- (116) Monk, P. M. S.; Rosseinsky, D. R.; Mortimer, R. J. Electrochromic Materials and Devices Based on Viologens. In *Electrochromic Materials and Devices*; Mortimer, R. J., Rosseinsky, D. R., Monk, P. M. S., Eds.; Wiley, 2013; pp 57–90. <https://doi.org/10.1002/9783527679850.ch3>.
- (117) Bird, C. L.; Kuhn, A. T. Electrochemistry of the Viologens. *Chem. Soc. Rev.* **1981**, 10 (1), 49–82. <https://doi.org/10.1039/CS9811000049>.
- (118) Mortimer, R. J.; Reynolds, J. R. An inSitu Colorimetric Measurement Study of Electrochromism in the Di-n-Heptyl Viologen System. *Displays* **2008**, 29 (5), 424–431. <https://doi.org/10.1016/j.displa.2008.02.002>.
- (119) Su, Y.; Yang, F.; Zhou, L.; Geng, Y.; Zhang, J.; Jiang, M. Flexible and Tailorable Alkylviologen/Cellulose Nanocrystals Composite Films for Sustainable Applications in Electrochromic Devices. *ChemElectroChem* **2018**, 5 (10), 1407–1414. <https://doi.org/10.1002/celc.201800113>.
- (120) Wang, J.; Wang, J.-F.; Chen, M.; Qian, D.-J.; Liu, M. Fabrication, Characterization, Electrochemistry, and Redox-Induced Electrochromism of Viologen-Functionalized Silica Core-Shell Nano-Composites. *Electrochimica Acta* **2017**, 251, 562–572. <https://doi.org/10.1016/j.electacta.2017.08.169>.
- (121) Corr, D.; Bach, U.; Fay, D.; Kinsella, M.; McAtamney, C.; O’Reilly, F.; Rao, S. N.; Stobie, N. Coloured Electrochromic “Paper-Quality” Displays Based on Modified Mesoporous Electrodes. *Solid State Ion.* **2003**, 165 (1), 315–321. <https://doi.org/10.1016/j.ssi.2003.08.054>.
- (122) Byker, H. J. Single-Compartment, Self-Erasing, Solution-Phase Electrochromic Devices, Solutions for Use Therein, and Uses Thereof. US4902108 (A), February 20, 1990. <https://worldwide.espacenet.com/publicationDetails/biblio?FT=D&date=19900220&DB=EP&DOC=US4902108A&CC=US&NR=4902108A&KC=A&ND=4> (accessed 2024-06-06).
- (123) Furukawa, Y. Electronic Absorption and Vibrational Spectroscopies of Conjugated Conducting Polymers. *J. Phys. Chem.* **1996**, 100 (39), 15644–15653. <https://doi.org/10.1021/jp960608n>.

- (124) Shirakawa, H.; Louis, E. J.; MacDiarmid, A. G.; Chiang, C. K.; Heeger, A. J. Synthesis of Electrically Conducting Organic Polymers: Halogen Derivatives of Polyacetylene, (CH)_x. *J. Chem. Soc. Chem. Commun.* **1977**, No. 16, 578–580. <https://doi.org/10.1039/C39770000578>.
- (125) Shin, H.; Kim, Y.; Bhuvana, T.; Lee, J.; Yang, X.; Park, C.; Kim, E. Color Combination of Conductive Polymers for Black Electrochromism. *ACS Appl. Mater. Interfaces* **2012**, 4 (1), 185–191. <https://doi.org/10.1021/am201229k>.
- (126) Kim, E.; Jung, S. Layer-by-Layer Assembled Electrochromic Films for All-Solid-State Electrochromic Devices. *Chem. Mater.* **2005**, 17 (25), 6381–6387. <https://doi.org/10.1021/cm051492n>.
- (127) Girotto, E. M.; de Paoli, M.-A. Polypyrrole Color Modulation and Electrochromic Contrast Enhancement by Doping with a Dye. *Adv. Mater.* **1998**, 10 (10), 790–793. [https://doi.org/10.1002/\(SICI\)1521-4095\(199807\)10:10<790::AID-ADMA790>3.0.CO;2-R](https://doi.org/10.1002/(SICI)1521-4095(199807)10:10<790::AID-ADMA790>3.0.CO;2-R).
- (128) Zhang, J.; Tu, J.; Zhang, D.; Qiao, Y.; Xia, X.; Wang, X.; Gu, C. Multicolor Electrochromic Polyaniline–WO₃ Hybrid Thin Films: One-Pot Molecular Assembling Synthesis. *J. Mater. Chem.* **2011**, 21 (43), 17316–17324. <https://doi.org/10.1039/C1JM13069B>.
- (129) Camurlu, P. Polypyrrole Derivatives for Electrochromic Applications. *RSC Adv.* **2014**, 4 (99), 55832–55845. <https://doi.org/10.1039/C4RA11827H>.
- (130) Howard, E. L.; Österholm, A. M.; Shen, D. E.; Panchumarti, L. P.; Pinheiro, C.; Reynolds, J. R. Cost-Effective, Flexible, and Colorful Dynamic Displays: Removing Underlying Conducting Layers from Polymer-Based Electrochromic Devices. *ACS Appl. Mater. Interfaces* **2021**, 13 (14), 16732–16743. <https://doi.org/10.1021/acsami.1c00463>.
- (131) Argun, A. A.; Aubert, P.-H.; Thompson, B. C.; Schwendeman, I.; Gaupp, C. L.; Hwang, J.; Pinto, N. J.; Tanner, D. B.; MacDiarmid, A. G.; Reynolds, J. R. Multicolored Electrochromism in Polymers: Structures and Devices. *Chem. Mater.* **2004**, 16 (23), 4401–4412. <https://doi.org/10.1021/cm049669l>.
- (132) Ma, C.; Taya, M.; Xu, C. Flexible Electrochromic Device Based on Poly (3,4-(2,2-Dimethylpropylenedioxy)Thiophene). *Electrochimica Acta* **2008**, 54 (2), 598–605. <https://doi.org/10.1016/j.electacta.2008.07.049>.
- (133) Zhou, Q.; Pan, M.; He, Q.; Tang, Q.; Chow, C.; Gong, C. Electrochromic Behavior of Fac-Tricarbonyl Rhenium Complexes. *New J. Chem.* **2022**, 46 (3), 1072–1079. <https://doi.org/10.1039/D1NJ04955K>.
- (134) Banasz, R.; Wałęsa-Chorab, M. Polymeric Complexes of Transition Metal Ions as Electrochromic Materials: Synthesis and Properties. *Coord. Chem. Rev.* **2019**, 389, 1–18. <https://doi.org/10.1016/j.ccr.2019.03.009>.
- (135) Kung, C.-W. et al. Metal–Organic Framework Thin Films Composed of Free-Standing Acicular Nanorods Exhibiting Reversible Electrochromism. *Chem. Mater.* **2013**, 25 (24), 5012–5017. <https://doi.org/10.1021/cm403726v>.

- (136) Zhang, N.; Jin, Y.; Zhang, Q.; Liu, J.; Zhang, Y.; Wang, H. Direct Fabrication of Electrochromic Ni-MOF 74 Film on ITO with High-Stable Performance. *Ionics* **2021**, *27* (8), 3655–3662. <https://doi.org/10.1007/s11581-021-04112-y>.
- (137) Neff, V. D. Electrochemical Oxidation and Reduction of Thin Films of Prussian Blue. *J. Electrochem. Soc.* **1978**, *125* (6), 886. <https://doi.org/10.1149/1.2131575>.
- (138) Itaya, K.; Uchida, I.; Neff, V. D. Electrochemistry of Polynuclear Transition Metal Cyanides: Prussian Blue and Its Analogues. *Acc. Chem. Res.* **1986**, *19* (6), 162–168. <https://doi.org/10.1021/ar00126a001>.
- (139) Lundgren, C.; Murray, R. W. Observations on the Composition of Prussian Blue Films and Their Electrochemistry. *Inorg. Chem.* **1988**, *27* (5), 933–939.
- (140) Feldman, B. J.; Melroy, O. R. Ion Flux during Electrochemical Charging of Prussian Blue Films. *J. Electroanal. Chem. Interfacial Electrochem.* **1987**, *234* (1), 213–227. [https://doi.org/10.1016/0022-0728\(87\)80173-0](https://doi.org/10.1016/0022-0728(87)80173-0).
- (141) Itaya, K.; Shibayama, K.; Akahoshi, H.; Toshima, S. Prussian-blue-modified Electrodes: An Application for a Stable Electrochromic Display Device. *J. Appl. Phys.* **1982**, *53* (1), 804–805. <https://doi.org/10.1063/1.329997>.
- (142) Hara, S.; Tanaka, H.; Kawamoto, T.; Tokumoto, M.; Yamada, M.; Gotoh, A.; Uchida, H.; Kurihara, M.; Sakamoto, M. Electrochromic Thin Film of Prussian Blue Nanoparticles Fabricated Using Wet Process. *Jpn. J. Appl. Phys.* **2007**, *46* (10L), L945. <https://doi.org/10.1143/JJAP.46.L945>.
- (143) Qian, J.; Ma, D.; Xu, Z.; Li, D.; Wang, J. Electrochromic Properties of Hydrothermally Grown Prussian Blue Film and Device. *Sol. Energy Mater. Sol. Cells* **2018**, *177*, 9–14. <https://doi.org/10.1016/j.solmat.2017.08.016>.
- (144) Lee, K.; Kim, A.-Y.; Kee Lee, J. Fullerene Coated Indium Tin Oxide Counter Electrode of Prussian Blue Electrode for Enhanced Electrochromic Properties. *Sol. Energy Mater. Sol. Cells* **2015**, *139*, 44–50. <https://doi.org/10.1016/j.solmat.2015.03.006>.
- (145) Liu, G.; Jian, Z.; Zhao, C.; Sun, H.; Zhang, N.; Qi, Y. Multicolor Reversible Prussian White Film with Application in Self-Powered Electrochromic Device. *New J. Chem.* **2024**, *48* (21), 9467–9473. <https://doi.org/10.1039/D3NJ05989H>.
- (146) Weiser, H. B.; Milligan, W. O.; Bates, J. B. X-Ray Diffraction Studies on Heavy-Metal Iron-Cyanides. *J. Phys. Chem.* **1942**, *46* (1), 99–111. <https://doi.org/10.1021/j150415a013>.
- (147) You, Y.; Wu, X.-L.; Yin, Y.-X.; Guo, Y.-G. High-Quality Prussian Blue Crystals as Superior Cathode Materials for Room-Temperature Sodium-Ion Batteries. *Energy Environ. Sci.* **2014**, *7* (5), 1643–1647. <https://doi.org/10.1039/C3EE44004D>.
- (148) Jo, I.-H.; Lee, S.-M.; Kim, H.-S.; Jin, B.-S. Electrochemical Properties of $\text{Na}_x\text{MnFe}(\text{CN})_6 \cdot z\text{H}_2\text{O}$ Synthesized in a Taylor-Couette Reactor as a Na-Ion Battery Cathode Material. *J. Alloys Compd.* **2017**, *729*, 590–596. <https://doi.org/10.1016/j.jallcom.2017.09.146>.

- (149) Chen, K.-C.; Hsu, C.-Y.; Hu, C.-W.; Ho, K.-C. A Complementary Electrochromic Device Based on Prussian Blue and Poly(ProDOT-Et₂) with High Contrast and High Coloration Efficiency. *Sol. Energy Mater. Sol. Cells* **2011**, *95* (8), 2238–2245. <https://doi.org/10.1016/j.solmat.2011.03.029>.
- (150) Chaudhary, A.; Pathak, D. K.; Ghosh, T.; Kandpal, S.; Tanwar, M.; Rani, C.; Kumar, R. Prussian Blue-Cobalt Oxide Double Layer for Efficient All-Inorganic Multicolor Electrochromic Device. *ACS Appl. Electron. Mater.* **2020**, *2* (6), 1768–1773. <https://doi.org/10.1021/acsaelm.0c00342>.
- (151) Ho, K.-C. Cycling and At-Rest Stabilities of a Complementary Electrochromic Device Based on Tungsten Oxide and Prussian Blue Thin Films. *Electrochimica Acta* **1999**, *44* (18), 3227–3235. [https://doi.org/10.1016/S0013-4686\(99\)00041-9](https://doi.org/10.1016/S0013-4686(99)00041-9).
- (152) Choi, D.; Son, M.; Im, T.; Ahn, S.-H.; Lee, C. S. Crack-Free Fabrication of Prussian Blue-Based Blending Film for the Dramatic Enhancement of Dual Electrochromic Device. *Ceram. Int.* **2020**, *46* (13), 21008–21013. <https://doi.org/10.1016/j.ceramint.2020.05.166>.
- (153) Kraft, A.; Rottmann, M. Properties, Performance and Current Status of the Laminated Electrochromic Glass of Gesimat. *Sol. Energy Mater. Sol. Cells* **2009**, *93* (12), 2088–2092. <https://doi.org/10.1016/j.solmat.2009.05.010>.
- (154) Yang, M.; Li, Y.; Yao, J.; Jiang, J.; Chen, X.; Xu, W. Fe-Co-Ni Trimetallic Prussian Blue Analogs with Tunable Electrochromic Energy Storage Properties. *Electrochimica Acta* **2024**, *481*, 143971. <https://doi.org/10.1016/j.electacta.2024.143971>.
- (155) Liao, H.-Y.; Liao, T.-C.; Chen, W.-H.; Chang, C.-H.; Chen, L.-C. Molybdate Hexacyanoferrate (MoOHCF) Thin Film: A Brownish Red Prussian Blue Analog for Electrochromic Window Application. *Sol. Energy Mater. Sol. Cells* **2016**, *145*, 8–15. <https://doi.org/10.1016/j.solmat.2015.06.062>.
- (156) Yonghong, Y.; Jiayu, Z.; Peifu, G.; Xu, L.; Jinfa, T. Electrochromism of Titanium Oxide Thin Films. *Thin Solid Films* **1997**, *298* (1), 197–199. [https://doi.org/10.1016/S0040-6090\(96\)08986-9](https://doi.org/10.1016/S0040-6090(96)08986-9).
- (157) Maček, M.; Orel, B. Electrochromism of Sol–Gel Derived Niobium Oxide Films. *Sol. Energy Mater. Sol. Cells* **1998**, *54* (1), 121–130. [https://doi.org/10.1016/S0927-0248\(98\)00062-2](https://doi.org/10.1016/S0927-0248(98)00062-2).
- (158) Özer, N.; Rubin, M. D.; Lampert, C. M. Optical and Electrochemical Characteristics of Niobium Oxide Films Prepared by Sol-Gel Process and Magnetron Sputtering A Comparison. *Sol. Energy Mater. Sol. Cells* **1996**, *40* (4), 285–296. [https://doi.org/10.1016/0927-0248\(95\)00147-6](https://doi.org/10.1016/0927-0248(95)00147-6).
- (159) Tai, C.-Y.; Wu, J.-Y. Observation of Optical Density Modulation Based on Electrochromic Tantalum Oxide Films. *J. Phys. Appl. Phys.* **2008**, *41* (6), 065303. <https://doi.org/10.1088/0022-3727/41/6/065303>.

- (160) Scarminio, J.; Lourenço, A.; Gorenstein, A. Electrochromism and Photochromism in Amorphous Molybdenum Oxide Films. *Thin Solid Films* **1997**, 302 (1), 66–70. [https://doi.org/10.1016/S0040-6090\(96\)09539-9](https://doi.org/10.1016/S0040-6090(96)09539-9).
- (161) Azens, A.; Vaivars, G.; Kullman, L.; Granqvist, C. G. Electrochromism of Cr Oxide Films. *Electrochimica Acta* **1999**, 44 (18), 3059–3061. [https://doi.org/10.1016/S0013-4686\(99\)00020-1](https://doi.org/10.1016/S0013-4686(99)00020-1).
- (162) Chigane, M.; Ishikawa, M. Manganese Oxide Thin Film Preparation by Potentiostatic Electrolyses and Electrochromism. *J. Electrochem. Soc.* **2000**, 147 (6), 2246. <https://doi.org/10.1149/1.1393515>.
- (163) Yoshino, T.; Kobayashi, K.; Araki, S.; Nakamura, K.; Kobayashi, N. Electrochromic Properties of Electrochemically Fabricated Nanostructure Nickel Oxide and Manganese Oxide Films. *Sol. Energy Mater. Sol. Cells* **2012**, 99, 43–49. <https://doi.org/10.1016/j.solmat.2011.08.024>.
- (164) Orel, B.; Maček, M.; Švegl, F.; Kalcher, K. Electrochromism of Iron Oxide Films Prepared via the Sol-Gel Route by the Dip-Coating Technique. *Thin Solid Films* **1994**, 246 (1), 131–142. [https://doi.org/10.1016/0040-6090\(94\)90742-0](https://doi.org/10.1016/0040-6090(94)90742-0).
- (165) Garcia-Lobato, M. A.; Martinez, A. I.; Perry, D. L.; Castro-Roman, M.; Zarate, R. A.; Escobar-Alarcon, L. Elucidation of the Electrochromic Mechanism of Nanostructured Iron Oxides Films. *Sol. Energy Mater. Sol. Cells* **2011**, 95 (2), 751–758. <https://doi.org/10.1016/j.solmat.2010.10.017>.
- (166) Lee, S.-H.; Liu, P.; Cheong, H. M.; Tracy, C. E.; Deb, S. K. Electrochromism of Amorphous Ruthenium Oxide Thin Films. *Solid State Ion.* **2003**, 165 (1), 217–221. <https://doi.org/10.1016/j.ssi.2003.08.035>.
- (167) Patil, P. S.; Kadam, L. D.; Lokhande, C. D. Studies on Electrochromism of Spray Pyrolyzed Cobalt Oxide Thin Films. *Sol. Energy Mater. Sol. Cells* **1998**, 53 (3), 229–234. [https://doi.org/10.1016/S0927-0248\(98\)00006-3](https://doi.org/10.1016/S0927-0248(98)00006-3).
- (168) Xia, X. H.; Tu, J. P.; Zhang, J.; Xiang, J. Y.; Wang, X. L.; Zhao, X. B. Cobalt Oxide Ordered Bowl-Like Array Films Prepared by Electrodeposition through Monolayer Polystyrene Sphere Template and Electrochromic Properties. *ACS Appl. Mater. Interfaces* **2010**, 2 (1), 186–192. <https://doi.org/10.1021/am900636g>.
- (169) Jeong, C. Y.; Abe, Y.; Kawamura, M.; Kim, K. H.; Kiba, T. Electrochromic Properties of Rhodium Oxide Thin Films Prepared by Reactive Sputtering under an O₂ or H₂O Vapor Atmosphere. *Sol. Energy Mater. Sol. Cells* **2019**, 200, 109976. <https://doi.org/10.1016/j.solmat.2019.109976>.
- (170) Patil, P. S.; Kavar, R. K.; Sadale, S. B. Electrochromism in Spray Deposited Iridium Oxide Thin Films. *Electrochimica Acta* **2005**, 50 (12), 2527–2532. <https://doi.org/10.1016/j.electacta.2004.10.081>.
- (171) Wen, R.-T.; Niklasson, G. A.; Granqvist, C. G. Electrochromic Iridium Oxide Films: Compatibility with Propionic Acid, Potassium Hydroxide, and Lithium Perchlorate in

Propylene Carbonate. *Sol. Energy Mater. Sol. Cells* **2014**, 120, 151–156. <https://doi.org/10.1016/j.solmat.2013.08.035>.

(172) Avendaño, E.; Azens, A.; Niklasson, G. A.; Granqvist, C. G. Electrochromism in Nickel Oxide Films Containing Mg, Al, Si, V, Zr, Nb, Ag, or Ta. *Sol. Energy Mater. Sol. Cells* **2004**, 84 (1), 337–350. <https://doi.org/10.1016/j.solmat.2003.11.032>.

(173) Richardson, T. J.; Slack, J. L.; Rubin, M. D. Electrochromism in Copper Oxide Thin Films. *Electrochimica Acta* **2001**, 46 (13), 2281–2284. [https://doi.org/10.1016/S0013-4686\(01\)00397-8](https://doi.org/10.1016/S0013-4686(01)00397-8).

(174) Talledo, A.; Granqvist, C. G. Electrochromic Vanadium–Pentoxide–Based Films: Structural, Electrochemical, and Optical Properties. *J. Appl. Phys.* **1995**, 77 (9), 4655–4666. <https://doi.org/10.1063/1.359433>.

(175) Seike, T.; Nagai, J. Electrochromism of 3d Transition Metal Oxides. *Sol. Energy Mater.* **1991**, 22 (2–3), 107–117. [https://doi.org/10.1016/0165-1633\(91\)90010-I](https://doi.org/10.1016/0165-1633(91)90010-I).

(176) Kadam, L. D.; Patil, P. S. Studies on Electrochromic Properties of Nickel Oxide Thin Films Prepared by Spray Pyrolysis Technique. *Sol. Energy Mater. Sol. Cells* **2001**, 69 (4), 361–369. [https://doi.org/10.1016/S0927-0248\(00\)00403-7](https://doi.org/10.1016/S0927-0248(00)00403-7).

(177) Mortimer, R. J.; Sialvi, M. Z.; Varley, T. S.; Wilcox, G. D. An in Situ Colorimetric Measurement Study of Electrochromism in the Thin-Film Nickel Hydroxide/Oxyhydroxide System. *J. Solid State Electrochem.* **2014**, 18 (12), 3359–3367. <https://doi.org/10.1007/s10008-014-2618-5>.

(178) Xu, Y. Z.; Qiu, M. Q.; Qiu, S. C.; Dai, J.; Cao, G. J.; He, H. H.; Wang, J. Y. Electrochromism of NiO_xH_y Films Grown by DC Sputtering. *Sol. Energy Mater. Sol. Cells* **1997**, 45 (2), 105–113. [https://doi.org/10.1016/S0927-0248\(96\)00021-9](https://doi.org/10.1016/S0927-0248(96)00021-9).

(179) Hüppauff, M.; Lengeler, B. Valency and Structure of Iridium in Anodic Iridium Oxide Films. *J. Electrochem. Soc.* **1993**, 140 (3), 598. <https://doi.org/10.1149/1.2056127>.

(180) Gottesfeld, S.; McIntyre, J. D. E. Electrochromism in Anodic Iridium Oxide Films: II. pH Effects on Corrosion Stability and the Mechanism of Coloration and Bleaching. *J. Electrochem. Soc.* **1979**, 126 (5), 742. <https://doi.org/10.1149/1.2129131>.

(181) Wen, R.; Granqvist, C. G.; Niklasson, G. A. Anodic Electrochromism for Energy-Efficient Windows: Cation/Anion-Based Surface Processes and Effects of Crystal Facets in Nickel Oxide Thin Films. *Adv. Funct. Mater.* **2015**, 25 (22), 3359–3370. <https://doi.org/10.1002/adfm.201500676>.

(182) Wu, C.-L.; Lin, C.-K.; Wang, C.-K.; Wang, S.-C.; Huang, J.-L. Annealing Induced Structural Evolution and Electrochromic Properties of Nanostructured Tungsten Oxide Films. *Thin Solid Films* **2013**, 549, 258–262. <https://doi.org/10.1016/j.tsf.2013.06.022>.

(183) Yang, H.; Shang, F.; Gao, L.; Han, H. Structure, Electrochromic and Optical Properties of WO₃ Film Prepared by Dip Coating-Pyrolysis. *Appl. Surf. Sci.* **2007**, 253 (12), 5553–5557. <https://doi.org/10.1016/j.apsusc.2006.12.084>.

- (184) de León, J. M. O.-R.; Acosta, D. R.; Pal, U.; Castañeda, L. Improving Electrochromic Behavior of Spray Pyrolysed WO₃ Thin Solid Films by Mo Doping. *Electrochimica Acta* **2011**, 56 (5), 2599–2605. <https://doi.org/10.1016/j.electacta.2010.11.038>.
- (185) Monk, P. M. S.; Chester, S. L. Electro-Deposition of Films of Electrochromic Tungsten Oxide Containing Additional Metal Oxides. *Electrochimica Acta* **1993**, 38 (11), 1521–1526. [https://doi.org/10.1016/0013-4686\(93\)80284-7](https://doi.org/10.1016/0013-4686(93)80284-7).
- (186) Green, S. V.; Pehlivan, E.; Granqvist, C. G.; Niklasson, G. A. Electrochromism in Sputter Deposited Nickel-Containing Tungsten Oxide Films. *Sol. Energy Mater. Sol. Cells* **2012**, 99, 339–344. <https://doi.org/10.1016/j.solmat.2011.12.025>.
- (187) Kirss, R. U.; Meda, L. Chemical Vapor Deposition of Tungsten Oxide. *Appl. Organomet. Chem.* **1998**, 12 (3), 155–160. [https://doi.org/10.1002/\(SICI\)1099-0739\(199803\)12:3<155::AID-AOC688>3.0.CO;2-Z](https://doi.org/10.1002/(SICI)1099-0739(199803)12:3<155::AID-AOC688>3.0.CO;2-Z).
- (188) Daily Metal Price: Free Metal Price Tables and Charts. <https://www.dailymetalprice.com/> (accessed 2024-06-12).
- (189) Monk, P. M. S.; Turner, C.; Akhtar, S. P. Electrochemical Behaviour of Methyl Viologen in a Matrix of Paper. *Electrochimica Acta* **1999**, 44 (26), 4817–4826. [https://doi.org/10.1016/S0013-4686\(99\)00225-X](https://doi.org/10.1016/S0013-4686(99)00225-X).
- (190) Hu, F.; Peng, H.; Zhang, S.; Gu, Y.; Yan, B.; Chen, S. PEDOT Nanoparticles Fully Covered on Natural Tubular Clay for Hierarchically Porous Electrochromic Film. *Sol. Energy Mater. Sol. Cells* **2019**, 199, 59–65. <https://doi.org/10.1016/j.solmat.2019.04.017>.
- (191) Liu, Y.; Yuan, J.; Wang, Y.; Zheng, R.; Liu, Q.; Shang, X.; Shao, J.; Wan, Z.; Luo, J.; Jia, C. Approach to Significantly Enhancing the Electrochromic Performance of PANi by In Situ Electrodeposition of the PANi@MXene Composite Film. *ACS Appl. Mater. Interfaces* **2023**, 15 (50), 58940–58954. <https://doi.org/10.1021/acsami.3c15548>.
- (192) Atak, G.; Bayrak Pehlivan, İ.; Montero, J.; Granqvist, C. G.; Niklasson, G. A. Electrochromic Tungsten Oxide Films Prepared by Sputtering: Optimizing Cycling Durability by Judicious Choice of Deposition Parameters. *Electrochimica Acta* **2021**, 367, 137233. <https://doi.org/10.1016/j.electacta.2020.137233>.
- (193) Lemos, R. M. J.; Alcázar, J. C. B.; Carreño, N. L. V.; Andrade, J.; Pawlicka, A.; Kanicki, J.; Gundel, A.; Azevedo, C. F.; Avellaneda, C. O. Influence of Molybdenum Trioxide Thin Film Thickness on Its Electrochemical Properties. *Mol. Cryst. Liq. Cryst.* **2017**, 655 (1), 40–50. <https://doi.org/10.1080/15421406.2017.1360689>.
- (194) Estrada, W.; Andersson, A. M.; Granqvist, C. G. Electrochromic Nickel-oxide-based Coatings Made by Reactive Dc Magnetron Sputtering: Preparation and Optical Properties. *J. Appl. Phys.* **1988**, 64 (7), 3678–3683. <https://doi.org/10.1063/1.341410>.
- (195) Sasaki, S.; Fujino, K.; Takéuchi, Y. X-Ray Determination of Electron-Density Distributions in Oxides, MgO, MnO, CoO, and NiO, and Atomic Scattering Factors of Their Constituent Atoms. *Proc. Jpn. Acad. Ser. B* **1979**, 55 (2), 43–48. <https://doi.org/10.2183/pjab.55.43>.

- (196) Kofstad, P. Defects and Transport Properties of Metal Oxides. *Oxid. Met.* **1995**, 44 (1), 3–27. <https://doi.org/10.1007/BF01046721>.
- (197) Adler, D.; Feinleib, J. Electrical and Optical Properties of Narrow-Band Materials. *Phys. Rev. B* **1970**, 2 (8), 3112–3134. <https://doi.org/10.1103/PhysRevB.2.3112>.
- (198) Deevi, K.; Immareddy, V. S. R. Synthesis and Characterization of Optically Transparent Nickel Oxide Nanoparticles as a Hole Transport Material for Hybrid Perovskite Solar Cells. *J. Mater. Sci. Mater. Electron.* **2019**, 30 (6), 6242–6248. <https://doi.org/10.1007/s10854-019-00927-8>.
- (199) Hugel, J.; Belkhir, M. Nature of the NiO Absorption Edge within a Spin Polarized Band Scheme. *Solid State Commun.* **1990**, 73 (2), 159–162. [https://doi.org/10.1016/0038-1098\(90\)91038-I](https://doi.org/10.1016/0038-1098(90)91038-I).
- (200) Niklasson, G. A.; Granqvist, C. G. Electrochromics for Smart Windows: Thin Films of Tungsten Oxide and Nickel Oxide, and Devices Based on These. *J. Mater. Chem.* **2006**, 17 (2), 127–156. <https://doi.org/10.1039/B612174H>.
- (201) Bouessay, I.; Rougier, A.; Poizot, P.; Moscovici, J.; Michalowicz, A.; Tarascon, J.-M. Electrochromic Degradation in Nickel Oxide Thin Film: A Self-Discharge and Dissolution Phenomenon. *Electrochimica Acta* **2005**, 50 (18), 3737–3745. <https://doi.org/10.1016/j.electacta.2005.01.020>.
- (202) Bode, H.; Dehmelt, K.; Witte, J. Zur Kenntnis Der Nickelhydroxidelektrode—I.Über Das Nickel (II)-Hydroxidhydrat. *Electrochimica Acta* **1966**, 11 (8), 1079–1087. [https://doi.org/10.1016/0013-4686\(66\)80045-2](https://doi.org/10.1016/0013-4686(66)80045-2).
- (203) Bode, H.; Dehmelt, K.; Witte, J. Zur Kenntnis der Nickelhydroxidelektrode. II. Über die Oxydationsprodukte von Nickel(II)-hydroxiden. *Z. Für Anorg. Allg. Chem.* **1969**, 366 (1–2), 1–21. <https://doi.org/10.1002/zaac.19693660102>.
- (204) Hall, D. S.; Lockwood, D. J.; Bock, C.; MacDougall, B. R. Nickel Hydroxides and Related Materials: A Review of Their Structures, Synthesis and Properties. *Proc. R. Soc. Math. Phys. Eng. Sci.* **2015**, 471 (2174), 20140792. <https://doi.org/10.1098/rspa.2014.0792>.
- (205) Carpenter, M. K.; Corrigan, D. A. Photoelectrochemistry of Nickel Hydroxide Thin Films. *J. Electrochem. Soc.* **1989**, 136 (4), 1022. <https://doi.org/10.1149/1.2096777>.
- (206) Carpenter, M. K.; Conell, R. S.; Corrigan, D. A. The Electrochromic Properties of Hydrated Nickel Oxide. *Sol. Energy Mater.* **1987**, 16 (4), 333–346. [https://doi.org/10.1016/0165-1633\(87\)90082-7](https://doi.org/10.1016/0165-1633(87)90082-7).
- (207) Delichère, P.; Joiret, S.; Goff, A. H.; Bange, K.; Hetz, B. Electrochromism in Nickel Oxide Thin Films Studied by OMA and Raman Spectroscopy. *J. Electrochem. Soc.* **1988**, 135 (7), 1856. <https://doi.org/10.1149/1.2096168>.
- (208) Avendaño, E.; Rensmo, H.; Azens, A.; Sandell, A.; Azevedo, G. de M.; Siegbahn, H.; Niklasson, G. A.; Granqvist, C. G. Coloration Mechanism in Proton-Intercalated Electrochromic Hydrated NiO_y and Ni_{1-x}V_xO_y Thin Films. *J. Electrochem. Soc.* **2009**, 156 (8), P132. <https://doi.org/10.1149/1.3148327>.

- (209) Ren, Y.; Chim, W. K.; Guo, L.; Tanoto, H.; Pan, J.; Chiam, S. Y. The Coloration and Degradation Mechanisms of Electrochromic Nickel Oxide. *Sol. Energy Mater. Sol. Cells* **2013**, *116*, 83–88. <https://doi.org/10.1016/j.solmat.2013.03.042>.
- (210) Passerini, S.; Scrosati, B.; Gorenstein, A. The Intercalation of Lithium in Nickel Oxide and Its Electrochromic Properties. *J. Electrochem. Soc.* **1990**, *137* (10), 3297. <https://doi.org/10.1149/1.2086202>.
- (211) Bressers, P. M. M. C.; Meulenkamp, E. A. The Electrochromic Behavior of Indium Tin Oxide in Propylene Carbonate Solutions. *J. Electrochem. Soc.* **1998**, *145* (7), 2225. <https://doi.org/10.1149/1.1838624>.
- (212) Poizot, P.; Laruelle, S.; Grugeon, S.; Dupont, L.; Tarascon, J.-M. Nano-Sized Transition-Metal Oxides as Negative-Electrode Materials for Lithium-Ion Batteries. *Nature* **2000**, *407* (6803), 496–499. <https://doi.org/10.1038/35035045>.
- (213) Laruelle, S.; Grugeon, S.; Poizot, P.; Dollé, M.; Dupont, L.; Tarascon, J.-M. On the Origin of the Extra Electrochemical Capacity Displayed by MO/Li Cells at Low Potential. *J. Electrochem. Soc.* **2002**, *149* (5), A627. <https://doi.org/10.1149/1.1467947>.
- (214) Campet, G. et al. Electrochemistry of Nickel Oxide Films in Aqueous and Li⁺ Containing Non-Aqueous Solutions: An Application for a New Lithium-Based Nickel Oxide Electrode Exhibiting Electrochromism by a Reversible Li⁺ Ion Insertion Mechanism. *Mater. Sci. Eng. B* **1991**, *8* (4), 303–308. [https://doi.org/10.1016/0921-5107\(91\)90051-V](https://doi.org/10.1016/0921-5107(91)90051-V).
- (215) Cappus, D.; Xu, C.; Ehrlich, D.; Dillmann, B.; Ventrice, C. A.; Al Shamery, K.; Kuhlbeck, H.; Freund, H.-J. Hydroxyl Groups on Oxide Surfaces: NiO(100), NiO(111) and Cr₂O₃(111). *Chem. Phys.* **1993**, *177* (2), 533–546. [https://doi.org/10.1016/0301-0104\(93\)80031-4](https://doi.org/10.1016/0301-0104(93)80031-4).
- (216) Boschloo, G.; Hagfeldt, A. Spectroelectrochemistry of Nanostructured NiO. *J. Phys. Chem. B* **2001**, *105* (15), 3039–3044. <https://doi.org/10.1021/jp003499s>.
- (217) Moulki, H. et al. Electrochromic Performances of Nonstoichiometric NiO Thin Films. *Thin Solid Films* **2014**, *553*, 63–66. <https://doi.org/10.1016/j.tsf.2013.10.154>.
- (218) Mihelčič, M.; Šurca Vuk, A.; Jerman, I.; Orel, B.; Švegl, F.; Moulki, H.; Faure, C.; Campet, G.; Rougier, A. Comparison of Electrochromic Properties of Ni_{1-x}O in Lithium and Lithium-Free Aprotic Electrolytes: From Ni_{1-x}O Pigment Coatings to Flexible Electrochromic Devices. *Sol. Energy Mater. Sol. Cells* **2014**, *120*, 116–130. <https://doi.org/10.1016/j.solmat.2013.08.025>.
- (219) Cao, F.; Pan, G. X.; Xia, X. H.; Tang, P. S.; Chen, H. F. Hydrothermal-Synthesized Mesoporous Nickel Oxide Nanowall Arrays with Enhanced Electrochromic Application. *Electrochimica Acta* **2013**, *111*, 86–91. <https://doi.org/10.1016/j.electacta.2013.07.221>.
- (220) Scherer, M. R. J.; Steiner, U. Efficient Electrochromic Devices Made from 3D Nanotubular Gyroid Networks. *Nano Lett.* **2013**, *13* (7), 3005–3010. <https://doi.org/10.1021/nl303833h>.

- (221) Xie, Z.; Liu, Q.; Lu, B.; Zhai, J.; Diao, X. Large Coloration Efficiency and Fast Response NiO Electrochromic Thin Film Electrode Based on NiO Nanocrystals. *Mater. Today Commun.* **2019**, *21*, 100635. <https://doi.org/10.1016/j.mtcomm.2019.100635>.
- (222) Dalavi, D. S.; Devan, R. S.; Patil, R. S.; Ma, Y.-R.; Kang, M.-G.; Kim, J.-H.; Patil, P. S. Electrochromic Properties of Dandelion Flower like Nickel Oxide Thin Films. *J. Mater. Chem. A* **2012**, *1* (4), 1035–1039. <https://doi.org/10.1039/C2TA00842D>.
- (223) Tian, Y.; Li, Z.; Dou, S.; Zhang, X.; Zhang, J.; Zhang, L.; Wang, L.; Zhao, X.; Li, Y. Facile Preparation of Aligned NiO Nanotube Arrays for Electrochromic Application. *Surf. Coat. Technol.* **2018**, *337*, 63–67. <https://doi.org/10.1016/j.surfcoat.2017.12.054>.
- (224) Xu, K.; Wang, L.; Xiong, S.; Ge, C.; Wang, L.; Wang, B.; Wang, W.; Chen, M.; Liu, G. Hydrothermally Prepared Ultra-Stable Multilayer Nanoflake NiO-Based Electrochromic Films. *Electrochimica Acta* **2023**, *441*, 141812. <https://doi.org/10.1016/j.electacta.2022.141812>.
- (225) Cai, G.; Wang, X.; Cui, M.; Darmawan, P.; Wang, J.; Eh, A. L.-S.; Lee, P. S. Electrochromo-Supercapacitor Based on Direct Growth of NiO Nanoparticles. *Nano Energy* **2015**, *12*, 258–267. <https://doi.org/10.1016/j.nanoen.2014.12.031>.
- (226) Zhao, F.; Chen, T.; Zeng, Y.; Chen, J.; Zheng, J.; Liu, Y.; Han, G. Nickel Oxide Electrochromic Films: Mechanisms, Preparation Methods, and Modification Strategies—a Review. *J. Mater. Chem. C* **2024**, *12* (20), 7126–7145. <https://doi.org/10.1039/D4TC00114A>.
- (227) Ren, Y.; Zhou, X.; Zhang, H.; Lei, L.; Zhao, G. Preparation of a Porous NiO Array-Patterned Film and Its Enhanced Electrochromic Performance. *J. Mater. Chem. C* **2018**, *6* (18), 4952–4958. <https://doi.org/10.1039/C8TC00367J>.
- (228) Zhao, C.; Chen, C.; Du, F.; Wang, J. Template Synthesis of NiO Ultrathin Nanosheets Using Polystyrene Nanospheres and Their Electrochromic Properties. *RSC Adv.* **2015**, *5* (48), 38533–38537. <https://doi.org/10.1039/C5RA04571A>.
- (229) Li, Z.; Yu, Z.; Wang, W.; Hou, J.; Gao, L.; Gu, X.; Su, G. Nickel Oxide Film with Tertiary Hierarchical Porous Structure and High Electrochromic Performance and Stability. *Mater. Chem. Phys.* **2021**, *269*, 124738. <https://doi.org/10.1016/j.matchemphys.2021.124738>.
- (230) Green, S. V.; Granqvist, C. G.; Niklasson, G. A. Structure and Optical Properties of Electrochromic Tungsten-Containing Nickel Oxide Films. *Sol. Energy Mater. Sol. Cells* **2014**, *126*, 248–259. <https://doi.org/10.1016/j.solmat.2013.04.001>.
- (231) Penin, N.; Rougier, A.; Laffont, L.; Poizot, P.; Tarascon, J.-M. Improved Cyclability by Tungsten Addition in Electrochromic NiO Thin Films. *Sol. Energy Mater. Sol. Cells* **2006**, *90* (4), 422–433. <https://doi.org/10.1016/j.solmat.2005.01.018>.
- (232) Lee, S.-H.; Park, Y.-S.; Joo, S.-K. Characterization of Ni–W Oxide Thin Film Electrodes. *Solid State Ion.* **1998**, *109* (3), 303–310. [https://doi.org/10.1016/S0167-2738\(98\)00093-9](https://doi.org/10.1016/S0167-2738(98)00093-9).
- (233) Lee, S. J.; Lee, T.-G.; Nahm, S.; Kim, D. H.; Yang, D. J.; Han, S. H. Investigation of All-Solid-State Electrochromic Devices with Durability Enhanced Tungsten-Doped Nickel

- Oxide as a Counter Electrode. *J. Alloys Compd.* **2020**, 815, 152399. <https://doi.org/10.1016/j.jallcom.2019.152399>.
- (234) Lee, S. H.; Lee, S. J.; Kim, R.; Kang, H.-W.; Seo, I.; Kim, B. H.; Han, S. H. Durability-Enhanced Monolithic Inorganic Electrochromic Devices with Tantalum-Doped Nickel Oxide as a Counter Electrode. *Sol. Energy Mater. Sol. Cells* **2022**, 234, 111435. <https://doi.org/10.1016/j.solmat.2021.111435>.
- (235) Makimura, Y.; Rougier, A.; Tarascon, J.-M. Cobalt and Tantalum Additions for Enhanced Electrochromic Performances of Nickel-Based Oxide Thin Films Grown by Pulsed Laser Deposition. *Appl. Surf. Sci.* **2006**, 252 (13), 4593–4598. <https://doi.org/10.1016/j.apsusc.2005.07.086>.
- (236) Antolini, E.; Giorgi, L. Morphological Characteristics of Low Density and High Lithium Content $\text{Li}_x\text{Ni}_{1-x}\text{O}$ Cathodes for Molten Carbonate Fuel Cells. *Ceram. Int.* **1998**, 24 (2), 117–124. [https://doi.org/10.1016/S0272-8842\(97\)00040-0](https://doi.org/10.1016/S0272-8842(97)00040-0).
- (237) Li, Z.; Wang, C.; Ma, X.; Yuan, L.; Sun, J. Synthesis, Structures and Electrochemical Properties of $\text{Li}_x\text{Ni}_{1-x}\text{O}$. *Mater. Chem. Phys.* **2005**, 91 (1), 36–39. <https://doi.org/10.1016/j.matchemphys.2004.10.043>.
- (238) Moulki, H.; Park, D. H.; Min, B.-K.; Kwon, H.; Hwang, S.-J.; Choy, J.-H.; Toupance, T.; Campet, G.; Rougier, A. Improved Electrochromic Performances of NiO Based Thin Films by Lithium Addition: From Single Layers to Devices. *Electrochimica Acta* **2012**, 74, 46–52. <https://doi.org/10.1016/j.electacta.2012.03.123>.
- (239) Zhou, J.; Luo, G.; Wei, Y.; Zheng, J.; Xu, C. Enhanced Electrochromic Performances and Cycle Stability of NiO-Based Thin Films via Li–Ti Co-Doping Prepared by Sol–Gel Method. *Electrochimica Acta* **2015**, 186, 182–191. <https://doi.org/10.1016/j.electacta.2015.10.154>.
- (240) He, Y.; Li, T.; Zhong, X.; Zhou, M.; Dong, G.; Diao, X. Lattice and Electronic Structure Variations in Critical Lithium Doped Nickel Oxide Thin Film for Superior Anode Electrochromism. *Electrochimica Acta* **2019**, 316, 143–151. <https://doi.org/10.1016/j.electacta.2019.05.112>.
- (241) Denayer, J. et al. Surfactant-Assisted Ultrasonic Spray Pyrolysis of Nickel Oxide and Lithium-Doped Nickel Oxide Thin Films, toward Electrochromic Applications. *Appl. Surf. Sci.* **2014**, 321, 61–69. <https://doi.org/10.1016/j.apsusc.2014.09.128>.
- (242) Tenent, R. C.; Gillaspie, D. T.; Miedaner, A.; Parilla, P. A.; Curtis, C. J.; Dillon, A. C. Fast-Switching Electrochromic Li^+ -Doped NiO Films by Ultrasonic Spray Deposition. *J. Electrochem. Soc.* **2010**, 157 (3), H318. <https://doi.org/10.1149/1.3279992>.
- (243) Gillaspie, D.; Norman, A.; Tracy, C. E.; Pitts, J. R.; Lee, S.-H.; Dillon, A. Nanocomposite Counter Electrode Materials for Electrochromic Windows. *J. Electrochem. Soc.* **2010**, 157 (3), H328–H331.

- (244) Lin, F. et al. Origin of Electrochromism in High-Performing Nanocomposite Nickel Oxide. *ACS Appl. Mater. Interfaces* **2013**, 5 (9), 3643–3649. <https://doi.org/10.1021/am400105y>.
- (245) Lin, F. et al. Electrochromic Performance of Nanocomposite Nickel Oxide Counter Electrodes Containing Lithium and Zirconium. *Sol. Energy Mater. Sol. Cells* **2014**, 126, 206–212. <https://doi.org/10.1016/j.solmat.2013.11.023>.
- (246) Redor, S.; Godeffroy, L.; Rouse, G.; Abakumov, A. M.; Li, B.; Kanoufi, F.; Tarascon, J.-M. Electrochromic Corundum-like Compound Based on the Reversible (De)Insertion of Lithium: $\text{Li}_2\text{Ni}_2\text{W}_2\text{O}_9$. *J. Am. Chem. Soc.* **2023**, 145 (23), 12823–12836. <https://doi.org/10.1021/jacs.3c03631>.
- (247) Redor, S.; Avdeev, M.; Hrabovsky, D.; Tarascon, J.-M.; Rouse, G. Magnetic Properties, Magnetic Structure, and Possible Magnetoelectric Effect in Orthorhombic Corundumlike $\text{Li}_2\text{Ni}_2\text{W}_2\text{O}_9$. *Phys. Rev. B* **2024**, 109 (5), 054105. <https://doi.org/10.1103/PhysRevB.109.054105>.
- (248) Kim, J.-S.; Choi, J.-H.; Jeong, B.-M.; Kang, H.-J. Luminescence Characteristics and Crystal Structure of CaWO_4 - Li_2WO_4 - Eu_2O_3 Phosphors. *J. Korean Ceram. Soc.* **2006**, 43 (1), 10–15. <https://doi.org/10.4191/KCERS.2006.43.1.010>.
- (249) Horiuchi, H.; Morimoto, N.; Yamaoka, S. The Crystal Structure of Li_2WO_4 II: A Structure Related to Spinel. *J. Solid State Chem.* **1979**, 30 (2), 129–135. [https://doi.org/10.1016/0022-4596\(79\)90094-X](https://doi.org/10.1016/0022-4596(79)90094-X).
- (250) Sasaki, S.; Fujino, K.; Takéuchi, Y. X-Ray Determination of Electron-Density Distributions in Oxides, MgO , MnO , CoO , and NiO , and Atomic Scattering Factors of Their Constituent Atoms. *Proc. Jpn. Acad. Ser. B* **1979**, 55 (2), 43–48. <https://doi.org/10.2183/pjab.55.43>.
- (251) Boultif, A.; Louër, D. Indexing of Powder Diffraction Patterns for Low-Symmetry Lattices by the Successive Dichotomy Method. *J. Appl. Crystallogr.* **1991**, 24 (6), 987–993. <https://doi.org/10.1107/S0021889891006441>.
- (252) Favre-Nicolin, V.; Černý, R. FOX, 'free Objects for Crystallography': A Modular Approach to Ab Initio Structure Determination from Powder Diffraction. *J. Appl. Crystallogr.* **2002**, 35 (6), 734–743. <https://doi.org/10.1107/S0021889802015236>.
- (253) González-Platas, J.; Rodríguez-Carvajal, J. GFourier: A Windows/Linux Program to Calculate and Display Fourier Maps. Program Available within the FullProf Suite. <https://www.ill.eu/sites/fullprof/php/programse811.html?pagina=Fourier> (accessed 2022-09-27).
- (254) Rietveld, H. M. A Profile Refinement Method for Nuclear and Magnetic Structures. *J. Appl. Crystallogr.* **1969**, 2 (2), 65–71. <https://doi.org/10.1107/S0021889869006558>.
- (255) Weitzel, H. Kristallstrukturverfeinerung von Wolframiten Und Columbiten. *Z. Für Krist.* **1976**, 144 (1–6), 238–258. <https://doi.org/10.1524/zkri.1976.144.1-6.238>.

- (256) Brown, I. D. VALENCE: A Program for Calculating Bond Valences. *J. Appl. Crystallogr.* **1996**, 29 (4), 479–480. <https://doi.org/10.1107/S002188989600163X>.
- (257) Robinson, K.; Gibbs, G. V.; Ribbe, P. H. Quadratic Elongation: A Quantitative Measure of Distortion in Coordination Polyhedra. *Science* **1971**, 172 (3983), 567–570. <https://doi.org/10.1126/science.172.3983.567>.
- (258) Kunz, M.; Brown, I. D. Out-of-Center Distortions around Octahedrally Coordinated d^0 Transition Metals. *J. Solid State Chem.* **1995**, 115 (2), 395–406. <https://doi.org/10.1006/jssc.1995.1150>.
- (259) Kang, S. K.; Tang, H.; Albright, T. A. Structures for d^0 ML_6 and ML_5 Complexes. *J. Am. Chem. Soc.* **1993**, 115 (5), 1971–1981. <https://doi.org/10.1021/ja00058a051>.
- (260) Finger, L. W.; Hazen, R. M. Crystal Structure and Compression of Ruby to 46 Kbar. *J. Appl. Phys.* **1978**, 49 (12), 5823–5826. <https://doi.org/10.1063/1.324598>.
- (261) Ding, L. et al. Noncollinear Magnetic Structure and Magnetoelectric Coupling in Buckled Honeycomb $Co_4Nb_2O_9$: A Single-Crystal Neutron Diffraction Study. *Phys. Rev. B* **2020**, 102 (17), 174443. <https://doi.org/10.1103/PhysRevB.102.174443>.
- (262) Newnham, R. E.; Meagher, E. P. Crystal Structure of Ni_3TeO_6 . *Mater. Res. Bull.* **1967**, 2 (5), 549–554. [https://doi.org/10.1016/0025-5408\(67\)90031-1](https://doi.org/10.1016/0025-5408(67)90031-1).
- (263) Feng, H. L. et al. High-Pressure Synthesis and Ferrimagnetism of Ni_3TeO_6 -Type Mn_2ScMO_6 ($M = Nb, Ta$). *Inorg. Chem.* **2019**, 58 (23), 15953–15961. <https://doi.org/10.1021/acs.inorgchem.9b02468>.
- (264) Guo, H.; Fang, L.; Jiang, X.; Li, J.; Lu, F.; Li, C. A Novel Low-Firing and Low Loss Microwave Dielectric Ceramic $Li_2Mg_2W_2O_9$ with Corundum Structure. *J. Am. Ceram. Soc.* **2015**, 98 (12), 3863–3868. <https://doi.org/10.1111/jace.13829>.
- (265) Zhao, M.-H. et al. Reversible Structural Transformation between Polar Polymorphs of Li_2GeTeO_6 . *Inorg. Chem.* **2019**, 58 (2), 1599–1606. <https://doi.org/10.1021/acs.inorgchem.8b03114>.
- (266) Tarakina, N. V.; Nikulina, E. A.; Hadermann, J.; Kellerman, D. G.; Tyutyunnik, A. P.; Berger, I. F.; Zubkov, V. G.; Van Tendeloo, G. Crystal Structure and Magnetic Properties of Complex Oxides $Mg_{4-x}Ni_xNb_2O_9$, $0 \leq x \leq 4$. *J. Solid State Chem.* **2007**, 180 (11), 3180–3187. <https://doi.org/10.1016/j.jssc.2007.09.007>.
- (267) Tailleur, E.; Martin, C.; Damay, F.; Fauth, F.; Maignan, A. Lack of Linear Magnetoelectric Effect in Ferrimagnetic Distorted Honeycomb $Ni_4Nb_2O_9$. *J. Appl. Phys.* **2020**, 127 (6), 063902. <https://doi.org/10.1063/1.5134056>.
- (268) Yamane, H.; Abe, S.; Tu, R.; Goto, T. A Ramsayite-Type Oxide, $Ca_2Sn_2Al_2O_9$. *Acta Crystallogr. Sect. E Struct. Rep. Online* **2010**, 66 (10), i72–i72. <https://doi.org/10.1107/S1600536810036445>.

- (269) Akimoto, J.; Gotoh, Y.; Oosawa, Y. Synthesis and Structure Refinement of LiCoO₂ Single Crystals. *J. Solid State Chem.* **1998**, 141 (1), 298–302. <https://doi.org/10.1006/jssc.1998.7966>.
- (270) Mizushima, K.; Jones, P. C.; Wiseman, P. J.; Goodenough, J. B. (Received April 3, 1980; Communicated by J. B. Goodenough). 15 (6), 7.
- (271) Ohzuku, T.; Makimura, Y. Layered Lithium Insertion Material of LiCo_{1/3}Ni_{1/3}Mn_{1/3}O₂ for Lithium-Ion Batteries. *Chem. Lett.* **2001**, 30 (7), 642–643. <https://doi.org/10.1246/cl.2001.642>.
- (272) Lu, Z.; MacNeil, D. D.; Dahn, J. R. Layered Li[Ni_xCo_{1-2x}Mn_x]O₂ Cathode Materials for Lithium-Ion Batteries. *Electrochem. Solid-State Lett.* **2001**, 4 (12), A200. <https://doi.org/10.1149/1.1413182>.
- (273) Subban, C. V.; Ati, M.; Rouse, G.; Abakumov, A. M.; Van Tendeloo, G.; Janot, R.; Tarascon, J.-M. Preparation, Structure, and Electrochemistry of Layered Polyanionic Hydroxysulfates: LiMSO₄OH (M = Fe, Co, Mn) Electrodes for Li-Ion Batteries. *J. Am. Chem. Soc.* **2013**, 135 (9), 3653–3661. <https://doi.org/10.1021/ja3125492>.
- (274) Satya Kishore, M.; Pralong, V.; Caignaert, V.; Malo, S.; Hebert, S.; Varadaraju, U. V.; Raveau, B. Topotactic Insertion of Lithium in the Layered Structure Li₄VO(PO₄)₂: The Tunnel Structure Li₅VO(PO₄)₂. *J. Solid State Chem.* **2008**, 181 (4), 976–982. <https://doi.org/10.1016/j.jssc.2008.01.044>.
- (275) Wernert, R.; Nguyen, L. H. B.; Iadecola, A.; Weill, F.; Fauth, F.; Monconduit, L.; Carlier, D.; Croguennec, L. Self-Discharge Mechanism of High-Voltage KVPO₄F for K-Ion Batteries. *ACS Appl. Energy Mater.* **2022**, 5 (12), 14913–14921. <https://doi.org/10.1021/acsaem.2c02379>.
- (276) Ebner, W.; Fouchard, D.; Xie, L. The LiNiO₂/Carbon Lithium-Ion Battery. *Solid State Ion.* **1994**, 69 (3–4), 238–256. [https://doi.org/10.1016/0167-2738\(94\)90413-8](https://doi.org/10.1016/0167-2738(94)90413-8).
- (277) Meng, X.; Dou, S.; Wang, W. High Power and High Capacity Cathode Material LiNi_{0.5}Mn_{0.5}O₂ for Advanced Lithium-Ion Batteries. *J. Power Sources* **2008**, 184 (2), 489–493. <https://doi.org/10.1016/j.jpowsour.2008.04.015>.
- (278) Mauger, A.; Julien, C. Olivine Positive Electrodes for Li-Ion Batteries: Status and Perspectives. *Batteries* **2018**, 4 (3), 39. <https://doi.org/10.3390/batteries4030039>.
- (279) Mauger, A.; Julien, C. M.; Armand, M.; Goodenough, J. B.; Zaghbi, K. Li(Ni,Co)PO₄ as Cathode Materials for Lithium Batteries: Will the Dream Come True? *Curr. Opin. Electrochem.* **2017**, 6 (1), 63–69. <https://doi.org/10.1016/j.coelec.2017.10.015>.
- (280) Hautier, G.; Jain, A.; Ong, S. P.; Kang, B.; Moore, C.; Doe, R.; Ceder, G. Phosphates as Lithium-Ion Battery Cathodes: An Evaluation Based on High-Throughput Ab Initio Calculations. *Chem. Mater.* **2011**, 23 (15), 3495–3508. <https://doi.org/10.1021/cm200949v>.
- (281) Song, J. H.; Park, H. J.; Kim, K. J.; Jo, Y. N.; Kim, J.-S.; Jeong, Y. U.; Kim, Y. J. Electrochemical Characteristics of Lithium Vanadate, Li_{1+x}VO₂, New Anode Materials for

- Lithium Ion Batteries. *J. Power Sources* **2010**, 195 (18), 6157–6161. <https://doi.org/10.1016/j.jpowsour.2009.12.103>.
- (282) Xu, K. Nonaqueous Liquid Electrolytes for Lithium-Based Rechargeable Batteries. *Chem. Rev.* **2004**, 104 (10), 4303–4418. <https://doi.org/10.1021/cr030203g>.
- (283) Kumar, R.; Gupta, P. K.; Agrawal, A.; Nagarale, R. K.; Sharma, A. Hydrothermally Synthesized Reduced Graphene Oxide-NiWO₄ Nanocomposite for Lithium-Ion Battery Anode. *J. Electrochem. Soc.* **2017**, 164 (4), A785–A795. <https://doi.org/10.1149/2.1181704jes>.
- (284) Merryweather, A. J.; Schnedermann, C.; Jacquet, Q.; Grey, C. P.; Rao, A. Operando Optical Tracking of Single-Particle Ion Dynamics in Batteries. *Nature* **2021**, 594 (7864), 522–528. <https://doi.org/10.1038/s41586-021-03584-2>.
- (285) Pandya, R. et al. Three-Dimensional Operando Optical Imaging of Single Particle and Electrolyte Heterogeneities inside Li-Ion Batteries. **2022**. <https://doi.org/10.48550/ARXIV.2207.13073>.
- (286) Xu, C.; Merryweather, A. J.; Pandurangi, S. S.; Lun, Z.; Hall, D. S.; Deshpande, V. S.; Fleck, N. A.; Schnedermann, C.; Rao, A.; Grey, C. P. Operando Visualization of Kinetically Induced Lithium Heterogeneities in Single-Particle Layered Ni-Rich Cathodes. *Joule* **2022**, 6 (11), 2535–2546. <https://doi.org/10.1016/j.joule.2022.09.008>.
- (287) Zhou, H.; Xin, F.; Pei, B.; Whittingham, M. S. What Limits the Capacity of Layered Oxide Cathodes in Lithium Batteries? *ACS Energy Lett.* **2019**, 4 (8), 1902–1906. <https://doi.org/10.1021/acsenerylett.9b01236>.
- (288) Peres, J. P.; Delmas, C.; Rougier, A.; Broussely, M.; Perton, F.; Biensan, P.; Willmann, P. The Relationship between the Composition of Lithium Nickel Oxide and the Loss of Reversibility during the First Cycle. *J. Phys. Chem. Solids* **1996**, 57 (6–8), 1057–1060. [https://doi.org/10.1016/0022-3697\(95\)00395-9](https://doi.org/10.1016/0022-3697(95)00395-9).
- (289) Choi, J.; Manthiram, A. Investigation of the Irreversible Capacity Loss in the Layered LiNi_{1/3}Mn_{1/3}Co_{1/3}O₂ Cathodes. *Electrochem. Solid-State Lett.* **2005**, 8 (8), C102. <https://doi.org/10.1149/1.1943567>.
- (290) Mugiraneza, S.; Hallas, A. M. Tutorial: A Beginner’s Guide to Interpreting Magnetic Susceptibility Data with the Curie-Weiss Law. *Commun. Phys.* **2022**, 5 (1), 95. <https://doi.org/10.1038/s42005-022-00853-y>.
- (291) Huang, C.-L. et al. Quantum Critical Point in the Itinerant Ferromagnet Ni_{1-x}Rh_x. *Phys. Rev. Lett.* **2020**, 124 (11), 117203. <https://doi.org/10.1103/PhysRevLett.124.117203>.
- (292) Hallas, A. M.; Sharma, A. Z.; Cai, Y.; Munsie, T. J.; Wilson, M. N.; Tachibana, M.; Wiebe, C. R.; Luke, G. M. Relief of Frustration in the Heisenberg Pyrochlore Antiferromagnet Gd₂Pt₂O₇. *Phys. Rev. B* **2016**, 94 (13), 134417. <https://doi.org/10.1103/PhysRevB.94.134417>.
- (293) Hallas, A. M.; Morosan, E. Sr(M,Te)₂O₆ (M = Cr, Mn, Fe, Co, Ni): A Magnetically Dilute Family of Honeycomb Tellurates. *Inorg. Chem.* **2019**, 58 (10), 6993–6999. <https://doi.org/10.1021/acs.inorgchem.9b00617>.

- (294) Hoppeé, J. I. Effective Magnetic Moment. *J. Chem. Educ.* **1972**, 49 (7), 505. <https://doi.org/10.1021/ed049p505>.
- (295) Kovalevsky, J.; Quinn, T. J. The International System of Units (SI). *Comptes Rendus Phys.* **2004**, 5 (8), 799–811. <https://doi.org/10.1016/j.crhy.2004.07.002>.
- (296) Carron, N. Babel of Units. The Evolution of Units Systems in Classical Electromagnetism. arXiv 2015. <https://doi.org/10.48550/ARXIV.1506.01951>.
- (297) Bertaut, E. F.; Corliss, L.; Forrat, F.; Aleonard, R.; Pauthenet, R. Etude de niobates et tantalates de métaux de transition bivalents. *J. Phys. Chem. Solids* **1961**, 21 (3–4), 234–251. [https://doi.org/10.1016/0022-3697\(61\)90103-2](https://doi.org/10.1016/0022-3697(61)90103-2).
- (298) Fischer, E.; Gorodetsky, G.; Hornreich, R. M. A New Family of Magnetoelectric Materials: $A_2M_4O_9$ ($A = Ta, Nb$; $M = Mn, Co$). *Solid State Commun.* **1972**, 10 (12), 1127–1132. [https://doi.org/10.1016/0038-1098\(72\)90927-1](https://doi.org/10.1016/0038-1098(72)90927-1).
- (299) Schwarz, B.; Kraft, D.; Theissmann, R.; Ehrenberg, H. Magnetic Properties of the $(Co_xMn_{1-x})_4Nb_2O_9$ Solid Solution Series. *J. Magn. Magn. Mater.* **2010**, 322 (5), L1–L3. <https://doi.org/10.1016/j.jmmm.2009.10.008>.
- (300) Fang, Y.; Zhou, W. P.; Yan, S. M.; Bai, R.; Qian, Z. H.; Xu, Q. Y.; Wang, D. H.; Du, Y. W. Magnetic-Field-Induced Dielectric Anomaly and Electric Polarization in $Mn_4Nb_2O_9$. *J. Appl. Phys.* **2015**, 117 (17), 17B712. <https://doi.org/10.1063/1.4913815>.
- (301) Maignan, A.; Martin, C. $Fe_4Nb_2O_9$: A Magnetoelectric Antiferromagnet. *Phys. Rev. B* **2018**, 97 (16), 161106. <https://doi.org/10.1103/PhysRevB.97.161106>.
- (302) Cao, Y. et al. High-Quality Single Crystal Growth and Magnetic Property of $Mn_4Ta_2O_9$. *J. Cryst. Growth* **2018**, 492, 35–38. <https://doi.org/10.1016/j.jcrysgro.2018.04.007>.
- (303) Curie, P. Sur La Symétrie Dans Les Phénomènes Physiques, Symétrie d'un Champ Électrique et d'un Champ Magnétique. *J. Phys. Théorique Appliquée* **1894**, 3 (1), 393–415. <https://doi.org/10.1051/jphysap:018940030039300>.
- (304) Birss, R. R. Macroscopic Symmetry in Space-Time. *Rep. Prog. Phys.* **1963**, 26 (1), 307–360. <https://doi.org/10.1088/0034-4885/26/1/309>.
- (305) O'Dell, T. H. The Electrodynamics of Magneto-Electric Media; Series of monographs on selected topics in solid state physics; North-Holland Publishing Company: Amsterdam, 1970.
- (306) Rivera, J.-P. On Definitions, Units, Measurements, Tensor Forms of the Linear Magnetoelectric Effect and on a New Dynamic Method Applied to Cr-Cl Boracite. *Ferroelectrics* **1994**, 161 (1), 165–180. <https://doi.org/10.1080/00150199408213365>.
- (307) Schmid, H. Some Symmetry Aspects of Ferroics and Single Phase Multiferroics *. *J. Phys. Condens. Matter* **2008**, 20 (43), 434201. <https://doi.org/10.1088/0953-8984/20/43/434201>.

- (308) Pauling, L.; Hendricks, S. B. THE CRYSTAL STRUCTURES OF HEMATITE AND CORUNDUM. *J. Am. Chem. Soc.* **1925**, 47 (3), 781–790. <https://doi.org/10.1021/ja01680a027>.
- (309) Khanh, N. D.; Abe, N.; Sagayama, H.; Nakao, A.; Hanashima, T.; Kiyanagi, R.; Tokunaga, Y.; Arima, T. Magnetoelectric Coupling in the Honeycomb Antiferromagnet $\text{Co}_4\text{Nb}_2\text{O}_9$. *Phys. Rev. B* **2016**, 93 (7), 075117. <https://doi.org/10.1103/PhysRevB.93.075117>.
- (310) Khanh, N. D.; Abe, N.; Kimura, S.; Tokunaga, Y.; Arima, T. Manipulation of Electric Polarization with Rotating Magnetic Field in a Honeycomb Antiferromagnet $\text{Co}_4\text{Nb}_2\text{O}_9$. *Phys. Rev. B* **2017**, 96 (9), 094434. <https://doi.org/10.1103/PhysRevB.96.094434>.
- (311) Deng, G. et al. Spin Dynamics and Magnetoelectric Coupling Mechanism of $\text{Co}_4\text{Nb}_2\text{O}_9$. *Phys. Rev. B* **2018**, 97 (8), 085154. <https://doi.org/10.1103/PhysRevB.97.085154>.
- (312) Jana, R. et al. Low-Temperature Crystal and Magnetic Structures of the Magnetoelectric Material $\text{Fe}_4\text{Nb}_2\text{O}_9$. *Phys. Rev. B* **2019**, 100 (9), 094109. <https://doi.org/10.1103/PhysRevB.100.094109>.
- (313) Wichmann, R.; Müller-Buschbaum, Hk. Eine neue Kristallstruktur des Nickel-Oxonibats: $\text{II-Ni}_4\text{Nb}_2\text{O}_9$. *Z. Für Anorg. Allg. Chem.* **1986**, 539 (8), 203–210. <https://doi.org/10.1002/zaac.19865390821>.
- (314) Ehrenberg, H.; Wltschek, G.; Weitzel, H.; Trouw, F.; Buettner, J. H.; Kroener, T.; Fuess, H. Ferrimagnetism in $\text{Ni}_4\text{Nb}_2\text{O}_9$. *Phys. Rev. B* **1995**, 52 (13), 9595–9600. <https://doi.org/10.1103/PhysRevB.52.9595>.
- (315) Thota, S. et al. Unraveling the Nature of Ferrimagnetism and Associated Exchange Interactions in Distorted Honeycomb $\text{Ni}_4\text{Nb}_2\text{O}_9$. *Phys. Rev. B* **2022**, 106 (13), 134418. <https://doi.org/10.1103/PhysRevB.106.134418>.
- (316) Bolletta, J. P.; Fauth, F.; Martin, C.; Maignan, A. Magnetization Reversal Tuning in Honeycomb Ferrimagnet $\text{Ni}_4\text{Nb}_2\text{O}_9$. *J. Appl. Phys.* **2022**, 132 (15), 153901. <https://doi.org/10.1063/5.0107661>.
- (317) Jiongo-Dongmo, J. N.; Bolletta, J. P.; Maignan, A.; Damay, F.; Martin, C. The $\text{Ni}_{4-x}\text{Co}_x\text{Nb}_2\text{O}_9$ Phase Diagram: From Magnetization Reversal to Linear Magnetoelectricity. *J. Mater. Chem. C* **2023**, 11 (15), 5092–5101. <https://doi.org/10.1039/D3TC00429E>.
- (318) Meng, B.; Ji, X. T.; Chen, X. H.; Fu, Q. S.; Li, C. L.; Chakrabarti, C.; Qiu, Y.; Yuan, S. L. Negative Magnetization Effect in Distorted Honeycomb $\text{Ni}_4\text{Nb}_2\text{O}_9$ Ceramics. *J. Low Temp. Phys.* **2022**, 207 (1–2), 115–126. <https://doi.org/10.1007/s10909-022-02682-3>.
- (319) Stryjewski, E.; Giordano, N. Metamagnetism. *Adv. Phys.* **1977**, 26 (5), 487–650. <https://doi.org/10.1080/00018737700101433>.
- (320) Reynaud, M.; Rodríguez-Carvajal, J.; Chotard, J.-N.; Tarascon, J.-M.; Rouse, G. Magnetic Structure and Properties of Orthorhombic $\text{Li}_2\text{Ni}(\text{SO}_4)_2$: A Possible Magnetoelectric Material. *Phys. Rev. B* **2014**, 89 (10), 104419. <https://doi.org/10.1103/PhysRevB.89.104419>.

- (321) Rodríguez-Carvajal, J. Recent Advances in Magnetic Structure Determination by Neutron Powder Diffraction. *Phys. B Condens. Matter* **1993**, 192 (1–2), 55–69. [https://doi.org/10.1016/0921-4526\(93\)90108-I](https://doi.org/10.1016/0921-4526(93)90108-I).
- (322) See Supplemental Material at [URL will be inserted by publisher] for the detailed results of the Rietveld refinements performed on the laboratory XRD and neutron powder diffraction data for Li₂Ni₂W₂O₉ samples. Simulations of neutron powder diffraction patterns for different models of the magnetic structure, and the .mcif file for the final magnetic structure of Li₂Ni₂W₂O₉ are also included.
- (323) Goodenough, J. B. *Magnetism and the Chemical Bond*; Interscience Publishers: University of Michigan, 1963.
- (324) Goodenough, J. B. An Interpretation of the Magnetic Properties of the Perovskite-Type Mixed Crystals La_{1-x}Sr_xCoO_{3-λ}. *J. Phys. Chem. Solids* **1958**, 6 (2–3), 287–297. [https://doi.org/10.1016/0022-3697\(58\)90107-0](https://doi.org/10.1016/0022-3697(58)90107-0).
- (325) Kanamori, J. Superexchange Interaction and Symmetry Properties of Electron Orbitals. *J. Phys. Chem. Solids* **1959**, 10 (2–3), 87–98. [https://doi.org/10.1016/0022-3697\(59\)90061-7](https://doi.org/10.1016/0022-3697(59)90061-7).
- (326) El Khayati, N.; Cherkaoui El Moursli, R.; Rodríguez-Carvajal, J.; André, G.; Blanchard, N.; Bourée, F.; Collin, G.; Roisnel, T. Crystal and Magnetic Structures of the Oxyphosphates MFePO₅ (M = Fe, Co, Ni, Cu). Analysis of the Magnetic Ground State in Terms of Superexchange Interactions. *Eur. Phys. J. B* **2001**, 22 (4), 429–442. <https://doi.org/10.1007/s100510170093>.
- (327) Yoshimori, A. A New Type of Antiferromagnetic Structure in the Rutile Type Crystal. *J. Phys. Soc. Jpn.* **1959**, 14 (6), 807–821. <https://doi.org/10.1143/JPSJ.14.807>.
- (328) Villain, J. La structure des substances magnetiques. *J. Phys. Chem. Solids* **1959**, 11 (3–4), 303–309. [https://doi.org/10.1016/0022-3697\(59\)90231-8](https://doi.org/10.1016/0022-3697(59)90231-8).
- (329) Lyons, D. H.; Kaplan, T. A. Method for Determining Ground-State Spin Configurations. *Phys. Rev.* **1960**, 120 (5), 1580–1585. <https://doi.org/10.1103/PhysRev.120.1580>.
- (330) Freiser, M. J. Thermal Variation of the Pitch of Helical Spin Configurations. *Phys. Rev.* **1961**, 123 (6), 2003–2012. <https://doi.org/10.1103/PhysRev.123.2003>.
- (331) Reynaud, M.; Rouse, G.; Chotard, J.-N.; Rodríguez-Carvajal, J.; Tarascon, J.-M. Marinite Li₂M(SO₄)₂ (M = Co, Fe, Mn) and Li₁Fe(SO₄)₂: Model Compounds for Super-Super-Exchange Magnetic Interactions. *Inorg. Chem.* **2013**, 52 (18), 10456–10466. <https://doi.org/10.1021/ic401280e>.
- (332) Rouse, G.; Rodríguez-Carvajal, J.; Wurm, C.; Masquelier, C. Magnetic Structural Studies of the Two Polymorphs of Li₃Fe₂(PO₄)₃: Analysis of the Magnetic Ground State from Super-Super Exchange Interactions. *Chem. Mater.* **2001**, 13 (12), 4527–4536. <https://doi.org/10.1021/cm011054q>.

- (333) Rouse, G.; Rodriguez-Carvajal, J.; Patoux, S.; Masquelier, C. Magnetic Structures of the Triphylite LiFePO_4 and of Its Delithiated Form FePO_4 . *Chem. Mater.* **2003**, *15* (21), 4082–4090. <https://doi.org/10.1021/cm0300462>.
- (334) Melot, B. C.; Rouse, G.; Chotard, J.-N.; Ati, M.; Rodríguez-Carvajal, J.; Kemei, M. C.; Tarascon, J.-M. Magnetic Structure and Properties of the Li-Ion Battery Materials FeSO_4F and LiFeSO_4F . *Chem. Mater.* **2011**, *23* (11), 2922–2930. <https://doi.org/10.1021/cm200465u>.
- (335) Melot, B. C.; Rouse, G.; Chotard, J.-N.; Kemei, M. C.; Rodríguez-Carvajal, J.; Tarascon, J.-M. Magnetic Structure and Properties of NaFeSO_4F and NaCoSO_4F . *Phys. Rev. B* **2012**, *85* (9), 094415. <https://doi.org/10.1103/PhysRevB.85.094415>.
- (336) Ghara, S.; Fauth, F.; Suard, E.; Rodriguez-Carvajal, J.; Sundaresan, A. Synthesis, Structure, and Physical Properties of the Polar Magnet DyCrWO_6 . *Inorg. Chem.* **2018**, *57* (20), 12827–12835. <https://doi.org/10.1021/acs.inorgchem.8b02023>.
- (337) Chaudhary, S.; Srivastava, P.; Kaushik, S. D.; Siruguri, V.; Patnaik, S. Nature of Magnetoelectric Coupling in Corundum Antiferromagnet $\text{Co}_4\text{Ta}_2\text{O}_9$. *J. Magn. Magn. Mater.* **2019**, *475*, 508–513. <https://doi.org/10.1016/j.jmmm.2018.09.071>.
- (338) Chaudhary, S.; Nagpal, V.; Patnaik, S. Magnetoelectric Response in Honeycomb Antiferromagnet $\text{Fe}_4\text{NbTaO}_9$. *J. Magn. Magn. Mater.* **2020**, *515*, 167305. <https://doi.org/10.1016/j.jmmm.2020.167305>.
- (339) Lu, Y. P.; Ji, C. X.; Sun, Y. L.; Fang, Y.; Zhang, L.; Han, Z. D.; Qian, B.; Jiang, X. F.; Zhou, W. P. Magnetic, Dielectric and Magnetoelectric Properties of Polycrystalline $\text{Nb}_2\text{Co}_4\text{O}_9$. *J. Alloys Compd.* **2016**, *679*, 213–217. <https://doi.org/10.1016/j.jallcom.2016.04.053>.
- (340) Lee, N.; Oh, D. G.; Choi, S.; Moon, J. Y.; Kim, J. H.; Shin, H. J.; Son, K.; Nuss, J.; Kiryukhin, V.; Choi, Y. J. Highly Nonlinear Magnetoelectric Effect in Buckled-Honeycomb Antiferromagnetic $\text{Co}_4\text{Ta}_2\text{O}_9$. *Sci. Rep.* **2020**, *10* (1), 12362. <https://doi.org/10.1038/s41598-020-69117-5>.
- (341) Choi, S. et al. Noncollinear Antiferromagnetic Order in the Buckled Honeycomb Lattice of Magnetoelectric $\text{Co}_4\text{Ta}_2\text{O}_9$ Determined by Single-Crystal Neutron Diffraction. *Phys. Rev. B* **2020**, *102* (21), 214404. <https://doi.org/10.1103/PhysRevB.102.214404>.
- (342) Deng, G.; Zhao, G.; Zhu, S.; Feng, Z.; Ren, W.; Cao, S.; Studer, A.; McIntyre, G. J. Spin Dynamics, Critical Scattering and Magnetoelectric Coupling Mechanism of $\text{Mn}_4\text{Nb}_2\text{O}_9$. *New J. Phys.* **2022**, *24* (8), 083007. <https://doi.org/10.1088/1367-2630/ac7cbe>.
- (343) Yamada, A.; Chung, S. C.; Hinokuma, K. Optimized LiFePO_4 for Lithium Battery Cathodes. *J. Electrochem. Soc.* **2001**, *148* (3), A224. <https://doi.org/10.1149/1.1348257>.
- (344) Lin, F.; Markus, I. M.; Nordlund, D.; Weng, T.-C.; Asta, M. D.; Xin, H. L.; Doeff, M. M. Surface Reconstruction and Chemical Evolution of Stoichiometric Layered Cathode Materials for Lithium-Ion Batteries. *Nat. Commun.* **2014**, *5* (1), 3529. <https://doi.org/10.1038/ncomms4529>.

- (345) Kim, J.-S.; Choi, J.-H.; Jeong, B.-M.; Kang, H.-J.; Kim, J.-S.; Choi, J.-H.; Jeong, B.-M.; Kang, H.-J. Luminescence Characteristics and Crystal Structure of $\text{CaWO}_4\text{-Li}_2\text{WO}_4\text{-Eu}_2\text{O}_3$ Phosphors. *J. Korean Ceram. Soc.* **43** (1), 10.
- (346) Ge, X.; Li, N.; Yu, X.; Cheng, J.; Chang, S.; Zhao, Q.; Cui, H.; Feng, K.; Liu, S.; Yang, X. $\text{Li}_2\text{Ni}(\text{WO}_4)_2/\text{C}$: A Potential Tungstate Anode Material for Lithium Ion Batteries. *J. Alloys Compd.* **2021**, 888, 161535. <https://doi.org/10.1016/j.jallcom.2021.161535>.
- (347) Sales, A. G. C. et al. Heat Treatment Influence on Structural and Optical Properties of NiWO_4 Crystals. *J. Solid State Chem.* **2023**, 318, 123773. <https://doi.org/10.1016/j.jssc.2022.123773>.
- (348) Yu, A.; Kumagai, N.; Liu, Z.; Lee, J. Y. Electrochemical Lithium Intercalation into WO_3 and Lithium Tungstates $\text{Li}_x\text{WO}_{3+x/2}$ of Various Structures. *J. Solid State Electrochem.* **1998**, 2 (6), 394–400. <https://doi.org/10.1007/s100080050116>.
- (349) Hashimoto, S.; Matsuoka, H.; Kagechika, H.; Susa, M.; Goto, K. S. Degradation of Electrochromic Amorphous WO_3 Film in Lithium-Salt Electrolyte. *J. Electrochem. Soc.* **1990**, 137 (4), 1300. <https://doi.org/10.1149/1.2086652>.
- (350) Wang, Z.; Chen, G.; Zhang, H.; Liang, L.; Gao, J.; Cao, H. In Situ TEM Investigation of Hexagonal WO_3 Irreversible Transformation to Li_2WO_4 . *Scr. Mater.* **2021**, 203, 114090. <https://doi.org/10.1016/j.scriptamat.2021.114090>.
- (351) Huang, X. H.; Tu, J. P.; Zhang, C. Q.; Zhou, F. Hollow Microspheres of NiO as Anode Materials for Lithium-Ion Batteries. *Electrochimica Acta* **2010**, 55 (28), 8981–8985. <https://doi.org/10.1016/j.electacta.2010.08.039>.
- (352) Verrelli, R.; Hassoun, J. High-Capacity NiO–(Mesocarbon Microbeads) Conversion Anode for Lithium-Ion Battery. *ChemElectroChem* **2015**, 2 (7), 988–994. <https://doi.org/10.1002/celec.201500069>.
- (353) Steiner, P.; Höchst, H. X-Ray Excited Photoelectron Spectra of LiNbO_3 : A Quantitative Analysis. *Z. Für Phys. B Condens. Matter* **1979**, 35 (1), 51–59. <https://doi.org/10.1007/BF01322081>.
- (354) Hamrin, K.; Johansson, G.; Gelius, U.; Nordling, C.; Siegbahn, K. Valence Bands and Core Levels of the Isoelectronic Series LiF, BeO, BN, and Graphite Studied by ESCA. *Phys. Scr.* **1970**, 1 (5–6), 277. <https://doi.org/10.1088/0031-8949/1/5-6/018>.
- (355) Schechter, A.; Aurbach, D.; Cohen, H. X-Ray Photoelectron Spectroscopy Study of Surface Films Formed on Li Electrodes Freshly Prepared in Alkyl Carbonate Solutions. *Langmuir* **1999**, 15 (9), 3334–3342. <https://doi.org/10.1021/la981048h>.
- (356) Dedryvère, R.; Laruelle, S.; Grugeon, S.; Gireaud, L.; Tarascon, J.-M.; Gonbeau, D. XPS Identification of the Organic and Inorganic Components of the Electrode/Electrolyte Interface Formed on a Metallic Cathode. *J. Electrochem. Soc.* **2005**, 152 (4), A689. <https://doi.org/10.1149/1.1861994>.

- (357) Mancheva, M. N.; Iordanova, R. S.; Klissurski, D. G.; Tyuliev, G. T.; Kunev, B. N. Direct Mechanochemical Synthesis of Nanocrystalline NiWO₄. *J. Phys. Chem. C* **2007**, 111 (3), 1101–1104. <https://doi.org/10.1021/jp065071k>.
- (358) Peck, M. A.; Langell, M. A. Comparison of Nanoscaled and Bulk NiO Structural and Environmental Characteristics by XRD, XAFS, and XPS. *Chem. Mater.* **2012**, 24 (23), 4483–4490. <https://doi.org/10.1021/cm300739y>.
- (359) Green, S. V.; Kuzmin, A.; Purans, J.; Granqvist, C. G.; Niklasson, G. A. Structure and Composition of Sputter-Deposited Nickel-Tungsten Oxide Films. *Thin Solid Films* **2011**, 519 (7), 2062–2066. <https://doi.org/10.1016/j.tsf.2010.10.033>.
- (360) Schulze, M.; Reissner, R.; Lorenz, M.; Radke, U.; Schnurnberger, W. Photoelectron Study of Electrochemically Oxidized Nickel and Water Adsorption on Defined NiO Surface Layers. *Electrochimica Acta* **1999**, 44 (23), 3969–3976. [https://doi.org/10.1016/S0013-4686\(99\)00172-3](https://doi.org/10.1016/S0013-4686(99)00172-3).
- (361) Biesinger, M. C.; Lau, L. W. M.; Gerson, A. R.; Smart, R. S. C. The Role of the Auger Parameter in XPS Studies of Nickel Metal, Halides and Oxides. *Phys. Chem. Chem. Phys.* **2012**, 14 (7), 2434–2442. <https://doi.org/10.1039/C2CP22419D>.
- (362) Li, D.; Li, H.; Danilov, D.; Gao, L.; Zhou, J.; Eichel, R.-A.; Yang, Y.; Notten, P. H. L. Temperature-Dependent Cycling Performance and Ageing Mechanisms of C₆/LiNi_{1/3}Mn_{1/3}Co_{1/3}O₂ Batteries. *J. Power Sources* **2018**, 396, 444–452. <https://doi.org/10.1016/j.jpowsour.2018.06.035>.
- (363) Li, D.; Li, H.; Danilov, D. L.; Gao, L.; Chen, X.; Zhang, Z.; Zhou, J.; Eichel, R.-A.; Yang, Y.; Notten, P. H. L. Degradation Mechanisms of C₆/LiNi_{0.5}Mn_{0.3}Co_{0.2}O₂ Li-Ion Batteries Unraveled by Non-Destructive and Post-Mortem Methods. *J. Power Sources* **2019**, 416, 163–174. <https://doi.org/10.1016/j.jpowsour.2019.01.083>.
- (364) Campion, C. L.; Li, W.; Lucht, B. L. Thermal Decomposition of LiPF₆-Based Electrolytes for Lithium-Ion Batteries. *J. Electrochem. Soc.* **2005**, 152 (12), A2327. <https://doi.org/10.1149/1.2083267>.
- (365) Wagner, C. D. *Handbook of X-Ray Photoelectron Spectroscopy: A Reference Book of Standard Data for Use in x-Ray Photoelectron Spectroscopy*, Perkin-Elmer.; Cornell University, 1979.
- (366) Birnie, D. P. Spin Coating Technique. In *Sol-Gel Technologies for Glass Producers and Users*; Aegerter, M. A., Mennig, M., Eds.; Springer US: Boston, MA, 2004; pp 49–55. https://doi.org/10.1007/978-0-387-88953-5_4.
- (367) Birnie, D. P. Spin Coating: Art and Science. In *Chemical Solution Deposition of Functional Oxide Thin Films*; Schneller, T., Waser, R., Kosec, M., Payne, D., Eds.; Springer: Vienna, 2013; pp 263–274. https://doi.org/10.1007/978-3-211-99311-8_11.
- (368) Meyerhofer, D. Characteristics of Resist Films Produced by Spinning. *J. Appl. Phys.* **1978**, 49 (7), 3993–3997. <https://doi.org/10.1063/1.325357>.

- (369) CRC Handbook of Chemistry and Physics, 102nd edition 2021-2022.; Rumble, J. R., Ed.; CRC Press: Boca Raton London New York, 2021.
- (370) Klejnot, O. J. Chloride Alkoxides of Pentavalent Tungsten. *Inorg. Chem.* **1965**, 4 (11), 1668–1670. <https://doi.org/10.1021/ic50033a034>.
- (371) Judeinstein, P.; Livage, J. Sol–Gel Synthesis of WO₃ Thin Films. *J Mater Chem* **1991**, 1 (4), 621–627. <https://doi.org/10.1039/JM9910100621>.
- (372) Bortoluzzi, M.; Guarra, F.; Marchetti, F.; Pampaloni, G.; Zacchini, S. Different Outcomes in the Reactions of WCl₆ with Carboxylic Acids. *Polyhedron* **2015**, 99, 141–146. <https://doi.org/10.1016/j.poly.2015.07.015>.
- (373) Kabir, I. I.; Sheppard, L. R.; Liu, R.; Yao, Y.; Zhu, Q.; Chen, W.-F.; Koshy, P.; Sorrell, C. C. Contamination of TiO₂ Thin Films Spin Coated on Rutile and Fused Silica Substrates. *Surf. Coat. Technol.* **2018**, 354, 369–382. <https://doi.org/10.1016/j.surfcoat.2018.09.009>.
- (374) Perera, S. S.; Munasinghe, H. N.; Yatooma, E. N.; Rabuffetti, F. A. Microwave-Assisted Solid-State Synthesis of NaRE(MO₄)₂ Phosphors (RE = La, Pr, Eu, Dy; M = Mo, W). *Dalton Trans.* **2020**, 49 (23), 7914–7919. <https://doi.org/10.1039/D0DT00999G>.
- (375) Scherrer, P. Bestimmung Der Größe Und Der Inneren Struktur von Kolloidteilchen Mittels Röntgenstrahlen. *Nachrichten Von Ges. Wiss. Zu Gött. Math.-Phys. Kl.* **1918**, 1918, 98–100.
- (376) Patterson, A. L. The Scherrer Formula for X-Ray Particle Size Determination. *Phys. Rev.* **1939**, 56 (10), 978–982. <https://doi.org/10.1103/PhysRev.56.978>.
- (377) Da Rocha, M.; Dunn, B.; Rougier, A. Faradaic and/or Capacitive: Which Contribution for Electrochromism in NiO Thin Films Cycled in Various Electrolytes? *Sol. Energy Mater. Sol. Cells* **2019**, 201, 110114. <https://doi.org/10.1016/j.solmat.2019.110114>.
- (378) Lu, Y. M.; Hwang, W. S.; Yang, J. S.; Chuang, H. C. Properties of Nickel Oxide Thin Films Deposited by RF Reactive Magnetron Sputtering. *Thin Solid Films* **2002**, 420–421, 54–61. [https://doi.org/10.1016/S0040-6090\(02\)00654-5](https://doi.org/10.1016/S0040-6090(02)00654-5).
- (379) Tuna, Ö.; Mak, A. K.; Öztürk, O.; Karabulut, M. Influence of Oxygen Partial Pressure on the Structural, Optical and Electrochromic Properties of NiO Thin Films Grown by Magnetron Sputtering. *Appl. Phys. A* **2023**, 129 (12), 820. <https://doi.org/10.1007/s00339-023-07090-2>.
- (380) Avramov, I.; Vassilev, Ts.; Penkov, I. The Glass Transition Temperature of Silicate and Borate Glasses. *J. Non-Cryst. Solids* **2005**, 351 (6–7), 472–476. <https://doi.org/10.1016/j.jnoncrysol.2005.01.044>.
- (381) Ojovan, M. I. Viscosity and Glass Transition in Amorphous Oxides. *Adv. Condens. Matter Phys.* **2008**, 2008, 1–23. <https://doi.org/10.1155/2008/817829>.
- (382) Belova, E. V.; Kolyagin, Ya. A.; Uspenskaya, I. A. Structure and Glass Transition Temperature of Sodium-Silicate Glasses Doped with Iron. *J. Non-Cryst. Solids* **2015**, 423–424, 50–57. <https://doi.org/10.1016/j.jnoncrysol.2015.04.039>.

- (383) Benharrat, L.; Guerbous, L.; Bradai, D.; Boukerika, A.; Manseri, A.; Selmi, N.; Rahal, B.; Hamroun, M. S. E. Preparation and Characterization of Luminescent YPO₄: Eu³⁺ Thin Films Using Sol Gel Spin Coating Method. *Thin Solid Films* **2020**, 694, 137738. <https://doi.org/10.1016/j.tsf.2019.137738>.
- (384) Shuji Nakamura, S. N. GaN Growth Using GaN Buffer Layer. *Jpn. J. Appl. Phys.* **1991**, 30 (10A), L1705. <https://doi.org/10.1143/JJAP.30.L1705>.
- (385) Nakamura, S.; Mukai, T.; Senoh, M. Candela-Class High-Brightness InGaN/AlGaIn Double-Heterostructure Blue-Light-Emitting Diodes. *Appl. Phys. Lett.* **1994**, 64 (13), 1687–1689. <https://doi.org/10.1063/1.111832>.
- (386) Kubelka, P.; Munk, F. Ein Beitrag Zur Optik Der Farbanstriche. *Z. Für Tech. Phys.* **1931**, 11a, 593–601.
- (387) Kubelka, P. New Contributions to the Optics of Intensely Light-Scattering Materials Part I. *J. Opt. Soc. Am.* **1948**, 38 (5), 448. <https://doi.org/10.1364/JOSA.38.000448>.
- (388) Lindberg, J. D.; Snyder, D. G. Determination of the Optical Absorption Coefficient of Powdered Materials Whose Particle Size Distribution and Refractive Indices Are Unknown. *Appl. Opt.* **1973**, 12 (3), 573. <https://doi.org/10.1364/AO.12.000573>.
- (389) Lv, P.; Chen, D.; Li, W.; Xue, L.; Huang, F.; Liang, J. Subsolidus Phase Relationships in the System ZnO–Li₂O–WO₃. *J. Alloys Compd.* **2008**, 460 (1), 142–146. <https://doi.org/10.1016/j.jallcom.2007.06.005>.
- (390) Wang, J.; Toby, B. H.; Lee, P. L.; Ribaud, L.; Antao, S. M.; Kurtz, C.; Ramanathan, M.; Von Dreele, R. B.; Beno, M. A. A Dedicated Powder Diffraction Beamline at the Advanced Photon Source: Commissioning and Early Operational Results. *Rev. Sci. Instrum.* **2008**, 79 (8), 085105. <https://doi.org/10.1063/1.2969260>.
- (391) Avdeev, M.; Hester, J. R. ECHIDNA: A Decade of High-Resolution Neutron Powder Diffraction at OPAL. *J. Appl. Crystallogr.* **2018**, 51 (6), 1597–1604. <https://doi.org/10.1107/S1600576718014048>.
- (392) La Fontaine, C.; Belin, S.; Barthe, L.; Roudenko, O.; Briois, V. ROCK: A Beamline Tailored for Catalysis and Energy-Related Materials from Ms Time Resolution to Mm Spatial Resolution. *Synchrotron Radiat. News* **2020**, 33 (1), 20–25. <https://doi.org/10.1080/08940886.2020.1701372>.
- (393) Ravel, B.; Newville, M. ATHENA , ARTEMIS , HEPHAESTUS : Data Analysis for X-Ray Absorption Spectroscopy Using IFEFFIT. *J. Synchrotron Radiat.* **2005**, 12 (4), 537–541. <https://doi.org/10.1107/S0909049505012719>.
- (394) van der Walt, S.; Schönberger, J. L.; Nunez-Iglesias, J.; Boulogne, F.; Warner, J. D.; Yager, N.; Gouillart, E.; Yu, T. Scikit-Image: Image Processing in Python. *PeerJ* **2014**, 2, e453. <https://doi.org/10.7717/peerj.453>.
- (395) Allan, Daniel B.; Caswell, Thomas; Keim, Nathan C.; van der Wel, Casper M.; Verweij, Ruben W. Soft-Matter/Trackpy: Trackpy v0.5.0, 2021. <https://doi.org/10.5281/ZENODO.4682814>.

- (396) Byrnes, S. J. Multilayer Optical Calculations. **2016**. <https://doi.org/10.48550/ARXIV.1603.02720>.
- (397) Aftab, M.; Butt, M. Z.; Ali, D.; Tanveer, M. U.; Hussnain, A. Effect of Molarity on the Structure, Optical Properties, and Surface Morphology of (002)-Oriented Ni₂O₃ Thin Films Deposited via Spray Pyrolysis: Effect of Molarity on the Properties of Ni₂O₃ Thin Films. *Proc. Pak. Acad. Sci. Phys. Comput. Sci.* **2021**, 57 (2), 51–74.
- (398) Abdelghani, L.; Said, L.; Said, B.; Okba, B. Spin Coating Method Deposited Nickel Oxide Thin Films with Various Film Thicknesses. *J. Chem. Res.* **2022**, 46 (1), 174751982110665. <https://doi.org/10.1177/17475198211066535>.

Coloration-bleaching mechanisms in nickel-tungsten mixed oxides

Abstract: The threats of climate change call for an immediate decrease in the amount of greenhouse gas emissions emitted globally. To achieve this, using energy efficient materials in the buildings sector is a key strategy. The electrochromic smart window is thus a very interesting technology to develop; in some commercially available products, a magnetron sputtered, nanocomposite Li-Ni-W mixed oxide is used as the positive electrode. However, many questions remain about the relationships between composition, structure, and electrochromic properties in such materials. The aim of this doctoral research is to bring some fundamental understanding on these nanocomposite Li-Ni-W-O thin films. At first, the $\text{Li}_2\text{O-NiO-WO}_3$ ternary phase diagram was completed by synthesizing and characterizing a new phase, $\text{Li}_2\text{Ni}_2\text{W}_2\text{O}_9$. Then, the electrochemical behavior and the XPS spectra of $\text{Li}_x\text{Ni}_y\text{W}_z\text{O}_n$ powders were compared to those of the reference nanocomposite thin film, revealing that the activity of the film at low potentials was due to a conversion reaction involving the $\text{Ni}^{2+}/\text{Ni}^0$ redox couple. Finally, by comparing spin-coated $\text{Li}_x\text{Ni}_y\text{W}_z\text{O}_n$ thin films and the reference nanocomposite thin film, it appears that the electrochromic properties in these systems at high potentials is allowed by the right balance of active NiO_z nanocrystallites and amorphous matrix. All of these observations lay the groundwork for an optimization of the electrochromic performances in nanocomposite Li-Ni-W-O thin films in the future.

Keywords: Electrochromism, Nanocomposite, Thin films, Nickel oxide, Synthesis

Mécanismes de coloration-décoloration dans les oxydes mixtes nickel-tungstène

Résumé : Les menaces du changement climatique demandent une diminution immédiate des quantités de gaz à effet de serre émises dans le monde. Pour se faire, il est essentiel d'utiliser des matériaux à haute efficacité énergétique dans le secteur du bâtiment. De fait, les vitrages électrochromes sont une technologie importante à développer ; certains, déjà disponible sur le marché, utilisent comme électrode positive une couche mince faite d'un oxyde mixte Li-Ni-W, obtenue par pulvérisation magnétron. Cependant, beaucoup d'incertitudes subsistent sur les relations entre la composition, la structure, et les propriétés électrochromes dans ces matériaux. Le but de ce projet doctoral est d'apporter une meilleure compréhension de ces couches minces Li-Ni-W-O nanocomposites. Tout d'abord, le diagramme de phase ternaire $\text{Li}_2\text{O-NiO-WO}_3$ a été complété par la synthèse et la caractérisation d'une nouvelle phase, $\text{Li}_2\text{Ni}_2\text{W}_2\text{O}_9$. Puis, le comportement électrochimique et les spectres XPS de poudres $\text{Li}_x\text{Ni}_y\text{W}_z\text{O}_n$ ont été comparés à ceux de la couche mince nanocomposite de référence, révélant que l'activité à bas potentiels de cette dernière est due à une réaction de conversion impliquant le couple rédox $\text{Ni}^{2+}/\text{Ni}^0$. Enfin, en comparant des couches minces $\text{Li}_x\text{Ni}_y\text{W}_z\text{O}_n$ obtenues par enduction centrifuge et la couche mince nanocomposite de référence, il apparaît que les propriétés électrochromes de ces systèmes à hauts potentiels est permise par des proportions équilibrées de nanocristaux de NiO_z d'un côté, et de matrice amorphe de l'autre. Toutes ces observations pavent le chemin vers l'optimisation des performances électrochromes de ces couches minces nanocomposites Li-Ni-W-O.

Mots-clés : Electrochromisme, Nanocomposite, Couches minces, Oxyde de nickel, Synthèse